Attenuating jet installation noise with a lobed nozzle

Master of Science Thesis

J. H. Mijjer

TUDelft

Attenuating jet installation noise with a lobed nozzle

Master of Science Thesis

by

J. H. Mijjer

to obtain the degree of Master of Science
at the Delft University of Technology,
to be defended publicly on the 27th of October, 2021.

Student number: 4459210
Project duration: December 1, 2020 – October 27, 2021

Thesis committee

Chair: Prof. Dr. ir. D. Casalino

Committee members: Dr. ir. D. Fiscaletti   (supervisor)
                          Dr. ir. W. J. Baars,   (supervisor)
                          Dr. ir. A. Gangoli Rao   (examiner)

An electronic version of this thesis is available at `http://repository.tudelft.nl/`.

TUDelft

Abstract

Over the last few decades, the bypass ratio and the nacelle diameter of modern turbofans have been increasing to achieve higher efficiencies. This trend has forces the under-wing-mounted engines to be coupled more closely to the wing surface and the flap system, which significantly enhances the low-frequency noise, known as *jet installation noise* (JIN). In this thesis, lobed nozzles are proposed and tested as a passive flow control technique for the reduction of the JIN. This work will be the first study that involves both jet aerodynamics and far-field acoustic measurements.

Previous research has shown that the lobed jet generates less low-frequency noise and more high-frequency noise than the circular jet. This is attributed to the faster development of the shear layer of the lobed jet, which results in a more multiscale flow than the circular jet. These conclusion have been verified with the measurements done in this work. In specific, it has been found that both jets initially experience a dominance of large-scale structures at the nozzle exit. For the circular jet, this dominance remains up to eight (circular nozzle exit) diameters downstream from the nozzle exit, whereas this dominance disappears already at five diameters downstream for the lobed jet.

When a plate is installed in proximity of the jet, the generated jet installation noise differs between the circular and lobed jet. The difference between the jets is dependent on the jet-plate configuration. For a plate with its the trailing-edge placed at a minimum of five diameters downstream from the nozzle exit, and with the plate positioned at a radial distance from the nozzle that is large enough to prevent grazing of the flow on the plate surface, it is expected that the investigated lobed nozzle generates less jet installation noise than the investigated circular nozzle. On top of that, it is expected that the generated low-frequency hump by the lobed jet shifts to higher frequencies than for the circular jet. This is expected with the observed difference in turbulence scales in the jets at this downstream region.

For configurations with the trailing-edge of the plate positioned more upstream, it is expected that the lobed jet does not generate less jet installation noise. It could be concluded that for such configurations the lobed jet generates a low-frequency hump that has more noise radiated at lower frequencies than for the circular jet. From the near-field pressure measurements of the lobed jet, it could be concluded that the hydrodynamic pressure waves at very low frequencies have a larger radial extent from the jet-axis than the circular jet. However, this could be attributed to the larger jet spread that is observed for the lobed jet with respect to the circular jet. For higher frequencies in the low-frequency region, it could be concluded that the hydrodynamic pressure waves have a larger radial extent for the circular jet than the lobed jet. Hence, the difference in the generated low-frequency hump by the installed jets is caused by the difference in intensity of the hydrodynamic pressure waves that are scattered at the trailing-edge.

In the high-frequency region, it could be concluded that the plate is more effective in blocking the noise radiated by the small-scale pressure waves for the lobed jet than the circular jet. This is visible along the sideline directions at the shielded side of the installed jet. On the contrary, at the unshielded side of the jet more high-frequency noise is observed for the lobed jet due to higher intensity of small-scale structures in the jet with respect to the circular jet.

Lastly, it could be concluded that the hydrodynamic pressure waves behave differently between the different jets. It could be observed that at low frequencies the hydrodynamic pressure waves are convected at a larger velocity for the circular jet than for the lobed jet. As a consequence, it could be observed that, compared to the far-field of the lobed jet, the low-frequency noise is perceived at higher frequencies in the far-field for the circular jet.

Acknowledgements

Contents

List of Figures

List of Tables

Nomenclature

List of Abbreviations

CN1   Baseline nozzle

Expt   Experimental data

FAA   Federal Aviation Authority

HWA   Hot-Wire Anemometry

ICAO   International Civil Aviation Organisation

LB1   Lobed nozzle 1

LB2   Lobed nozzle 2

LES   Large-Eddy Simulation

OASPL Overall Sound Pressure Level

PIV   Particle-Image Velocimetry

PSD   Power Spectral Density

SPL   Sound Pressure Level

TI   Turbulence Intensity

TKE   Total Kinetic Energy

UHBR Ultra-High Bypass Ratio

Greek Symbols

α	Streamwise wavenumber	$[m^{-1}]$
β	Spreading rate of the jet	$[deg]$
Δs	Minimum distance between microphone 1 of the linear array and the baseline lipline	$[m]$
δ_β	Thickness of the annular shear layer of a jet	$[m]$
δ_c	Transversal diameter of the potential core	$[m]$
ϵ	Lobe penetration rate	$[-]$
ω	Vorticity	$[rad/s]$
ρ	Density	$[kg/m^3]$
ρ_{xy}	Normalized cross-correlation coefficient	$[-]$
σ	Radial coordinate with respect to the nozzle exit centre, square-root of the variance	$[m],[W^{0.5}]$
τ	Time-delay factor	$[s]$
θ	Observation, polar angle	$[deg]$
φ	Azimuthal angle	$deg]$

$L_{\Delta\theta}$	Radial turbulence length scale	$[m]$
L_η	Azimuthal turbulence length scale	$[m]$
L_ζ	Axial turbulence length scale	$[m]$

Latin Symbols

a	Speed of sound	$[m/s]$
a_m	Cosine mode number m	$[-]$
b_m	Sine mode number m	$[-]$
D	Diameter of the baseline nozzle exit	$[m]$
E	Voltage	$[V]$
f	Frequency	$[Hz]$
G_{uu}	Power	$[W]$
H	Separation distance between the jet-axis and the plate	$[m]$
I	Current	$[A]$
Im	Imaginary part of complex number	$[-]$
k	Wavenumber	$[m^{-1}]$
L	Streamwise distance between the nozzle exit and the trailing-edge of the plate	$[m]$
M	Mach number	$[-]$
m	Mode number	$[-]$
N	Number of lobes	$[-]$
P	Lobe penetration	$[m]$
p	Pressure	$[Pa]$
p'	Pressure fluctuations	$[Pa]$
P_a	Acoustic power	$[W]$
R	Mean radius of nozzle exit lipline	$[m]$
r	Distance between the observer and the sound source	$[m]$
R_w	Resistance of the wire	$[\square]$
Re	Real part of complex number	$[-]$
St	Strouhal number	$[-]$
T	Temperature	$[°C]$
t	Time	$[s]$
U	Velocity	$[m/s]$
u'	Streamwise velocity fluctuations	$[m/s]$
v',w'	Transverse velocity fluctuations	$[m/s]$
x	Streamwise distance from the nozzle exit	$[m]$
X_c	Potential core length	$[m]$
y	Radial distance from the jet-axis	$[m]$

1

Introduction

Since the early 1950s the aircraft noise has been considered as a bottleneck. Aircraft noise is a significant problem for the passengers and crew within the aircraft cabin [9, 60]. Since then, this noise problem has been reduced significantly to a magnitude that does not result in a deterioration of the physical and mental health of the aircraft passengers and crew [16, 27]. However, the noise generated by aircraft is not only perceived within the cabin, but also on the ground. As a result, certifications and regulations have been created and are used internationally in order to limit the noise perceived on the ground during take-off, cruise and landing [18, 26].

Additionally, the aircraft industry is pushed to operate in a more sustainable way and thus new technologies and procedures are constantly introduced. One of the improvements to make turbofan engines more efficient is the development of Ultra-High Bypass engines. These turbofans result in a significantly lower fuel consumption, cost and emissions [15]. With this increase in the bypass ratio, the aircraft can fly at lower velocities for the same generation of thrust [25]. As a consequence, the jet noise generated during the flight phases is reduced. However, the described increase of the bypass ratio triggers a different mechanism of sound production [41]. In order to sustain the ground clearance with under-wing-mounted engines, the high bypass engines are positioned closer to the wing surface. Subsequently, the jet exhaust flow experiences a stronger interaction with the wing surface and trailing-edge during flight, which leads to the generation of the so-called *jet installation noise* [52, 53].

To comply with the future, stricter noise regulations, this noise source should be attenuated. To do so, a passive method has been introduced in research, namely the use of a nozzle with an azimuthally lobed profile instead of the conventional circular profile [39]. The present work is aimed at investigating the use of a lobed nozzle geometry to attenuate the jet installation noise. Firstly, this chapter introduces the research objective with the research questions. On top of that, the coordinate system for this work is presented. This is followed by chapter 2 with the current state-of-the-art of the problem. Afterwards, the methods of analysis are presented in chapter 3. A detailed analysis of the data obtained from the measurements and its discussion is performed in chapter 4 to chapter 6. From the data analysis, conclusions will be drawn in order to assess whether the lobed nozzle is effective in attenuating the jet installation noise. A summary of the conclusions will be presented in chapter 7. Lastly, this work will end with a discussion of this work and recommendations for future work, presented in chapter 8.

1.1. Research Objective

The research objective is defined based on recent research on the previously described passive control method to reduce jet installation noise [37, 39]. As mentioned, little research has been done regarding the effect of this passive control method on the jet flow and specifically on the noise generated by these highly coupled jet-wing configurations. This MSc Thesis will be used to gain more insights into this knowledge gap.

The main research objective of this Thesis is:

"In order to attenuate the jet installation noise, a passive method involving a nozzle with a lobed profile instead of a conventional circular profile will be explored. Experimental analyses will be performed to investigate how the geometry of the lobed nozzle affects the jet installation noise."

Firstly, a literature survey will be conducted. This literature survey includes a review of the flow characteristics of an isolated subsonic jet flow, which is aimed at assessing how a lobed nozzle affects the jet flow. In order to make conclusions regarding the change in noise generation, a review will be conducted concerning the different sound sources in the jet that radiate noise to the far-field. This involves also the directivity of the sound sources, which will be examined during the experimental study to draw conclusions on the change in their relative contributions. Combining the aerodynamics with the aeroacoustics for a subsonic jet allows for a comparison in performance between the circular nozzle and the lobed nozzle.

On top of that, the change in jet and noise propagation due to the placement of a flat solid body nearby will be reviewed. This solid body is a surrogate for the wing surface. From the analysis of this review and of the flow characteristics of an isolated jet, the physical effects produced by the fluid-solid interaction will be clarified. These insights combined with the change in noise propagation enables to have a better understanding of the jet installation noise.

Lastly, a review of the research on lobed nozzles will be done, even though this is scarce to date. The review will give an overview of the current state-of-the-art of free jets from lobed nozzles. Identifying the change in the jet flow characteristics (in comparison to the circular jet) and the physical phenomena gives an insight into the potential change of the noise generation. Moreover, the noise generation of a jet from a lobed nozzle will also be studies in this review. An additional motivation for the described review is to validate the results from the experimental study object of the present research project. The experimental study will be based on the theory that is proposed in the research by Lyu and Dowling [39] concerning a jet from lobed nozzles with a flat plate in proximity.

The experimental campaign that is conducted will be presented in chapter 3. This campaign is used to answer the questions arising from the literature survey, and to verify the conclusion from current work. Moreover, all post-processing procedures will be presented in order for the reader to understand the data analysis that will follow this chapter.

1.2. Research Questions

The main research question that will be answered by reaching the project goal is:

"What is the effect of a lobed nozzle on the generated jet installation noise, when compared to a conventional circular nozzle?"

In order to answer the main research question, the following sub-questions need to be answered.

1. How does the lobed nozzle affect the flow development downstream of the nozzle, compared to the jet from the conventional circular nozzle?

   a. What is the change in the potential core length and the jet flow spreading rate?

   b. How does the radial velocity profile vary downstream of the nozzle exit?

   c. What is the change in the radial profile of the turbulence intensities downstream of the lobed nozzle exit?

   d. What is the change in the energy of turbulent scales that occur downstream of the nozzle exit?

   e. What is the change in magnitude of the hydrodynamic pressure waves that are convected downstream?

2. How does the isolated lobed nozzle affect the overall radiated noise, compared to the isolated conventional circular nozzle?

    a. What is the change in the Sound Pressure Level (SPL) contribution of the different sound sources?

    b. What is the change in the directivity of the different sound sources?

3. How does the lobed nozzle affect the jet installation noise generated when a flat plate is placed close to the jet?

    a. How does the lobe penetration affect the far-field sound?

    b. How does the number of lobes affect the far-field sound?

    c. How does the lobe length affect the far-field sound?

Answering these research questions will result in a complete understanding of the noise generation for an installed lobed nozzle. On top of that, it will ensure that a link can be made between the noise and the aerodynamic characteristics of the jet flow.

1.3. Coordinate system

Throughout this work, a consistent coordinate system will be used, which is presented in Figure 1.1 where a circular nozzle close is positioned closely to a flat plate. This coordinate system will also be used for the isolated jets with no plate installed in proximity. As can be observed in Figure 1.1a, the x-axis coincides with the centreline of the jet, with the y-axis perpendicular to the flat plate. The observer location is expressed in terms of polar angle θ. The sideline directions, which will be referred to in this work, correspond to an polar angle θ of $-90°$ and $90°$. The former polar angle is located at the unshielded side, whereas the latter is located at the shielded side. As shown, the shielded side corresponds to the region where the flat plate is in-between the observer and the jet, whereas the unshielded side is the region where no physical barrier exists between the observer and the jet. Moreover, with the presented coordinate system, shallow polar angles correspond to an observer location close to the jet-axis, between $-30° \leq \theta \leq 30°$.

As shown in Figure 1.1b, the z-axis is parallel to the flat plate, i.e. parallel to the span of the wing. Additionally, the azimuthal angle φ is introduced, with again an indication of the shielded and unshielded side. An azimuthal angle of $0°$ corresponds to unshielded side, whereas an angle of $180°$ corresponds to the shielded side. When looking at the front view, identified by the nozzle exit plane (Figure 1.1b), an observer located at a polar angle of $90°$ is equivalent to an observer located at an azimuthal angle of $180°$.

(a) Side view.

(b) Front view, observed from downstream of the nozzle exit and faced towards the nozzle exit.
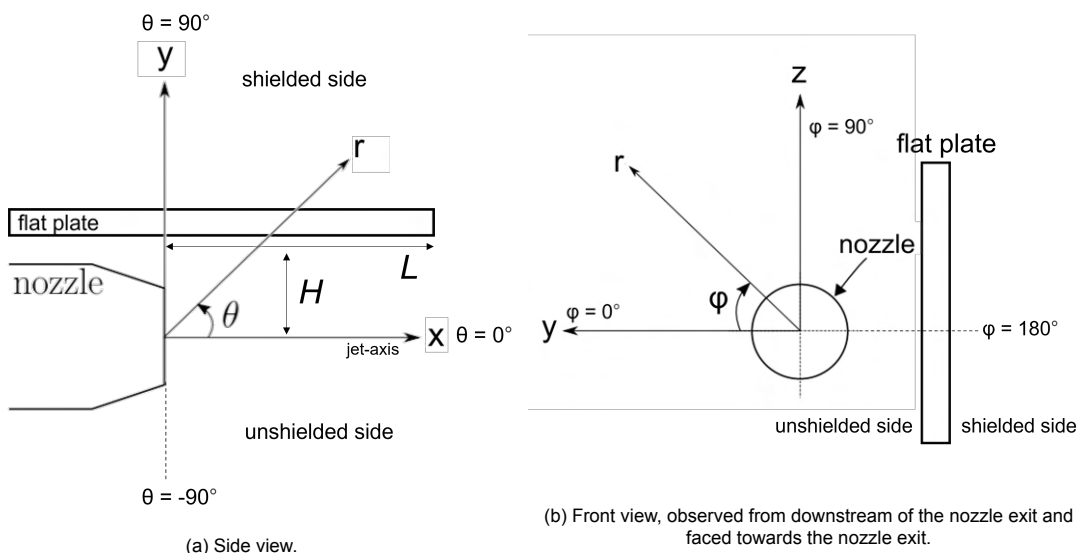
Figure 1.1: Illustration of the coordinate system used in this work [52].

In this work the jet is assumed to be a cold and subsonic jet. The jet itself will be single-stream and axisymmetric, and hence does not include the effect of an aircraft pylon or of a fuselage in proximity.

The flight velocity is considered to be parallel to the jet axis. Moreover, the wing that will be positioned in proximity of the jet is modelled as a flat plate with zero sweep angle. The flat plate will not include any flaps.

The configuration of the subsonic jet with a plate is defined by the separation distance H and the axial distance L, as shown in Figure 1.1. The former distance is the radial distance between the jet-axis and the plate surface. The latter distance is defined as the streamwise distance between the nozzle exit and the trailing-edge of the flat plate. Such a configuration will from now on be indicated as an *installed jet*. Both distances H and L will be expressed in terms of D in this work, corresponding to the diameter of the nozzle exit of the circular jet.

2

Literature Review

This chapter includes an overview of the literature survey conducted for this thesis work. The state-of-the-art of the aerodynamics and aeroacoustics of an isolated circular jet is given in section 2.1. This is followed by a similar overview for a circular jet with a plate installed in proximity, presented in section 2.2. The chapter will finish with an overview of the state-of-the-art of the jet from a lobed nozzle in section 2.3.

2.1. The Isolated Circular Jet

This section is aimed at analysing the fundamentals of an isolated subsonic jet. Firstly, the physical quantities characterising a jet are presented in subsection 2.1.1. Secondly, in subsection 2.1.2 the near-field and far-field of the jet is analysed with respect to the influence of the jet. Lastly, the link between the jet and the perceived far-field noise is presented in subsection 2.1.3.

2.1.1. General Aspects on the Jet Development

A schematic overview of an isolated subsonic jet is shown in Figure 2.1. This jet comprises a subsonic, circular jet within a quiescent ambient surroundings. The jet is assumed to be a single stream, unheated jet.
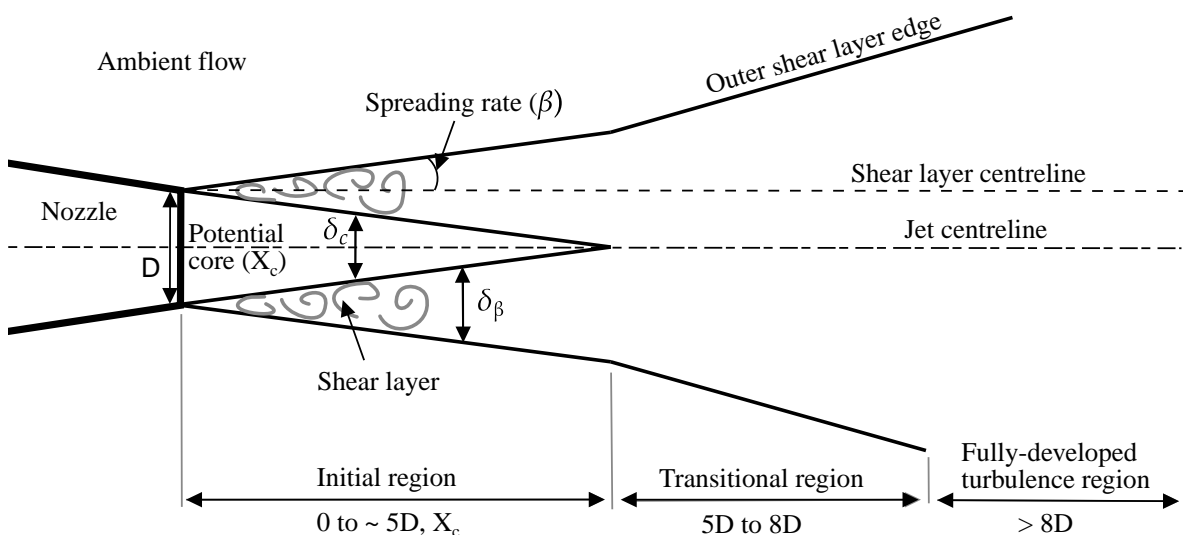
Figure 2.1: Schematic illustration of the flow regions in a single stream, isolated, subsonic jet.

The jet can be divided into several regions. Downstream of the nozzle exit the potential core (X_c) exists, which is initially the region of laminar and parallel flow from inside of the nozzle. Between the

potential core and the ambient flow, a thin turbulent shear layer forms, which contains turbulent eddies that develop downstream of the nozzle exit due to the presence of flow instabilities. The presence of the eddies results in mixing between the turbulent jet flow and the quiescent ambient fluid, thus producing a transfer of momentum and heat. The shear layer thickness (δ_β) grows with axial distance from the nozzle exit due to the injection of ambient flow. This process is called entrainment, and the region outside of the shear layer is considered as the entrainment region which is characterised by an unsteady irrotational flow. The increase of the mixing layer thickness leads to a reduction of the transversal diameter of the potential core (δ_c) as the distance from the nozzle increases, as shown in Figure 2.1. Do note that the jet is three-dimensional and thus an annular shear layer exists. The axial location where the annular shear layer merges is considered to be the beginning of the transitional region. At this location, the jet spreads at a greater spreading rate (β) than it did in the initial mixing region. After the transitional region, the turbulent flow is fully-developed [34, 50, 52].

Some observations can be made regarding the flow velocity development throughout the different regions. Firstly, the longitudinal mean velocity component is much larger than the transverse mean velocity component throughout the jet. The velocity fluctuations on the contrary are in all directions of the same order of magnitude [52]. The development of the mean velocity of the flow can be observed in Figure 2.2. A top-hat velocity profile occurs at the nozzle exit, which is smoothened out radially further downstream of the nozzle exit. The jet mean velocity profile can be approximated by assuming a turbulent round jet that spreads linearly, as shown in Equation 2.1 [52]. In this equation, U_{max} corresponds to the mean streamwise velocity component of the jet, y to the radial distance from the jet centreline and x to the streamwise distance from the nozzle exit. It can be observed in Figure 2.2 that the analytical relationship in Equation 2.1 agrees well with experimental data. Hence, the mean velocity in the jet is directly related to the potential core width and the thickness of the annular shear layer.

$$U(x,y) = \begin{cases} U_{\text{max}} \exp\left[-\dfrac{(y \pm \delta_c/2)^2}{\left(\delta_\beta/2\right)^2}\right] & \text{if } |y| > \delta_c/2 \\ U_{\text{max}} & \text{if } |y| \le \delta_c/2 \end{cases} \qquad (2.1)$$
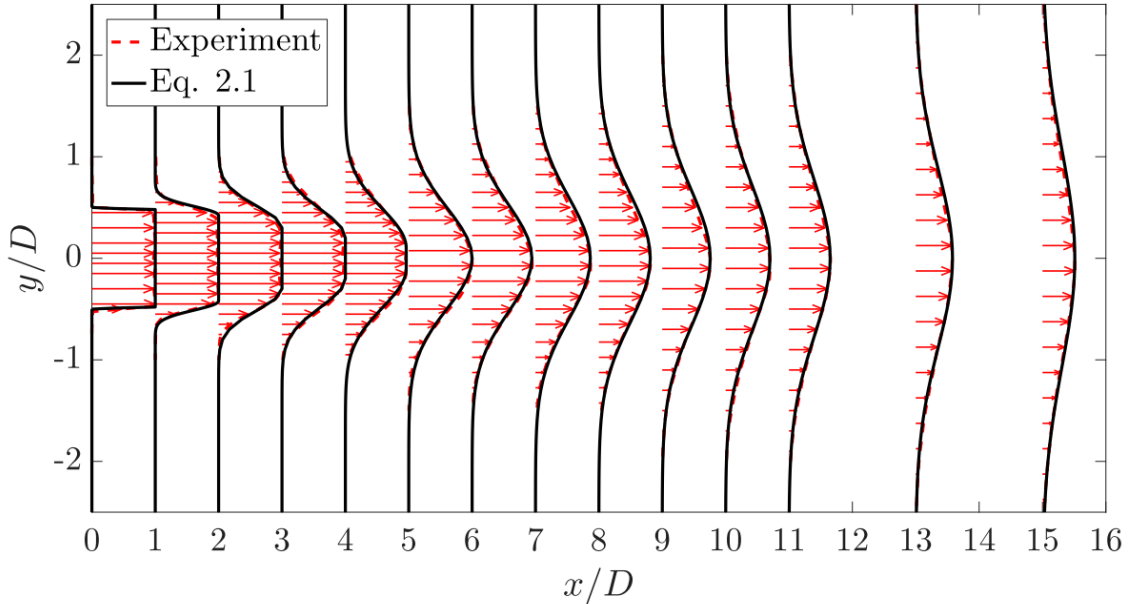
Figure 2.2: The radial profiles of the mean streamwise velocity of a single stream, isolated, subsonic jet, based on experimental data and on Equation 2.1 [52].

In the initial mixing region, the mean velocity profile and the jet spreading rate are independent of

the Reynolds number, which implies that the turbulence within the jet is statistically self-similar [50]. Thus, even though a higher Reynolds number results in a larger range of turbulent length scales, the flow development is similar as the statistical properties at all scales are the same. For the first half of the potential core, the jet flow can be considered two-dimensionally self-similar, while afterwards the flow can be considered fully axisymmetrically self-similar [34].

As mentioned before, the velocity fluctuations in all three directions are of similar magnitude, as well as self-similar. This is true in case the turbulence is homogeneous and isotropic locally [50]. Turbulence and its development are of significance to the far-field noise as the change in turbulence energy effects the produced noise. The development of the turbulence intensity in the axial direction is shown in Figure 2.3. The centreline of the shear layer experiences the highest turbulence intensity. This maximum intensity of the axial velocity component is approximately 15% of the jet velocity U_j, which exists at the end of the potential core. Farther downstream the turbulence intensity profile flattens out to an uniform distribution, indicating the end of the transitional region, i.e. the end of the turbulence development [32]. The mean turbulence intensity (TI) corresponds to the ratio of the local root-mean-square of the unsteady velocity component $\sqrt{u'^2}$ and the jet exit velocity U_j. The total turbulence intensity, i.e. the turbulent kinetic energy (TKE), can be computed using Equation 2.2. The distributions of the turbulence fluctuations in the two tranverse directions are similar to those shown in Figure 2.3.

$$TKE = \frac{1}{2}\left(\overline{u'^2} + \overline{v'^2} + \overline{w'^2}\right) \tag{2.2}$$
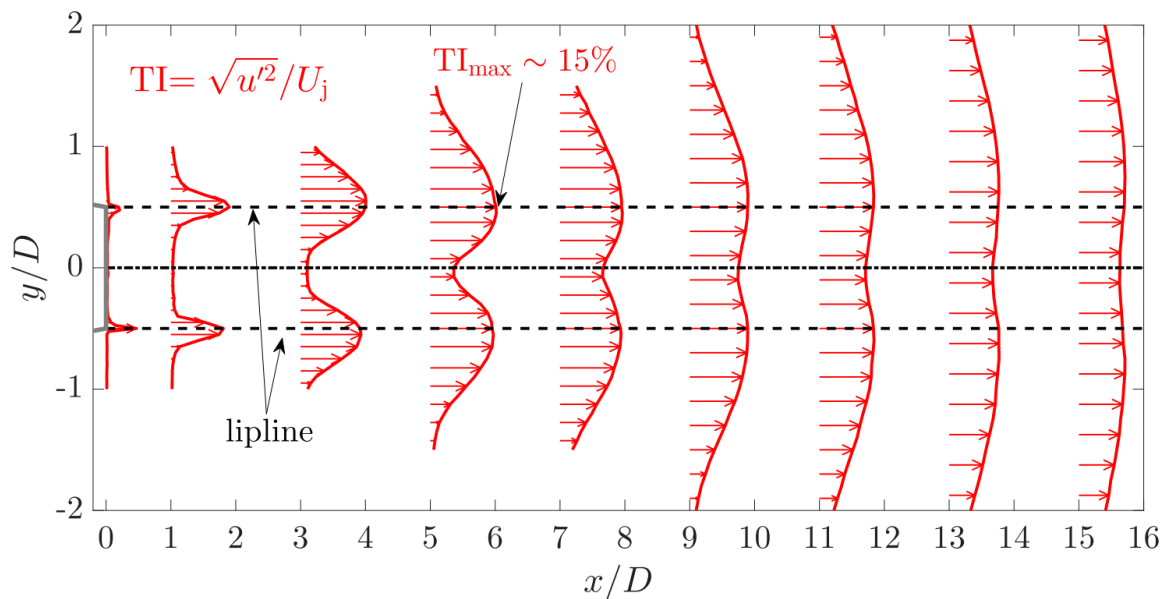
Figure 2.3: The radial profiles of the turbulence intensity (TI) distribution of a single stream, isolated, subsonic jet, based on experimental data [52].

2.1.2. The Near-field and Far-field of the Jet

As mentioned before, the noise generated is a consequence of a change in turbulence energy. The interaction between the three fluctuating components with the mean flow results in the shear stress that subsequently generates sound, dubbed as *jet mixing noise*. However, only a small part of the turbulent kinetic energy is converted into noise. Hence, a change in the turbulence does not directly result in variations of the acoustic field [52].

The far-field sound is generated by small pressure fluctuations. Research done by Arndt et al. (1997) involves the use of proper orthogonal decomposition (POD) of the pressure fluctuations that surround the turbulent jet [1]. This POD was applied to the irrotational entrainment region in order to study the spectral behaviour of the near-field pressure fluctuations. It was found that these fluctuations can be divided into two types, namely acoustic fluctuations that propagate acoustic energy to the far-field, and hydrodynamic fluctuations that only involve hydrodynamic pressure waves which rapidly decay in amplitude. The former are in phase with the velocity fluctuations, whereas the latter are 90° out of phase with the velocity fluctuations. The hydrodynamic fluctuations are confined to the near-field, whereas the acoustic disturbances manifest themselves also in the far-field [1].

The acoustic region and the hydrodynamic region can be characterised by the rate of decay of the near-field pressure fluctuations. This can be done with the product of the wavenumber k with the radial distance between the observer and the sound sources in the jet, expressed by r. The pressure fluctuations decay proportionally to kr^{-2}, $kr^{-6.67}$ and $kr^{-7/3}$ if they lie within the acoustic, irrotational linear hydrodynamic or rotational non-linear hydrodynamic region of the jet, respectively. Arndt et al. (1997) made the conclusion that for values larger than $kr = 2$, the hydrodynamic near-field does not affect the radiation of acoustic energy [1]. Only the acoustic field of the jet is radiated from this distance onwards. This can be visualized in Figure 2.4. For a larger vertical distance from the jet, the pressure decays to a negligible value for the hydrodynamic pressure waves. The position of the different regions and their decay is frequency-dependent (or wavenumber-dependent). The linear hydrodynamic region, for example, is located closer to the jet-axis and has a more significant decay for high frequencies.
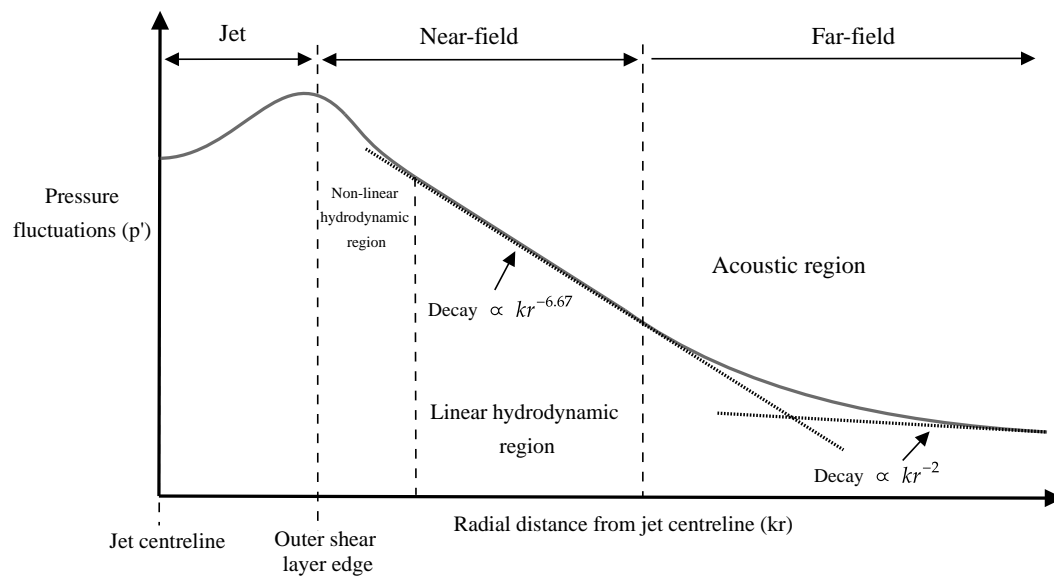
Figure 2.4: Change in near-field pressure fluctuations p' in radial direction, in terms of the wavenumber k and the distance r, for a subsonic jet.

The turbulent jet consists of both large-scale and small-scale eddies, as first found by Crow & Champagne (1971) [12]. The hydrodynamic region comprises relatively small energetic turbulent structures, whereas the acoustic region comprises coherent pressure waves. This difference between both fields is illustrated in Figure 2.5, with the coloured region indicating turbulent disturbances and the black and white regions indicating pressure waves. In the left figure, a side-view of the jet in the near-field can be observed, clearly indicating the shear layer development and showing the potential core downstream of the nozzle exit. In the right figure, a cross-section in the post-transitional region of the jet is shown. The black and white circular profiles around the jet correspond to the acoustic pressure waves, and thus also show the radiation of acoustic energy to the far-field.
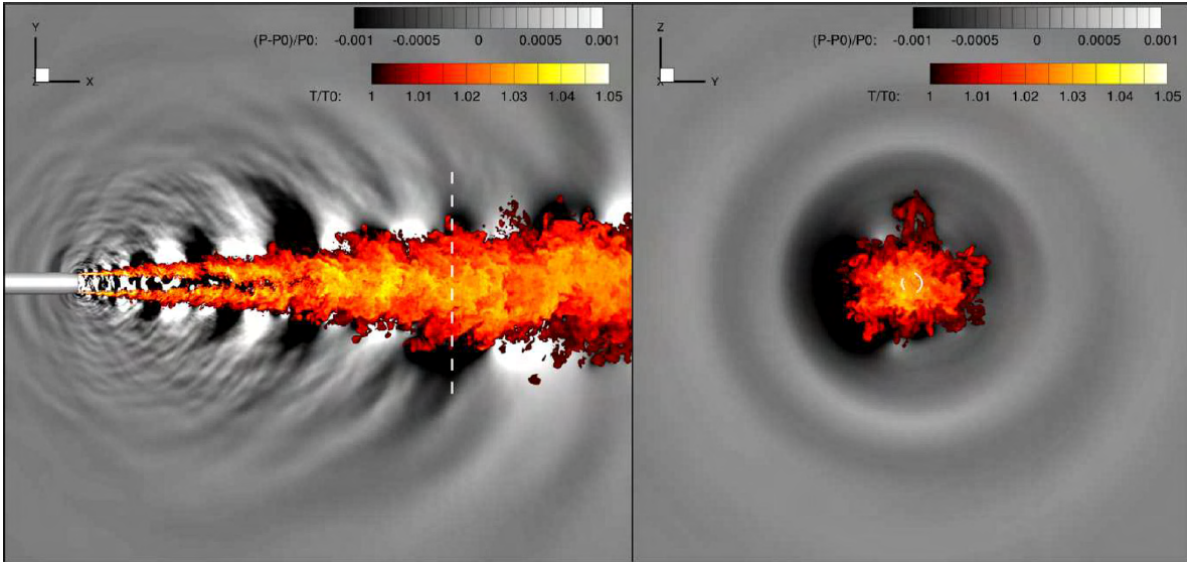
Figure 2.5: Illustration of the near-field of a jet with Mach number 0.9. The colours represent temperature fluctuations, indicating the turbulent disturbances, while the black and white regions show pressure fluctuations. [5].

2.1.3. General Aspects on the Jet Aeroacoustics

The noise produced by an isolated, subsonic jet within a medium at rest, can be modelled with a distribution of quadrupole sound sources, as first derived by Lighthill [36]. The quadrupole sound sources generate small amplitude density fluctuations that are comparable to the pressure fluctuations in a jet. A representation of this is shown in Figure 2.6. This model leads to the well-known *eight power law* for the acoustic field power, as presented in Equation 2.3, where the acoustic power is expressed in Joules per second [36]. The acoustic power, and thus the noise, has a velocity dependence corresponding to U_j^8. Hence, increasing the jet velocity will result in an increase in the generated noise.

$$P_a \sim \rho_0 a_0^{-5} D^2 U_j^8 \tag{2.3}$$
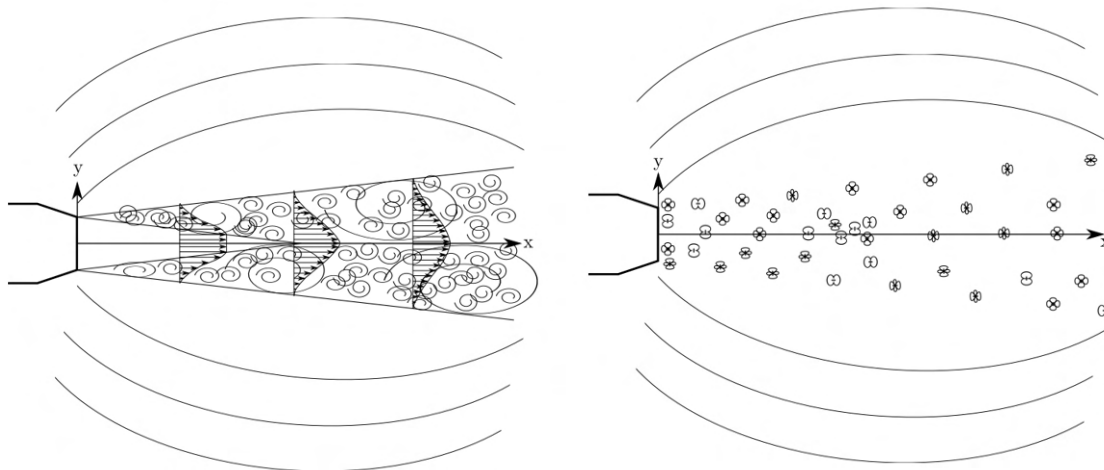
(a) Illustration of an jet with sound waves propagating to the far-field.

(b) Illustration of the jet as a stationary medium with a distribution of quadrupole sound sources radiating sound waves to the far-field.

Figure 2.6: Illustration of a jet propagating sound waves to the far-field [52].

The small-scale turbulence behaves as a compact source, whereas the large-scale turbulence behaves as a non-compact source. The smaller scales have dimensions that are significantly smaller than the jet diameter and the larger scales are comparable in size to the jet diameter. The larger tur-

bulent structures originate at the nozzle exit in the shear layer and are broken down through merging and cascading to small turbulent scales downstream of the potential core end [61].

The coherent large structures of the jet are the main source of the sound perceived at shallow observation angles θ, i.e. close to the jet-axis [61]. On the contrary, the small-scale turbulence of the jet is considered to be dominant along the sideline directions of the jet. A representation of this system can be found in Figure 2.7. The small-scale turbulence sound source is located just downstream of the potential core end.
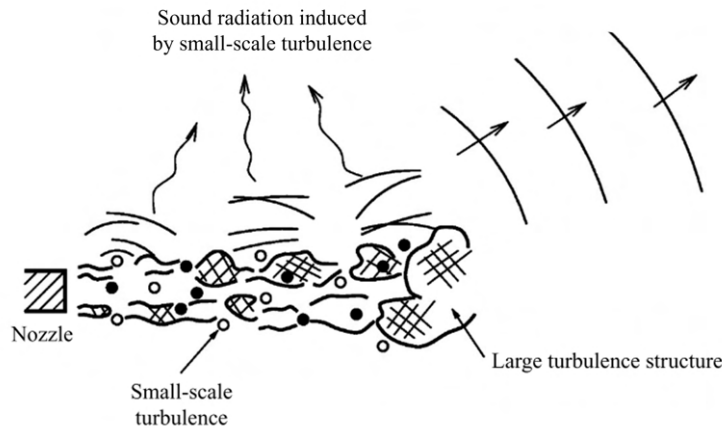
Figure 2.7: Illustration of the radiation directivity of the different turbulent scales [61].

The large-scale turbulence can be represented by jet instability waves that grow rapidly downstream until they reach their maximum amplitude, after which they decrease in amplitude. This process can be observed in Figure 2.5 by following the alternating black and white regions surrounding the jet, indicating wavepackets. The growth and decay of the jet instability waves is considered to be important for the noise generation [61].

Coherent pressure fluctuations (often modelled and referred to as wavepackets) can have an axial extent of six to eight nozzle diameters [11]. Modelling the organized structures within a turbulent jet as axially developed wavepackets gives the possibility to assess the stability characteristics regarding the spatial amplification and decay of the waves. This can then be used to assess the noise generated by the large-scale structures within the jet.

In order to analyse the structure of the different sound sources responsible for the radiated sound field, the pressure fluctuations can be decomposed into azimuthal Fourier modes. Many aspects regarding the flow physics could be gained after applying this analysis [10, 11, 17, 31, 46]. Research based on this analysis also includes the configuration with a flat plate installed closely, as well as a jet from a lobed nozzle. The results of this research will be analysed later in the report.

The decomposition of the near-field pressure in azimuthal Fourier modes outputs the axisymmetric mode 0 and the helical higher-order modes. The higher-order azimuthal modes can be defined as positive and negative modes, e.g. mode 1 and -1. The difference in sign is due to the fact that the higher-order modes are helical modes and the direction of rotation of these modes has an effect on the radiation of these wavepackets. The axisymmetric mode and the first helical mode of the wavepackets can be visualized in Figure 2.8. In the jet the helical modes do not have any preferred direction of rotation [46].

The region close to the jet axis, corresponding to low polar angles, is dominated by the axisymmetric mode 0 [8, 11]. This is in particular true for the peak frequency, i.e. the frequency at which the maximum energy occurs in the pressure spectrum. This latter observation indicates that the axisymmetric mode 0 is dominant in radiating sound to the far-field. The directivity of the axisymmetric mode and the second and third azimuthal modes are shown in Figure 2.9. The OASPL in this figure corresponds to the Overall Sound Pressure Level at the different observer locations, which is determined by integrating the Sound Pressure Level (SPL) over the entire range of frequencies. The sound is defined per frequency with

(a) Axisymmetric pressure wavepacket (m = 0).

(b) First helical pressure wavepacket (m = 1).
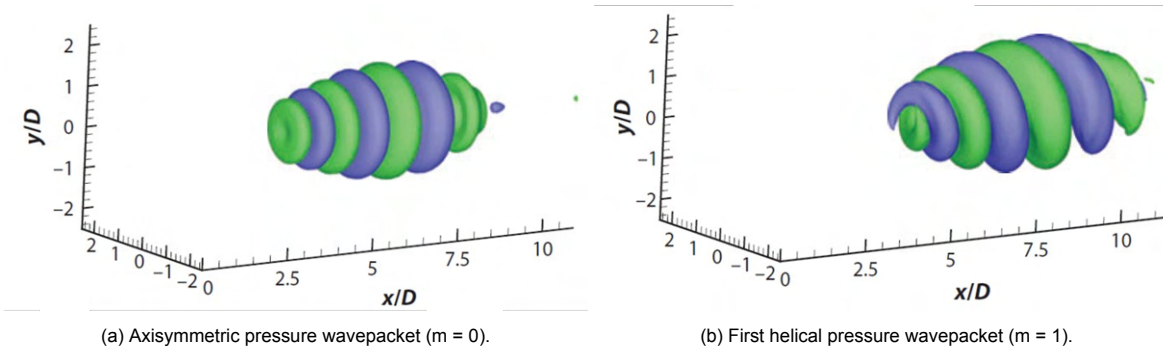
Figure 2.8: Illustration of the pressure wavepackets [28].

the SPL, which corresponds to the logarithmic scale of the ratio between the root-mean-square of the pressure fluctuations and the reference pressure, as shown in Equation 2.4. The reference pressure corresponds to the hearing threshold at $1\ kHz$, which is equal to $2x10^{-5}\ Pa$ [55].

$$SPL = 10 \log_{10} \left(\frac{p_{RMS}^2}{p_{ref}^2} \right) \tag{2.4}$$

These modes shown in Figure 2.9 are the most dominant modes in radiating noise [8, 11, 28, 49]. Examining Figure 2.9 shows that the trend of the total noise perceived is a combination of the first three modes, and thus is not only generated by the axisymmetric mode 0. Moreover, it can also be observed that the helical modes do not have a superdirectivity, as shown with the axisymmetric mode 0. Mode 0 shows a significant peak in the far-field noise at low polar angles, whereas the higher-order modes show smaller difference in far-field noise over the entire range of observation angles.
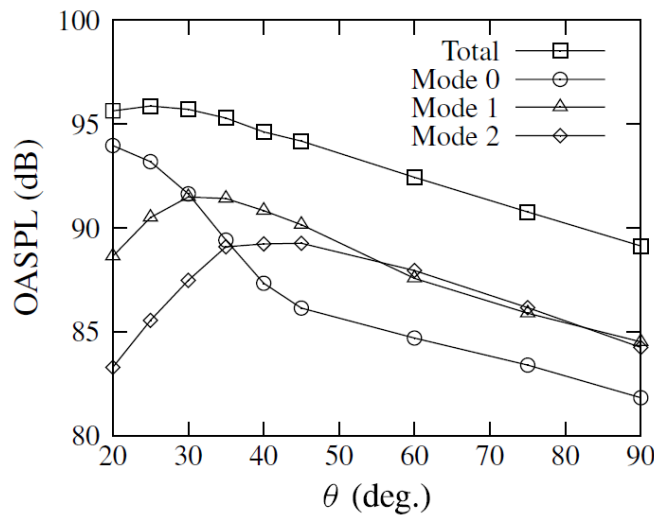
Figure 2.9: Directivity of azimuthal Fourier modes for an isolated jet with a Mach number equal to 0.6 [11].

Comparing the higher-order azimuthal modes with the axisymmetric mode shows that the latter mode is more dependent on the velocity. The energy carried by these modes is associated with turbulence scales. The Strouhal number is a non-dimensional frequency for which you need a length and velocity scale of the problem [50]. It is defined as shown with Equation 2.5, where f corresponds to the characteristic frequency, D to the jet diameter and U_j to the jet flow velocity.

$$St = \frac{f \cdot D}{U_j} \qquad\qquad (2.5)$$

Hence, at low Strouhal numbers the modes are energetic due to the large-scale turbulence, whereas for higher Strouhal numbers the modes are less energetic as the small-scale turbulence is less energetic. On the contrary, the axisymmetric mode scales with the Helmholtz number, which is defined as the ratio between acoustic wavelength and the source length scale. It was estimated that the corresponding source length is in the order of six to eight times the jet diameter. Hence, this observation shows that for an increasing jet Mach number the sound amplitude radiated by mode 0 has a larger increase than the increase in sound amplitude radiated by the helical modes. This difference is in particular most pronounced at the spectral peak.

In addition, the sound radiation at the lower polar angles decreases exponentially as $(1 - M_c \cos(\theta)^2)$ for subsonic jets [11]. Within this relation, M_c corresponds to the Mach number based on the phase velocity U_c of the convected wave. This parameter is scale-dependent as different scale sizes comprise different convection velocities, as well as it exhibits a spatial dependence.

In the next section the effect of a flat plate in the near-field of the jet is analysed. The effect on both the aerodynamic and aeroacoustic properties is examined.

2.2. The Installed Circular Jet

This section is aimed at gaining more insights into the effects of positioning a flat plate in the proximity of a jet. Firstly, the jet installation noise will be introduced in subsection 2.2.1. This will be followed by presenting the difference between the isolated and installed jet regarding the directivity. Afterwards, Figure 2.2.2 will discuss the dependence of jet velocity on the generated jet installation noise. In addition, the potential effect of the plate on the jet flow development will be analysed in subsection 2.2.3 by analysing the velocity and turbulence intensity velocity. The section will finish with presenting the azimuthal modes of the jet instability waves that carry the jet installation noise to the far-field.

2.2.1. Jet Installation Noise

The problem of jet noise received great attention from the aerospace industry in the past, and several methods have been proposed for its mitigation. One of the most effective methods to address this problem is to increase the engine diameter in order to reduce the jet exit velocity, while keeping the thrust equal. The described increase in the engine diameter resulted in a reduction of approximately $20\ dB$ [9]. However, this arrangement is accompanied by a narrower gap between the engines and the aircraft wing. As a consequence, the noise content at low-frequencies is significantly increased for these aircraft configurations. This phenomenon was first noticed by Bushell (1975) by comparing the noise generated by a full-scale static isolated jet and the noise of an installed jet in-flight [7]. Later this phenomenon was dubbed as the *jet installation noise*.

The effect of the jet installation noise can be visualised in Figure 2.10, where the SPL versus the Strouhal number is plotted. The plate installation results in a significant low-frequency noise increase for both the shielded and unshielded sides with respect to an isolated jet [33]. In the low-frequency region the measured noise is slightly larger at the unshielded side than at the shielded side. In the high-frequency region the measured noise at the shielded side is significantly lower than both the unshielded side and the isolated jet. Compared to the isolated jet, the noise at the unshielded side of the installed jet is also significantly larger in the high-frequency region [33].

The enhancement of noise in the low-frequency region when a jet is installed is caused by the interaction of the plate with the jet flow field [53]. The enhancement is dependent on the location of the plate with respect to the jet. If the flat plate is located in the jet acoustic field no significant change in far-field noise is found with respect to the isolated jet noise. There is also a difference observed between the flat plate being positioned either in the irrotational or in the rotational region of the hydrodynamic field of the jet. If the plate is located in the irrotational entrainment region of the jet, the increase in low-frequency noise is caused by the scattering of hydrodynamic pressure waves of the jet at the trailing-
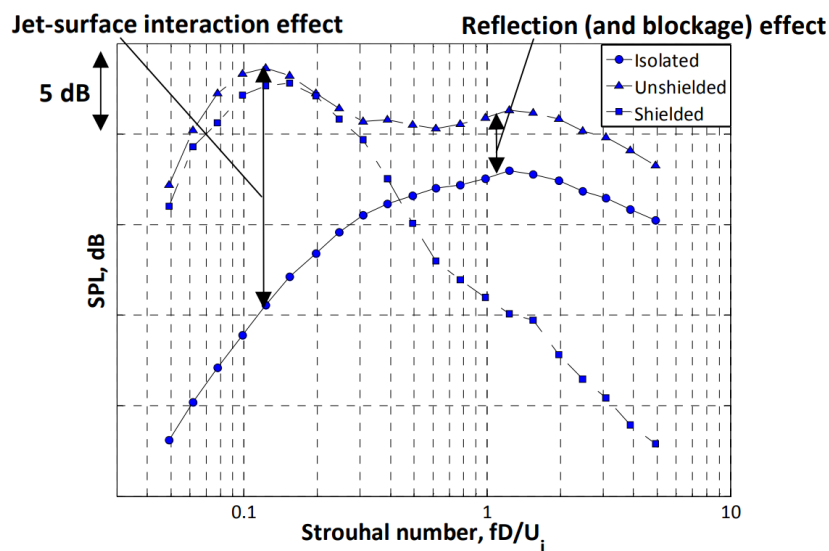
Figure 2.10: Breakdown of jet installation effects at a polar angle of $90°$ (shielded side) and $-90°$ (unshielded side) in case of a jet Mach number of 0.9, with the distances $H/D = 0.67$ and $L/D = 10.0$ [33].

edge, as previously found by Ffowcs-Williams & Hall (1970) [64]. Secondly, if the plate is located in the rotational shear layer of the jet, an even larger enhancement of low-frequency noise is caused by the unsteady loads that act on the plate surface as a result of the jet flow field being blocked by the plate surface [13]. This phenomena is defined as *grazing of the flow* on the surface of the plate. However, this is often neglected in aircraft applications as the high velocity and temperature of the jet prevents this situation [53]. Both sources of the enhancement of low-frequency noise are caused by large-scale structures within the jet flow field [33, 52].

For frequencies higher than the noise peak frequency, the sound pressure level drops significantly faster at the shielded side than at the unshielded side. At the unshielded side, the noise is larger compared to the isolated jet, which is caused by the reflection of pressure waves. This noise increase does not occur at the shielded side of the plate. Moreover, the plate blocks the jet mixing noise at the shielded side, resulting in a significant reduction in noise perceived. [20, 34, 52].

The relative distances L and H have a different effect on the generated jet installation noise in the entire frequency range. Increasing the distance between the nozzle exit and the plate its trailing-edge, corresponding to L, results in an increase in low-frequency jet installation noise. On top of that, this results in a shift of the peak noise to a lower frequency. Both effects can be observed in Figure 2.11a [20, 58]. In addition, it can be observed that the high-frequency noise decreases for an increasing streamwise distance L. Larger values of L enable the turbulence eddies in the shear layer to develop and grow into larger structures before they reach the trailing-edge, were they generate noise by scattering. The fact that a larger eddy radiates noise at a lower frequency explains the observed shift of the low-frequency noise peak [62]. In addition, it is known that large-scale eddies carry more energy than small-scale eddies, explaining the described increase in noise [33, 53].

On the contrary, an increase in low-frequency jet installation noise occurs when the separation distance H is decreased. This increase is accompanied by a shift of the noise peak to a higher frequency [20, 33, 53]. It is expected that a significant noise increase is a result of grazing of the jet flow on the plate surface. It can be seen that there is a significant increase if the distance H is decreased from $2D$ to $1D$. This difference is more significant than the difference between the radial distances $2D$ and $4D$, as well as the difference between $1D$ and $0.67D$. In the high-frequency region insignificant differences can be observed between the different separation distances.

2.2.2. Directivity of Jet Installation Noise

The different sound sources in an installed jet show different polar directivity. For the scattering of jet instability waves at the trailing-edge, the sound source can be modelled as a dipole at the edge, with its

(a) Varying streamwise distance H.

(b) Varying separation distance H.
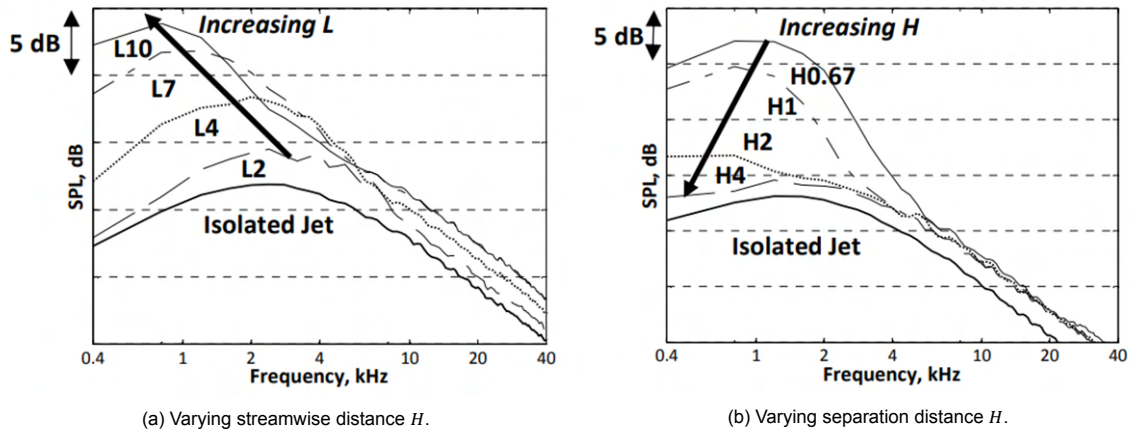
Figure 2.11: Perceived noise at the unshielded side along the sideline direction, for an installed subsonic jet with varying separation distance H and varying streamwise distance L [33].

axis normal to the flat plate surface [13, 20]. The resulting two lobed directivity pattern, can be clearly seen in Figure 2.12. Next to this, due to the dipole noise source, a phase difference of 180° exists between the far-field acoustics at the shielded and the unshielded sides [33, 53].
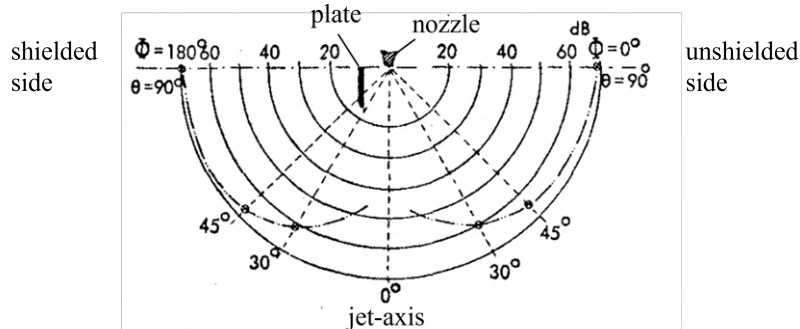
Figure 2.12: Initial peak intensity in the observation plane, measured by Head & Fisher (1976) [20].

Although the scattering of the instability waves at the trailing-edge behaves as a dipole source, the directivity differs between the unshielded and shielded sides of the flat plate. The unshielded side shows a more omnidirectional pattern compared to the isolated jet noise, as can be seen in Figure 2.13a and in the previous presented Figure 2.10. On top of that, in the forward jet arc, corresponding to a polar angle greater than 90°, significantly more noise is measured at the unshielded side compared to the shielded side and the isolated jet. Regarding the shielded side, a typical sinus dipole pattern can be observed, as expected. This difference between the shielded and unshielded sides is thought to be mainly due to the noise induced by the interaction of the reflected waves and the jet flow at the unshielded side [33].

The jet-plate interaction has a similar dipole behaviour for the azimuthal directivity, which is in contrary to the omnidirectional azimuthal directivity of the jet mixing noise [20, 53]. This difference can be clearly observed in Figure 2.13b, where the jet mixing noise is shown by the isolated jet. The dipole pattern is enhanced and experiences a larger maximum SPL for a larger value of L. This effect is smaller at the shielded side, corresponding to an azimuthal angle of 180°, as the perceived noise at this location does not involve the reflected pressure waves.

Effect of jet velocity on jet installation noise
Varying the jet velocity does not only alter the jet mixing noise of an isolated jet, but also the jet installation noise. A larger jet velocity results in the peak noise intensity to occur at a higher frequency [34,

(a) Polar directivity.

(b) Azimuthal directivity.
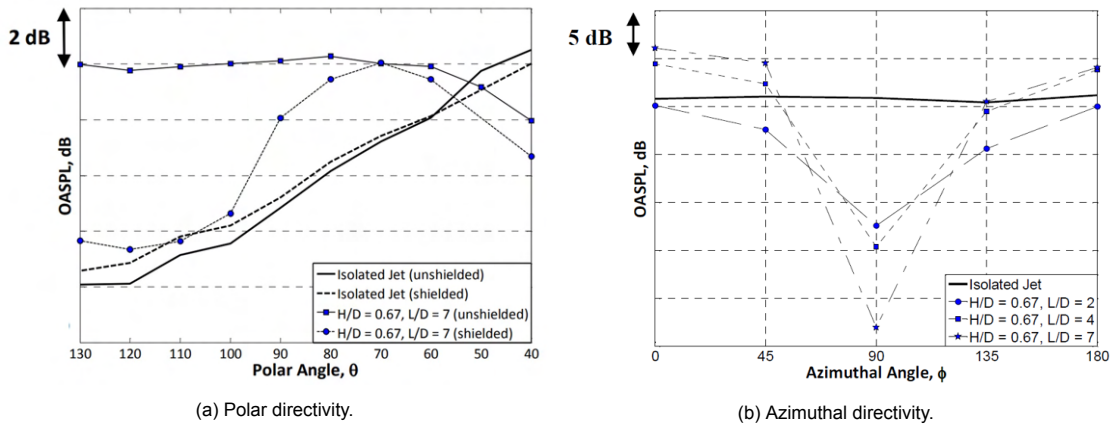
Figure 2.13: Overall Sound Pressure Level (OASPL) directivity measured along the jet-axis for an isolated jet and installed jet at a jet Mach number of 0.75 [33].

52]. This velocity dependency can be observed in Figure 2.14a, where M_a corresponds to the acoustic Mach number. The acoustic Mach number is defined the ratio between the flow velocity and the local speed of sound. It can be observed that the isolated jet noise, and thus the jet mixing noise, has a greater dependence on the jet velocity. For a lower Mach number the jet installation noise is relatively more significant than for higher subsonic jet velocities [34]. It can even be observed in Figure 2.14 that for an acoustic Mach number equal to 0.9 the jet installation noise is relatively small.
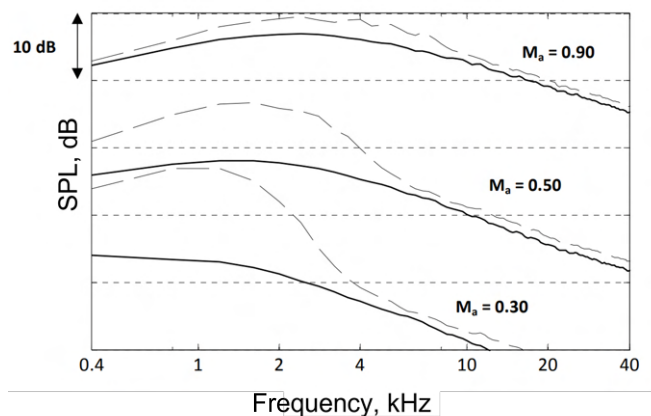
Figure 2.14: Velocity dependence for an isolated jet (solid lines) and for an installed jet (dashed lines) along the sideline direction at the unshielded side with H/D = 0.67 and L/D = 2 [33].

2.2.3. Jet Flow Turbulence of Installed Circular Jet

Next to the change in far-field noise, the change in the turbulence statistics for installed subsonic circular jets have been investigated. In this subsection, the effect of the installation of the plate on the jet development is presented.

Firstly, hot-wire anemometry measurements were conducted by Proença et al. (2020) to examine the turbulence development in a jet flow with a flat plate installed in its proximity [51]. The axial mean velocity profile was measured, as can be observed in Figure 2.15, where the different configurations correspond to the description in Table 2.1. Configuration $B0$ corresponds to the isolated jet, whereas $B1$ and $B2$ are characterised by a flat plate close to the jet. For configuration $B1$ the plate is positioned closer to the jet centreline than for $B2$, as shown by the separation distance H in Table 2.1.

From Figure 2.15a it can be observed that a slight difference occurs in the upper part of the annular

(a) $X/D = 2$.
(b) $X/D = 4$.
(c) $X/D = 6$.
(d) $X/D = 10$.
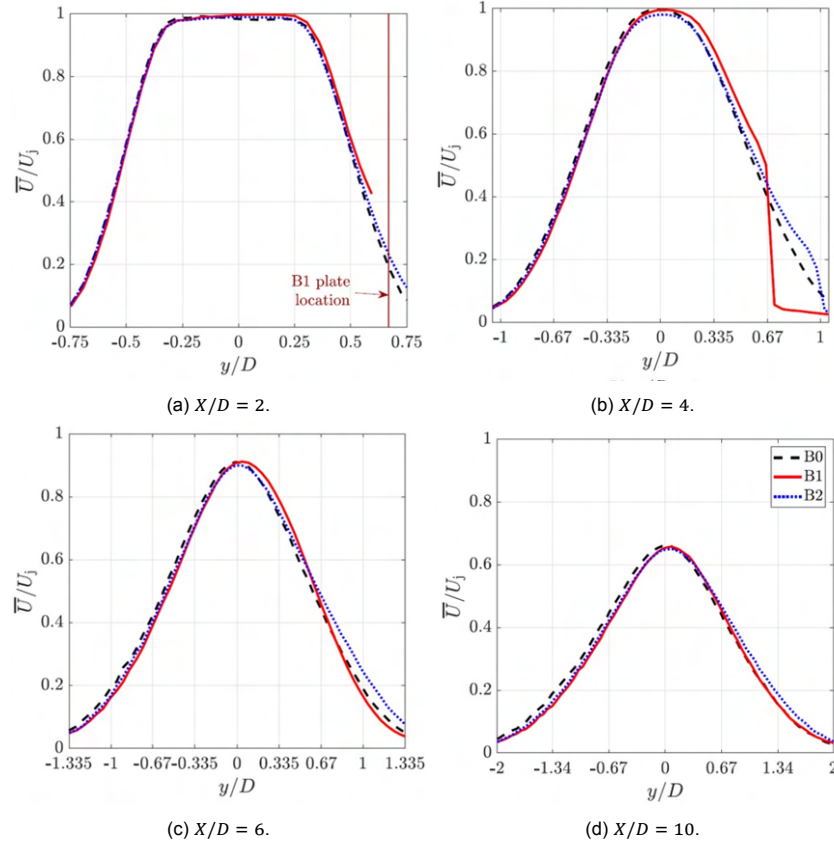
Figure 2.15: The jet mean axial velocity profiles measured for the different configurations used in the experiment conducted by Proença et al. (2020). The nominal jet Mach number during the conducted experiment was equal to 0.6 [51]

Table 2.1: Configurations used for the experimental study of Proença et al. (2020), corresponding to the parameters used in Figure 2.15 [51].

	B0	B1	B2
H	-	$0.67D$	$1.00D$
L	-	$4.00D$	$4.00D$

shear layer (i.e. $y/D > 0$), which is also measured at the axial locations upstream of $x/D = 2$. For this specific experiment grazing of the jet flow on the plate surface occurs for configuration $B1$. The shear layer is expected to wet the plate surface at an axial location of $x/D \approx 1.4$ for the $B1$ configuration [51]. Downstream of this axial location the mean velocity in the upper shear layer for configuration $B1$ remains higher than for the isolated case and for the $B2$ configuration, as shown in Figure 2.15b. The steep decay in the axial jet mean flow occurs at the trailing-edge of the flat plate.

These observations enable to draw multiple conclusions. Firstly, local jet mean flow acceleration occurs in the upper flow region of the rotational hydrodynamic field of the installed jet in comparison with the isolated jet. This local acceleration can be explained by the transfer of the restricted momentum in y-direction into streamwise momentum that subsequently results in more energy in the axial flow direction [51]. Moreover, for both configurations the part of the jet flow close to the trailing-edge interacts with the plate, as shown in Figure 2.15b by the deviation of the velocity decay of $B1$ and $B2$ with respect to the decay for the isolated jet. This effect results in the jet flow impacting the plate earlier than expected, as can be clearly observed for configuration $B2$ [51]. This earlier impingement of the jet flow is due to the Coandă effect, corresponding to the change in entrainment of the jet flow which results in the flow being directed towards the flat plate itself [3, 4, 49].

With the analysis of Figure 2.15c and Figure 2.15d, it is shown that the local acceleration for con-

figuration $B1$ reduces downstream. For configuration B the aforementioned redirection of the flow can be observed even 10 diameters downstream of the nozzle exit, as shown in Figure 2.15d.

The measurements confirm that the lower part of the annular shear layer of the jet experiences little change in axial velocity profile, with the presence of the flat plate. The above measurements were also done for two configurations similar to $B1$ and $B2$, but both with a smaller flat plate length equal to $2D$. These configurations do not involve grazing of the jet flow on the plate surface. Both showed no significant difference with the isolated jet [51].

The turbulence levels in the jet flow also experience changes due to the presence of a plate installed nearby. The turbulence levels for the three different configurations are shown in Figure 2.16. In Figure 2.16a the radial profiles of the axial intensity levels are shown for two different axial locations, namely at the nozzle exit and four diameters downstream of the nozzle exit. Additionally, Figure 2.16b depicts the intensity levels at the jet centreline and at the lipline of the upper shear layer of the jet.

(a) Turbulence intensity radial profiles   (b) Turbulence intensity axial profiles
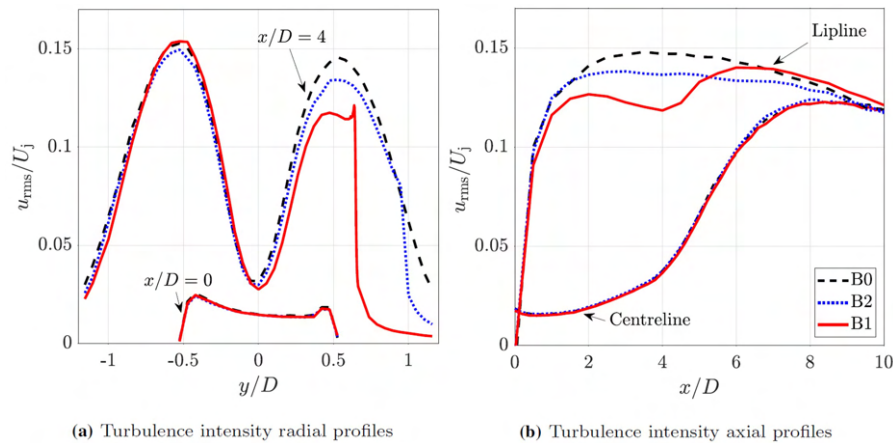
Figure 2.16: Jet turbulence intensity profiles measured for the different configurations used in the experiment conducted by Proença et al. (2020). The radial intensity profile at the nozzle exit and $x/D = 4$ is given in a) and the axial intensity profile is given in b) for the jet centreline and the jet lipline closest to the flat plate. The nominal jet Mach number during the conducted experiment was equal to 0.6 [51].

From Figure 2.16a it can be observed that for all configurations the flow at the nozzle exit is asymmetric in radial direction, which could be attributed to a measurement error. Nevertheless, it can be observed that the configurations with an installed flat plate collapse well with the isolated jet, as expected as the same nozzle is used [51]. Farther downstream an insignificant difference occurs for the lower part of the annular shear layer (i.e. $y/D < 0$), shown by the left lobe of the pattern in Figure 2.16a. This strengthens the previously made comment that the jet axial mean velocity is barely altered for the lower shear layer. For the upper part of the annular shear layer the plate results in a significant difference in turbulence levels. In specific, configuration $B1$, which has its plate the closest to the jet, experiences the largest decrease in turbulence levels. At the location of the plate the turbulence levels decrease close to zero for both configurations $B1$ and $B2$.

In addition, in Figure 2.16b the axial profiles of the turbulence levels along the jet centreline can be observed. Both configurations with a plate collapses well with the isolated jet close to the nozzle exit. This remains true downstream of the nozzle exit. However, for the upper lipline a significant decrease occurs, where again configuration $B1$ experiences a larger decrease in turbulence intensity than configuration $B2$. Configuration $B1$ also experiences a rise in turbulence intensity at the trailing-edge of the plate. This rise is explained with the detachment of the turbulent boundary layer on the plate [41, 51]. Downstream of the trailing-edge, the upper shear layer tends to collapse again with the profile of the isolated jet.

For both the radial and axial turbulence fluctuations a decrease in intensity occurs in the upper part of the shear layer for the installed jets compared to the isolated jet. This is observed despite the local acceleration of the streamwise velocity close to the flat plate. A local acceleration will result in a higher Reynolds number and subsequently in higher velocity fluctuations, which would have been seen as a rise in the turbulence intensity. However, this does not occur as the plate restricts the development of the upper shear layer and thus the development of large, coherent eddies [34, 51]. Taking into account

that the large eddies have the largest energy content, it can be clarified that a lower turbulence intensity is seen as a result of this restriction. This hypothesis was verified by Proença et al. (2020) by analysing for low and high frequencies the Power Spectral Density (PSD), which defines the average power of the sound during a time range and for a specified frequency range. A large difference between the isolated and the installed jets in the low frequency region was found. In the high-frequency region this difference is less evident [51].

The size of the eddies in the upper part of the annular shear layer can be verified with the turbulence characteristic length scales in the flow. As shown in Table 2.2, the axial length scale L_ζ is lower in case a plate is placed close to the upper lipline [51]. This strengthens the earlier made conclusion regarding the eddy sizes. It can be observed that this decrease in eddy size is still visible downstream of the plate its trailing-edge.

The azimuthal and radial length scales, corresponding to L_η and $L_{\Delta\theta}$ respectively, also experience a decrease in size. Hence, the plate limits the development of the turbulence structures in all directions for the upper shear layer. This effect is more pronounced when the plate is placed closer to the jet-axis. In specific, the azimuthal length scales experience relatively the largest limitation in growth. However, the recovery is also relatively fast downstream of the trailing-edge of the plate compared to the axial and the radial length scale. Hence, in the transitional and fully-developed turbulent region of the jet, the presence of the flat plate has a stronger effect on the longitudinal structures than the transverse structures.

Table 2.2: Turbulence characteristic length scales in the upper part of the annular shear layer as found by Proença et al. (2020), normalized by the annular shear layer thickness δ_β [51].

Scale	B0		B1		B2	
x/D	4	8	4	8	4	8
L_ζ / δ_β	0.31	0.31	0.27	0.29	0.28	0.29
L_η / δ_β	0.19	0.19	0.16	0.18	0.18	0.18
$L_{\Delta\theta}$ / δ_β	0.14	0.15	0.09	0.13	0.10	0.13

All in all, the presence of a plate in proximity can alter the jet development. This corresponds to both the jet mean velocity and the turbulence intensity in the part of the shear layer that is closest to the plate. This effect is more severe for a smaller distance between the jet-axis and the plate, especially for configurations where grazing of the flow on the plate surface occurs. If the plate is positioned such that the distances H and L ensure a sufficient distance between the jet and the trailing-edge, the jet is insignificantly altered.

2.2.4. Jet Instability Waves of the Installed Circular Jet

Research has been done regarding the effects of installing a plate on the jet instability waves that are generated in the jet flow. This was aimed on getting a better understanding of the physics behind the increase in noise. As such, Faranosov et al. (2019) performed research on the azimuthal structures of the low-frequency noise in case of an installed jet [17]. This is based on earlier research that showed very low correlations between different measurement locations with an installed jet configuration. A good example is the previously mentioned dipole-type field behaviour at the trailing-edge, which radiates noise to certain azimuthal angles. These observations indicate that the additional installation jet noise is dominant at particular azimuthal modes.

Faranosov et al. (2019) conducted an experiment with microphones azimuthally placed around a circular nozzle with a flat plate in the near-field [17]. It was observed that of the azimuthal modes it was the odd cosine modes a_1 and a_3 show a significant increase in noise for the installed jet compared to the isolated jet. The odd cosine modes and the sine modes correspond to the negative and positive helical modes discussed in section 2.1, respectively. This significant difference between an isolated

jet and an installed jet can be observed in Figure 2.17. The axisymmetric mode a_0 and the other asymmetric higher-modes do not change significantly in noise radiation, and it is concluded that these modes mainly carry the jet mixing noise.

(a) For an isolated jet.

(b) For an installed jet.
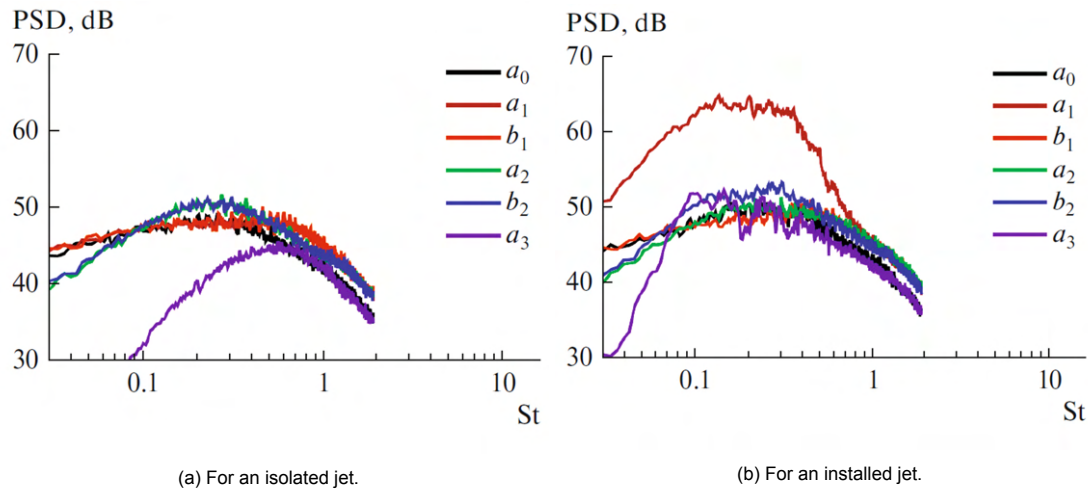
Figure 2.17: The noise radiation for the different azimuthal modes of the jet instability waves [8].

For lower operating Mach numbers this relative difference becomes more significant. In addition, a high level of correlation between the modes a_1 and a_3 exists. This indicates that the odd cosine modes are generated by the same sound source. Both cosine modes are due to the scattering of the near-field axisymmetric and the first cosine modes at the trailing-edge of the flat plate. The contribution of the dipole term a_1 is the highest for the scattered field at the trailing-edge, with corrections made by the cosine mode a_3. [8].

2.3. Jet from a Lobed Nozzle

In this section, the most salient results on the research involving a jet from a lobed nozzle is reviewed. The aerodynamics of a jet from a lobed nozzle has been investigated more extensively than the aeroacoustics. The main focus of the research was the mixing enhancement gained from the application of lobed nozzles. The research rarely focuses on the jet mixing noise or the change in noise when the near-field of the jet interacts with a plate in proximity.

The state-of-the-art on jets from isolated lobed nozzles will first be presented. Afterwards, the recent investigations on jet installation noise involving lobed nozzles will be presented.

Before presenting the state-of-the-art, the parameters used to define the lobed nozzle geometry are illustrated in Figure 2.18. The lobed lipline is defined by the number of lobes N and the lobe penetration, which defines the radial distance between the outer and inner diameter of the lobed lipline. Lastly, the lobe length of the nozzle is defined by the axial distance between the transition of a circular lipline to a lobed lipline, as sketched in Figure 2.18.

2.3.1. General Aspects on the Lobed Jet Development

In this section, the isolated lobed nozzle will be analysed. Firstly, the change in turbulence characteristics of the jet is presented. This is followed by a discussion on the development and evolution of vorticity structures.

It is believed that the lobed geometry enhances mixing due to the larger amount of entrainment that occurs with the larger pheriphery of the nozzle exit compared to the jet from the circular nozzle [6, 43, 44, 65]. This statement can be strengthened by examining the effect of the lobed geometry on the jet's potential core length.

Firstly, the point at which the axial velocity along the jet centreline starts to decay, which indicates the end of the laminar flow in the potential core, is more upstream for the jet from the lobed nozzle than

(a) Front view.

(b) Side view.
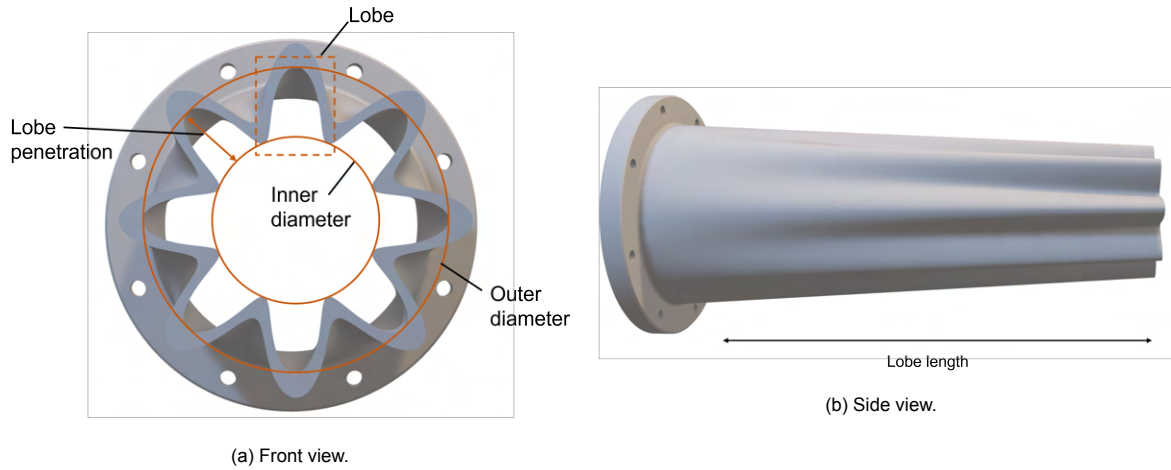
Figure 2.18: Illustration of the lobed nozzle parameters.

for the jet from the baseline nozzle [30, 48]. This result can be observed in Figure 2.19a, where the lobe penetration P stands for the difference between the maximum and minimum radius of the lipline profile. The length of the nozzle is $50\ mm$ and the average exit diameter equals $40\ mm$. Figure 2.19a and Figure 2.19b clearly show that the specific geometry of the lobed nozzle determines the decrease in the downstream extensions of the laminar region of the jet flow, with respect to the conventional circular nozzle (shown by the experimental data in Figure 2.19).

Increasing the lobe penetration P results in the mean velocity decay to shift significantly more upstream, as shown Figure 2.19a. A larger penetration results in a larger nozzle periphery, and thus also in a larger entrainment.

On the contrary, a large number of lobes does not significantly modify the decay rate of the centreline velocity, as can be observed in Figure 2.19b. The difference in potential core length between the six and eight lobes is significantly less than the difference between four and six lobes. This suggests an exponential relation between the number of lobes and the potential core length, and thus for a lower number of lobes an increase or decrease in the amount of lobes has a more significant effect [30, 48].

Varying the axial length of the lobes has an insignificant effect on the potential core length [48]. Hence, to shift the decay of the mean velocity along the centreline upstream, a high lobe penetration in combination with a moderate number of lobes should be used.

(a) Varying the lobe penetration for a lobed nozzle with 4 number of lobes.

(b) Varying the number of lobes for a lobed nozzle with a lobe penetration of $10\ mm$.
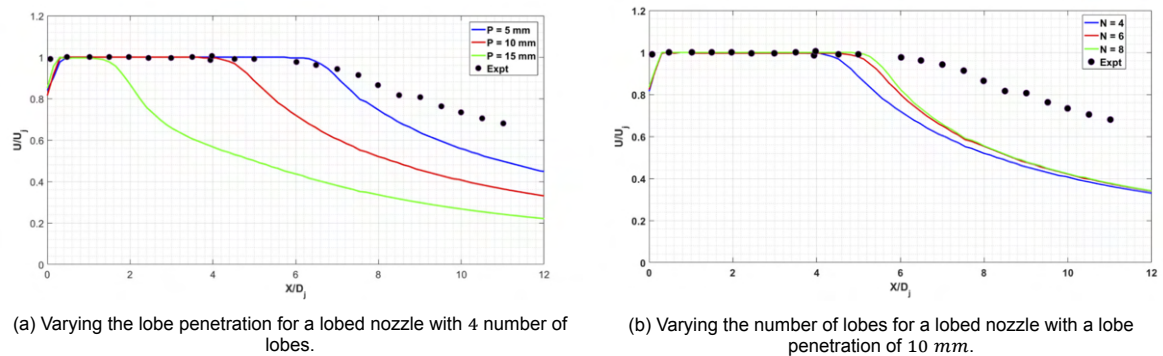
Figure 2.19: The axial velocity along the centreline of a jet operating at a Mach number of 0.75 for varying lobed nozzle parameters, where "Expt" stands for experimental values of a conventional round nozzle [48].

The aforementioned effects can also be observed in the change in the radial velocity profile, shown in Figure 2.20. The typical top-hat velocity profile at the nozzle exit for the conventional circular nozzle is not experienced in case of a nozzle with a relatively extreme lobed lipline. The lobed radial velocity profile at the lobed nozzle exit develops into a profile with a peak at the jet centreline in the transitional region of the jet. Hence, farther downstream the radial velocity profile is similar to the conventional

circular nozzle [48, 65].

Increasing the penetration of the lobes results in a significantly more lobed radial velocity profile of the streamwise component at the nozzle exit, as shown in Figure 2.20a. This clearly evidences an enhancement of the flow mixing. Farther downstream a large lobe penetration will result in a radial velocity profile more similar to the conventional round nozzle.

In Figure 2.20b it can be observed that for these flow characteristics the effect of the number of lobes is less significant than the penetration rate. Nevertheless, an increase in the number of lobes results in a radial velocity profile that has more distinct lobes at the outer regions of the jet. Again, this effect is seen to be relatively less strong after a certain number of lobes due to the previous mentioned exponential relationship [30, 48].

As it was observed previously, the lobe length does not have any significant effects on the radial velocity profile.
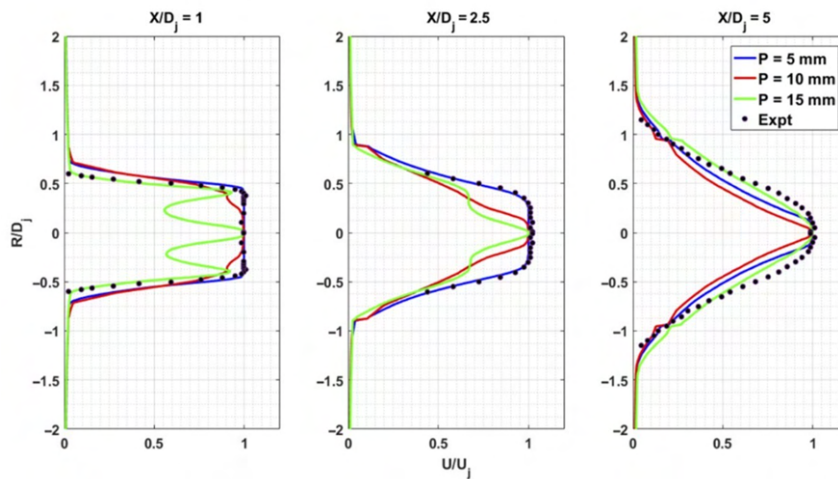
(a) Varying the lobe penetration for a lobed nozzle with 4 number of lobes.
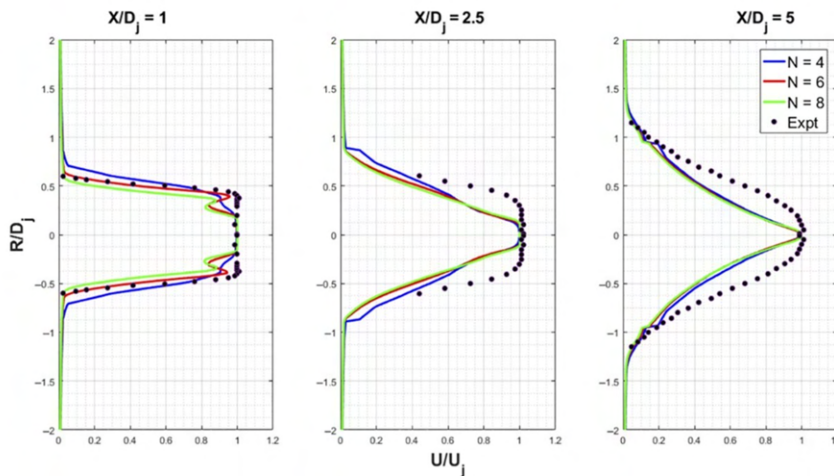
(b) Varying the number of lobes for a lobed nozzle with a lobe penetration of 10 mm.

Figure 2.20: The radial profile of the mean velocity at different locations downstream of the nozzle for varying lobed nozzle parameters, where "Expt" stands for experimental values of a conventional round nozzle [48].

As expected with the aforementioned changes in the jet from a lobed nozzle, the turbulence downstream of the nozzle is also affected due to the lobed lipline. As shown in Figure 2.21, the turbulence intensity in the centre of the jet increases earlier for a nozzle with a relatively extreme lobed lipline, which can be linked with a smaller potential core length [32]. Just downstream of the nozzle exit, the turbulence profile of a lobed nozzle has a large drop at the jet centreline, similar to for the conventional

circular nozzle. However, the jets from the lobed nozzles show a drop within the lobes in the outer region of the nozzle as well, whereas the conventional round nozzle has a radial bucket-shape profile [47, 48, 65].

Figure 2.21a shows the effect of a varying penetration rate. The significant decrease of the potential core length due to a high lobe penetrations results in large turbulence fluctuations just downstream of the nozzle exit, which compared to the conventional nozzle are smoothened out relatively fast downstream of the nozzle exit.

Increasing the number of lobes moves the location of fully-developed turbulence farther downstream, satisfying the aforementioned effects of the lobe count. This can be observed in Figure 2.21b.

Lastly, the lobe length has again no significant effect on the development of the turbulence intensity [48].

From these results it seems that in order to achieve a fully-developed turbulent flow quickly downstream of the nozzle exit, the lobe penetration should be kept high, in combination with a moderate number of lobes.
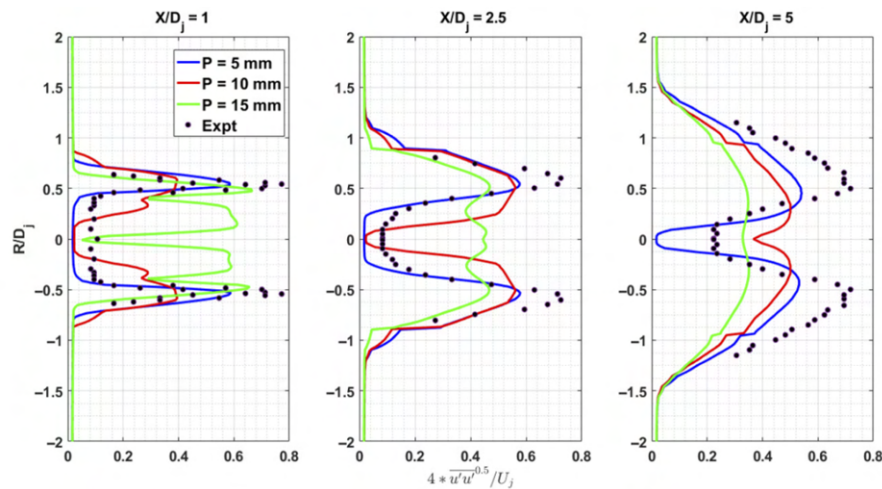
(a) Varying the lobe penetration for a lobed nozzle with 4 number of lobes.
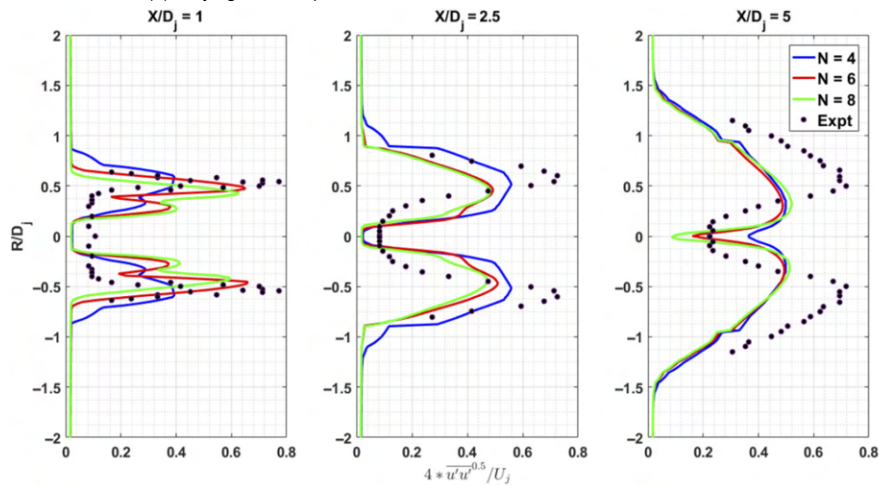
(b) Varying the number of lobes for a lobed nozzle with a lobe penetration of 10 mm.

Figure 2.21: The radial profile of the turbulence intensity at different locations downstream of the nozzle for varying lobed nozzle parameters, where "Expt" stands for experimental values of a conventional round nozzle [48].

The above found changes in the jet characteristics from a lobed nozzle with respect to the conventional circular nozzle, can be explained by examining the vortices that occur downstream of the nozzle exit with a lobed lipline. In case of a lobed nozzle with a moderate number of lobes and a strong lobe penetration the different vortices can be clearly identified. This has been done with, for example, multiple Particle Image Velocimetry (PIV) and laser-induced fluorescence measurements, in the near-field

jet from lobed nozzles [21, 22, 35]. The measurements include a lobed nozzle of a diameter of $40\ mm$ with a mean jet exit velocity of $20\ m/s$, corresponding to a Reynolds number of $5.5x10^5$. The lobed nozzle used is shown in Figure 2.22a, with a lobe width of $6\ mm$ and a lobe height of $15\ mm$.

One of the most important changes in the jet from the lobed nozzle exit is the appearance of patches of flow for the velocity components in radial direction [21]. Large-scale cross-stream flow spreads outward along the lobes, while simultaneously large-scale ambient flow is injected inwards through the lobe valleys. This process is illustrated in Figure 2.22b. This can also be observed in Figure 2.23 with the direction of the arrows indicating the flow velocity, where it must be noted that Z/D corresponds to x/D as defined in this work. It can be observed that the jet spreads outward radially at the lobes when the flow is convected downstream at a high streamwise velocity. Additionally, in Figure 2.23a it can be observed that the high velocity region at the jet centre has troughs of lower velocity regions, which reflects the nozzle geometry. Similarly, high velocity crests occur at azimuthal positions corresponding to the lobes. The occurrence of high flow velocity at the lobe crests in the jet centre region match the radial profile of the streamwise velocity as presented before with Figure 2.20.

(a) Nozzle used for experiment.

(b) Flow injection and expansion.
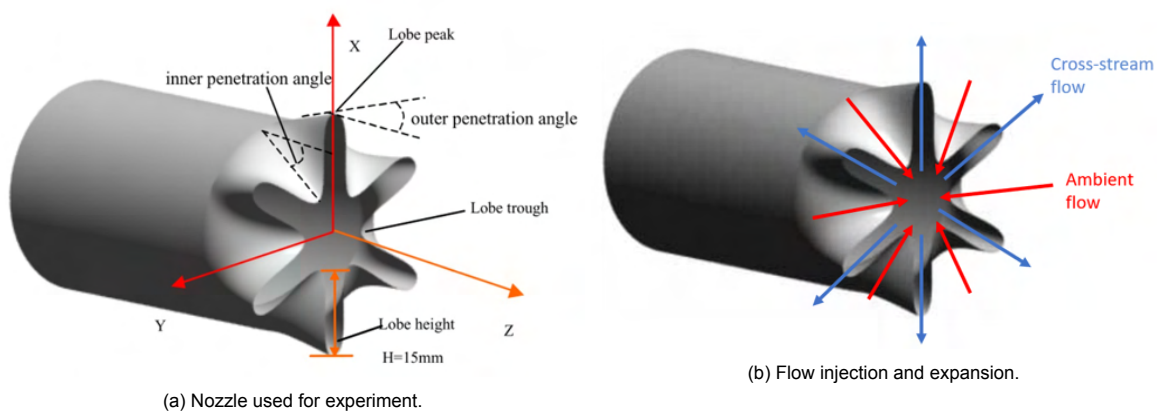
Figure 2.22: Illustration of the nozzle geometry used for the experiment conducted by Hu et al. (2005) [21] and of the large-scale cross-stream flow expansion and the large-scale ambient flow injection [22].

(a) Half a diameter downstream of the nozzle exit.

(b) Two diameters downstream of the nozzle exit.
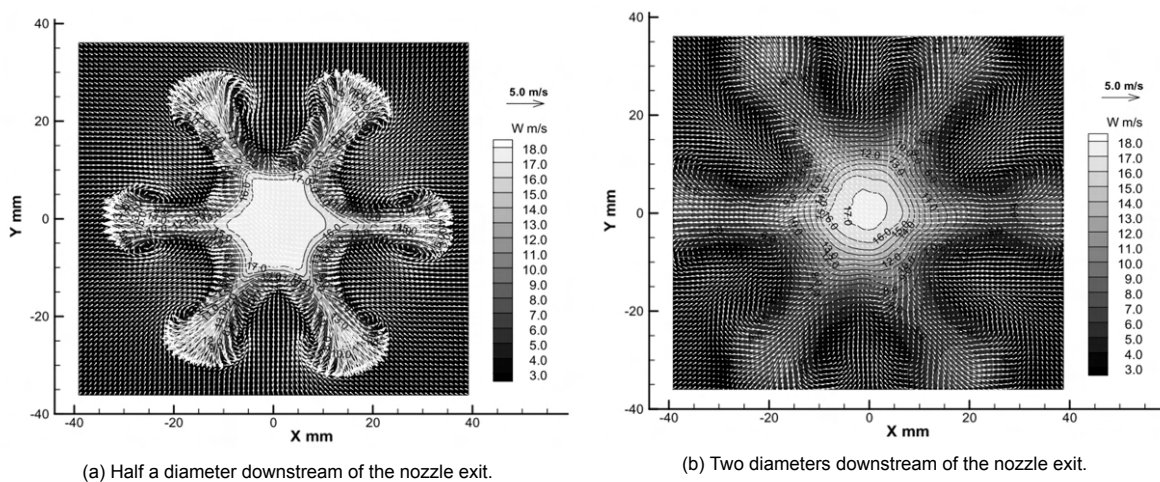
Figure 2.23: Ensemble-averaged velocity field obtained by the Dual-Plane Stereoscopic PIV conducted by Hu et al. (2005) at different downstream locations [21].

The strong cross-stream flow results in the generation of pairs of counter-rotating large-scale streamwise vortices at the sides of a lobe. This can be visualized with the green arrows shown in Figure 2.24a and from the streamwise vorticity measurement shown in Figure 2.25a. The streamwise vortices enhance mixing and promote flow entrainment, as sketched in Figure 2.24b [6, 21, 54]. The large-scale

vortices spread outwards downstream of the nozzle, as can be observed by comparing Figure 2.25a and Figure 2.25b. In addition, the ensemble-averaged streamwise vorticity decreases significantly when the flow is convected downstream. This is in line with the conclusion made previously that the turbulence reaches its fully-developed regime over a short streamwise span. The large-scale streamwise vortices are gradually break down into small-scale streamwise vortices, which have similar maximum vorticity values [21].

A larger lobe penetration results in the generation of stronger large-scale streamwise vortices, and thus in a faster downstream mixing of the jet. In addition, a larger number of lobes result in the generation of more large-scale streamwise vortices, which also enhances the jet mixing. It must be noted that it is expected that the number of lobes has an effect on the generated large-scale streamwise vortices. From the use of chevrons it is known that a too large number of chevrons results in a spacing between the generated streamwise vortices that is too small. As a consequence, the streamwise vortices annihilate each other quickly downstream of the nozzle exit, and thus the desirable effect of enhanced mixing is rapidly lost [24].

(a) Three-dimensional sketch [6].

(b) flow stirring that occurs due to the streamwise vortices [54].
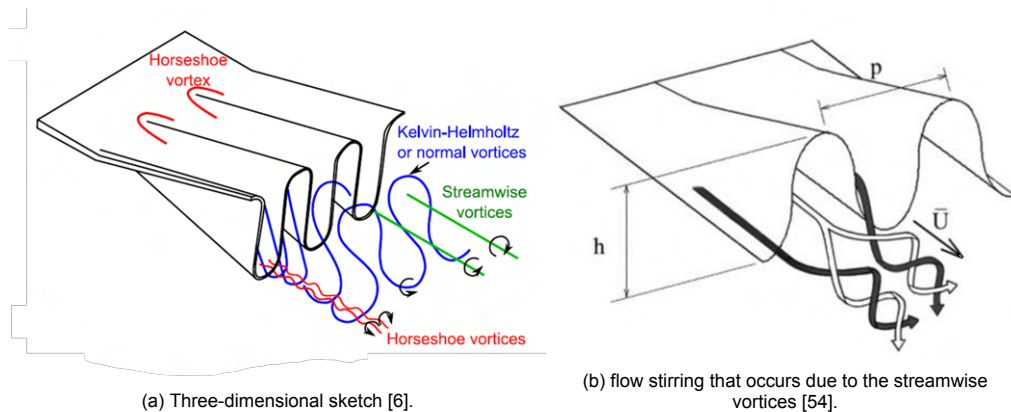
Figure 2.24: Illustration of the vortices that are generated in a jet from a lobed nozzle.

(a) Half a diameter downstream of the nozzle exit.

(b) Two diameters downstream of the nozzle exit.
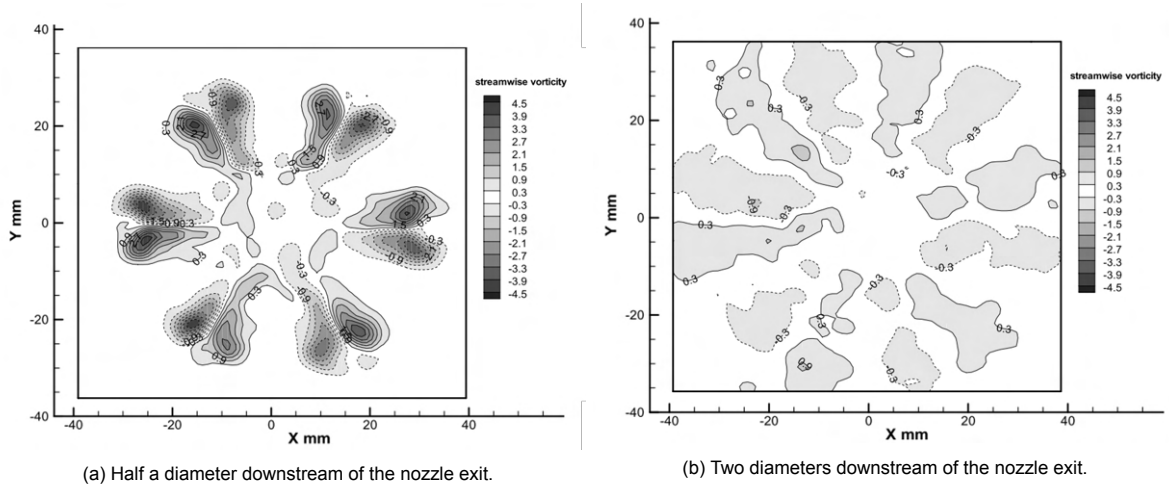
Figure 2.25: Ensemble-averaged streamwise vorticity distribution obtained by the Dual-Plane Stereoscopic PIV conducted by Hu et al. (2005) at different downstream locations [21].

In case of non-stationary ambient flow horseshoe vortices occur upstream of the nozzle. These occur at the axial location along the nozzle where the round periphery of the nozzles transitions to the lobes, as illustrated in Figure 2.24a. These vortices are convected as counter-rotating pairs at the trailing-edge of the lobe valleys. They can be recognized as smaller and weaker streamwise vortices at the lobe valleys. This can be observed in the instantaneous snapshot of the streamwise vorticity distribution, shown in Figure 2.26, as measured by Hu et al. (2005) [21]. A contrast can be seen between the pairs of the large-scale strong streamwise vortices at the lobe peaks and the smaller and weaker

streamwise vortices that are located between the lobes, closer to the jet centre.
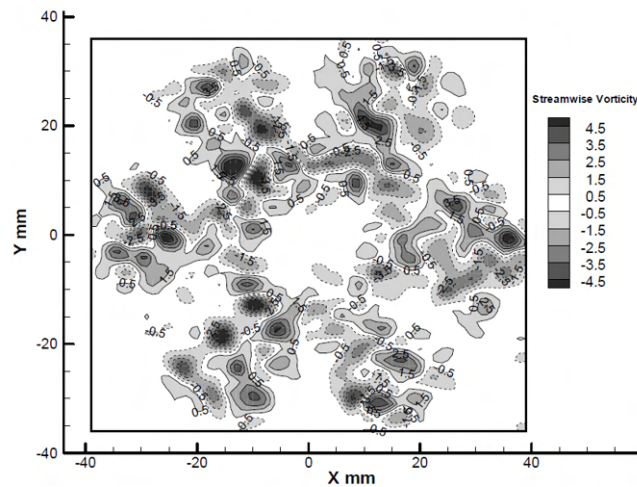
Figure 2.26: Instantaneous streamwise vorticity distribution obtained by the Dual-Plane Stereoscopic PIV conducted by Hu et al. (2005) at one diameter downstream of the nozzle exit [21].

Next to the above mentioned vortices, a normal vortex is created at the lipline of the nozzle. Azimuthal vortex structures roll up at the nozzle trailing-edge due to the Kelvin-Helmholtz instability, resulting in these normal vortices [6, 21]. In case of the conventional circular nozzle these vortices are circular, whereas for the lobed nozzle the normal vortices have the same lobed shape as the nozzle exit. The normal vortices, also known as the Kelvin-Helmholtz vortices, are sketched in Figure 2.24a and Figure 2.27.

The normal vortices are convected downstream and the lobe shape deforms into a circular ring with pinched-off structures [6]. This pinch-off effect can be observed in Figure 2.27. As shown, the interaction of the normal vortex with the streamwise vortices pushes the sides of a lobe towards each other until the lobe peaks are separated from the jet centre. When the lobes peaks are broken down into substructures a new circular structure is formed when the lobe valleys reattach to each other. The outside broken structures form crescents structures that eventually dissipate and fade out. This process can be observed in Figure 2.28, which shows the ensemble-averaged azimuthal vorticity distribution.
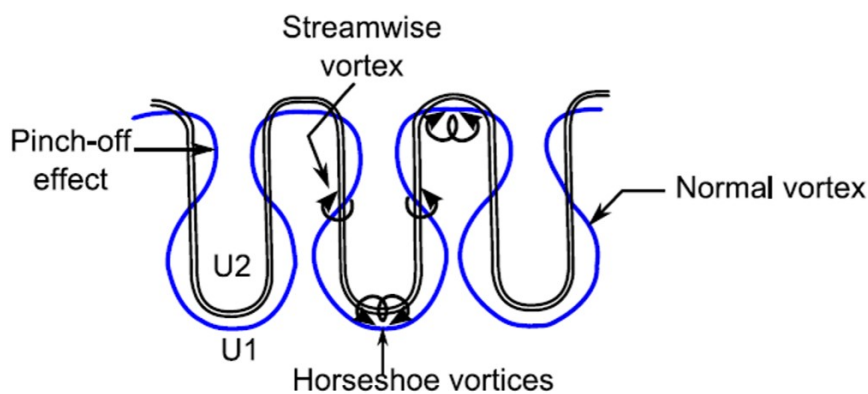
Figure 2.27: Planar view of the vortices that are generated in case of a lobed nozzle [6].

Both the streamwise and azimuthal vorticity have a similar fast decay downstream of the nozzle exit. The decay of both types of vorticity can be observed in Figure 2.29. After the fast decay of the vorticity strength, the vorticity gradually decays even farther downstream. Again, this fast decay indicates the faster turbelence intensity development for a jet exhausted by a lobed nozzle. After the initial

(a) Half a diameter downstream of the nozzle exit.

(b) Two diameters downstream of the nozzle exit.
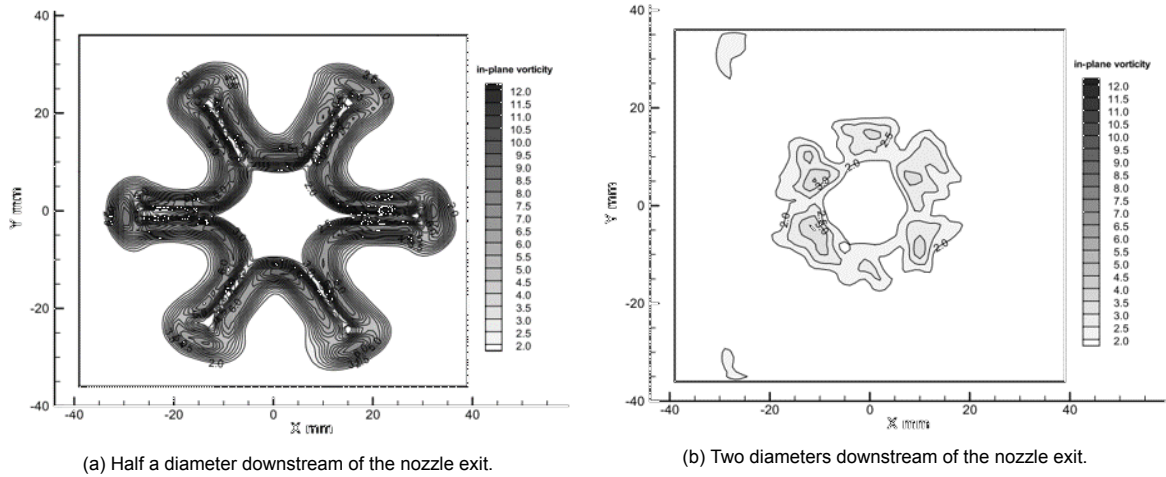
Figure 2.28: Ensemble-averaged azimuthal vorticity distribution, obtained by the Dual-Plane Stereoscopic PIV conducted by Hu et al. (2005) at different downstream locations [21].

fast decay, the gradual decay of the vorticity, and thus also the mixing process, is similar to for the conventional circular nozzle [21].
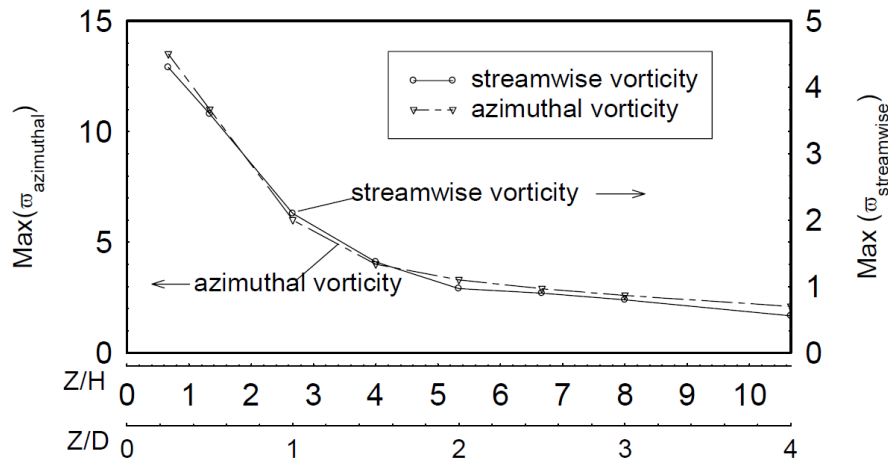
Figure 2.29: The development of the ensemble-averaged streamwise and azimuthal vorticity, found by Hu et al. (2005) [21].

It can be concluded that the lobed nozzle enhances the turbulence development for multiple reasons. First of all, the lobed profile of the nozzle results in a multiscale flow that enhances both the large-scale and the small-scale development. The former due to the large-scale streamwise vorticity that stirs the ambient flow with the jet flow. On top of that, these vortices are broken down into small-scale vortices with similar strength downstream, which enhances the mixing on small-scale level. Farther downstream the fully-developed turbulent flow behaves similar to the jet from the conventional circular nozzle.

2.3.2. Effect on the Characteristics on the Jet Instability Waves

As introduced earlier in this report, decomposition of pressure wavepackets into azimuthal Fourier modes gives insight into the scattering of noise to the far-field. Lyu et al. (2019) performed a temporal stability analysis of the jet instability waves in case a lobed nozzle is used [39]. This has been done in order to investigate the effect on the characteristics of the different azimuthal modes of the jet instability waves.

Simple lobed profiles were used in the analysis, which can be expressed with Equation 2.6. In this relation ϵ corresponds to the lobe penetration rate. The constant R given in Equation 2.6 is chosen such that the exit area of the lobed nozzle is equal to the exit area of the circular nozzle. Hence, the value of R varies with the lobe penetration rate as it corresponds to the mean radius of the area.

$$\sigma = R \cdot (1 + \epsilon \cdot cos(N\varphi)) \tag{2.6}$$

Varying the lobed nozzle parameters gives the geometries shown in Figure 2.30. It can be observed that one lobe does not show a significant change in radial profile compared to the conventional circular nozzle, whereas the higher number of lobes gives a more prominent lobed profile.

(a) $\epsilon = 0.1$. (b) $\epsilon = 0.2$.
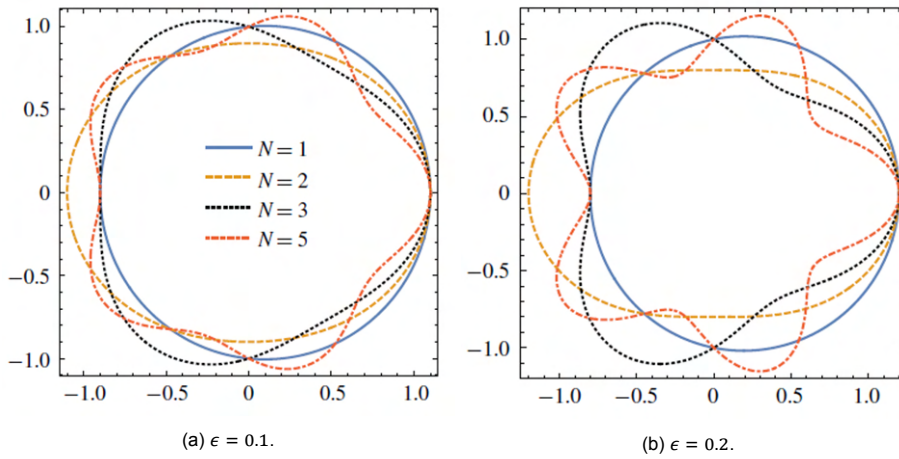
Figure 2.30: Lobed profiles used by Lyu et al. (2019) for different lobe penetration rates ϵ [39].

The flow has been modelled by the linear Navier-Stokes equations as an incompressible flow with the assumption that the mean flow is steady. Additionally, it is assumed that the jet flow is a parallel flow of vortex-sheet type, as shown in Figure 2.31. This simplification is considered to be sufficient for the analysis of low-frequency stability waves close to the nozzle [39]. In reality though, as shown before, the jet mean flow diverges slowly and its shear layer expands downstream [34, 52, 65].
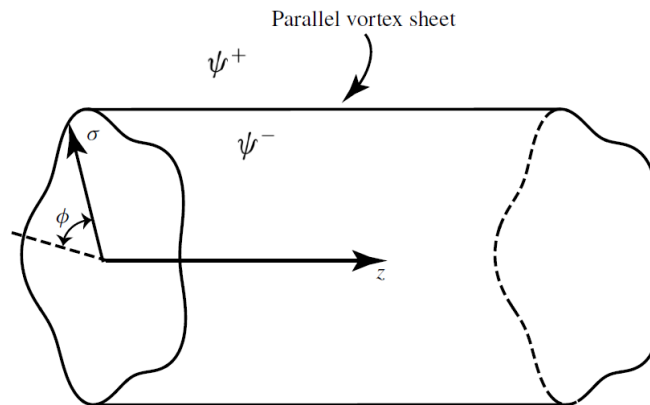
Figure 2.31: Visualisation of a vortex sheet from a nozzle with 5 lobes, where ϕ represents the anti-clockwise azimuthal angle [39].

Solving the system presented by Lyu et al. (2019) gives an insight in the effect of a lobed nozzle on the convection velocity and the temporal growth rate of the instability waves within the jet. It is expected that the temporal growth rate is not significantly different than the spatial growth rate [39]. The convection velocity and the spatial growth rate both affect the jet installation noise. A decrease in the former parameter results in a less efficient scattering of the jet instability waves into sound. A decrease

in the growth rate results in less strong jet instability waves that are scattered at the trailing-edge of the plate. Thus, such changes are considered to be favourable for reducing the noise generated [29, 31]. It is believed that the change in growth rate of the wavepackets will have the most effect on the radiated jet installation noise [39]. The change in these parameters have been examined for different lobed profiles with a penetration rate ranging from 0 to 0.15, and with a number of lobes ranging from 1 to 5. The different liplines for these nozzles can be observed in Figure 2.30. This has been done for the axisymmetric mode 0 and the first two higher-order modes, under the assumption that these are the dominant modes [37].

Firstly, the result for the axisymmetric mode 0 is shown in Figure 2.32. The real part of U_c, indicated with Re, defines the convection velocity, and the imaginary part Im of U_c represents the growth rate. Both characteristics are normalized by the velocity U. Do note, a normalized growth rate below a value of one corresponds to a decay. Furthermore, the normalized frequency is used for the x-axis, indicated by αa where α corresponds to the streamwise wavenumber [39].

It can be observed that for the axisymmetric mode 0 varying both lobed nozzle parameters has little effect. Only for a nozzle with a lobed lipline of 5 lobes, a slight increase in the normalized convection velocity and a slight decrease in the growth rate can be observed for a high penetration rate. This same observation was made for nozzles with chevrons [59]. Nevertheless, as concluded in section 2.2, the axisymmetric mode 0 is not the main contributor to the jet installation noise itself, and thus this little effect on the mode 0 is expected to be not of importance.
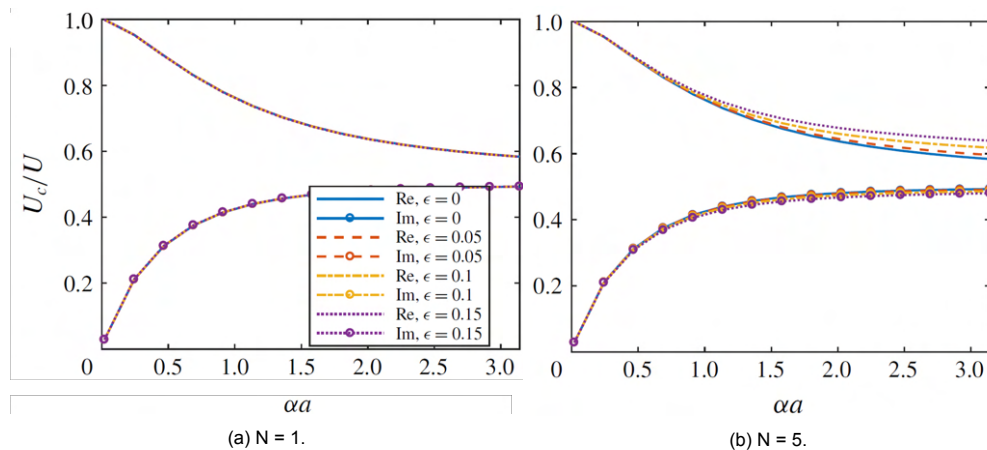
Figure 2.32: The convection velocity (Re) and growth rate (Im) of the jet instability wave mode 0 for a circular and a lobed nozzle [39].

The results for the helical mode 1 can be found in Figure 2.33. For this mode that a high penetration rate and a high number of lobes results in a significant increase in the convection velocity, and also a noticeable decrease in the temporal growth rate. On top of that, it can be seen that the convection velocity has a higher relative increase in the low-frequency region. This is not true for the growth rate as the maximum change is observed in the moderate frequency region. These effects are identical for the negative mode -1 in case of nozzle liplines of three and five lobes.

Interestingly, it can be observed that for mode -1 a nozzle lipline with two lobes has the opposite effect on the convection velocity and temporal growth rate than for mode 1, as shown in Figure 2.34. The former characteristic of mode -1 decreases and the latter characteristic increases for a higher penetration rate. For mode 1 this is not observed. This difference in behaviour is due to the fact that the eigenvalues of both modes are not equal in this case. Subsequently, the even and odd eigenfunctions of the simplied stability problem, that correspond to the modes 1 and -1 respectively, are independent. This independence results in the different effect of the lobed nozzle on the characteristics of the jet instability waves of modes 1 and -1.

For the modes 2 and -2 of the jet instability waves it was also observed that no difference occurs between both modes for a lipline with one lobe. For a nozzle lipline with two lobes, corresponding to

(a) N = 1.

(b) N = 2.

(c) N = 3.

(d) N = 5.
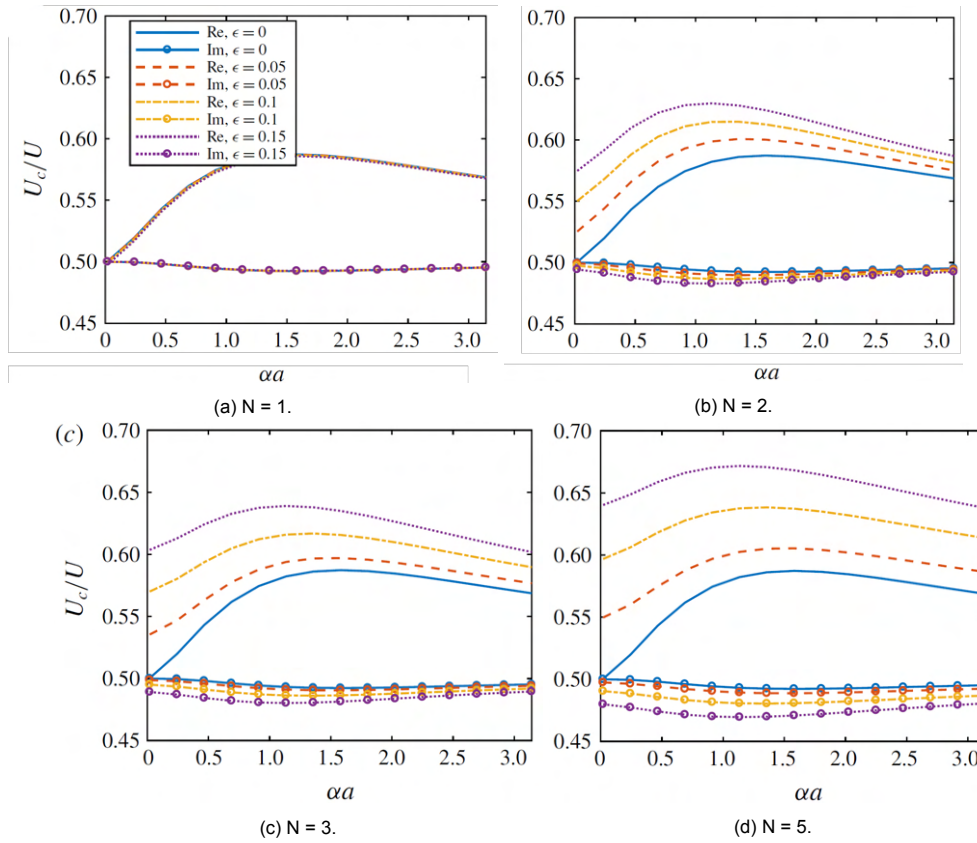
Figure 2.33: The convection velocity (Re) and growth rate (Im) of the jet instability wave mode 1 for different type of nozzles [39].
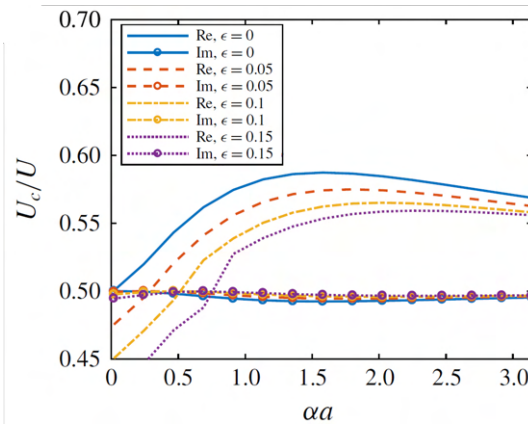
Figure 2.34: The convection velocity (Re) and growth rate (Im) of the jet instability wave mode -1 for a lobed nozzle with two lobes [39].

an elliptical nozzle lipline, both the positive and negative modes show an opposite behaviour for an increasing lobe penetration. However, this difference in characteristics is insignificant. For a lobed lipline with three or five number of lobes, identical behaviour can be observed between the positive and negative modes. For the lobed lipline with three number of lobes, an insignificant difference can be observed in the growth rate but a decrease in convection velocity is observed for a higher lobe penetration rate. For a lobed lipline of five lobes, increasing the lobe penetration results in a similar difference in pressure wave characteristics as for mode 1 and -1.

The effect of changing the convection velocity and the temporal growth rate has an effect on the

pressure field of the jet, which is also analysed by Lyu et al. [39]. Firstly, the negligible change in the convection velocity and the temporal growth rate for mode 0, can be clearly observed in its pressure field, shown in Figure 2.35. In the top contour plots, the result for a low frequency is given, representing the jet installation noise. The lower contour plots shows the result for a high frequency. It can be clearly observed that at a low frequency there is no difference between the jet's pressure waves from the five lobed nozzle and the one lobed nozzle, which is similar to the conventional round nozzle. For both cases an axisymmetric decay outside of the vortex field is observed. Regarding the high frequency pressure field, it can be clearly observed that the high frequency indeed decays rapidly outside of the vortex sheet [39]. .

(a) At a low normalized frequency αa of 0.25.

(b) At a high normalized frequency αa of 2.5.
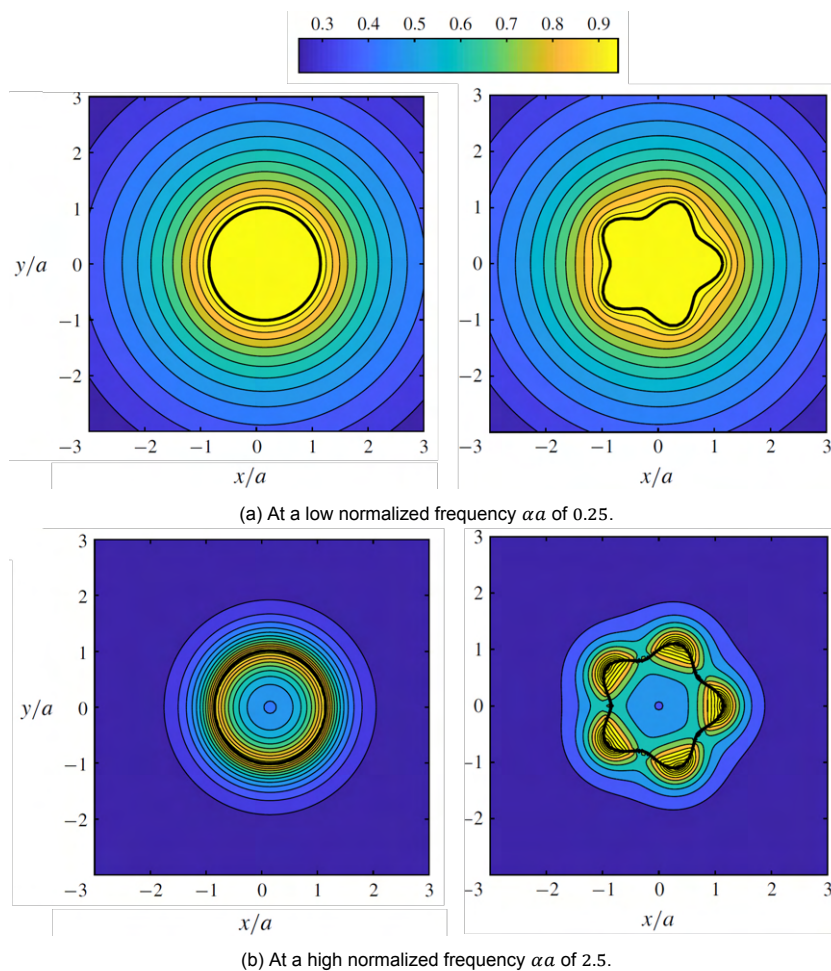
Figure 2.35: Contour plot of the jet's pressure field of mode 0 for a circular nozzle (left) and a lobed nozzle with five number of lobes and a lobe penetration rate of 0.15 (right) [39].

As expected, due to the change in stability characteristics a difference in the pressure field is seen for mode -1. This result is shown in Figure 2.36, at a low frequency. The antisymmetry with respect to a zero azimuthal angle can be seen for $N = 1$. Comparing the pressure field of $N = 1$ with the higher lobed jets show that a faster decay in amplitude can be observed when the lipline deviates from the circular lipline. Moreover, a clear change in the shape of the mode can be found for a lobe number count of 3 and 5, as shown in Figure 2.36c and Figure 2.36d respectively. For the three lobed nozzle, the two lobes of the pressure field are located at two lobes of the vortex sheet profile. This shows the effect of the convection velocity and temporal growth rate [39]. For the lipline of five lobes some additional small changes can be observed at the two other additional lobes.

At a high frequency this mode behaves the same as for mode 0, namely a rapid decay of the instability waves outside the vortex sheet occurs [39]. This suggests that changing the characteristics does not have a significant effect on this pressure field.

(a) N = 1.

(b) N = 2.

(c) N = 3. Illustrated are the lobed profile symmetry planes
(solid white lines), and the antisymmetric pressure field
plane (dashed black line).

(d) N = 5.
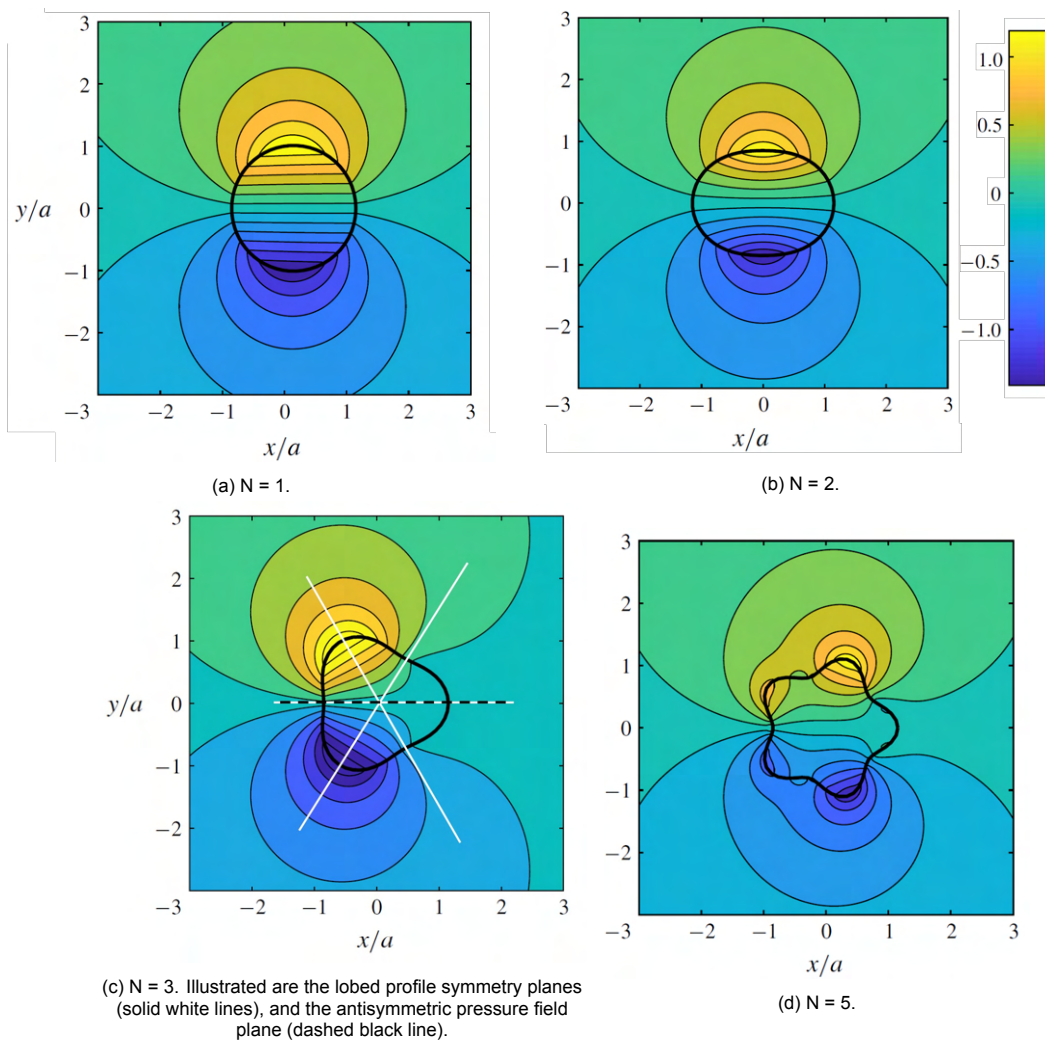
Figure 2.36: Contour plot of the jet's pressure field of mode -1 at a low normalized frequency αa equal to 0.25, for different
nozzle liplines that have a lobe penetration rate of 0.15 [39].

As mentioned before, the effect of the lobed profile showed a different behaviour on the stability
characteristics when the eigenvalues are not identical. This can be explained as follows.

In case of two lobes, the lobed profile has two symmetry planes, i.e. along the vertical and the
horizontal directions. The pressure field experiences in those directions a symmetric and antisymmetric
plane respectively. On the contrary, for a three lobed nozzle this coherence is not present, as shown in
Figure 2.36c. The lobed profile experiences three symmetric planes with an angular spacing of 120°,
where only one of the planes corresponds to the antisymmetric plane in the pressure field. Rotating the
pressure field by 120° or 140° results in a pressure field that also corresponds to an eigensolution of
this stability problem, with the same eigenvalue [39]. In order to ensure this, and thus equal behaviour
between the even and odd instability waves of the same order, it is important that not every symmetry
plane in the lobed vortex plane also corresponds to a symmetric or antisymmetric plane in the pressure
field of the mode shape.

It is expected that the behaviour is opposite between even and odd modes when the mode n equals
$\pm N/2$, $\pm N$, $\pm 3N/2$, $\pm 2N$, and so on. This is expected as for a conventional circular nozzle, the pres-
sure field of mode n corresponds to $2n$ lobes [39]. This expectation can be verified with the earlier
made observations. For mode 1 and -1 in case of a nozzle with two lobes, the behaviour is not equal.
On top of that, for mode 2 and -2 this is also true. Hence, in order to avoid the opposite behaviour
between even and off modes for a high number of high-order modes, a high number of lobes is required.

Lastly, the result of a lobed vortex sheet on the pressure field of mode 2 is shown in Figure 2.37. The same conclusions can be made regarding the degeneracy. Furthermore, in Figure 2.37d, the effect of changing the stability characteristics is clearly shown. The increase in decay of the stability waves, compared to the less lobed nozzles, is shown to be higher for most of the lobes. The pressure field at a high frequency for this mode shows the same behaviour as was mentioned for the other modes.

(a) N = 1.

(b) N = 2.

(c) N = 3.

(d) N = 5.
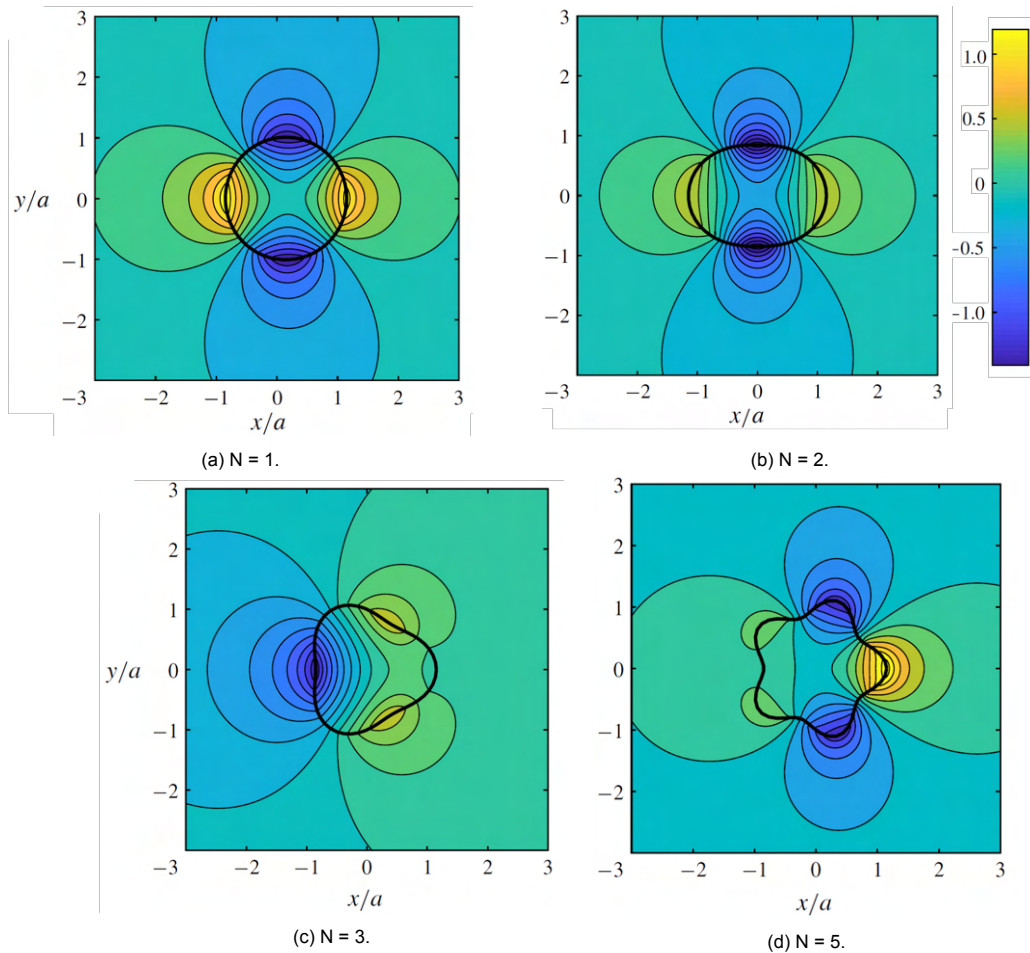
Figure 2.37: Contour plot of the jet's pressure field of mode 2 at a low normalized frequency αa equal to 0.25, for different nozzle liplines that have a lobe penetration rate of 0.15 [39].

2.3.3. Jet Installation Noise for Lobed Nozzles

Based on the temporal stability analysis presented above, an experimental study on reducing the jet installation noise by using a lobed nozzle was conducted [37]. The lobed nozzle used for this experiment consists of the geometry described in Equation 2.6, with a penetration rate of 0.3 and five number of lobes. The lobe length is approximately four nozzle diameters. A visualization of the lobed nozzle is given in Figure 2.38.

For the experiment a flat plate was used with the trailing-edge of the plate placed at a distance L downstream of the nozzle exit. Moreover, the vertical distance between the flat plate and the jet nozzle equals H. The former distance L was varied between $6D$ and $4D$. The separation distance H was varied between $1.25D$ and $3D$. The three configurations that will be analysed in this section are shown in Table 2.3.

The lobed nozzle showed different effects on the generated jet installation noise. As presented before, the highest jet installation noise is achieved with the largest value of the horizontal distance L and the smallest value of the separation distance H. In the experiment this corresponds to configuration 2.
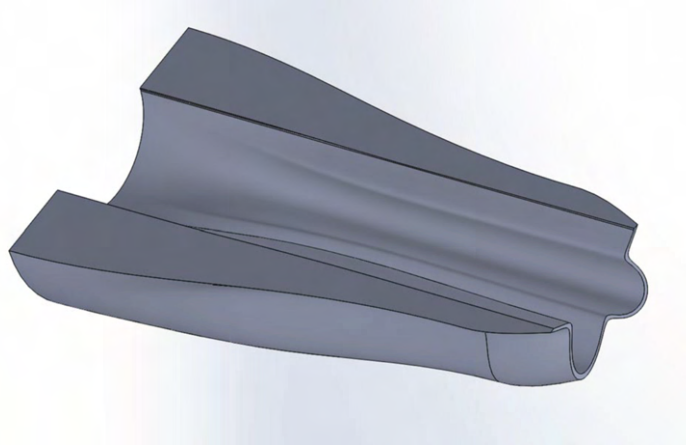
Figure 2.38: Lobed nozzle used in the experimental study conducted by Lyu et al. (2019) [37].

Table 2.3: Configurations used for the experimental study of Lyu et al. (2019), corresponding to the parameters used in Figure 2.39 [37].

	Configuration 1	Configuration 2	Configuration 3
L	6D	6D	4D
H	3D	1.5D	1.25D

Different observation angles with respect to the jet centreline are shown, where $30°$ corresponds to the shallow angles close to the jet-axis, and $90°$ corresponds to the sideline directions of the jet.

From the measurements it became evident that for both nozzles the most intense jet installation noise occurs indeed for configuration 2, as shown in Figure 2.39b for both the shielded and the unshielded sides. Comparing the PSD levels between configuration 2 and the configuration 1, which is closest to an isolated jet it can be concluded that for both nozzles the jet installation noise is mainly observed at observation angles of $60°$ and $90°$, as shown in Figure 2.39b and Figure 2.39a, respectively. The large humps correspond to the scattering of the jet instability waves at the trailing-edge of the flat plate [37]. Moreover, small PSD humps can also be observed for the shallow angle of $30°$ in case of configuration 2, which also shows the influence of jet instability waves scattering.

Comparing the PSD of the unshielded and the shielded sides for all configurations shows that the shielded side does not include the reflected jet waves, which is shown in the high-frequency region at the unshielded side. Moreover, as explained before, the lobed nozzle will result in enhanced jet mixing and subsequently in a lower potential core length of the jet. Comparing a round nozzle with the lobed nozzle for the same jet-plate configuration shows this effect with the less perceived noise at the shielded side of the plate. The reduction in potential core length, and thus a flow development located more upstream, increases the flow shielding efficiency of the plate. These observations are consistent with the earlier presented conclusions from literature.

The difference in far-field noise between the jets from the different nozzles is little. At the shielded side, it can be observed that the jet from the lobed nozzle generates slightly less far-field noise in the entire frequency region. This difference becomes more evident for the configurations that generate more jet installation noise. Nevertheless, this difference remains insignificant.

At the unshielded side, it can be observed that the jet from the lobed nozzle generates more far-field noise in the high-frequency region than the jet from the circular nozzle. In the low-frequency and mid-frequency region the jet from the lobed nozzle generates less far-field noise. The difference between the jets is larger at the shallow observation angles. This can be attributed to the enhanced mixing by the jet of the lobed nozzles which results in less large-scale structures in the jet, which dominate the radiation of far-field noise to the shallow observation angles. Nevertheless, this difference is again

insignificant.

(a) $L = 6D$, $H = 3D$.

(b) $L = 6D$, $H = 1.5D$.

(c) $L = 4D$, $H = 1.25D$.
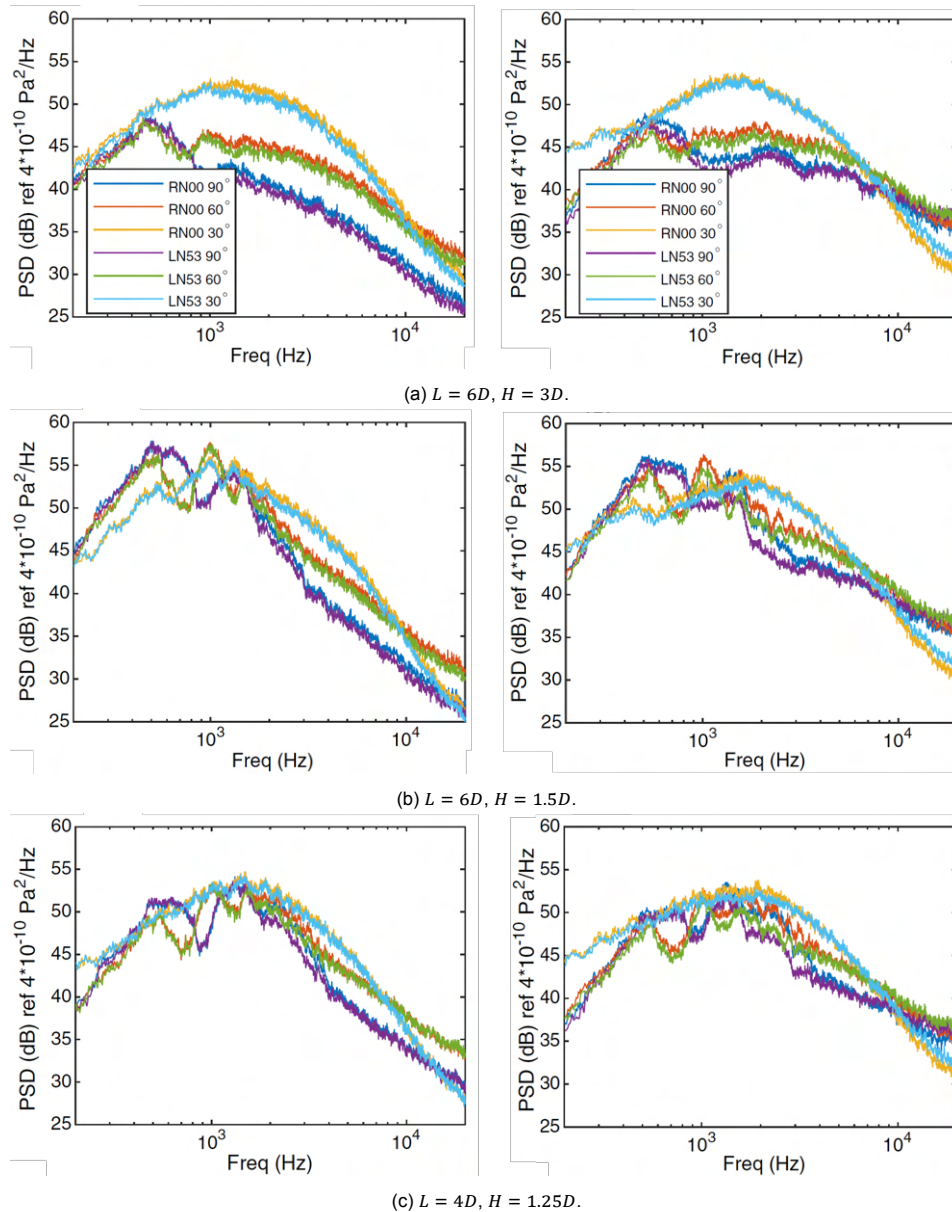
Figure 2.39: Installed jet noise for a round nozzle (RN00) and a lobed nozzle (LN53) at an jet Mach number of 0.5, with different flat plate positions for the shielded side (*left*) and the unshielded side (*right*) shielded side [37].

The effect of the Mach number on the isolated jet noise has also been investigated by comparing the PSD level between a Mach number of 0.5 and 0.7. For the isolated jet noise in case of the former Mach number, it was found that the use of the lobed nozzle results in a noise reduction of approximately $1.5 - 2 \ dB$ in the intermediate frequency region, as can be observed in Figure 2.40a. In the low-frequency region, corresponding to $f < 500 \ Hz$, there was no significant noise reduction. On the contrary, in the high-frequency region, corresponding to $f > 8 \ kHz$, there is a noise increase observed. The noise reduction and increase is mostly observed along the sideline direction of $90°$, whereas this is little for an shallow angle of $30°$. For a higher Mach number it can be observed that the changes in noise are as large as $3 \ dB$ in the intermediate frequency range. On top of that, for lower observation angles the change in noise becomes significant. In the high-frequency region it can be seen that the lobed nozzle does not result in an increase in noise, but in a slight decrease.

All in all, it can be concluded that the noise reduction achieved in the experimental study is little,
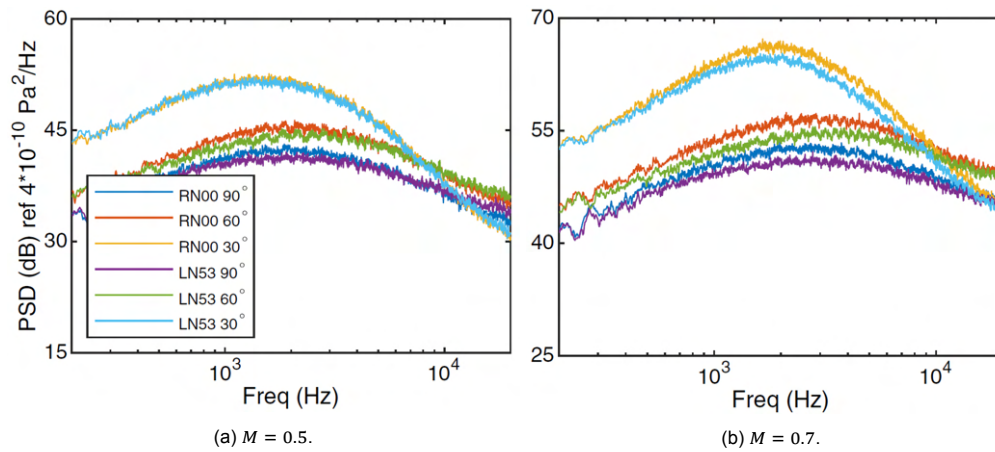
Figure 2.40: Isolated jet noise for a round (RN00) and lobed (LN53) nozzle at an different jet Mach numbers [37].

despite the conclusion made in the described temporal stability analysis. It was suggested that this could be due to the dominance of the axisymmetric mode of the jet instability waves, of which the characteristics are little affected by the lobed profile. However, this is in contradiction with the findings from Bychkov et al. (2020) [8], who concluded that the jet installation noise is carried by the higher-order modes and not by the axisymmetric mode. Another reason for not achieving significant noise reduction could be that the jet mean flow becomes axisymmetric again relatively rapidly downstream of the nozzle exit. After the jet is fully developed, the flow behaves similarly as in case of the conventional circular nozzle. In order to make a conclusion regarding these contradictions, flow measurements need to be done to analyse the jet flow behaviour downstream of the nozzle. This can be done with either pressure measurements or a velocity distribution measurement.

3

Method of Analysis

In this chapter, the method of analysis is presented. In order to answer the research questions of this work an experimental campaign has been done. First of all, the wind tunnel used for the experiment will be described in this chapter. This will be followed by presenting the jet nozzles used for the experimental campaign. Moreover, the measurement techniques will be presented. Lastly, the method of post-processing the acquired measurement data is discussed.

3.1. Anechoic Wind Tunnel

The experiment was conducted in the vertical anechoic open-jet wind tunnel at Delft University of Technology[1], as shown in Figure 3.1a. The used anechoic wind tunnel has an open-jet configuration to enable the development of a jet from a nozzle exit. As shown in Figure 3.1a, the test chamber consists of ambient air and a flow is blown through a circular outlet in the centre of the room in the vertical direction. For the experiment a contraction nozzle has been used, shown in Figure 3.1b, which is flush-mounted to the flow outlet. The nozzle contracts the flow to achieve higher subsonic velocities. On top of the nozzle, different jet nozzles are installed for the experiment. The jet nozzles with their outlet flow represent the simplified system as a single-stream and cold jet.

It is important to note that the single-stream jet is mostly a reasonable approximation for high-bypass ratio engines where the secondary jet dominates the far-field noise [52]. This approximation cannot be made for small bypass ratio engines as the hot core generates significant noise in the far-field for these jets. In addition, for the experiment a jet flow parallel to the flight direction is approximated and thus configurations during landing and take-off are not simulated.

In order to be able to perform acoustic measurements that do not contain any reflections, the test chamber has acoustic foam wedges on the wall, floor and ceiling. The wedges prevent unwanted reflections for frequencies larger than $173.5\ Hz$ as defined by the criterion that the height of a wedge should not be smaller than a quarter of the wavelength in order to absorb the incoming sound waves [56]. The upper limit of measurements without reflections is $20\ kHz$ [45]. On the ground a metal grid is placed to enable the access to the wind tunnel and the placement of the instrumentation. The grid consists of squared holes of $10x10mm$, which prevents unwanted reflections [45].

The turbulence intensity in the flow exhausted from the flow outlet in the tunnel is below 0.22% for any nozzle or flow velocities. For larger velocities it has been measured to be even lower [45]. This is sufficient as the measurements will be done with a minimum nozzle exit velocity of $50\ m/s$, of which the maximum possible measurement velocity for this wind tunnel is $75\ m/s$ with the use of the above mentioned contraction nozzle.

---

[1]https://www.tudelft.nl/en/ae/organisation/departments/aerodynamics-wind-energy-flight-performance-and-
propulsion/facilities/low-speed-wind-tunnels/a-tunnel

(a) The anechoic vertical wind tunnel [45].   (b) Model of the contraction nozzle and a jet nozzle.
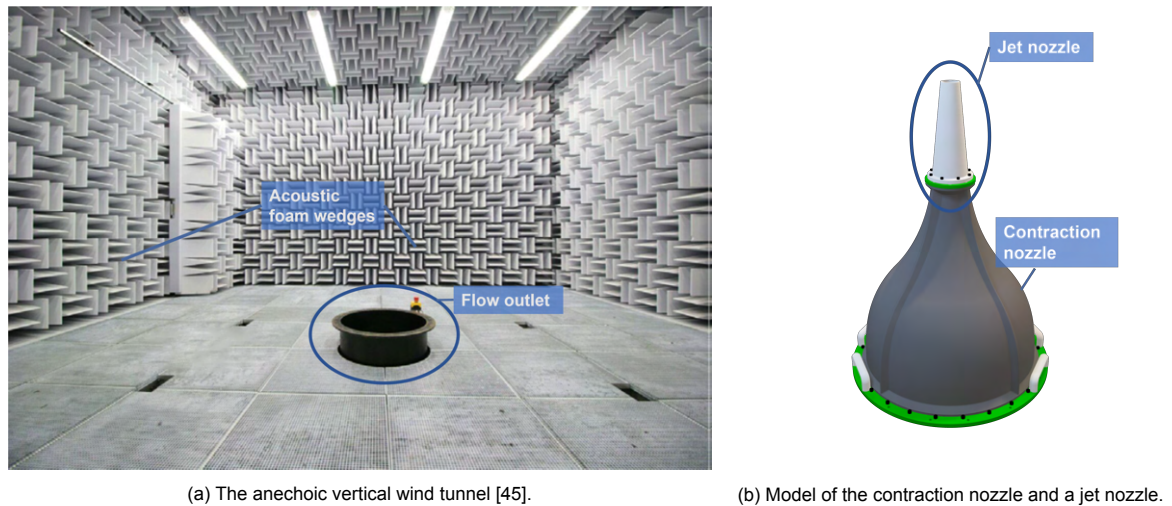
Figure 3.1: Wind tunnel set-up used for the experiments.

3.2. Jet Nozzles

For the experiment it was decided to measure the jet from three different nozzles. First of all, a conventional circular nozzle will be used as the baseline nozzle. Next to this, two nozzles with a lobed lipline will be tested to assess the effects of the nozzle geometry on the jet chracterics and the aeroacoustics. This section will first present the nozzle exit profiles for the three jet nozzles. Afterwards, the design of the full nozzles will be illustrated.

3.2.1. Nozzle Exit Profiles

The geometry of the lobed nozzles is based on the nozzle lipline as defined by Lyu and Dowling (2019) [39], given by the earlier presented Equation 3.1. The mean radius R is chosen such that the area of the lobed nozzles exits is equal to the area of the baseline nozzle exit.

$$\sigma = R \cdot (1 + \epsilon \cdot cos(N\varphi)) \tag{3.1}$$

It was decided to use this same method for determining the lobed nozzles liplines as this gives the possibility to compare the results obtained in this work with the results obtained by the extensive research of Lyu and Dowling [37–40]. Therefore, a nozzle with 5 lobes and a lobe penetration rate of 0.3 is investigated. Furthermore, it was decided to study the effect of the penetration rate on the aeroacoustic emissions, which is missing in the previous research.

From the state-of-the-art review it became evident that large penetration rates have a favourable effect when used in combination with a large number of lobes. Both parameters show optimal values in relation to the aeroacoustic performance. Moreover, it was concluded that a larger penetration rate has a more beneficial effect than increasing the number of lobes. Hence, it has been decided to investigate a second lobed nozzle with the same amount of lobes but with a larger lobe penetration rate of 0.4. A comparison between the conventional circular nozzle and the two lobed nozzles can be observed in Figure 3.2. The geometric parameters of the three investigated nozzles are summarized in Table 3.1. For the rest of this work, the baseline nozzle will be addressed as *CN1*, the lobed nozzle with a lobe penetration rate of 0.3 as *LB1* and the lobed nozzle with a lobe penetration rate of 0.4 as *LB2*.

3.2.2. Jet Nozzles Design

The three jet nozzles consists of two parts. This has been done as it gives the opportunity to 3D-print the jet nozzles as the printers limit the dimensions of the printed parts. On top of that, previous research showed that reducing the axial lobe length of the lobed nozzle does not significantly change the jet characteristics, and thus there is no loss in benefits for reducing the axial lobe length. All the three nozzles share the same base contraction part, shown in Figure 3.3. The component is made from
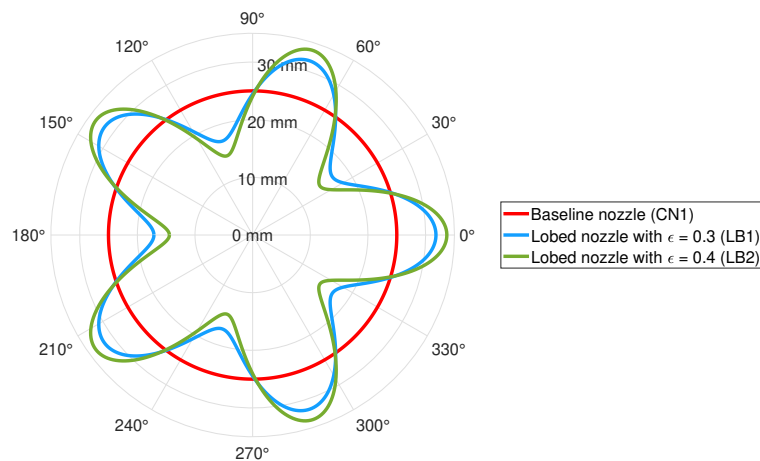
Figure 3.2: Liplines of the circular nozzle and the lobed nozzles (in millimeters).

Table 3.1: Geometry parameters of the nozzles.

Nozzle	Label	Mean radius (r/a)	Number of lobes N	Lobe penetration ϵ	Geometry exit area
Circular nozzle	CN1	$25\ mm$	−	−	$1.96x10^3\ mm^2$
Lobed nozzle 1	LB1	$24.46\ mm$	5	0.3	$1.96x10^3\ mm^2$
Lobed nozzle 2	LB2	$24.06\ mm$	5	0.4	$1.96x10^3\ mm^2$

aluminium by CNC to ensure a smooth surface inside of the contraction component. It will connect the wind tunnel test chamber with the different jet nozzles while also further contracting the inner cone diameter. The bottom flange can be mounted with bolts onto the wind tunnel test chamber, where an O-ring is used to prevent leakage. The top flange is used to mount the jet nozzles on top of the contraction.
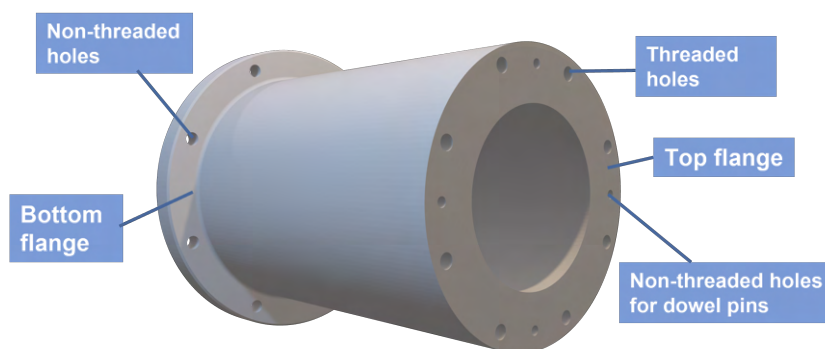
Figure 3.3: Bottom contraction component of the jet nozzles.

The jet nozzles are made of 3D-printed material by Stereolithography (SLA). The production was done at the company 3D Hubs[2] and the material used was the Formlabs standard resin. This type of 3D-printing with the corresponding material has been chosen as it allows the production of the complex geometries of the lobed nozzles. The strength of the standard resin is also sufficient as the jet nozzles will not be exposed to large loads during operation. In addition, both the production time and the costs are significantly less with respect to other production techniques, which is beneficial for future work.

---

[2]3D Hubs website: https://www.hubs.com/

Lastly, the nozzles have a smooth finishing with a tolerance of 0.5% with a lower limit of approximately $0.15\ mm$. A three-dimensional view of the different nozzles is given in Figure 3.4.

| Baseline nozzle (CN1) | Lobed nozzle 1 (LB1) | Lobed nozzle 2 (LB2) |
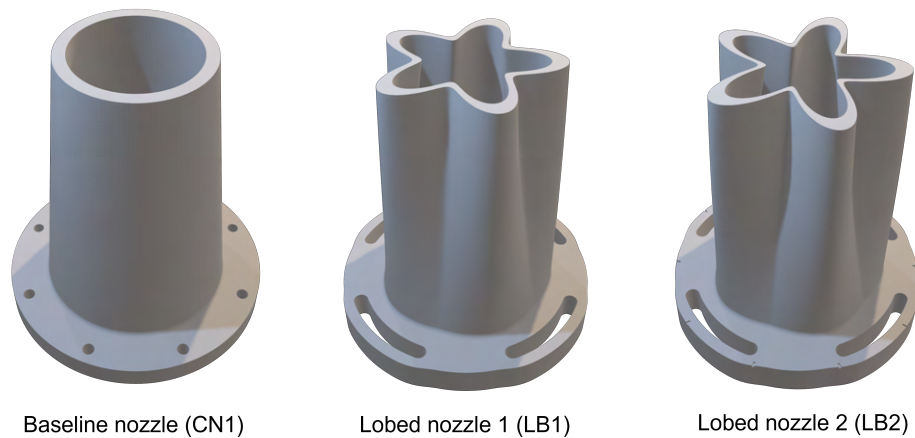
Figure 3.4: Jet nozzles that will be used in this work.

The three jet nozzles are mounted on the contraction part by bolts and by dowel pins. The dowel pins are used to flush the inner shaft of the bottom part with the inner shaft of the jet nozzles. This ensures that the flow is not affected by the transition from the bottom part to the nozzle. Moreover, the jet nozzles have an O-ring channel at the bottom surface of their bottom flange, which enables the use of an O-ring to prevent leakages. The O-ring channel can be visualised with the bottom view of the flange of LB1, as depicted in Figure 3.5. Do note that for the lobed nozzles the bolt holes are connected by the use of 4 slots. This creates the possibility to align a lobe peak or a lobe valley directly towards the fixed measurement probe without any need of fully dismount the nozzle itself, but simply by rotating it. This is not a problem for the experimental study conducted in this work as the flow will have a maximum jet exit velocity of $75\ m/s$. and thus inducing only a little load on the components attached to the settling chamber.
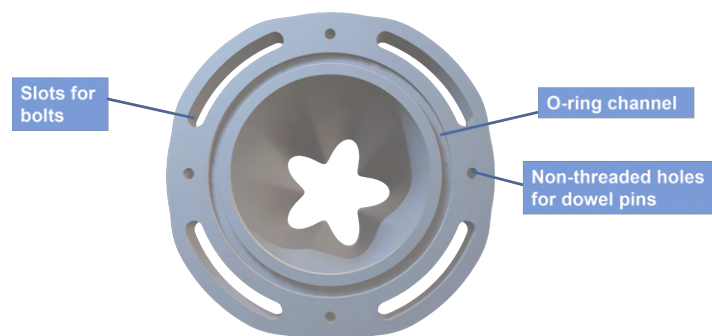
Figure 3.5: Bottom view of the bottom flange of LB1.

The contraction of the inner shaft of the three nozzles can be visualised with the cut-through view shown in Figure 3.6. The baseline nozzle follows the linear contraction of the bottom component, whereas the lobed nozzles follow a non-linear contraction which varies in azimuthal direction. The transition from the start of a lobed nozzle to a lobe valley results in a transition from a linear slope in the internal wall to a wall that is nearly parallel to the axial direction. On the contrary, the presence of a lobe peak results in a significantly larger slope of the internal wall. It is ensured for the lobed jet nozzles that the transition from the settling chamber to the nozzle exit is smooth in order to prevent separation and keep the flow laminar.

Baseline nozzle (CN1)   Lobed nozzle 1 (LB1)   Lobed nozzle 2 (LB2)
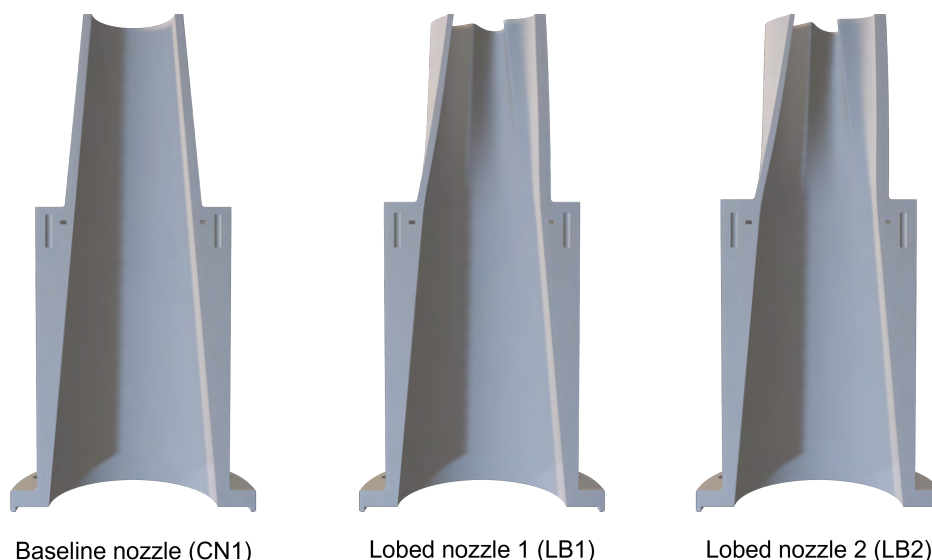
Figure 3.6: The contraction of the inner shaft for the three jet nozzles, including the bottom component of the nozzles with the initial linear contraction.

The actual dimensions of the bottom part and the three jet nozzles can be found in the CAD drawings provided in Appendix A.

3.3. Experimental Set-up

The experimental campaign involves multiple different measurements. Firstly, hot-wire anemometry is used to characterize the jet development of the different nozzles in terms of the velocity and turbulence development in the flow. This method is presented in subsection 3.3.1. Moreover, as presented in subsection 3.3.2, near-field microphone measurements are done with a linear array that is positioned along the shear layer of the jets, which is aimed at gaining insights into the behaviour of the pressure waves. The far-field noise is measured with a polar arc and a beamforming panel to assess the acoustic performance of the jets, as presented in subsection 3.3.3. Lastly, section 3.4 presents the post-processing of the obtained data from the three different type of measurements.

3.3.1. Hot-wire Anemometry Measurements

The hot-wire anemometer (HWA) is a thermal sensor which detects within a flow the velocity by measuring the amount of heat transfer between the sensor and the flow. The time series obtained from a measurements gives the possibility to determine the mean velocity and the turbulence intensity with the measured velocity fluctuations. The thermal sensor is a thin electrical wire that has an electrical current send through it. When electrical current flows through the wire, electrical energy is dissipated and transformed into thermal energy by the Joule effect.

The hot-wire anemometer that is used is a Constant Temperature Anemometer (CTA). This works with the principle that the temperature of the wire is kept constant through a bridge circuit. Therefore, the heat losses are balanced by the heat generation in order to keep the temperature constant. The heat losses occur due to convection, conduction and radiation. However, the contributions of both conduction and radiation are negligible compared to the losses due to the convection [57]. If the velocity changes, the heat losses due to the convection also changes and thus the heat production needs to be increased or decreased to keep the temperature constant. The heat production is achieved by varying the current through the wire. The variation in current will result in a varying voltage, as can be explained using the relation shown in Equation 3.2. The resistance of the wire (R_w) is constant and thus a varying current (I) results in a varying measured voltage (E).

$$E^2 = I^2 R_w^2 \tag{3.2}$$

Using the required heat equilibrium, King's law can be derived [57]. King's law, defined as shown

in Equation 3.3, defines the relation between the measured voltage and the flow properties. This relation can be used to determine the flow velocity (U) as expressed by Equation 3.4. The coefficients (C_N) are determined with the calibration by measuring different flow velocities with a pitot tube and by simultaneously measuring the voltage with the HWA system. The calibration included the working flow temperature in order to prevent errors when this temperature varies over time.

From this relation it becomes evident that for an voltage increase, the flow velocity increases as more heat is dissipated due to convection.

$$E^2 = A + B \cdot U^{0.5} \tag{3.3}$$

$$U = C_0 + C_1 \cdot E + C_2 \cdot E^2 + C_3 \cdot E^3 + C_4 \cdot E^4 \tag{3.4}$$

For the measurements a Dantec Dynamics probe type 55P15 was used. This type of probe has straight prongs with a tungsten wire sensor in between them, as can be observed with the sketch shown in Figure 3.7. The properties of the wire are shown in Table 3.2. The probe can be used to measure the mean and fluctuation flow velocities in one direction. Hence, the wire and probe needs to be positioned perpendicular to the flow direction.
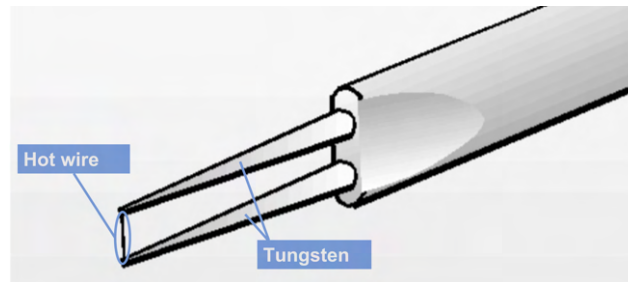
Figure 3.7: Dantec Dynamics probe type 55P15 [14].

Table 3.2: Properties of the hot-wire anemometer Dantec wire.

Property	Value
Diameter	5 μm
Length	1.25 mm
Resistance at 20°C	3.40 Ω
Leads resistance	0.50 Ω
Overheat ratio α_{20}	0.36%

For the measurements, the hot-wire probe is connected to a two-axis Zaber system that gives the ability to move the probe in a plane parallel to the nozzle exit. The Zaber system is mounted onto a steel bar that can be moved up and down, corresponding to the jet's upstream and downstream direction, respectively. The probe is connected to a Wheatstone bridge IFA 300 that uses a feedback circuit to maintain the constant wire temperature. The bridge gives an output that is sent to a computer via a National Instruments data acquisition board.
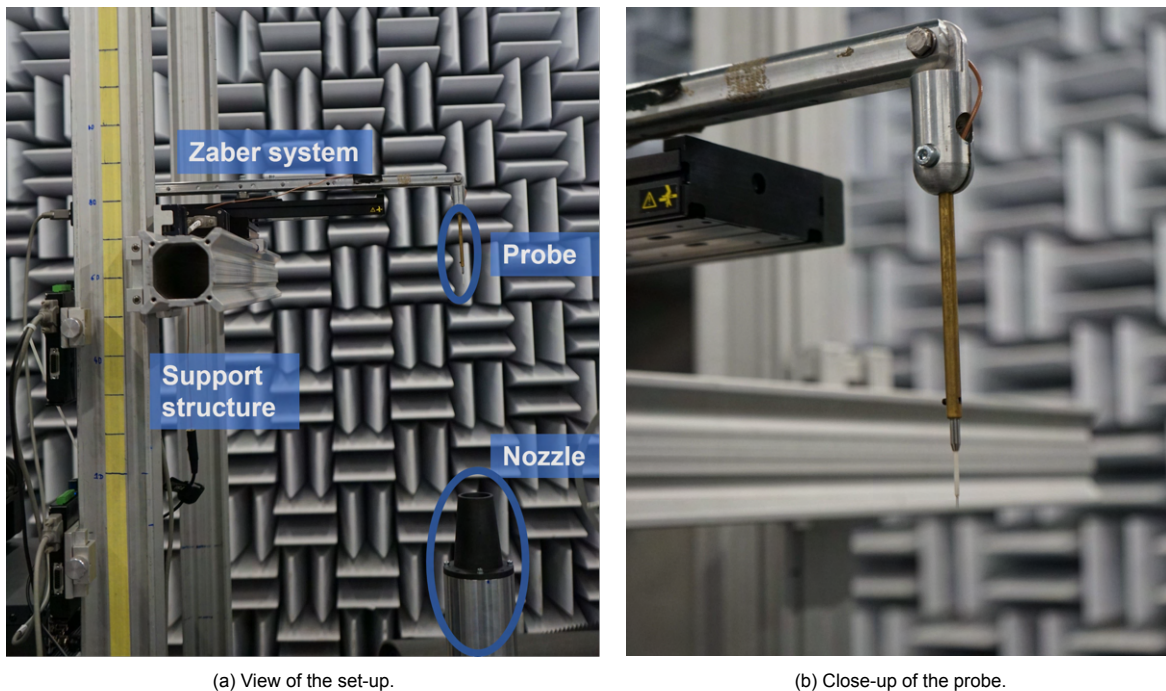
(a) View of the set-up.   (b) Close-up of the probe.

Figure 3.8: Test set-up of the hot-wire anemometer with the baseline nozzle (CN1).

The HWA experimental campaign involves acquisitions at different downstream locations from the nozzle exit plane. A radial profile is made that captures the flow from one outer shear layer edge to the opposite outer shear layer edge. These measurements are done from one baseline diameter downstream to ten diameters downstream of the nozzle exit plane. For the lobed nozzles it is ensured that the cut-through was done from a lobe peak to a lobe valley.

In addition, measurements were done just above the nozzle exit plane to capture the initial boundary layer at the exhaust. The measurements were done in a range of one to two centimetres, with the nozzle lipline in the centre of the range to get the boundary layer profiles of the nozzles. For the lobed nozzles, a measurement is done for a lobe peak and a measurement is done for a lobe valley.

The measurements for the three jets were done at a constant sampling frequency of $51200\ Hz$. The measurement period was varied. For the first measurements, conducted at one diameter downstream, a measurement time of 12 seconds was used. For the other measurements a measurement time of 15 seconds was used.

3.3.2. Near-field Pressure Measurements

A linear microphone array is used to capture the development of the near-field pressure waves. The array consists of a bar that houses 56 GRAS 46PH microphones, which have a $1\ dB$ accuracy for the range of 50 Hz to 5 kHz[3]. The microphones are placed at a constant spacing of $12\ mm$. The first microphone is positioned at the nozzle exit, while the last microphone is positioned at approximately 0.65 m downstream of the nozzle exit, which corresponds to approximately 13 baseline nozzle diameters downstream.

A picture of the test set-up of the linear array is given in Figure 3.9. Using the HWA measurements an average jet spreading of $8°$ is determined, and thus the linear array is positioned along the shear layer with an angle of $8°$ degrees with respect to the vertical jet-axis.

Pressure measurements are done in the conditions as presented in Table 3.3. The near-field of the isolated jets is measured at three different velocities, namely 50, 60 and $70\ m/s$. On top of that, measurements are done at different locations from the nozzle lipline, namely at 25, 50 and $75\ mm$ from the baseline lipline. The test set-up for a distance of $25\ mm$ is shown in Figure 3.9b. At these locations

---

[3]https://www.grasacoustics.com/products/special-microphone/array-microphones/product/ss_
export/pdf2?product_id=178

(a) View of the entire set-up.   (b) Close-up of the test set-up.
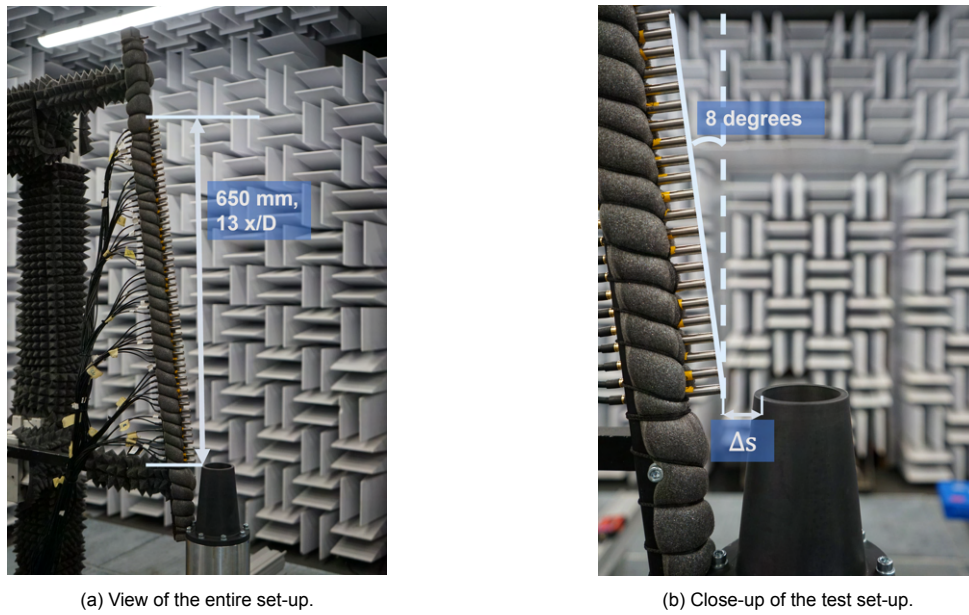
Figure 3.9: Test set-up of the linear array placed at 25 mm from the lipline of the baseline nozzle.

the linear array is fixed while measuring the different jets, and thus the distance between the first micro-phone of the array and the liplines of the different nozzles differs. For each configuration, the near-field of the lobed jet is measured twice, depending on the azimuthal position of the linear array with respect to either the lobe peak or lobe valley, as shown in Figure 3.10a and Figure 3.10b, respectively.

Table 3.3: Conditions of the linear array measurements per nozzle.

Test number	Velocity (U_j)	Distance from the baseline lipline Δs	Measurement time per point
1	50 m/s	25 mm	15s
2	60 m/s	25 mm	12s
3	70 m/s	25 mm	15s
4	50 m/s	50 mm	15s
5	60 m/s	50 mm	15s
6	70 m/s	50 mm	15s
7	50 m/s	75 mm	15s
8	60 m/s	75 mm	15s
9	70 m/s	75 mm	15s

Next to the isolated configurations, measurements have also been performed with a flat plate in-stalled close to the jet nozzles. For this a streamwise distance L between the nozzle exit and the plate its trailing edge of three baseline diameters has been taken. Moreover, a separation distance H of one baseline diameter has been used for this. The test-setup for these measurements is shown in Figure 3.11, where a distinction is made between the unshielded and the shielded measurement.

For the unshielded measurement, the flat plate is installed on the opposite side of the nozzle com-pared to the linear array position, as shown in Figure 3.11a. As shown in Figure 3.11b, the flat plate is installed in between the jet nozzle and the linear array for the shielded measurement.

For these measurements the same conditions are used as the measurements of the isolated jet

(a) Lobed nozzle with peak orientated to the linear array.
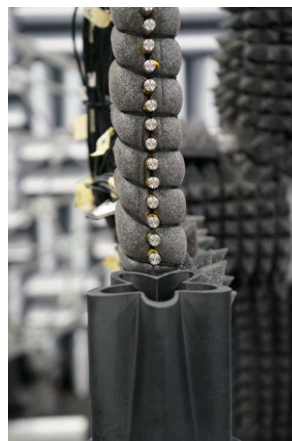
(b) Lobed nozzle with valley orientated to the linear array.

Figure 3.10: Orientation of the lobed nozzles for the linear array measurements.

nozzles. For every nozzle a measurement is done at the shielded side and the unshielded side, of which the same three different velocities are measured. For the lobed nozzles an additional measurement is done in order to orientate both a lobe valley and a lobe peak towards the flat plate.
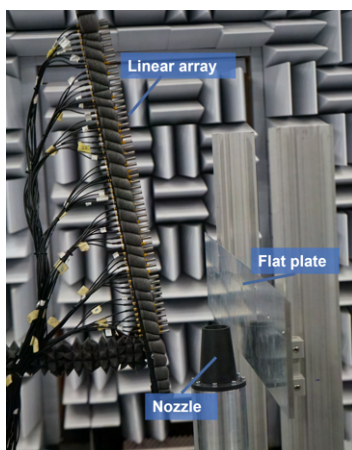
(a) Unshielded measurement.
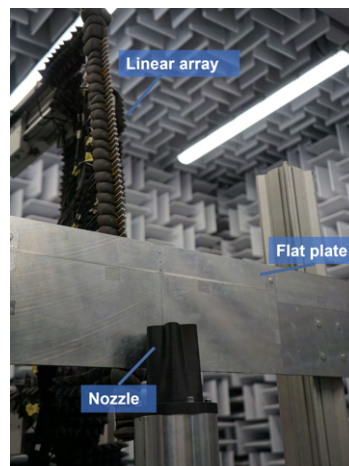
(b) Shielded measurement.

Figure 3.11: Set-up of linear array measurements with a flat plate installed next to the jet nozzle.

3.3.3. Far-field Pressure Measurements

The set-up of the far-field measurements is shown in Figure 3.12. The set-up involves two different microphone configurations. Firstly, the beamforming panel, depicted on the right of the jet nozzle in Figure 3.12. Secondly, a polar arc with a radius of $120\ cm$ is used, as shown on the left of the nozzle. Both have been developed by the Delft University of Technology. The beamforming panel is positioned at $120\ cm$ from the jet-axis and the microphone in the centre of the polar arc is also positioned at $120\ cm$ from the jet-axis.

The beamforming panel houses 64 GRAS 46PH microphone, which are distributed as shown in Figure 3.13a. For the measurements done, the beamforming panel is positioned such that microphone 42 is located in the same plane as the nozzle lipline. Hence, microphone 42 measures the far-field noise along the positive sideline direction. At the other side of the nozzle, the polar arc houses of 8 GRAS 40PH microphones that have an equidistant angular spacing of 10 degrees, of which microphone 68 measures the noise along the negative sideline direction. The distribution of the microphones is shown in Figure 3.13b.
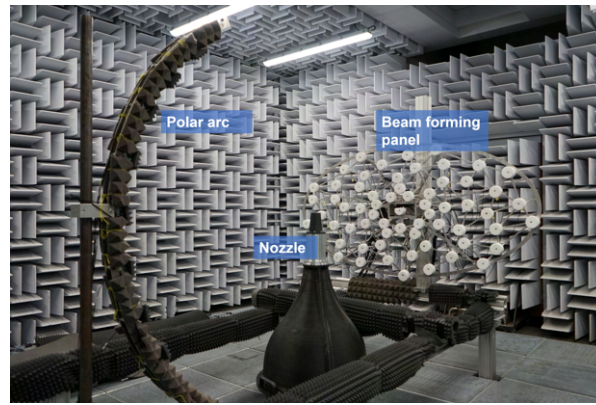
Figure 3.12: Test set-up of the far-field measurements with the isolated baseline nozzle.

(a) Distribution in the beamforming panel.

(b) Distribution in the polar arc.
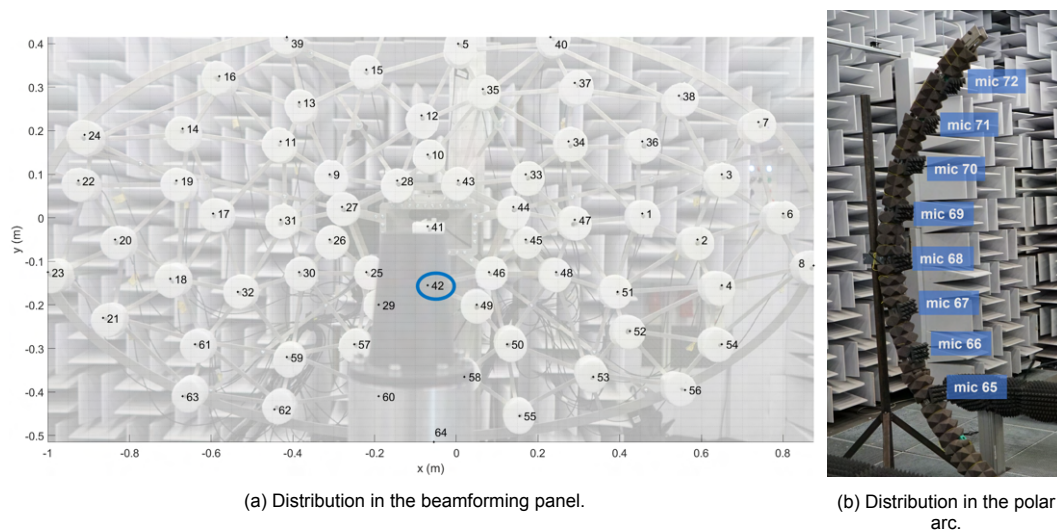
Figure 3.13: Microphone distribution during the far-field measurements.

Analogously to the linear array, the aeroacoustic measurements are conducted at the three different nozzle exit velocities. Comparing the results with the linear array microphone measurements will give insights into the propagation of the different pressure waves to the far-field. In contrast to the linear array measurements, the orientation of the lobed nozzles is not considered of importance as the measurements are done in the far-field, and thus an uniform spherical sound propagation is expected.

Next to the isolated jet nozzles, measurements are done with the flat plate in proximity. The plate is placed between the polar arc and the jet nozzle, as shown in Figure 3.14a. The tested configurations can be found in Table 3.4, which is done for all the three nozzles. The streamwise distance L was varied, and the separation distance H was also varied. Configuration 4 has also been investigated in the experimental campaign conducted by Lyu and Dowling [37] as presented in subsection 2.3.3. However, do note that this has been done at a Mach number of 0.5, which corresponds to a jet exit velocity of approximately 170 m/s. The measurements in this work are performed at the same three velocities as was done for the isolated jet. For the jets from the lobed nozzles, the described measurements are performed twice in relation to the azimuthal position of the lobe peak and valley, as previously described.

For the analysis of the obtained measurements, the coordinate system displayed in Figure 3.14b will be used. In case the measurements are done without a flat plate, corresponding to the isolated configurations, there will naturally not be a distinction made between the shielded and unshielded side. However, the same system for the polar angle θ will be used, where a polar angle of positive 90 degrees

Table 3.4: Configurations used for the far-field measurements per installed nozzle.

Configuration	H	L
1	1D	2D
2	1D	3D
3	1.25D	3D
4	1.25D	4D
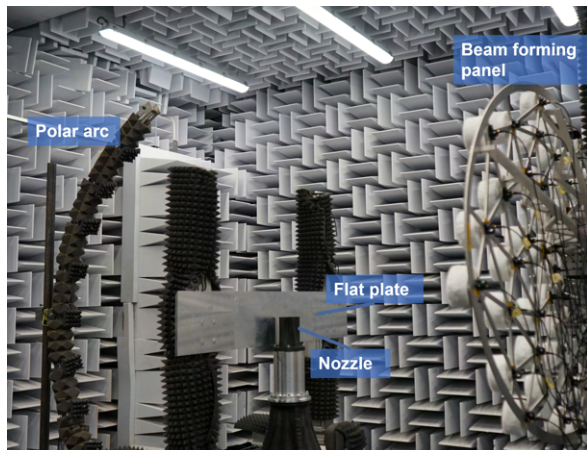
(a) Test set-up of the far-field measurements for a nozzle with a flat plate in proximity.
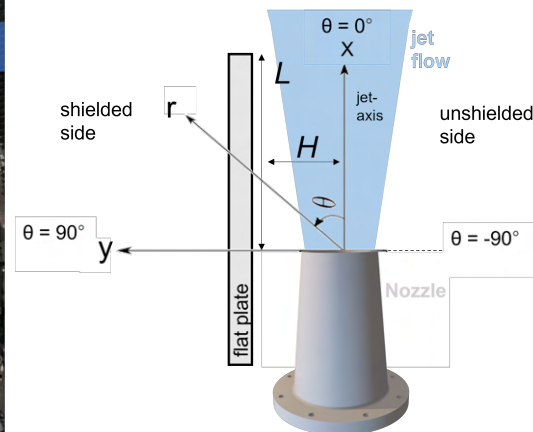
(b) The coordinate system used for the set-up of the far-field measurements.

Figure 3.14: Overview of far-field measurements test set-up.

corresponds to the microphone in the polar arc that is located in the same plane as the nozzle lipline. A polar angle equal to -90 degrees corresponds to the microphone in the beamforming panel that is also located in the same plane as the nozzle lipline.

3.4. Post-processing

In this section, the post-processing of the data of the different type of measurements will be presented. First the data processing concerning the HWA measurements will be explained. This will be followed by the analysis of the pressure signals.

3.4.1. HWA Post-processing

The HWA measurements will give a series of measured flow velocities. The data will be transformed to the signal in the amplitude domain and in the frequency domain. First, the conversion to the amplitude domain will be presented, which will give insights in the jet velocity and turbulence intensity development. Afterwards, the conversion to the frequency domain will be presented, which gives the opportunity to assess the turbulent scales development in the jet.

The time series of the signal of the HWA provides information of the mean velocity and the velocity fluctuations within the jet. The jet flow will be characterised by the mean velocity and the root-mean-square of the velocity fluctuations, which quantifies the energy content within the turbulent flow. The mean velocity is computed using Equation 3.5, and it is used to compute the root-mean-square (RMS) of the fluctuations as expressed in Equation 3.6. The signals can therefore be characterised as shown in Figure 3.15. The signal of samples in the x-axis can be transformed into a time series, which enables to process the data in the amplitude domain.

$$U_{\text{mean}} = \frac{1}{N} \sum_{i=1}^{N} U_i \tag{3.5}$$

$$U_{\text{RMS}} = \sqrt{\frac{1}{N-1} \sum_{i=1}^{N} |U_i - U_{\text{mean}}|^2} \tag{3.6}$$
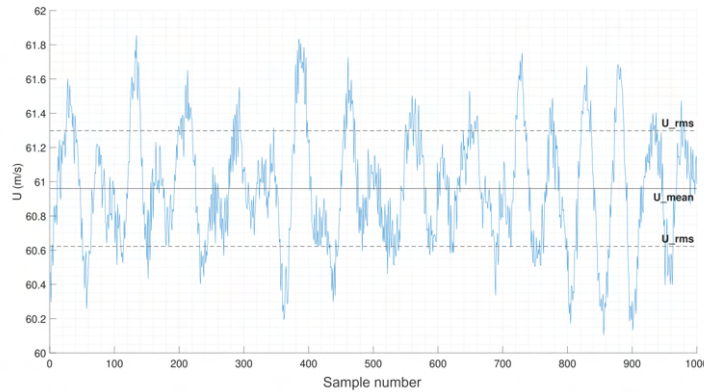
Figure 3.15: Piece of a HWA time series signal at a measurement coordinate.

The jet is also characterised by the turbulence intensity, as was discussed in chapter 2. The turbulence intensity (TI) is computed using Equation 3.7.

$$TI = \frac{U_{\text{RMS}}}{U_{\text{mean}}} \tag{3.7}$$

Next to the turbulence intensity, the signal is transformed to the frequency domain in order to quantify the amount of turbulent kinetic energy that is contained at different discrete frequencies. This is valuable as it gives the possibility to assess how the energy is distributed among the different turbulence length scales, using the knowledge that the turbulent scale size is directly related to the frequency. The method of conversion of the signal to the energy in the frequency spectrum is shown in Figure 3.16.
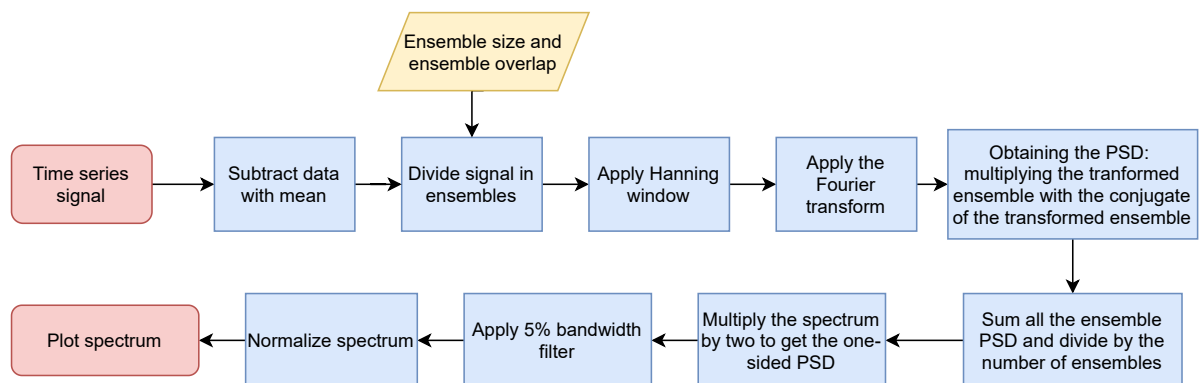
Figure 3.16: Flowchart of obtaining the one-sided Power Spectral Density (PSD) plot from a time series signal.

Firstly, the mean of the data is subtracted to get the fluctuations of the signal. The signal is divided into ensembles of a constant number of samples. The defined ensemble size is a trade-off between the smoothness and the accuracy of the outputted spectra. A smaller ensemble size produces an averaging of the spectrum as the signal has a lower amount of frequencies it can be decomposed into.

Consequently, a less accurate spectrum is obtained which is more smooth than a signal with a large ensemble size.

Besides this, the ensemble size also sets the lowest resolved frequency. A higher ensemble size results in a lower resolved frequency and vice versa. It can be observed in Figure 3.17b that the lowest resolved Strouhal number of the original signal is approximately 0.19 for an ensemble size of 2^{11}, corresponding to a frequency of approximately $230\ Hz$. If an ensemble size of 2^{17} is used, shown in Figure 3.17a, the lowest resolved Strouhal number is approximately $2.5 \cdot 10^{-3}$ which corresponds to a frequency of $3\ Hz$. As there is little energy in the lowest frequencies, it is not necessary to resolve such a low frequency. On top of that, it can be observed that with a smaller ensemble size the spectrum without bandwidth filter is already smoothly converged due to the increased number of averages, which is not the case for the largest ensemble size. Therefore, for the spectral analysis it was decided to use an ensemble size of 2^{11} samples.

(a) Ensemble size of 2^{17} samples. (b) Ensemble size of 2^{11} samples.
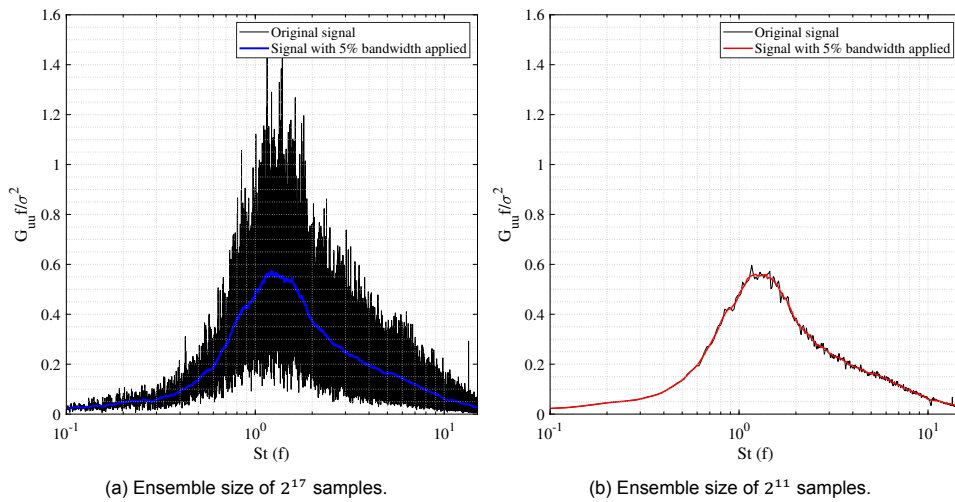
Figure 3.17: Frequency spectrum for different used ensemble sizes.

Moreover, the spectral analysis of the signal is done by ensemble averaging with a 50% overlap between the different ensemble blocks. The signal is divided into blocks of the defined ensemble size as shown in Figure 3.18. For each ensemble the hanning window is applied in order to correct the spectrum. This is required as the sampling of the signal results in discontinuities. Often the size chosen in the sampling process cuts the harmonic signal in a manner that the start and the end of the signal portion do not match reciprocally, as shown in Figure 3.19. These discontinuities add energy at certain frequencies in the power spectrum. In order to prevent these errors in the power spectrum the data is multiplied by the Hanning window function in advance, which outputs a signal without discontinuities, as can be visualised with Figure 3.19.

This is followed by taking the discrete Fourier transform to get the signal in the frequency domain. The Fourier transform is defined as expressed with Equation 3.8. Part of the pressure signal is defined by $p(n)$, of which n defines the ensemble number. In addition, N corresponds to the number of ensembles the signal is divided into, and f and t corresponds to the frequency and time, respectively.

$$P(f) = \sum_{n=0}^{N-1} p(n)e^{-i2\pi nt} dt \tag{3.8}$$

The obtained ensemble in the frequency domain is multiplied by the conjugate of itself in order to obtain the spectrum per ensemble. The obtained spectra for all the ensembles is summed up and divided by the number of ensembles to get the signal average in the two-sided spectrum. The left side of the spectrum, corresponding to the negative frequencies, shows the energy in the cosine waves and the positive side of the power spectrum shows the energy in the sine waves. As the two-sided spectrum is symmetric with respect to the zero frequency axis and as the division in cosine and sine waves is not
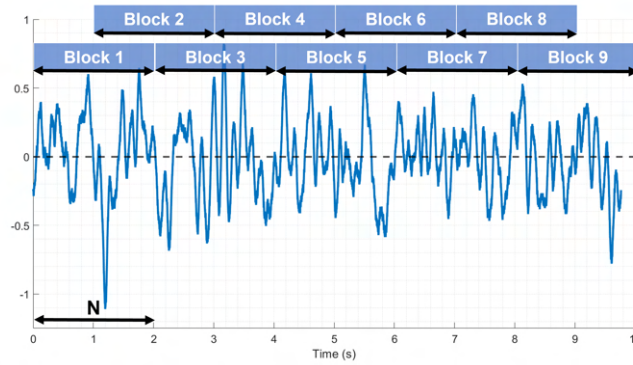
Figure 3.18: Sample signal divided in blocks of N samples with an overlap of 50%.
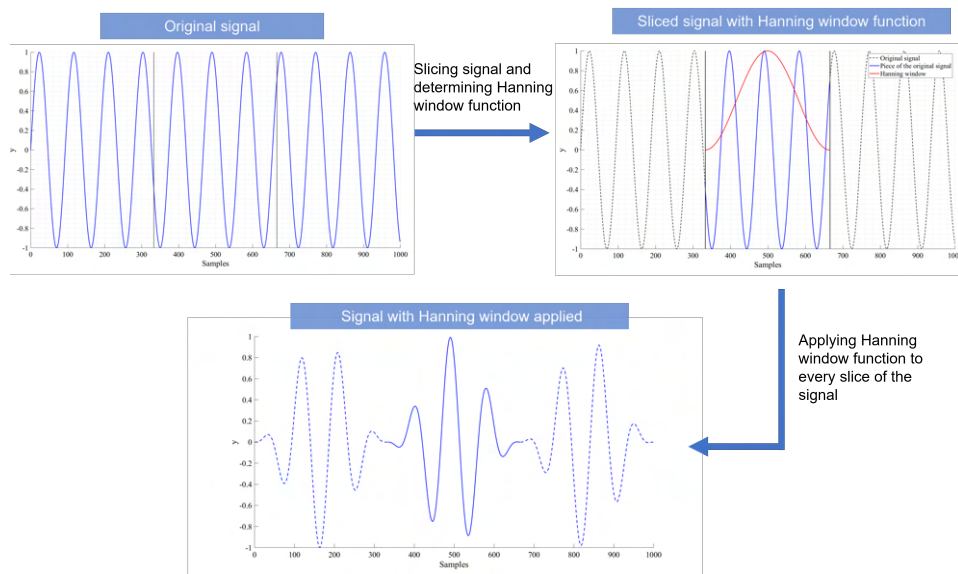
Figure 3.19: Sketch of the application of the Hanning window to a sliced signal.

of importance, only the one-sided spectrum is presented. The one-sided spectrum is multiplied by two to compensate for the removal of the negative part.

This was followed by scaling the spectrum to the Power Spectral Density (PSD) per df, corresponding to the frequency resolution that is computed by multiplying the ensemble size by the sampling frequency. This was done by multiplying the spectrum with the record time of one sample and dividing by the ensemble size squared.

Lastly, the one-sided PSD a 5% bandwidth-moving filter is used to obtain the final PSD, which is expressed as G_{uu}.

The spectrum with scaling was checked by using Parseval's theorem, stating that the sum of the squared signal function should equal the sum of the squared transform. Meaning that total energy in the frequency spectrum should equal the variance of the signal. Integrating the spectrum and computing the variance showed that this is true for all the measurements that will be analysed.

3.4.2. Near-field Pressure Post-processing

From the near-field pressure measurements, an estimation of the convection velocity of the hydro-dynamic pressure waves can be obtained. This can be done using two different methods. The first method uses the space-time domain of the measurements. The second method uses the frequency-wavenumber spectra of the measurements.

Firstly, the space-time domain will be presented. Plotting the signal in the space-time domain gives a plot as for the subset shown in Figure 3.20a, where the convection of the structures over time can be observed [2, 62]. The slope of the coherent pressure fluctuations, dx/dt, gives a first estimation on the convection velocity of the near-field pressure waves. In order to estimate the average convection velocity for these dominant pressure waves, a cross-correlation is done. Such a cross-correlation can be observed in Figure 3.20b by using Equation 3.9 where ρ_{xy} corresponds to the normalized cross-correlation coefficient. This gives to what extent the signals observed from the microphones, indicated by y in Equation 3.9, matches with the signal observed by the chosen reference microphone, indicated by x in Equation 3.9. For microphones farther downstream of the reference microphone, a decrease in amplitude of the correlation can be observed, as well as a time delay. It can be observed in Figure 3.20b that close to the reference microphone the signals are largely correlated, whereas farther downstream and upstream this correlation attenuates. Using the cross-correlation gives the ability to estimate the convection velocity with the inclination of the contour levels shown in Figure 3.20b. Do note that the influence of the acoustic pressure waves is insignificant as the hydrodynamic pressure waves have a much larger energy, and thus the estimated convection velocity corresponds to the most dominant hydrodynamic pressure waves [42, 62, 63].

$$\rho_{xy} = \frac{\sum_{i=0}^{N-1} (x_i - x_{mean}) * (y_{i-t} - y_{mean})}{\sqrt{\sum_{i=0}^{N-1} (x_i - x_{mean})^2} \sqrt{\sum_{i=0}^{N-1} (y_{i-t} - y_{mean})^2}} \tag{3.9}$$
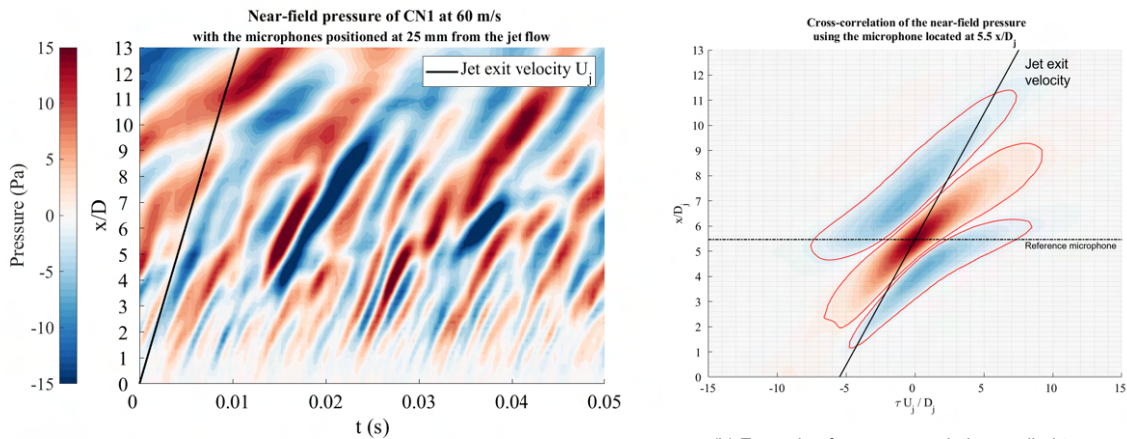
(a) Example of a sample of the pressure time signal for all the microphones in the linear array.

(b) Example of a cross-correlation applied to a microphone at 5.5 x/D downstream of the nozzle exit.

Figure 3.20: Overview of space-time domain.

The second method to estimate the convection velocities of the pressure waves is to analyse the frequency-wavenumber spectra of the measurements. This can be done using the two-dimensional Fourier transform of a space-time pressure field as expressed by Equation 3.10, where $W(x)$ corresponds to a Hanning window as the signal is divided into ensembles. The ensemble size is the same as used for the conversion of the HWA measurements into the frequency spectrum. The ensemble-averaged spectrum is then obtained by multiplying the obtained pressure in the frequency-wavenumber domain with its conjugate, as expressed with Equation 3.11 [62].

$$p(k_x - f) = \frac{1}{2\pi} \iint p(x,t)W(x)e^{-i(k_x x + 2\pi f t)} \mathrm{d}x \, \mathrm{d}t \tag{3.10}$$

$$\hat{P}(k_x - f) = \langle p(k_x - f) p^*(k_x - f) \rangle \tag{3.11}$$

In case the microphone array measures different pressure waves having similar convection veloci-
ties but different wavelengths, the spectrum shown in Figure 3.21b is obtained. It is possible to estimate
the convection velocity as the slope of the linear curve connecting the dot with the origin of the axes,
indicated by U_c. If the microphone array observes a broadband signal such as that in a jet, the pres-
sure waves have different wavelengths and different convection velocities, the spectrum as shown in
Figure 3.21c is obtained. From this spectra it is possible to determine the convection velocities of the
energetic pressure waves. This method assumes a linear convection velocity and thus the method is
most effective in the first region of the jet and for a small part of the region [19, 62].

(a) For a a single pressure wave.

(b) For different pressure waves with
different wavelength but with the same
convection velocity.

(c) For different pressure waves with
different wavelength and with different
convection velocities.
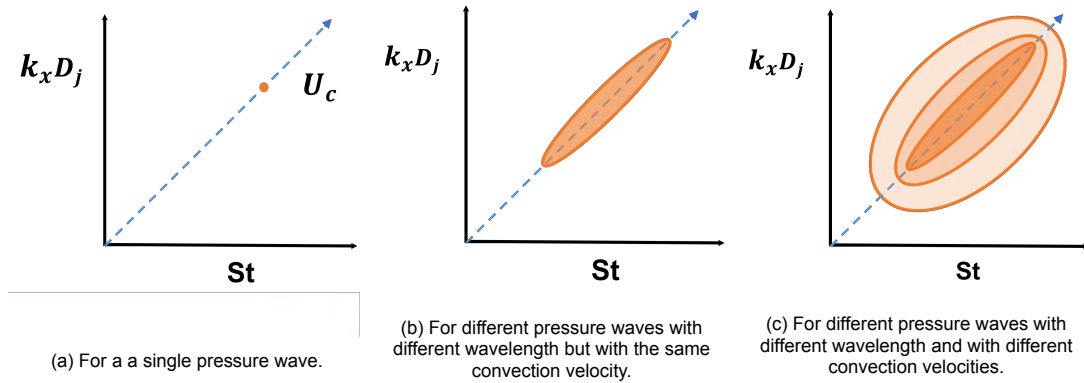
Figure 3.21: Frequency-wavenumber spectra for different type of signals.

An example of a frequency-wavenumber spectrum of a circular jet with a core flow and a secondary
flow is shown in Figure 3.22. As can be observed, the spectrum shows a pattern constituted by the
three lobes, which become more distinct and pronounced for increasing wavenumber and frequency.
The lobe located below the dashed curve, indicating the speed of sound, represents the dominant
acoustic pressure waves. This is slightly larger than the speed of sound as the acoustic pressure
waves convect to the far-field as spherical waves, and thus the linear array does not measure the
actual speed of sound. Hence, this small deviation can be observed in the spectrum.

The peak in the contour level above the dashed curves represents pressure waves characterised
by significantly lower convection velocities. Based on this observation, these pressure waves can be
classified as hydrodynamic [19, 42, 62]. Therefore, the frequency-wavenumber spectrum can be used
to separate the dominant hydrodynamic waves from the relatively low-amplitude acoustic pressure
waves. Analysing the spectrum at different downstream regions of the jet will also give valuable insight
into the development of the hydrodynamic and acoustic pressure waves.
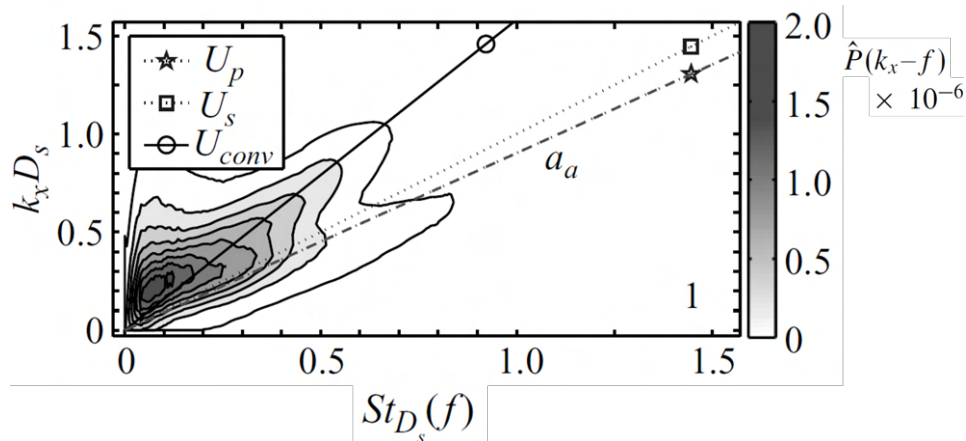
Figure 3.22: Example of a wavenumber-frequency spectrum for a circular jet with a primary U_p and secondary flow (U_s. The
speed of sound a is indicated by the dashed line and the convection velocity U_{conv} with the solid curve. [62]

3.4.3. Far-field Pressure Post-processing

The far-field pressure measurements by the microphones are also divided in ensembles, similarly as for the post-processing of the near-field pressure measurements. The ensemble size used for the measured signals is 2^13 samples. As presented previously, the far-field pressure is shown in SPL, which is computed using Equation 3.12. The reference pressure equals $2x10^{-5}\ Pa$, which corresponds to the hearing threshold at $1\ kHz$ [55]. The root-mean-square of the pressure fluctuations is computed with Equation 3.13

$$SPL = 10\log_{10}\left(\frac{p_{RMS}^2}{p_{ref}^2}\right) \tag{3.12}$$

$$p_{\text{RMS}} = \sqrt{\frac{1}{N-1}\sum_{i=1}^{N}|p_i - p_{\text{mean}}|^2} \tag{3.13}$$

<div align="right">

4

</div>

Jet Flow Development

In this chapter the analysis of the data obtained by the hot-wire anemometry is presented. First the flow characteristics will be analysed. This will be followed with a more in-depth analysis of the development of the range of scales in the jet.

4.1. Jet Characteristics

In this section the development of the mean velocity and turbulence intensity development in the jet will be analysed in order to estimate the jet flow characteristics.

Firstly, the baseline nozzle (CN1) will be compared with lobed nozzle 2 (LB2) of which the difference in nozzle geometry is largest between these two nozzles. The mean velocity normalized by the jet exit velocity is shown in Figure 4.1. As shown, the part of the shear layer that originates from the upper lipline of $y/D = 0.5$ originates at a lobe valley lipline for LB2. On the contrary, the part of the shear layer originating from the lower lipline of $y/D = -0.5$ originates at a lobe peak for LB2.
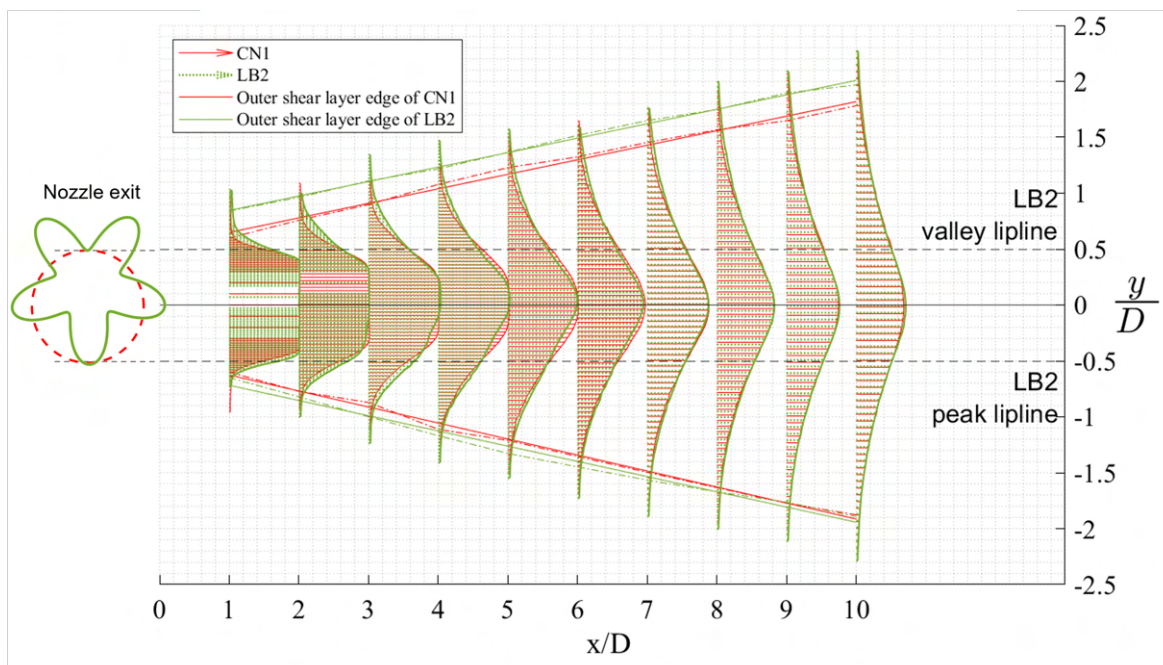
Figure 4.1: Development of the mean velocity of the jet from the baseline nozzle (CN1) and the lobed nozzle 2 (LB2).

For the baseline nozzle (in red) it can be observed that the radial profiles of the normalized velocity are symmetric with respect to the jet-axis (i.e. $y/D = 0$). This is evidence for an axisymmetric jet from the axisymmetric baseline nozzle, which is consistent with the current state-of-the-art [52].

Examining the radial velocity profiles of the jet from LB2 (in green) shows that the jet is not axisymmetric over the first five diameters downstream from the nozzle exit. However, over this downstream region the velocity profiles become gradually symmetric. Hence, it appears that the jet from LB2 is initially not symmetric, but after five diameters downstream of the nozzle exit the jet becomes almost symmetric. This is consistent with previous literature studies [21, 44, 48].

In addition, it can be observed in Figure 4.1 that the jet from LB2 has a larger radial extent than the jet from the baseline nozzle. This difference gradually disappears in downstream direction. This is expected as in the literature it is suggested that a lobed nozzle has a larger jet spread due to the enhanced development of turbulence in the jet [21, 48].

More significant differences can be observed between the different jets when comparing the development of the turbulence intensity (TI), as shown in Figure 4.2 for the jets from CN1 and LB2. These radial profiles also evidences that CN1 exhausts an axisymmetric jet, whereas this is not true for LB2. For the jet from LB2 it can be observed with the width of the two radial profile peaks that the shear layer thickness varies azimuthally. In addition, the maximum turbulence intensity also varies with azimuthal position. Initially, the shear layer part originating from a lobe valley experiences a larger thickness and a smaller turbulence intensity peak, compared to the shear layer originating from a lobe peak. Nevertheless, quickly downstream of the nozzle exit it appears that the part of the shear layer originating from a lobe peak grows a thicker shear layer than the part from a lobe valley. In addition, it can be observed that the jet from LB2 behaves similarly to the jet from CN1 after five diameters downstream from the nozzle exit. Nevertheless, a small difference can even still be observed at ten diameters downstream from the nozzle exit.

The radial profiles of the turbulence intensities show a more significant difference in jet spreading between the jets from CN1 and LB2. Again, the larger jet spreading and the larger shear layer development for the jet from LB2 with respect to the jet from CN1, is consistent with what is found in literature [21, 22, 48, 65].
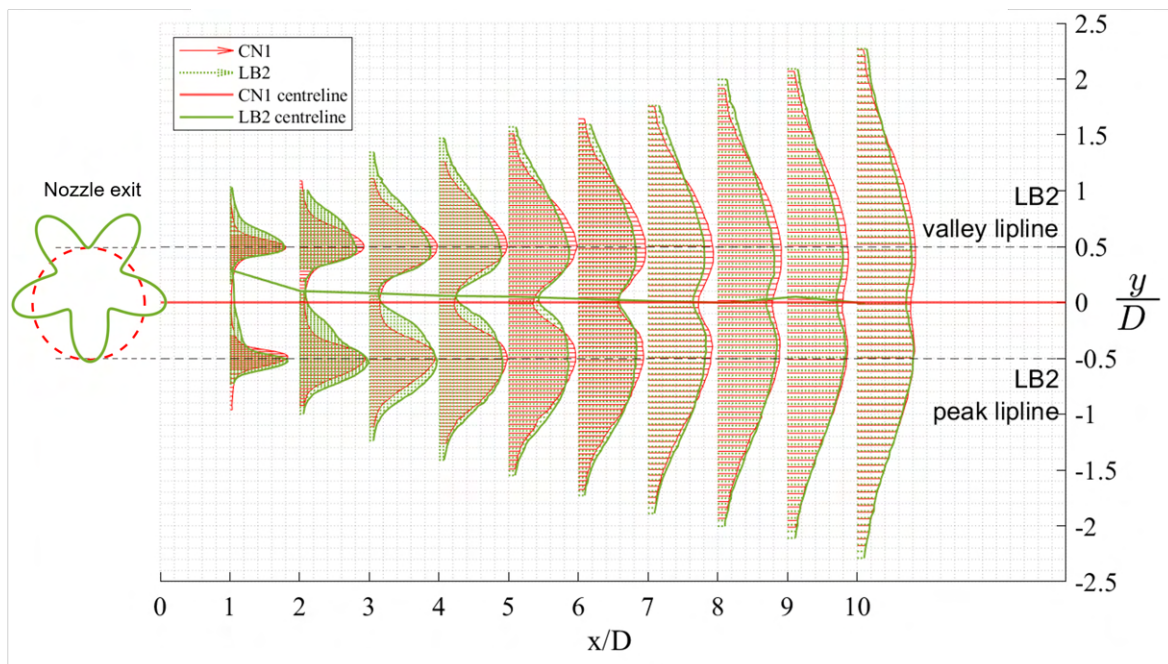
Figure 4.2: Development of the turbulence intensity in the jet from the baseline nozzle (CN1) and the lobed nozzle 2 (LB2).

In Figure 4.2 also the centreline of the different jets are shown, which is determined by the y/D location where the minimum turbulence intensity occurs. It can be observed that for the jet from LB2 an offset with respect to the jet-axis of CN1 occurs for the first six diameters downstream of the nozzle exit. This suggests that the potential core, defined by the valley in the radial profile of TI [52], is not located in the geometric centre of the jet from LB2. On top of that, a direct result of the thicker shear layers in the jet from LB2 is a significantly thinner laminar potential core for the jet from LB2 than for the jet from CN1.

With the knowledge that LB2 has a larger penetration rate than LB1, it is expected that the development of the jet mean velocity and the turbulence intensity in the jet from LB1 is an intermediate step between the jets from CN1 to LB2. For the mean velocity development no significant difference can be observed between LB1 and LB2. It can only be concluded that the width of the jet is larger for LB2 than for LB1 for most of the measurement locations. This can be observed in Figure B.1, in Appendix B.

More evident differences can be observed with the turbulence intensity, as presented in Figure 4.3. From the centreline locations, it can be observed that the potential core occurs to $y/D = 0$ for LB1. Moreover, the shear layer is less thick for LB1 than for LB2 for the first five diameters downstream. These observations agree with the hypothesis that LB1 produces a jet having turbulence characteristics that are intermediate between those obtained from the jets issuing from CN1 and LB2. In addition, the jet from LB1 differs significantly less with the jet from LB2 than the jet from CN1.
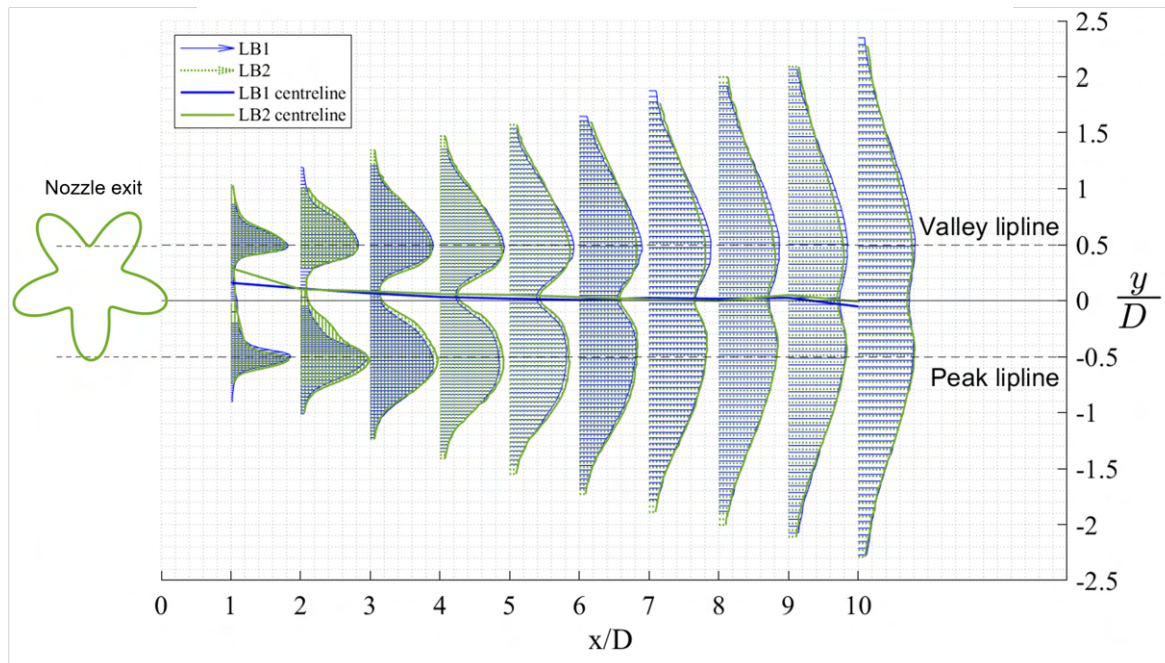
Figure 4.3: Development of the turbulence intensity in the jet from the lobed nozzle 1 (LB1) and the lobed nozzle 2 (LB2).

At the nozzle exit, it can also be observed that the jet issuing from LB1 has an intermediate behaviour compared to the jets from CN1 and LB2. The mean velocity in the shear layers of the jets at the nozzle exit is shown in Figure 4.4. For the boundary layer originating from a lobe peak of LB1, it can be observed that it is slightly thicker than for LB2 and significantly thinner than the boundary layer of CN1. The shear layer originating from a lobe valley of LB1 is slightly thinner than that from the valley of LB2, and significantly thicker than the shear layer from CN1.

The spreading rate and the potential cores have also been defined. A comparison between the three different nozzles concerning these parameters will be presented next.

4.1.1. Jet spreading rate
The spreading rate of the different jets is presented in Table 4.1. It has been determined by assuming a linear shear layer edge defined by the y/D locations where the mean velocity in the radial profiles, decreased to below 5% of the jet exit velocity.

It can be observed that for all three jets, the spreading rate differs significantly between the upper part of the shear layer and the lower part of the shear layer. This is definitely not expected for the jet from the circular nozzle. This suggests that the jet might not be completely axisymmetric. This difference could also be attributed to the presence of the measurement apparatus or due to inaccuracies in the positioning of the HWA sensor. On top of that, the assumption that the spreading rate is linear for
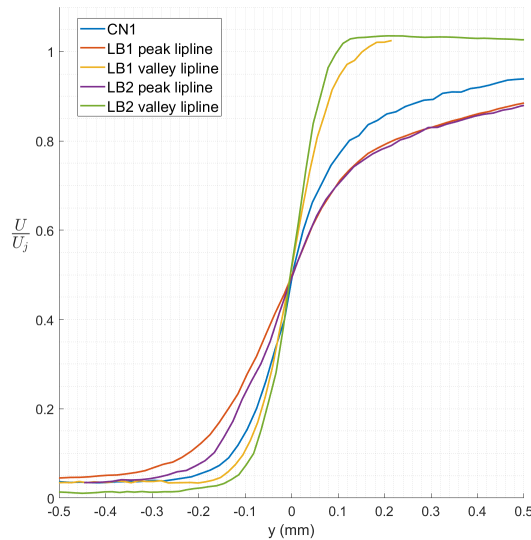
Figure 4.4: Mean velocity normalized by the jet exit velocity at the nozzle exit of the three different nozzles

the range of one to ten diameters downstream might also explain the observed discrepancy, as it is expected that after the potential core end the jet spreading rate increases [51, 52].

Nevertheless, it appears that in average the jet from CN1 and LB1 experiences a similar spreading rate, and the jet from LB2 experiences a smaller spreading rate relatively. Do note that the radial extent of the jet from LB2 was observed to be larger than for the other jets. Hence, the smaller spreading rate for the jet from LB2 does not necessarily result in a smaller transverse diameter of the jet. On top of that, with the discrepancy for the jet from CN1, it can be argued whether the determined spreading rates are accurate.

Table 4.1: Jet spreading rates for the different nozzles.

	CN1	LB1	LB2
Spreading rate β upper shear layer	7.4°	7.3°	7.4°
Spreading rate β lower shear layer	8.1°	8.3°	7.7°

4.1.2. Potential Core Length

The length of the laminar potential core is determined using different methods based on the flow properties along the centreline. The first method estimates the end of the laminar potential core with the downstream location were the mean velocity at the jet centreline reaches 95% of the jet exit velocity. The second method estimates this length by applying a linear to the mean velocity decay along the centreline. In this procedure, the potential core length is taken at the location where the linear slope reaches a mean velocity value that is lower than the jet exit velocity. The third method defines this length by determining the downstream location where the turbulence intensity reaches a value of 10% of the mean maximum intensity. The results of the three different method are presented below.

Method 1

The result of method 1 can be visualised from Figure 4.5, where the mean velocity along the centreline is presented. According to this method, the lobed nozzles produce a smaller potential core length than the conventional circular nozzle, of which LB2 is associated to the smallest length. Nevertheless, it can be shown that for all three nozzles the respective potential core length ends at around six diameters downstream of the nozzle exit.

In addition, the mean velocity along the centreline shows a differences between the jets that were not clearly visible from the radial profiles presented before.

It can be observed that the lobed jets start their mean velocity decay between three and four nozzle diameters downstream of the nozzle, whereas this occurs between four and five diameters downstream for the baseline jet. Farther downstream, however, the jet from the baseline nozzle has a steeper decay in mean velocity and, as a consequence, the mean velocity is lower than for the jets from LB1 and LB2 after six-and-a-half diameter and seven-and-a-half diameter downstream, respectively.

Comparing the two lobed nozzles shows that the decay occurs most upstream for the jet from LB2, which also shows a steeper decay than the jet from LB1.

These observations satisfy the hypothesis that the lobed nozzles enhance turbulence developmen and, as a consequence, the end of the potential core end is shifted upstream. However, in the transitional region of the jet, the jet from CN1 appears to have a faster development than the lobed jets, and thus it is expected that the fully-developed turbulence region is reached earlier for the jet from CN1 than for the jets from the lobed nozzles.
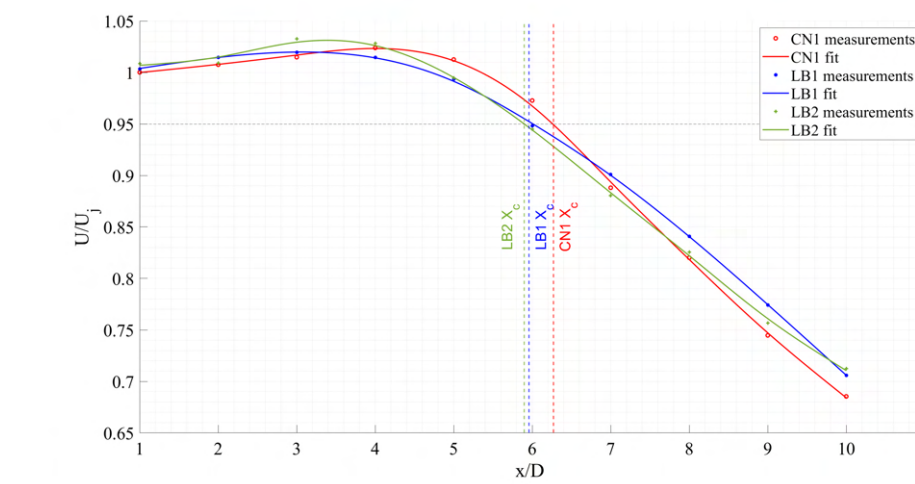
Figure 4.5: Mean velocity development along the jet centreline with the end of the potential core represented by the dashed lines, which are determined according to method 1.

Method 2

The result of the second method can be visualised in Figure 4.6. For this method a linear fit has been applied to the measurements between five and ten diameters downstream to represent the decay of the mean velocity. This second method results in a similar trend regarding to the differences in the length of the potential core. The jet from CN1 experiences the longest potential core, whereas the jet from LB2 experiences the shortest potential core length. Compared to the previous method, the potential core ends for all three nozzles approximately one diameter more upstream.

This method clearly shows the differences in the mean slope of the velocity decay for the three jets. The jet from CN1 experiencs a larger decay which occurs more downstream than for the jets from the lobed nozzles. This is consistent with method 1. However, the jet from LB1 has a similar decay as the jet from LB2, which could not be clearly observed with method 1.

Method 3

The result of the last method can be visualised with Figure 4.7. Compared to the previous methods a significantly smaller potential core length occurs for all three nozzles. The potential core ends around two diameters downstream of the nozzle exit. Interestingly, the end of the potential core of LB1 ends slightly more upstream than LB2. However, it must be noted that this method is very sensitive to the threshold chosen to determine the potential core end. The threshold chosen in Figure 4.7 corresponds to 10% of the mean maximum nozzles of all three nozzles, which equals a turbulence intensity of 1.3%. If a slightly higher threshold of 2% is chosen, the baseline jet will even have a smaller potential core
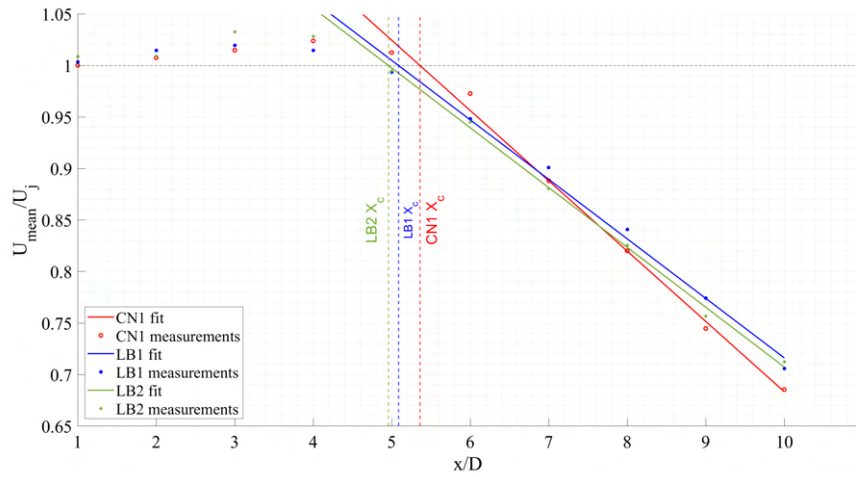
Figure 4.6: Mean velocity development along the jet centreline with the potential core being represented by the dashed lines, which are determined according to method 2.

length than the lobed jets.

The rise in turbulence intensity along the centreline for the three jets follow a similar trend as for the mean velocity decay. Initially, the jet from LB2 shows a higher rise in intensity than the jets from LB1 and CN1, which results in a higher turbulence intensity between four and six diameters downstream of the nozzle. After the initial rise in intensity, the jet from CN1 reaches higher intensity levels than the jet from the lobed nozzles. At the end of the transitional region, CN1 experiences the largest turbulence intensity and LB2 the smallest turbulence intensity.

From these observations, the same conclusions can be drawn as for method one.
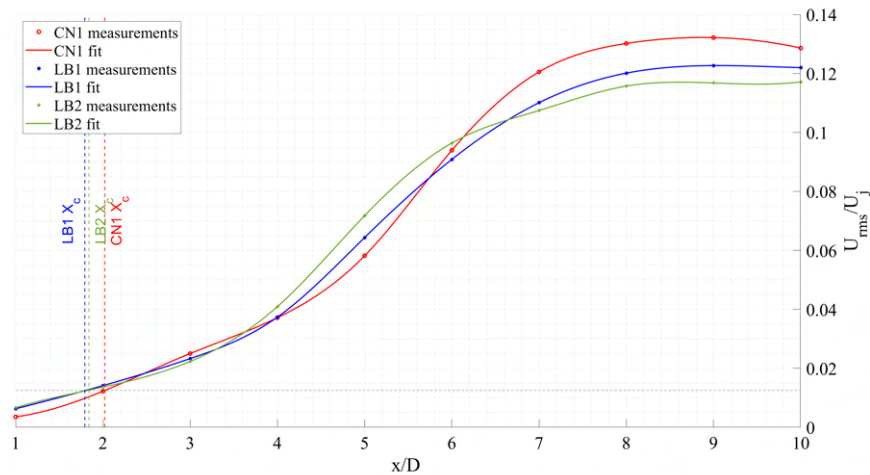
Figure 4.7: Turbulence intensity development along the jet centreline with the potential core being represented by the dashed lines, which are determined according to method 3.

The results of the three methods is summarized in Table 4.2. Among these three methods, LB2 shows the lowest potential core length, followed by LB1 and CN1, respectively. Methods one and two show a potential core length that is more similar, with differences in the order of only one diameter. Method two shows a significantly lower potential core length, although its robustness is questionable.

It can be concluded from the three methods, that up to five to six diameters downstream the lobed jets experience a faster flow development. The turbulence development is stronger in the jet from LB2 than the jet from LB1. However, in the transitional region of the jet the flow development of is the slowest

Table 4.2: Location of the potential core end according to different methods.

	X_c/D		
	CN1	LB1	LB2
Method 1	6.3	6.0	5.9
Method 2	5.4	5.1	5.0
Method 3	2.0	1.8	1.8

for LB2 and the flow development is the fastest for CN!. At the end of this region, between nine and ten diameters downstream, different flow characteristics are observed. The jet from the conventional circular nozzle experiences a lower mean velocity at the jet centreline, with a higher turbulence intensity compared to the jets from LB1 and LB2. Lastly, it can be concluded that the jet from LB1 does not show an intermediate behaviour betwen the jets from CN1 and LB2 for the entire downstream region.

4.1.3. Conclusion
All in all, the following can be concluded from the analysis above.

From the analysis it it suggested that the lobed nozzles initially enhance the development of the turbulence as a consequence of their asymmetric jet flow compared to the jet from the baseline nozzle. The shear layer of the jets from the lobed nozzles spreads more quickly, and thus producing a shorter potential core than compared to the baseline nozzle. It has been found that a larger lobe penetration results in an enhancement of the mentioned differences.

After this initial development region, located around five to six diameters downstream, the jets from the lobed nozzles behave more similar to the jet from the baseline nozzle. At this point the jet from the baseline nozzle seems to experience a faster turbulence development than the jets from the lobed nozzles. Again, it seems that a larger lobe penetration results in a more enhanced difference compared to the baseline nozzle.

The reason for this attenuation in turbulence development rate for the jets from the lobed nozzles can be attributed to the fact that the jets from the lobed nozzles behave more similarly to a circular jet in the transitional region, as found by literature [6, 21, 23]. This is satisfied by the radial profiles in the mean velocity and turbulence intensity of the lobed nozzles, which showed to become symmetric farther downstream. As was shown with the azimuthal vorticity development in Figure 2.28 by Hu et al. [21], the lobed shear layer deforms into a circular ring with pinched-off structures. The lobe peaks convect away from the jet centre and the lobe valleys form the circular ring [6, 21]. This results in a circular ring that is actually expected to be smaller than the shear layer of the jet originating from the baseline nozzle. This can be clearly visualised in the nozzle exit profiles shown in Figure 4.8, where a circular ring formed from the lobe valley would have a significantly smaller radius than for CN1. Do note that this does not keep the different spreading rates of the jets from CN1 and LB2 into account.

The above made analysis gives insights into the development of the jet. However, it does not provide information on the development of scales in the jet. This can be obtained by the frequency spectra, which will be presented in the following section.
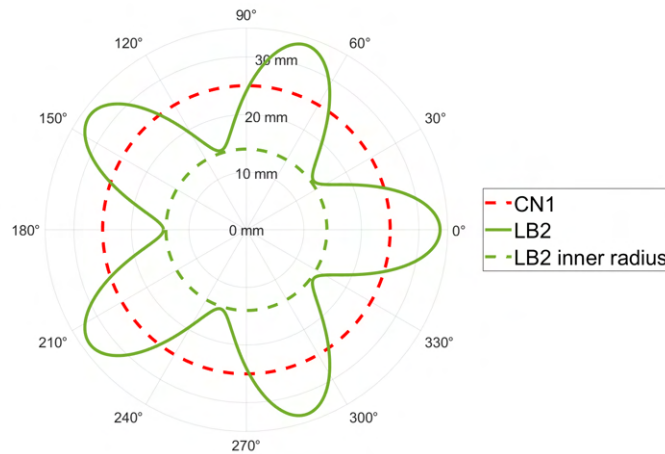
Figure 4.8: Visualisation of the nozzle exit profiles of CN1 and LB2.

4.2. Turbulent Scales Development

Converting the time signal with the Fourier transform to the frequency domain gives insights into how the energy is spread over the frequencies, and thus over the turbulent scales. In this section, the normalized frequency spectra of the different nozzles will be analysed.

4.2.1. Frequency Spectrum Analysis

The frequency spectra for the first diameter downstream of the nozzle exit is shown in Figure 4.9a and Figure 4.9b for the jets from CN1 and LB2, respectively. It can be observed that for CN1 a uniform shear layer develops for both the upper and the lower part of the shear layer, with its energy distributed over a similar range of Strouhal numbers. From Figure 4.9b it can be observed that the distribution over the Strouhal number range is not similar for the two different parts of the shear layer of the jet from LB2. The thicker part of the shear layer, originating from the lobe valley, has energy distributed over a smaller range of frequencies than for the thinner part of the shear layer. This can be observed in a more evident way in the energy located at the lipline axes, as presented in Figure 4.9c. It can be clearly observed that there is a slight deviation in the range of turbulent scales that carry energy, of which the lower lipline axis involves significantly more turbulence than the upper lipline axis.

Figure 4.9c shows that the peak energy is located at a lower frequency for the jet from CN1, which indicates larger turbulent structures. Moreover, it can be observed that the average peak energy at the lipline axes is also larger for the jet from CN1. Hence, it appears that the jet from CN1 involves more and larger turbulent structures than the jet from LB2.

If we examine the spectra farther downstream, at three diameters downstream, it can be observed that the energy is shifted to low Strouhal numbers, as shown in Figure 4.10a and Figure 4.10b for the jet from CN1 and LB2, respectively. From this it can be concluded that the turbulent scales have grown in size with respect to one diameters downstream of the nozzle exit. For the jet from the baseline nozzle a small difference can be observed between the different part of the shear layers. However, from Figure 4.10b, it becomes evident that the shear layer presents a significant variation along the azimuthal direction in the jet from LB2. The lower shear layer has energy distributed over a larger range of frequencies, and thus over a larger range of eddy scales, than the upper shear layer. On top of that, the lower shear layer contains a larger amount of energy than the upper shear layer. For the shear layer of the jet from CN1, a similar energy magnitude can be observed as for the lower shear layer of the jet from LB2. From Figure 4.10c this is even more evident.

Comparing the two jets in Figure 4.10c shows that the jet from LB2 experience a lower average peak in energy than the jet from CN1. However, the shear layers of the jet from LB2 have a larger thickness and thus there energy is located over a larger y/D range. Moreover, it appears that the jet from the baseline nozzle carries energy at a lower Strouhal number than the jet from LB2.

(a) CN1   (b) LB2

(c) At the liplines axes of CN1 and LB2.
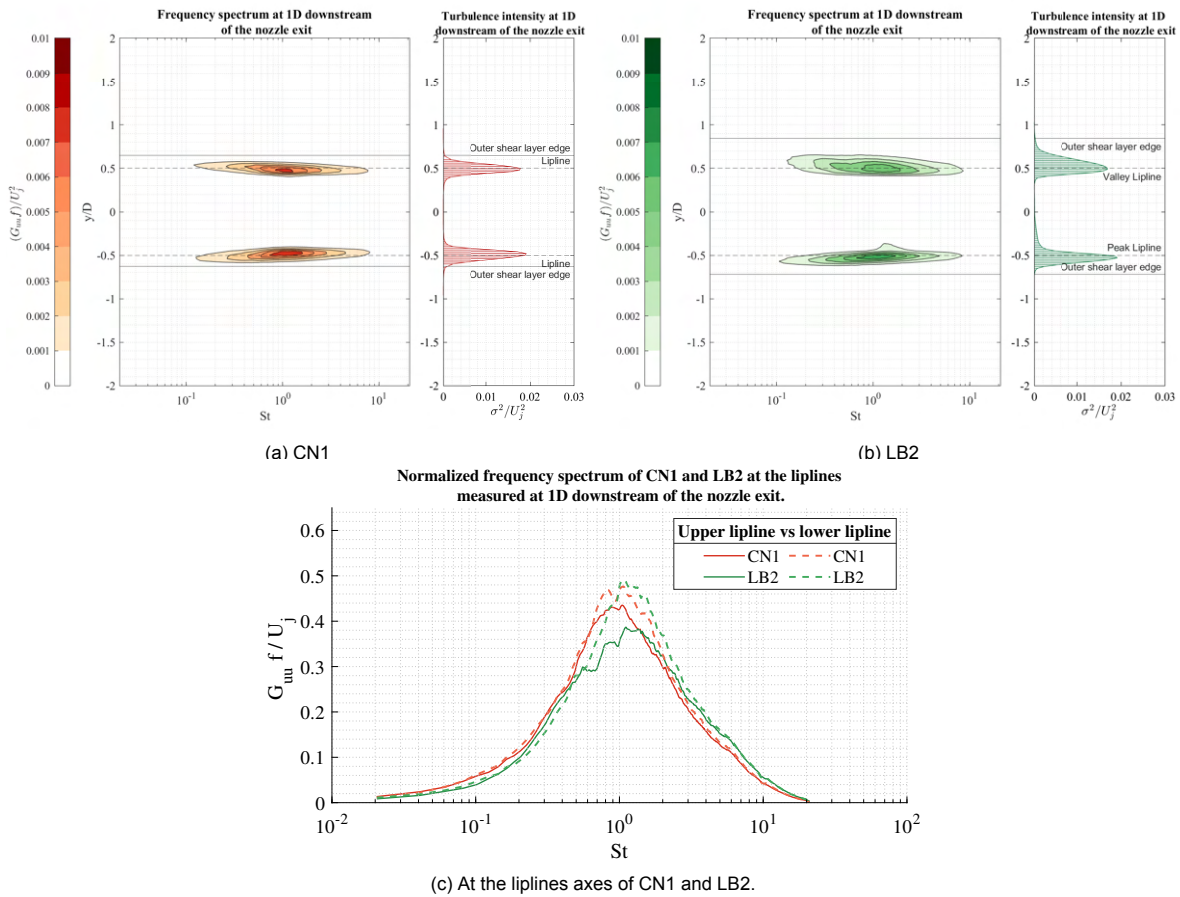
Figure 4.9: Normalized energy frequency spectra of the jets from the baseline nozzle (CN1) and lobed nozzle 2 (LB2) at one diameter downstream of the nozzle exit.

Farther downstream, at five diameters downstream, the end of the laminar core flow can be clearly observed in Figure 4.11a and Figure 4.11b for CN1 and LB2 respectively. The end of the potential core can be visualized as the different parts of the shear layers are connected at the jet centreline [52]. This is more evident for the jet from LB2 than for the jet from CN1, and it is thus expected that the potential core end is located more upstream for LB2, which satisfies the conclusions that were made previously.

In addition, it can be observed that for both jets the instabilities have grown. For the lobed jet, the two different parts of the shear layer seem to behave more similarly between each other than upstream. This can also be visualized with the peak energy content and location at the lipline axes, as shown in Figure 4.11c. This is consistent with what was observed with the velocity and turbulence intensity development in the jets.

Regarding the structures size, it can be observed that the dominant structures have grown larger in the jet from LB2 than in the jet from CN1, as the peak energy is located at a lower Strouhal number. This can be clearly observed in the contour spectra, as well as the spectrum at the liplines shown in Figure 4.11c.

The energy frequency spectra in the transitional region of the jets, estimated to be seven to ten diameters downstream of the nozzle, can be observed in Figure 4.12. The jet from the baseline nozzle shows that the peak energy gradually decreases,and it is expected that this trend continues farther downstream. From seven to ten diameters downstream of the nozzle, the peak continues its movement towards a lower frequency region, meaning that the instabilities in the flow grow larger. However, the reduction in the magnitude of the peak energy and the increase in Strouhal number range shows that more instabilities of different scales are present in the jets.

Following the development in the jet from LB2 shows that the difference between the two parts of the shear layer decreases, and as a consequence the jet develops to an axisymmetric jet flow. At $x/D = 7$

(a) CN1   (b) LB2

(c) At the liplines axes of CN1 and LB2.
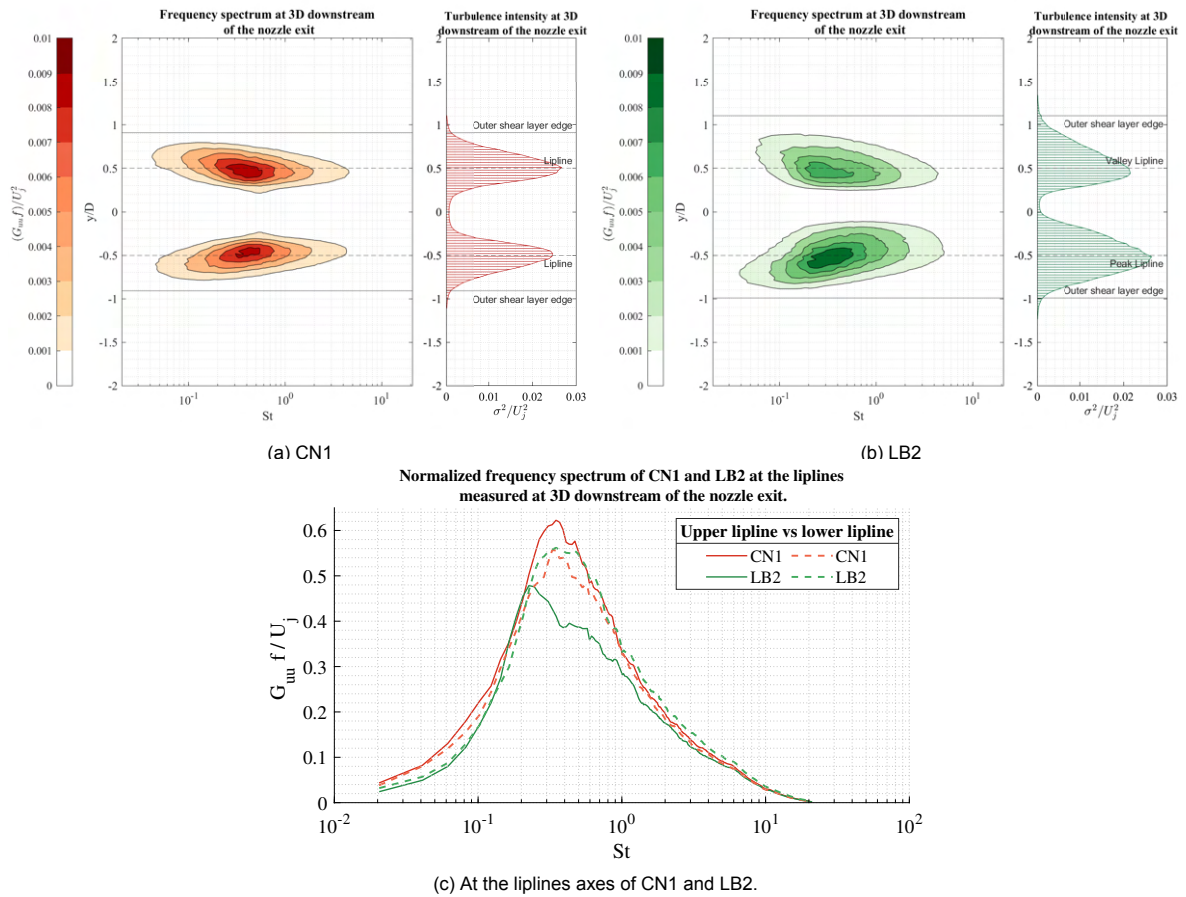
Figure 4.10: Normalized energy frequency spectra of the jets from the baseline nozzle (CN1) and lobed nozzle 2 (LB2) at three diameters downstream of the nozzle exit.

it appears that the jet from LB2 contains a wider range of scales than for the jet from CN1, which still has a lot of the energy located within the peak frequency. Compared to the jet from CN1, the jet from LB2 again experiences a shift of its peak to a lower frequency region than CN1, and thus larger scales are present in the jet from LB2 than the jet from CN1 at ten diameters downstream. Nevertheless, at this downstream location the spectra of the jets from CN1 and LB2 become very similar. This satisfies the previous observations that the jet from the lobed nozzle develops to a circular jet at some point downstream from the nozzle exit.

(a) CN1   (b) LB2

(c) At the liplines axes of CN1 and LB2.
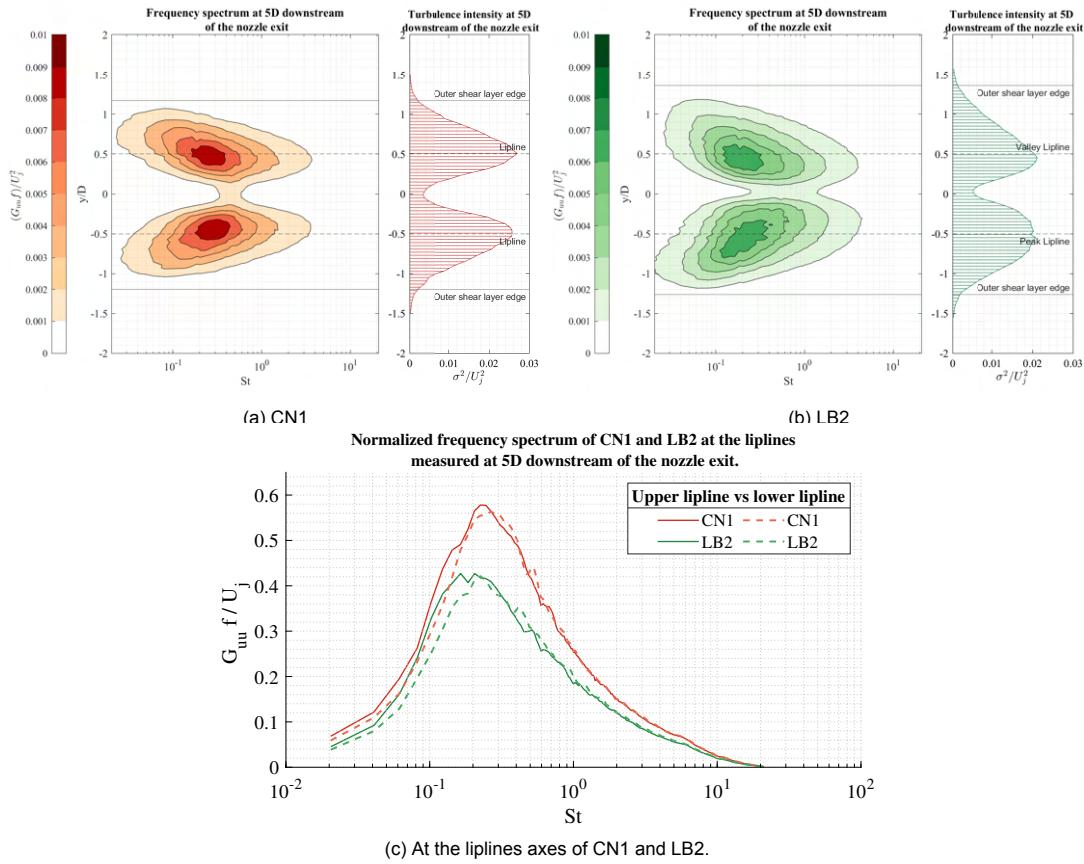
Figure 4.11: Normalized energy frequency spectra of the jets from the baseline nozzle (CN1) and lobed nozzle 2 (LB2) at five diameters downstream of the nozzle exit.

The spectra from all the measured downstream locations and the three jets can be found in Appendix B.

The lobed nozzle 1 showed a development of turbulent scales that satisfies the earlier made observation that LB1 has an intermediate behaviour between the jets from CN1 and LB2. Interestingly, this resulted in different behaviour of the jet between three to five diameters downstream of the nozzle exit. Initially, the jet from LB1 behaves similarly to LB2 for the first two diameters, with its peak energy located in the lower part of the shear layer. From three diameters on wards, it becomes evident that the upper part of the shear layer of LB1 develops fast, and the energy content grows rapidly. The peak energy content is similar for the jets from CN1 and LB2 for this range of downstream locations. However, the energy content is located at a lower frequency range for the jet from LB1 compared to the jet from CN1, analogously to what observed for LB2.

The resulting spectrum at five diameters downstream can be observed in Figure 4.13a and Figure 4.13b for the jet from LB1 and LB2, respectively. A clear difference can be observed in peak energy between the upper and lower parts of the shear layer. This difference does not only occur in the energy content, but in also the dominance of larger structures for the upper part of the shear layer. This suggests that the faster growing instabilities have not dissolved yet into the more fine scale structures in the jet from LB1.

As a consequence, it can also be observed that LB1 is less developed and thus the upper and lower part of the shear layers seem to be just connected with each others. This is consistent with the earlier determined difference in potential core length between the three different jets.

Farther downstream, at seven diameters, it can be observed that the jet from LB1 behaves more similarly to the jet from LB2, as shown in Figure 4.13c and Figure 4.13d. It can be observed that the most dominant large-scale structures have dissolved into structures of finer scales. It was observed that for the jet from CN1 the energy within the shear layer is still mainly contained at the large-scales.

(a) CN1 at 7D

(b) LB2 at 7D

(c) CN1 at 10D

(d) LB2 at 10D
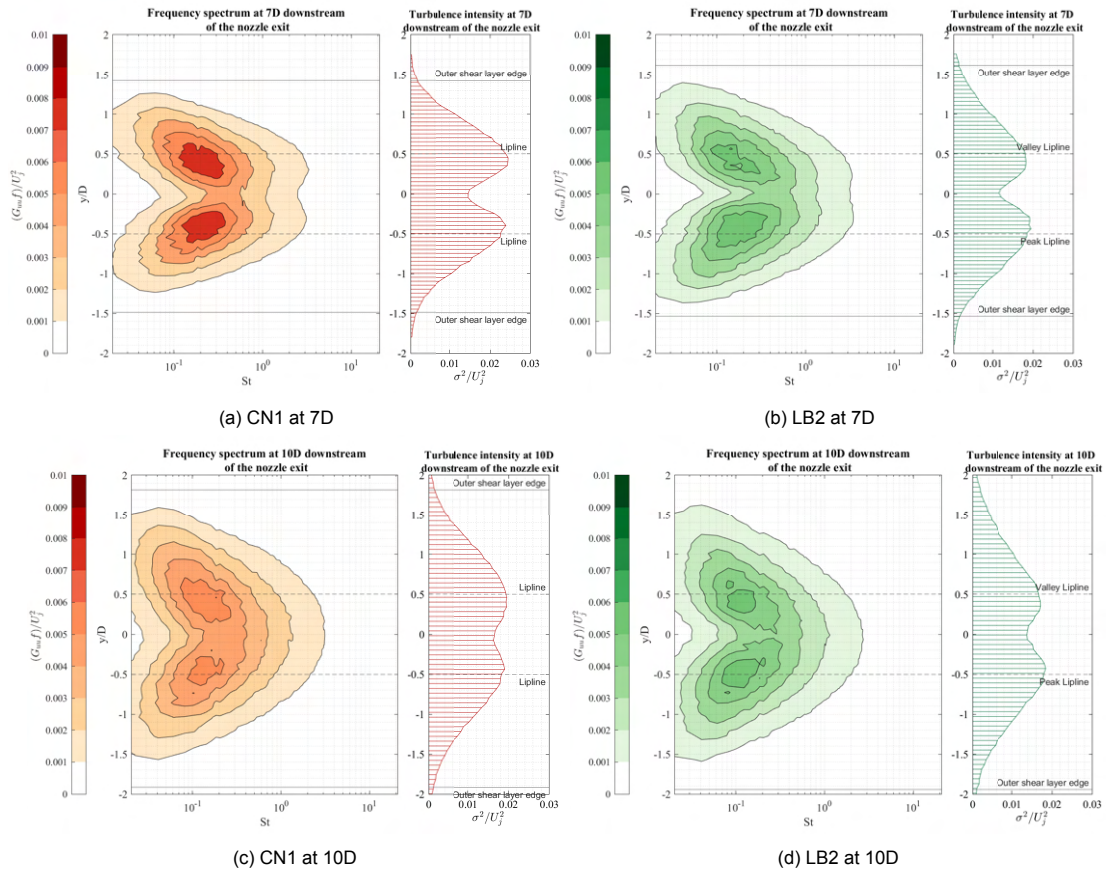
Figure 4.12: Normalized energy frequency spectra of the jets from the baseline nozzle (CN1) and lobed nozzle 2 (LB2) at seven and ten diameters downstream of the nozzle exit.

Again, this would suggests that the jet from LB1 behaves as intermediate step.

4.2.2. Conclusion

The described analysis shows that in the shear layer between the jet and the quiescent fluid the distribution of energy among the different scales of turbulence changes when using nozzles of different geometries.

The jets from the lobed nozzles consists of a shear layer that develop significantly faster, and as a result become thicker and contain a larger range of scales than the jet from CN1. In the annular shear layer from CN1, a small part of the range of scales remains dominant even up to seven diameters downstream, whereas for LB2 this dominant part is already disappearing at five diameters downstream. This is consistent with the expected behaviour as illustrated by Lyu et al. [38], according to whom their model predicted that the temporal growth rate of higher order pressure modes is lower for a lobed jet. On top of that, as the decay in energy is stronger in the jet from LB2 than in the jet from LB1, it can also be verified that increasing the lobe penetration results in a faster flow development.

Nevertheless, it has been found that while the jet from CN1 initially produces a shear layer of larger scales, the shear layer of the lobed nozzle consists of scales that grow faster. As a consequence, from two to seven diameters downstream of the nozzle exit, the lobed jet experiences eddies of larger size than the circular jet.

Furthermore, from this analysis it appears that the potential core actually already ends at or before five diameters downstream, which is slightly more upstream than what was found before. Nevertheless, from this analysis it also became clear that the potential core length is shorter for the lobed nozzle.

(a) LB1 at 5D

(b) LB2 at 5D

(c) LB1 at 7D

(d) LB2 at 7D
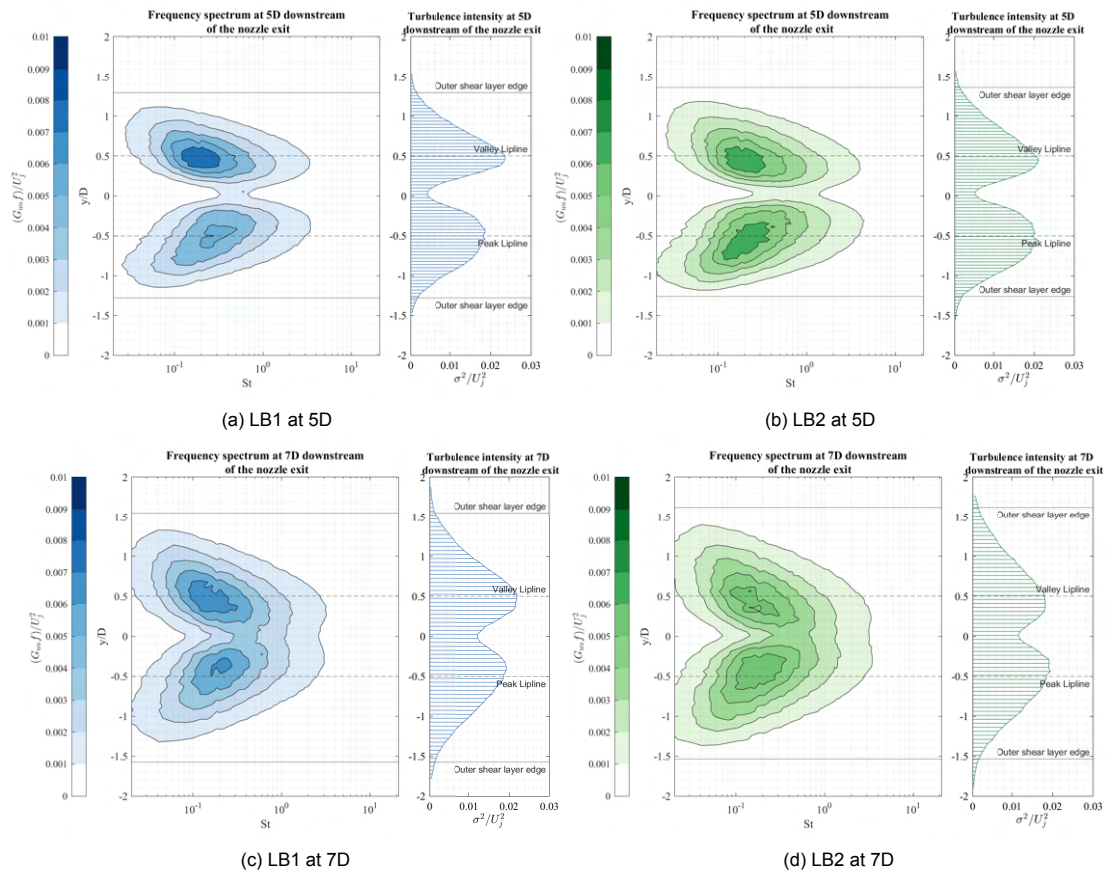
Figure 4.13: Normalized energy frequency spectra of the jets from the lobed nozzle 1 (LB1) and lobed nozzle 2 (LB2) at five and seven diameters downstream of the nozzle exit.

Lastly, from the analysis it became evident that it takes more time for the jet to become axisymmetric than what was concluded before, namely after six diameters downstream. A difference in scale content between the two parts of the shear layers of the lobed jet, can still be observed at seven diameters downstream of the nozzle exit.

<div style="text-align: right; font-size: 3em;">5</div>

Near-field Pressure of the Jet

In this chapter the analysis of the data obtained by the near-field pressure measurements from the linear array of microphones is presented. First, the space-time domain of the near-field of the different isolated jets will be analysed. This will be used to gain insights into the average convection velocities of the dominant structures in the shear region of the different jets. Moreover, an in-depth analysis of the near-field behaviour will be conducted by examining the frequency-wavenumber spectra. This will give insights into the convection velocities of the different scales in the shear region of the jets, as well as the decay in amplitude of the hydrodynamic pressure waves.

Afterwards, the space-time domain and the frequency-wavenumber spectra will be analysed for the jets when a flat plate is installed in proximity. This will give insights into the change in the turbulent structures and their intensity in the near-field of the jet, as well as the effect of the plate on the intensity of the acoustic pressure waves.

5.1. Isolated Jet Nozzles

In this section the analysis of the near-field pressure of the jets from the isolated nozzles will be presented. The pressure fluctuations in the near-field of the jets are dominated by the turbulence in the form of pressure waves.

Firstly, the space-time domain will be analysed, which will give insights into the most dominant pressure fluctuations. The corresponding convection velocity and decay of the pressure fluctuations will provide a prediction on the acoustic efficiency. Afterwards, the frequency-wavenumber spectra will be analysed in order to distinguish the hydrodynamic pressure waves and the acoustic pressure waves. Moreover, this will give insights into the convection velocities over the entire range of turbulent scales. The section will end with an analysis on the decay of the pressure waves in radial distance from the jet, which will give the opportunity to assess the region of influence of the hydrodynamic pressure waves.

5.1.1. Convection Velocity of the Large-scale Structures

This section presents the analysis of the space-time domain. For these measurements, the linear array has been placed at a radial distance Δs of $25\ mm$ from the lipline, as shown in Figure 3.9b in chapter 3.

The time evolution of the near-field pressure of the jet from the baseline nozzle, with a jet exit velocity of $60\ m/s$, is shown in Figure 5.1. The convection of the pressure waves can be clearly visualized, and it is represented by the inclination of the different patterns of pressure fluctuations. It can be observed that the pressure waves have a slightly lower convection velocity than the jet exit velocity. Hence, these dominant pressure waves are hydrodynamic as the acoustic pressure waves move with the speed of sound, which is significantly larger than the jet exit velocity.

Examining the patterns of the pressure fluctuations for the downstream range of 0 to 13 diameters downstream of the nozzle exit, it can be observed that the inclination of the patterns is not a constant. From zero to approximately six diameters downstream, the convection velocity appears to be constant. However, after six diameters downstream, the convection velocity decays. This is consistent with the observation that the potential core ends between 5 and 6 diameters downstream from the nozzle exit,

depending on the used nozzle geometry. The transition from the potential core region to the transitional region involves a decay in jet velocity, as was observed in the mean velocity analysis in the previous chapter. A decay in jet velocity results in a decay of the convection velocity of the hydrodynamic pressure waves, which explains the observed variation in the inclination of the structures of pressure fluctuations.
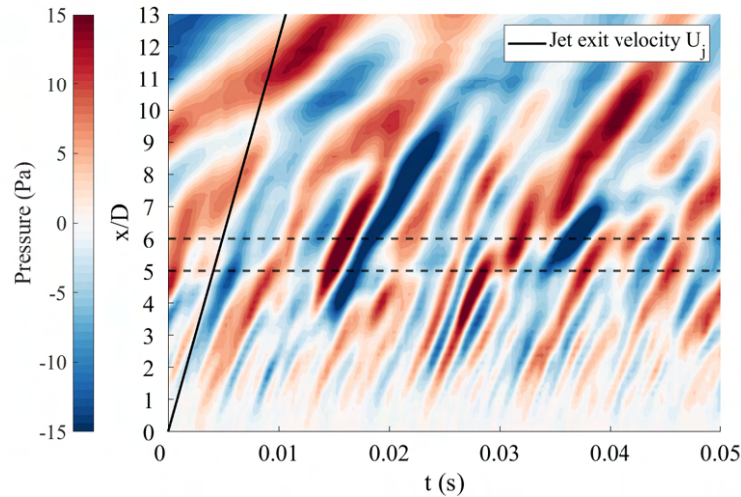
Figure 5.1: Space time plot of a sample of the measurements done for the isolated baseline nozzle (CN1) at $60\ m/s$, and with the linear array positioned at $25\ mm$ from the lipline.

The near-field pressure of the jet from LB2 is shown in Figure 5.2, which corresponds to the measurement with a lobe peak aligned with the linear array. In Figure B.6 in Appendix B, the measurements with a lobe valley directed to the linear array can be found.

The same trend regarding the convection velocity can be observed in the near-field of the lobed nozzle. However, compared to the baseline nozzle, the jet from the lobed nozzle shows a decay of the convection velocity that occurs more upstream. It seems that the convection velocity begins to decrease at a slightly shorter distance downstream from the nozzle exit. This is consistent with the conclusion made on the difference in downstream location where the decay in flow velocity starts, as a consequence of the end of the laminar potential core. Nevertheless, it must be noted that the observed pressure fluctuations are dominated by the most energetic structures, i.e. the low-frequency scales.

In addition, comparing Figure 5.1 with Figure 5.2 shows that the near-field of the jet from LB2 consists of pressure waves of a larger amplitude than the near-field of the jet from CN1. This could be attributed to the array simply being closer to the shear layer, which is a result of the larger jet spread for the jet from LB2. Thus, in order to compare the pressure wave intensities at the same radial distance from the shear layer, it is required to normalize the pressure such that the decay of the pressure over distance is not included. This requires, however, the missing insights into the pressure waves decay over a certain distance.

The measurement of LB2 with a lobe valley aligned with the linear array shows a similar trend as for the lobe peak measurement. This is expected as both parts of the shear layer originating from the lobe peak and lobe valley influence each other as the jet is three-dimensional.

All in all, it can be concluded that the jets from the two nozzles experience a varying convection velocity, of which the variation depends on the lipline geometry. In order to obtain the average convection velocities of the pressure fluctuations in the jets, a cross-correlation is performed.

The difference in convection velocities between the two nozzles becomes more evident with the two point cross-correlation. For this analysis, the two-point cross-correlation is done separately for the potential core and for the transitional region. It has to be noted, though, that the cross-correlation gives an weighted average of the convection velocity, which is mostly determined by the most energetic scales.
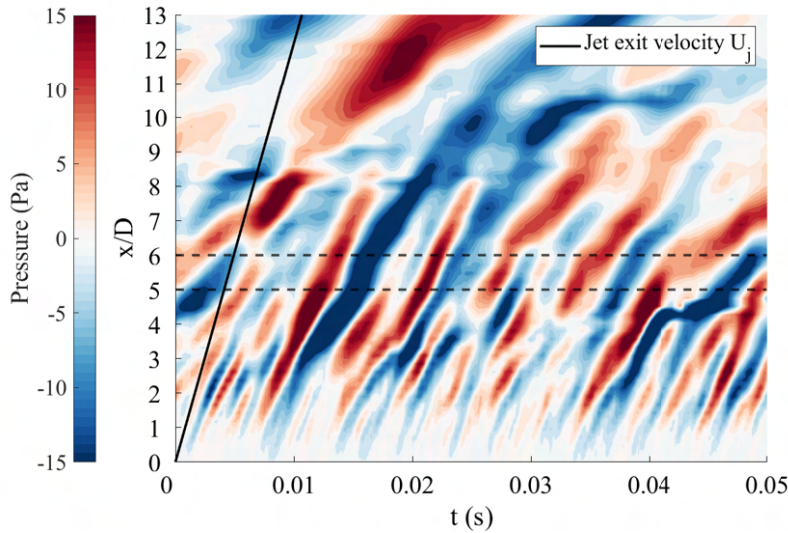
Figure 5.2: Space time plot of a sample of the measurements done for the isolated lobed nozzle 2 (LB2) at $60\ m/s$, and with the linear array positioned at $25\ mm$ from the lipline. For this measurement, a lobe peak was directed towards the linear array.

Firstly, the analysis is done using the cross-correlation for microphone 6, corresponding to approximately $x/D = 1.2$. The cross-correlation is shown in Figure 5.3a, where the contour lines represent 10% of the normalized cross-correlation coefficient. It can be observed that, initially, the pressure waves in the jets from both nozzles have similar convection velocities. For the jet from CN1 a convection velocity that is approximately 63% of the jet exit velocity is observed, whereas for the jet from LB2 a convection velocity of 57% of the jet exit velocity is observed.

Furthermore, as observed already in the space-time domain, the convection velocity for the lobed nozzle decays more upstream than for the baseline nozzle. This is indicated in Figure 5.3a with the bent in the contour that occurs with respect to the initial linear slope of the contour, which is only visible for the lobed nozzle measurements. This is even more evident for the part of the shear layer that originates from the lobe valley.

(a) Potential core region.

(b) Transitional region.
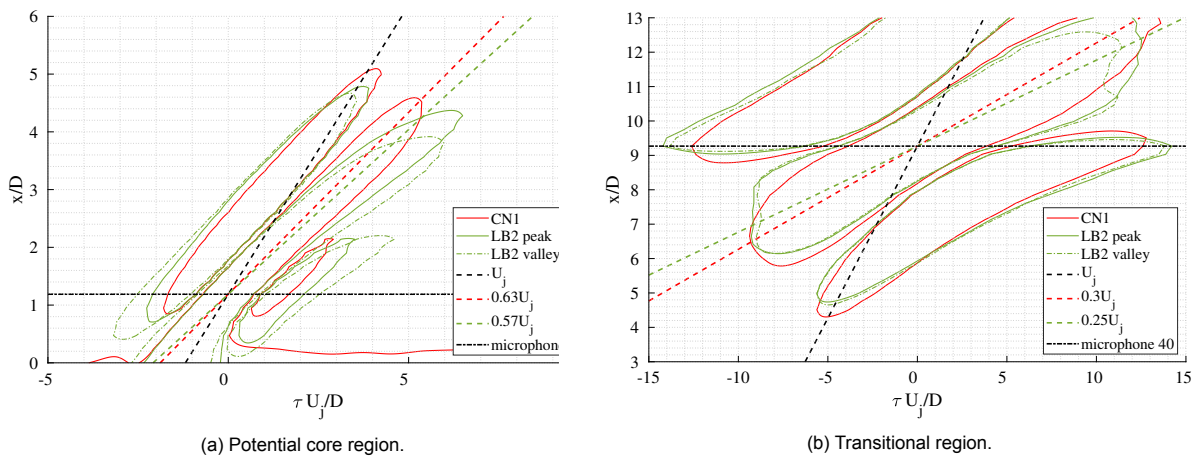
Figure 5.3: Two-point cross-correlation with microphone 6 and 40 for the baseline nozzle (CN1) and lobed nozzle 2 (LB2), while operating at a jet exit velocity of $60\ m/s$.

The cross-correlation in the transitional region is done at a downstream location of approximately $x/D = 9.3$, corresponding to microphone 40, which is shown in Figure 5.3b. The cross-correlation verifies that the convection velocity of the pressure waves decays in the transitional region of the jets. The decay is larger for the lobed nozzle than for the baseline nozzle. The jet from the baseline nozzle ex-

periences a decay to 30% of the jet exit velocity, whereas this is to 25% for the jet from the lobed nozzle.

In addition to the above made comparison, the cross-correlation has also been done for the jet from LB1 and it is compared with the jet from LB2, as shown in Figure B.14a and Figure B.14b in Appendix B for the potential core region and the transitional region, respectively. In the potential core region, both jets show difference between the two different measurements done per nozzle. This difference between the lobe peak and lobe valley measurement is more significant in the jet from LB2 than in the jet from LB1. Nevertheless, assuming that the behaviour of the average convection velocity in the near-field of the jet corresponds to the average between the two different lobe orientation measurements, shows that the convection velocity decays more downstream in the jet from LB1 than in the jet from LB2. On the contrary, the location of decay in the jet from LB1 appears to be more upstream than the location of the decay in the jet from CN1.

In the transitional region, the convection velocity for both lobed nozzles is similar. The convection velocity of the pressure fluctuations from LB1 is slightly larger than that from LB2, but slightly lower than in the jet from CN1. Both regions of hte jet from LB1 show a behaviour that is consistent with the conclusion that the jet from LB1 shows an intermediate behaviour between the jets from CN1 and LB2.

Hence, from the space-time domain it appears that the large-scale structures in the near-field of the jets show different convection velocities. With the observed lower convection velocity for the lobed jets, compared to the circular jet, it is expected that the circular jet carries energy at higher frequencies than the lobed jets. Moreover, as it is known that large-scale structures radiate sound to low polar angles, it is also expected that this difference is mostly visible at shallow polar angles. However, it is expected that the small difference in convection velocity will also only have a small effect on the difference in acoustic efficiency.

A better insight into the entire range of scales with their corresponding convection velocity can be given with the frequency-wavenumber spectra. This analysis will be done in the following subsection.

5.1.2. Convection Velocities of the Entire Range of Scales

The potential core region and the transitional region will be again analysed separately.

The ensemble-averaged frequency-wavenumber spectra of the first 14 microphones for the jets from CN1 and LB2, are shown in Figure 5.4. This corresponds to the region from the nozzle exit to approximately three diameters downstream. It has been decided to use a region with a smaller downstream extent than the potential core region as this analysis assumes a linear relation to determine the convection velocity. From the cross-correlation it became evident, in specific for the jets from the lobed nozzles, that a constant convection velocity does not occur for the entire potential region. A constant convection velocity was observed in all jets up to three diameters downstream of the nozzle exit.

Examining the spectra shows that at high frequencies, i.e. for small turbulent scales, the convection velocity is larger for the lobed jet than for the baseline jet. It appears that the jet from LB2 experiences a convection velocity of 70% of the jet exit velocity or larger for these scales, whereas the jet from CN1 experiences approximately a convection velocity of 60% of the jet exit velocity. On top of that, it appears that these scales experience a larger range of convection velocities in the jet from LB2. On the contrary, the convection velocities of the energetic low-frequency scales exhibits small differences between the jets from LB2 and CN1. This is consistent with the average convection velocity found by the cross-correlation in the first three diameters downstream, which is largely influenced by the low-frequency scales.

In addition, the spectra of both the lobe peak and lobe valley for LB2 are shown in Figure 5.4. It can be observed that despite similar convection velocities are estimated for both spectra, the range of the velocities differs. For the lobe valley measurement, a larger range of velocities can be observed compared to the lobe peak measurement. On top of that, a smaller amount of energy can be observed in the lobe valley measurement, as shown by the smaller area enclosed by the contour lines of the lobe valley measurement with respect to the lobe peak measurement.

Do note that for the lowest contour level, the spectra of the lobe peak measurement appears to be limited, as a flat contour line appears around $k_x D$ of 1.5. This could be attributed to the limitation of the

maximum resolved wavenumber. The maximum resolved wavenumber is computed by one over the minimum wavelength. The minimum wavelength that can be measured corresponds to the length covered by three microphones, as can be visualized with the sketch in Figure 5.5a. Hence, the minimum wavelength corresponds to twice the spacing of $12\ mm$ between the microphones, which subsequently corresponds to a maximum resolved wavenumber normalized by the jet diameter of approximately 2.1. As shown in Figure 5.4, the maximum resolved normalized wavenumber ($k_{Nyquist}D$) is significantly lower. This shows that during the measurements, the minimum wavelength measured by the first 14 microphones is actually larger than $24\ mm$. This could be attributed to the linear array that holds the microphones during measurements. Due to the dimensions of the linear array, a large part of the microphones sticks out of the array structures, as can be visualized with Figure 5.5b. As a consequence, the microphones are not placed perfectly perpendicular to the linear array, and thus the spacing between the microphones is not exactly $12\ mm$. The spacing between the different microphones varies, and thus the minimum resolved wavenumber differs over the linear array.
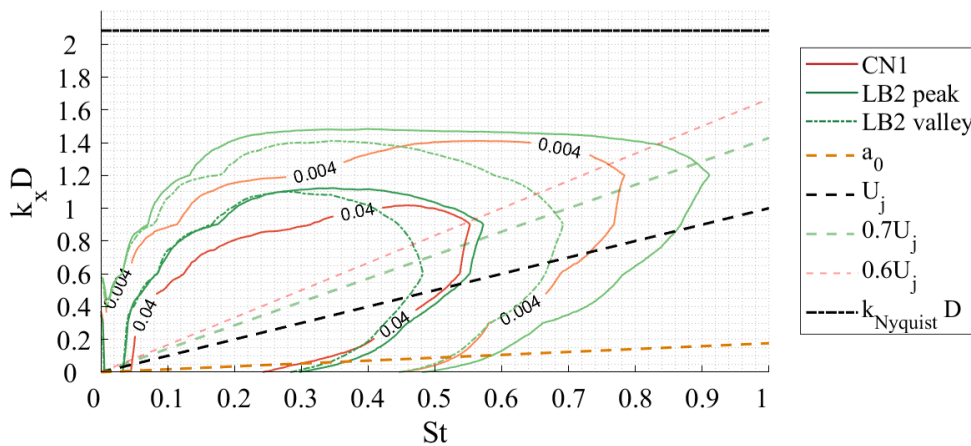
Figure 5.4: Ensemble-averaged frequency-wavenumber spectra for the first 14 microphone measurements of the baseline nozzle (CN1) and lobed nozzle 2 (LB2) at a jet exit velocity of 60 m/s, and the linear array positioned 25 mm from the baseline lipline.

(a) Sketch of a pressure signal with the minimum wavelength that can be measured by a series of microphones of the linear array.

(b) Exaggerated sketch of the deformed positioning of the microphones in the linear array.
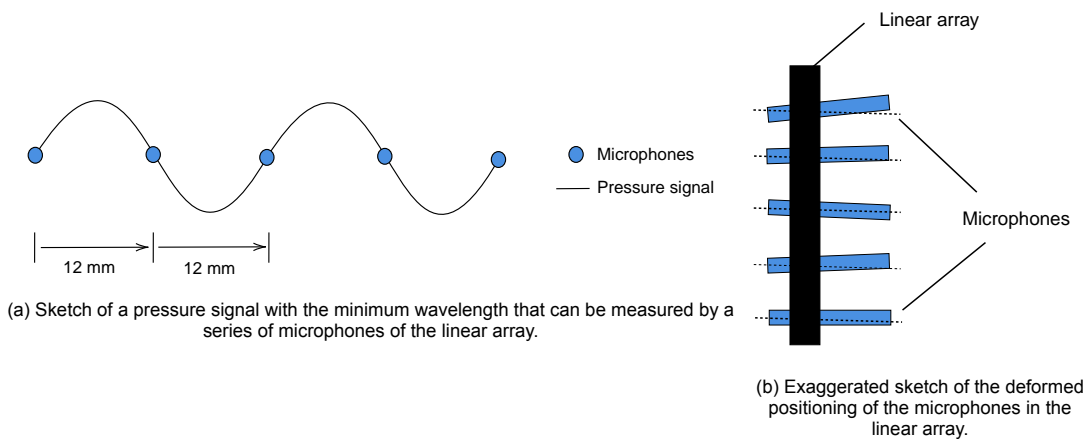
Figure 5.5: Sketches for understanding of the Nyquist wavenumber resolved in the frequency-wavenumber spectra.

The transitional region is analysed by the downstream region from 30 to 56 microphones, spanning approximately 7 diameters to 13 diameters downstream of the nozzle exit. Not the entire transitional region is analysed, for the same reason as for the analysis of the potential core region. The spectra can be observed in Figure 5.6. The acoustic propagation waves appear to be dominant in this region, as indicated by the spectra lobe underneath the line representing the speed of sound (a_0). It can be observed that the intensity of the acoustic pressure waves is larger for the baseline jet for the

Strouhal number range of 0.1 to 0.4, as shown by the larger lobe underneath the speed of sound line. At a Strouhal number above 0.4, it appears that the lobed jet result in a larger intensity of the acoustic pressure waves. This suggests that the baseline jet is more acoustically efficient in the low-frequency region, whereas the lobed jet is more acoustically efficient in the high-frequency region.
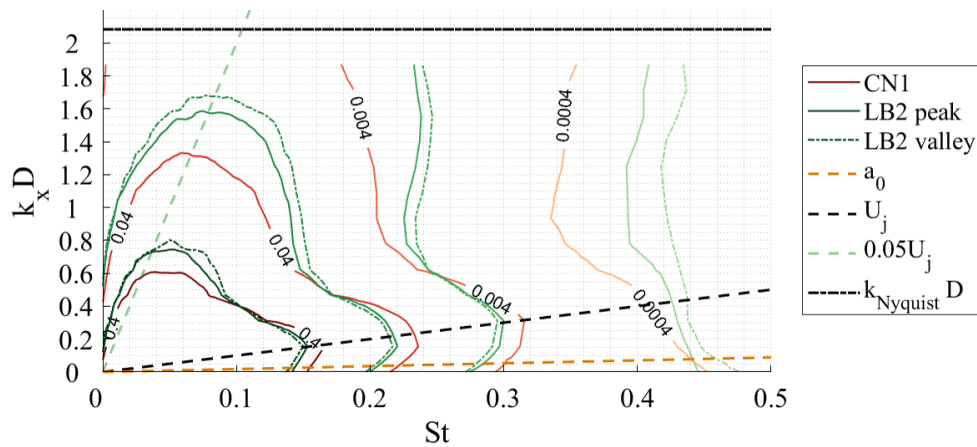
Figure 5.6: Ensemble-averaged frequency-wavenumber spectra for the microphone measurements 30 to 56 of the baseline nozzle (CN1) and lobed nozzle 2 (LB2) at a jet exit velocity of 60 m/s, and the linear array positioned 25 mm from the baseline lipline.

For both discussed regions, the jet from LB1 shows an intermediate behaviour with respect to the jets from CN1 and LB2. The comparison between the jets from LB1 and LB2 can be found in Figure B.15 and Figure B.16 in Appendix B, where the former is related to the potential core region and the latter to the transitional region of the jet.

From the regions analysed, it becomes evident that initially there is a difference in the convection velocities of the small-scale structures between the different jets. In the transitional region, insignificant differences occur between the pressure near-fields of the jets. This is consistent with the differences between the jets that were found with the analyses of the HWA measurements. It was observed that the jets from the lobed nozzles develops faster than the jet from the baseline nozzle, and the difference in turbulent scales becomes more significant after three diameters downstream. Farther downstream, from ten diameters downstream from the nozzle exit, the different jets start to behave similarly. Nevertheless, it is also expected that the spectra for the region between three diameters downstream until ten diameters downstream of the nozzle, will show significant differences between the different jets. However, the convection velocity is difficult to estimate in this region as the convection velocity varies and the exact location of the transition in convection velocity is not known. Hence, in order to analyse the differences in this region, the spectra of the entire linear array will be compared. This will not be able to give insights into the quantitative convection velocity development in the jet, but it will give insights into the average difference in convection velocities between the jets.

The spectra of the entire linear array of microphones for CN1 and LB2 are shown in Figure 5.7. In contrary to the observation in the potential core region, the hydrodynamic waves in the near-field of the jet from the baseline nozzle experience a larger convection velocity for the entire range of scales. This is most evident for the large-scale structures (low wavenumber k). From taking the previous analysis into account, which showed initially a convection velocity difference in the small-scale structures of the jet and insignificant difference in the transitional region, evidences that the observed differences can be attributed to the differences that occur in the region from three to seven diameters downstream of the nozzle exit. This is consistent with the conclusions from the analysis of the HWA measurements. Moreover, the low-frequency scale behaviour is consistent with the earlier made observation in the space-time domain.

It can also be observed that at a low Strouhal number, the circular jet shows stronger intensity in hydrodynamic pressure waves, whereas the lobed jet shows a larger intensity in these pressure waves

at higher Strouhal numbers. Thiis is also consistent with the observed difference in turbulence scales in the jets, as presented with the HWA analyses.

In addition, it can be clearly visualized that the hydrodynamic pressure is dominant in the near-field region as the acoustic pressure waves, indicated by the peak along the acoustic speed of sound, are only visible at a low intensity level.
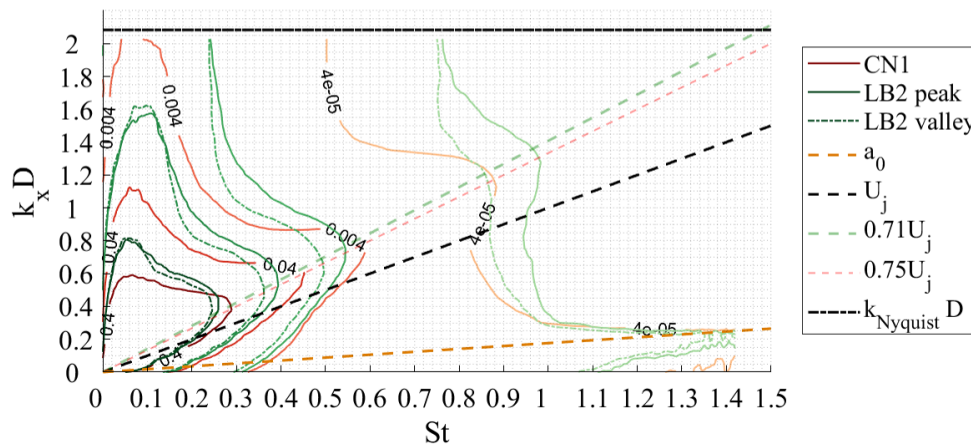
Figure 5.7: Ensemble-averaged frequency-wavenumber spectrum for the entire linear array measurement of CN1 and LB2 at a jet exit velocity of 60 m/s and the linear array positioned 25 mm from the baseline lipline.

All in all, it is expected that the difference between the jets results in different far-field noise spectra. For an increase in convection velocity, it is expected that the far-field noise is carried at a higher frequency. In addition, for a larger intensity of hydrodynamic pressure waves, it is expected that the far-field noise increases for the corresponding frequency range.

5.1.3. Rate of Decay of the Hydrodynamic Pressure Waves

In order to analyse the decay of the hydrodynamic pressure waves in radial distance, the spectra of the potential core region will be compared for different radial distances Δs from the nozzle lipline, namely at 25, 50 and $75\ mm$. This is again done by analysing the region from zero to three diameters downstream of the nozzle exit, and not the entire potential core region. This region is analysed as for the tested installed configuration, the trailing-edge is positioned at three diameters downstream of the nozzle exit. Hence, it is expected that a change in hydrodynamic pressure waves characteristics in this downstream region has an effect on the scattered pressure waves that generate the jet installation noise.

Firstly, the measurement with the array positioned at a radial distance of $25\ mm$ from the jet showed that for small-scale structures there could be a difference in convection velocities observed between the jets from LB2 and CN1. The jet from LB2 experiences higher convection velocities.

Examining the pressure waves at a larger radial distance from the jet, namely at $50\ mm$, shows more significant differences. The spectra can be observed in Figure 5.8. For the Strouhal number range of 0.4 to 0.8, it appears that the jet from the lobed nozzle experiences a larger convection velocity than the jet from the baseline nozzle. Only for low-frequency scales no significant difference is observed. For the entire range of scales it can be observed that the pressure waves have become less energetic, and thus also the acoustic pressure waves are more visible. It appears that the near-field of the jet from LB2e experiences pressure waves with a higher energy than for the jet from CN1, as can be observed with the larger area enclosed by the contour lines of LB2. This could be attributed to the smaller distance between the linear array and the shear layer of the jet from LB2, compared to the jet from CN1. Hence, it is difficult to asses if the jets experience a different decay in pressure waves amplitude as the distance between the microphones and the jet is different for the two nozzles.

Taking these observations into account, for a plate with its trailing-edge located at a similar position of three diameters downstream of the nozzle exit, it is expected that the jet installation noise differs between the CN1 and LB2 configurations. As the hydrodynamic pressure waves and acoustic pressure

waves are more energetic for LB2 than for CN1, it is expected that the jet installation noise would be larger for LB2 than for CN1 in the entire frequency region. The most evident differences are expected in the low-frequency region.

Figure 5.8: Ensemble-averaged frequency-wavenumber spectra for the first 14 microphones of the array with the baseline nozzle (CN1) and the lobed nozzle (LB2) at a jet exit velocity of 60 m/s, and the linear array positioned 50 mm from the baseline lipline.

The spectra of the measurement with the linear array positioned at a radial distance of $75\ mm$ from the jet, can be observed in Figure 5.9. The relative intensity of the acoustic pressure waves with respect to the hydrodynamic pressure waves has increased for both jets. It appears that the decay of the hydrodynamic pressure waves is larger in the near-field of the jet from the lobed nozzle than of the jet from the baseline nozzle. This can be observed by the significantly smaller difference between the pressure waves in the near-fields of the jets from CN1 and LB2, while taking into account the significant differences between the spectra that are observed for the measurement done at $50\ mm$.

With these observations it is expected that if a plate is installed with its trailing-edge at $75\ mm$ from the jet, the hydrodynamic pressure waves still have an effect on the scattered pressure waves at the edge. The difference between both installed nozzles is expected to be visible in the perceived low-frequency region in the far-field. In addition, it is expected that there will be no significant difference in jet installation noise if the lobe orientation of the lobed nozzle is changed. This can be concluded from the small difference in spectra between the lobe valley and the lobe peak measurement, shown in Figure 5.9.

Figure 5.9: Ensemble-averaged frequency-wavenumber spectra for the first 14 microphones of the array with the baseline nozzle (CN1) and the lobed nozzle (LB2) at a jet exit velocity of 60 m/s, and the linear array positioned 75 mm from the baseline lipline.

5.2. Effect of Flat Plate on the Near-field of the Jet

In this section the installed jet nozzles will be analysed. For these measurements, the linear array of microphones is positioned at a radial distance Δs of $75\ mm$. This has been done at both the shielded and the unshielded sides of the nozzle-plate configurations. For the lobed nozzles, the same distinction as for the isolated nozzles has been made regarding the lobe orientation with respect to the linear array. The flat plate is positioned for the installed configurations at a radial distance of one diameter from the jet-axis, and with its trailing-edge at a downstream distance of three diameters from the nozzle exit.

Firstly, the difference in the dominant pressure waves is analysed by presenting the space-time domain. This is followed by analysing the difference in hydrodynamic and acoustic pressure waves using frequency-wavenumber spectra. Both analyses involve the comparison with the near-field of the isolated jets, as well as a comparison between the near-field of the installed jets from the different nozzles.

5.2.1. Intensity of the Dominant Pressure Waves

In the previous section, the near-field pressure fluctuations for the array positioned at a radial distance of $75\ mm$ have not been analysed. Therefore, in order to analyse the difference with a plate installed, the space-time domain of the isolated jets at this position is analysed. The measurements of the isolated jet from the baseline nozzle is shown in Figure 5.10a. From the frequency-wavenumber spectra at this radial distance it was observed that the difference in lobe orientation was insignificant for the jet from the isolated lobed nozzle. Hence, only the pressure near-field of one of the LB2 measurements is shown in Figure 5.10b.

It can be observed that for both jets the amplitude of the pressure waves has decreased significantly in intensity, compared to the measurement done at a radial distance Δs of $25\ mm$, as presented before. Do note that the pressure range depicted here is for a maximum magnitude of $10\ Pa$, whereas for the plots previously shown there was a range used with a maximum magnitude of $15\ Pa$. This decay in strength is as expected as the hydrodynamic pressure waves experience a fast decay in radial direction, as was observed in the previous section. It appears that the hydrodynamic waves have a larger amplitude for CN1 than for LB2.

(a) Near-field pressure of the jet from CN1.

(b) Near-field pressure of the jet from LB2.
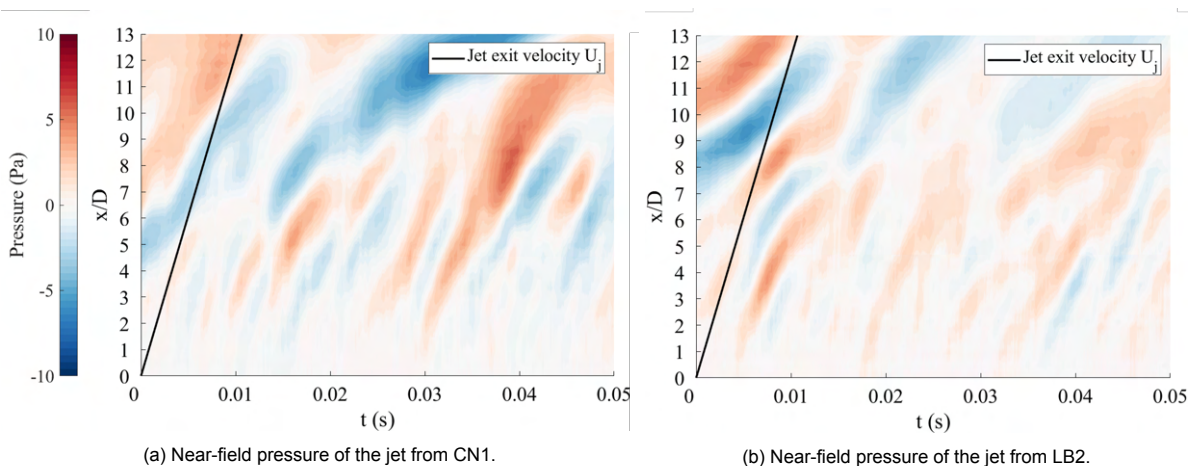
Figure 5.10: Space time plot of the measurements for the jet from the isolated baseline nozzle (CN1) and lobed nozzle (LB2) at $60\ m/s$, and with the linear array positioned at $75\ mm$ from the lipline.

The effect of placing a flat plate in the near-field of the jets differs between the shielded and the unshielded sides of the configuration. Firstly, the near-fields of the jets from CN1 and LB2 at the shielded side of the configuration can be observed in Figure 5.11a and Figure 5.11b, respectively. The latter includes the LB2 measurement with a lobe peak directed towards the plate and the linear array.

The intensity of the hydrodynamic pressure waves perceived by the linear array has significantly increased compared to the isolated jets (shown in Figure 5.10). Again, it can be observed that the hydrodynamic waves in the near-field of the jet from CN1 have a larger amplitudee than for the jet from

LB2. This difference could be attributed to the observation that in the jet from the lobed nozzle, the energy is distributed over a larger range of length scales.

(a) Near-field pressure of the jet from CN1.

(b) Near-field pressure of the jet from LB2.
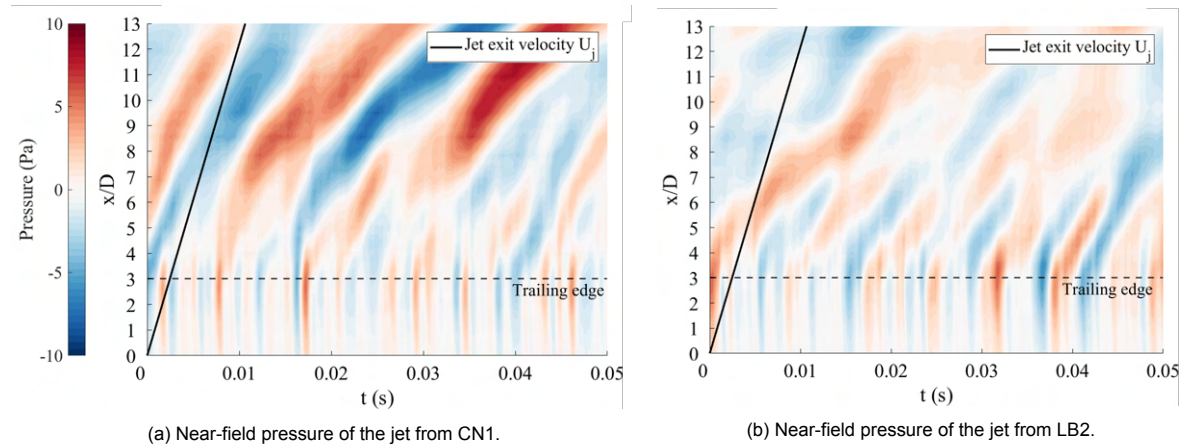
Figure 5.11: Space time plot of the measurements at the shielded side for the installed baseline nozzle (CN1) and lobed nozzle (LB2) at $60\ m/s$, and with the linear array positioned at $75\ mm$ from the lipline. For the measurement of LB2, a lobe peak is directed towards the flat plate.

A comparison between the space-time domain for the two LB2 measurements is shown in Figure 5.12a and Figure 5.12b for the lobe peak and lobe valley measurement, respectively. Stronger hydrodynamic pressure waves are observed for the former LB2 measurement. This could be attributed to the asymmetry in the lobed jet.

(a) With a lobe peak directed towards the flat plate and linear array.

(b) With a lobe valley directed towards the flat plate and linear array.
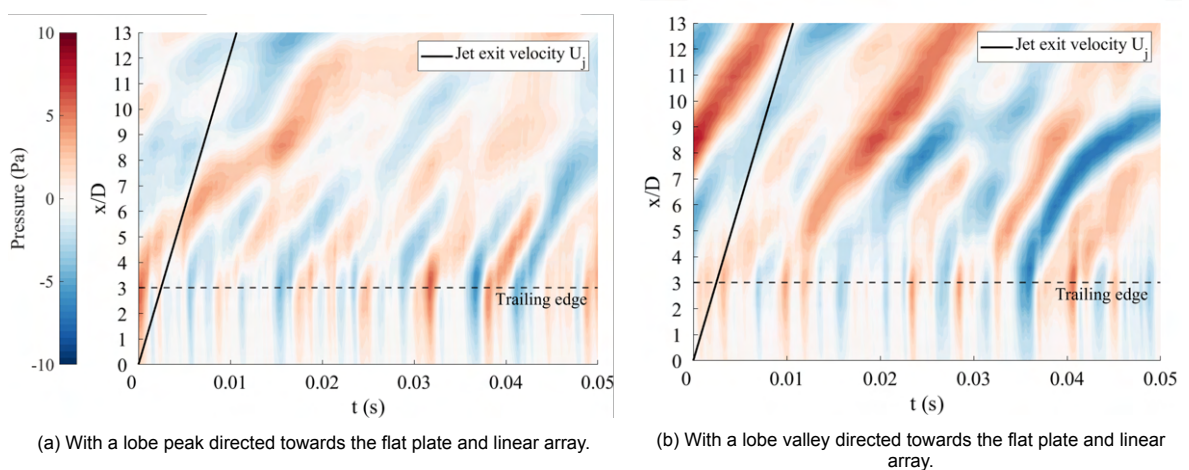
Figure 5.12: Space time plot of the measurements at the shielded side for the installed lobed nozzle (LB2) at $60\ m/s$, and with the linear array positioned at $75\ mm$ from the lipline.

The first consequence of the asymmetry of the lobed jet from LB2 is that the orientation of the nozzle affects the mean distance between the lobed jet and the plate. In case a lobe peak is directed towards the plate, a large part of the jet is positioned farther away from the plate, compared to the jet from the baseline nozzle. This can be visualised with the sketch in Figure 5.13b. In addition, it can be observed that if a lobe valley is directed towards the plate, a larger part of the jet is positioned close to the plate than for the configuration with a lobe peak directed towards the plate. Hence, it is expected that if a lobe valley is directed towards the plate, the trailing-edge of the plate will experience more scattering of hydrodynamic pressure waves from the jet from the lobed nozzle.

Moreover, at the downstream distance of three diameters from the nozzle exit, the jet from the lobed nozzle experiences differences in turbulent scales in the azimuthal direction. From the frequency spectra obtained with the HWA measurements at this downstream location, as shown in Figure 5.13a, it was concluded that the part of the shear flow originating from a lobe peak experiences a significant

amount of energy in the low-frequency domain. This is similar to what was observed for the shear region of the jet from CN1. On the contrary, the part of the shear region of the jet from LB2 that originates from a lobe valley, experiences a significantly lower amount of energy in the low-frequency domain. Hence, in case a lobe valley is directed towards the plate, part of the shear flow originating from two lobe peaks is positioned close to the plate. As a consequence, it is expected that a larger amount of large-scale structures are scattered at the trailing-edge of the plate if a lobe valley is directed towards the plate.

All in all, it can be concluded that the lobe orientation affects the scattering of the hydrodynamic pressure waves at the trailing-edge of the plate in case LB2 is used as jet nozzle.
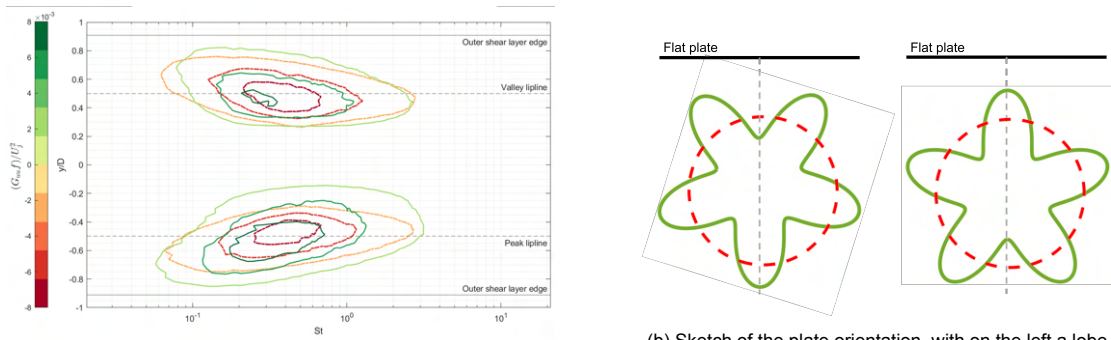
(a) Frequency spectra at 3 diameters downstream of the nozzle exit, for CN1 (red) and LB2 (green). For comparison purposes the magnitude of CN1 has been plotted as negative values.

(b) Sketch of the plate orientation, with on the left a lobe valley directed towards the flat plate and on the right a lobe peak directed towards the flat plate.

Figure 5.13: Frequency spectra of the jet from the baseline nozzle (CN1) and lobed nozzle (LB2) at three diameters downstream of the nozzle exit, and the nozzle orientation configurations with respect to the flat plate.

For the jet from the baseline nozzle, the measurements at the unshielded side of the plate-jet configurations perceive significantly less strong hydrodynamic pressure waves than at the shielded side, as can be observed in Figure 5.14a. This is as expected as the linear array is now positioned at a larger distance from the trailing-edge of the plate, and thus also from the scattering of the hydrodynamic pressure waves.

(a) Near-field pressure of the jet from CN1.

(b) Near-field pressure of the jet from LB2.
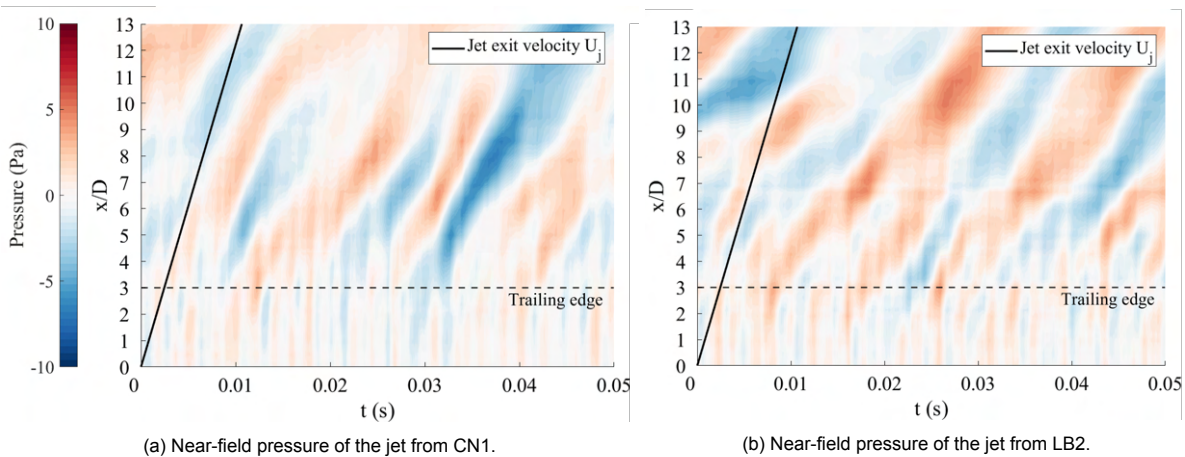
Figure 5.14: Space time plot of the measurements at the unshielded side for the installed baseline nozzle (CN1) and lobed nozzle (LB2) at $60\ m/s$, and with the linear array positioned at $75\ mm$ from the lipline. For the measurement of LB2, a lobe valley is directed towards the flat plate.

Interestingly, for the jet from the lobed nozzle, significant differences can be found with respect to the orientation of the lobed nozzle. Do note that for these configurations, a lobe valley directed towards the linear array corresponds to the configuration with a lobe peak directed towards the plate, and vice versa. For the configuration with a lobe peak directed towards the plate, as shown in Figure 5.14b, little

difference between the shielded and unshielded sides can be observed. On the contrary, for the configuration with a lobe valley directed towards the plate, as shown in Figure 5.15, a significant reduction in the amplitude of the hydrodynamic pressure waves can be observed, similar to for the jet from the baseline nozzle. Again, from these observations it appears that the lobe orientation is of importance for the near-field pressure when a plate is installed in proximity to the lobed nozzle.

Nevertheless, compared to the near-pressure field of the isolated nozzles, an increase in the strength of the hydrodynamic pressure waves can be observed. From this it can be concluded that the flat plate results in an enhancement of the perceived large-scale pressure waves at the unshielded side.
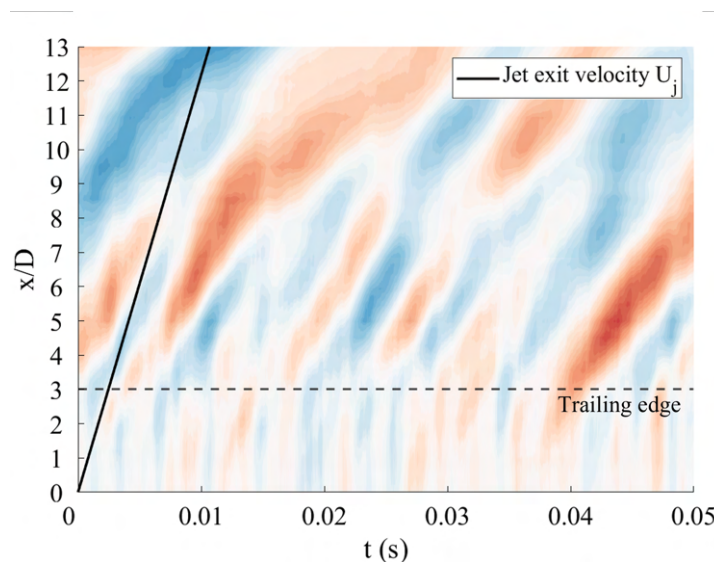
Figure 5.15: Space time plot of a sample of the measurements done at the unshielded side for the installed lobed nozzle 2 (LB2) at $60 \ m/s$ and with the linear array positioned at $75 \ mm$ from the lipline. For this measurement a lobe peak is directed towards the flat plate.

All in all, it can be concluded that a flat plate in proximity of the jet results in a larger region where the hydrodynamic pressure waves are visible. This clearly shows that at the trailing-edge the hydrodynamic waves are scattered. As a consequence, the hydrodynamic waves are perceived at the shielded side with a significantly larger strength than for the isolated nozzles, of which it appears that this effect is stronger for the jet from CN1 than for the jet from LB2. On the contrary, compared to the isolated nozzles, at the unshielded side a less significant increase in strength of the hydrodynamic waves can be perceived for the jets from CN1 and LB2. This increase is most significant for the jet from the lobed nozzle.

Lastly, it could be clearly observed that the lobe orientation has a significant effect on the near-field pressure. Orienting a lobe peak to the plate results in less strong large-scale structures at both the shielded and unshielded sides, than for a configuration where a lobe valley is directed towards the flat plate.

From this analysis conclusions have been made on the most energetic pressure waves. In order to analyse the change in hydrodynamic and acoustic pressure waves separately, when a flat plate is installed, the frequency-wavenumber spectra has to be analysed. This will be presented next.

5.2.2. Intensity of the Hydrodynamic and Acoustic Pressure Waves

The frequency-wavenumber spectra for the isolated jets from CN1 and LB2 are shown in Figure 5.16, using the entire downstream region from zero to approximately 13 diameters downstream of the nozzle exit. The spectra at the shielded side of the installed configurations of CN1 and LB2 are shown in Figure 5.17.
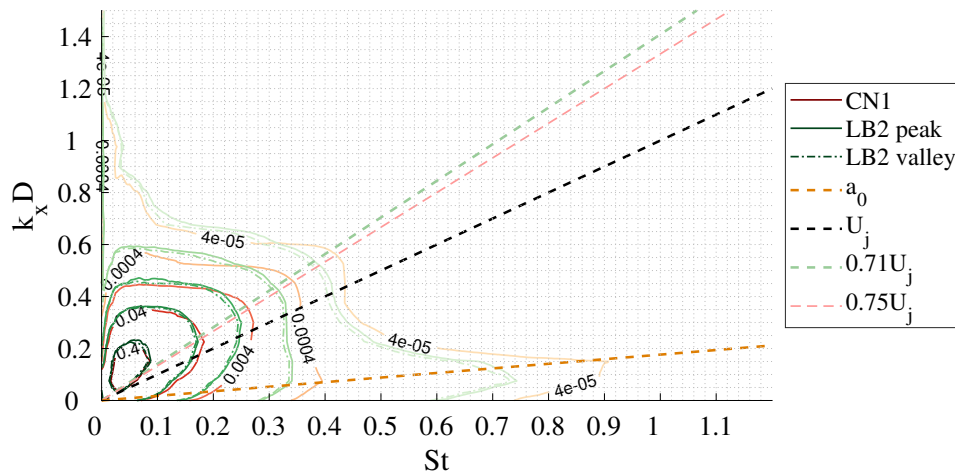
Figure 5.16: Ensemble-averaged frequency-wavenumber spectra for the entire linear array measurement of the isolated baseline nozzle (CN1) and lobed nozzle (LB2) at a jet exit velocity of 60 m/s.
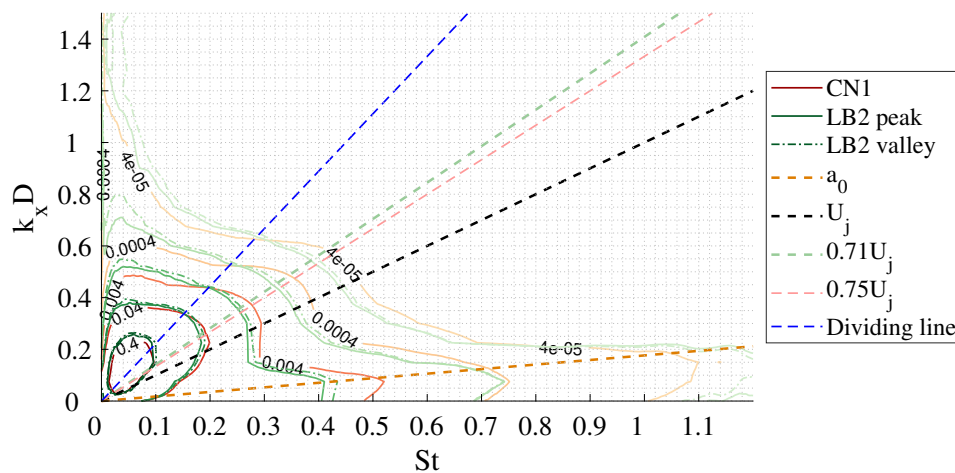
Figure 5.17: Ensemble-averaged frequency-wavenumber spectra for the entire linear array measurement at the shielded side of the installed baseline nozzle (CN1) and lobed nozzle (LB2) at a jet exit velocity of 60 m/s.

When comparing the spectra of the isolated nozzles with the installed configurations, observed at the shielded side, remarkable differences can be observed. For both nozzles, the intensity of the acoustic pressure waves increases significantly when a plate is installed. This shows that introducing the flat plate results in an enhancement of energy in the acoustic pressure waves observed in the near-field.

Comparing the spectra of the two jets shows that the near-field of the jet from CN1 experiences the highest intensity in acoustic pressure waves at low Strouhal numbers. However, at higher frequencies, it can be observed that the near-field of the jet from LB2 experiences a higher intensity. In addition, it appears that the near-field of LB2 experiences a higher intensity of large-scale hydrodynamic pressure waves. On the contrary, the near-field of CN! experiences the highest intensity of hydrodynamic pressure waves at higher Strouhal numbers. The dividing line shown in Figure 5.17, clearly shows this difference in intensity of the hydrodynamic pressure waves. A similar trend can be observed for the isolated spectra, shown in Figure 5.16.

In contrary to the space-time domain, it can be observed that the frequency-wavenumber spectra of the near-field of the installed jet from LB2 does not differ significantly for the two different lobe orientations. Nevertheless, a slightly larger amount of energy can be observed in the measurement with a lobe valley directed towards the flat plate. This can be both observed for the hydrodynamic pressure waves, as well as the acoustic pressure waves.

At the unshielded side, presented in Figure 5.18, similar observations can be made. Compared to

the isolated nozzle an increase in the intensity of the acoustic pressure waves can be observed, which is less than observed at the shielded side. Nevertheless, also at the unshielded side the baseline nozzle results in the highest intensity of acoustic pressure waves. Moreover, it can again be observed that the difference between CN1 and LB2 differs over the Strouhal number range. For very low Strouhal numbers the near-field of LB2 experiences more large-scale structures, whereas after a certain Strouhal number the near-field of CN1 experiences more hydrodynamic pressure waves.

Lastly, it can be observed that the lobe orientation of LB2 does not result in significantly different spectra at the unshielded side.
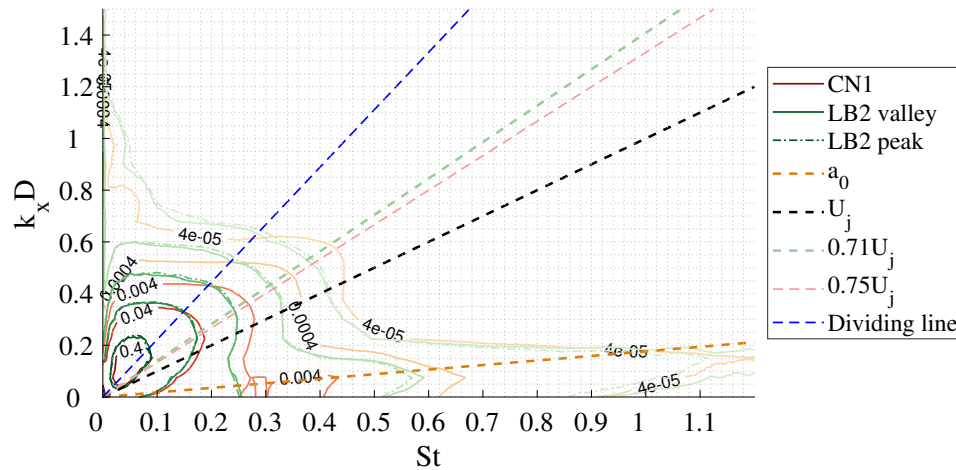
Figure 5.18: Ensemble-averaged frequency-wavenumber spectra for the entire linear array measurement at the unshielded side of the installed baseline nozzle (CN1) and lobed nozzle (LB2) at a jet exit velocity of 60 m/s.

From the frequency-wavenumber spectra of the near-field of the jet from LB1 an intermediate behaviour between LB2 and CN1 can be observed, as shown with Figure B.17 and Figure B.18 in Appendix B. The intensity of the acoustic pressure waves in the near-field of the jet from LB1 is larger than for LB2, whereas the intensity of the large-scale structures is larger in the near-field of LB2 with respect to the near-field of LB1.

All in all, the spectra confirm that the installation of the plate results in an increase in the strength of the hydrodynamic pressure waves that are perceived at the shielded side. At the unshielded side, this increase is not as significant. Moreover, at both sides a significant increase can be observed in the acoustic pressure waves intensity. This is more prominent for the near-field of the jet from CN1 than of the jet from LB2 at low Strouhal numbers, whereas this is vice versa at high Strouhal numbers. This suggests that the installed jet with the lowest far-field noise is frequency dependent.

Nevertheless, it is also observed that at very low Strouhal numbers the lobed nozzles results in a larger intensity of the large-scale hydrodynamic waves, whereas after a certain Strouhal number this is not true. It is expected that this will also have an effect on the perceived far-field noise.

6

Far-field Acoustics

In this chapter the acoustic performance of the different jets will be analysed. This is done by presenting the spectra of the far-field Sound-Pressure Level (SPL). Firstly, the perceived far-field for the isolated jets will be presented. Afterwards, the far-field noise of the installed jets will be analysed.

6.1. Isolated Jet Nozzles

In this section the far-field noise for the isolated nozzles with a jet exit velocity of 60 m/s will be analysed. Firstly, the jets are compared at the most shallow angles, where the jet mixing noise is dominant. Afterwards, the jets are compared along the sideline directions, i.e. at polar angles of 90 and -90 degrees, where the jet installation noise are expected to be dominant. The coordinate presented in subsection 3.3.3 will be used for this analysis.

The spectra of the far-field noise for the microphones positioned at the most shallow angles, with respect to the jet-axis, are shown in Figure 6.1. These angles correspond to 50 and -63 degrees for the polar arc and the beamforming panel, respectively. The spectra evidences a significant discrepancy in the output of the two microphones. This could be attributed to the difference in polar angles and in distance between the jet and microphone between the two microphones. However, this same discrepancy is observed for spectra obtained from the microphones of the beamforming panel and the polar arc positioned at similar distances from the jet. For example, this discrepancy will also be visible along the sideline directions, as will be shown later in this section. This is unexpected as the nozzles are isolated and especially for the baseline nozzle an axisymmetric jet occurs. On top of that, in the far-field, the lobed lipline of the lobed nozzles results in uniform characteristics of the acoustic pressure waves in azimuthal direction, as could be concluded from the frequency-wavenumber spectra in the previous chapter. Hence, it is concluded that the performances of both microphones is not similar.

Despite of the observed discrepancy between the polar arc and beamforming panel microphones, two observations can be made that are valid for both microphones. It can be observed that for the three jets, the average noise in the high-frequency region is the lowest. The highest amount of noise is generated in the low-frequency region.

Comparing the spectra shows that the acoustic performance differs per frequency region. In the low-frequency region, the jet from the baseline nozzle generates more far-field noise than the jet from the lobed nozzles. On the contrary, in the high-frequency region, the jet from the lobed nozzles generate more far-field noise. This difference in far-field noise between the isolated jets is consistent with what was found in current literature. The lobed nozzles enhance turbulence development, which results in a more multiscale jet than the jet from the baseline nozzle. As a consequence, the jet from the lobed nozzle consists of less large-scale structures that generate low-frequency noise, whereas it consists of more small-scale structures, which generate high-frequency noise. The difference is more visible in the low-frequency region as the large-scale structures radiate noise at shallow angles, whereas the small-scale structures induce far-field noise along the sideline directions.

Moreover, the near-field pressure measurements also showed that at low Strouhal numbers the
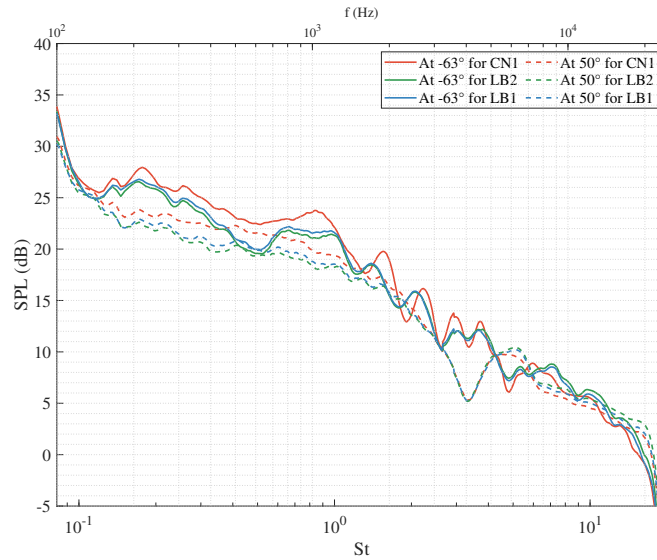
Figure 6.1: Sound-Pressure Level of the isolated nozzles at a jet exit velocity of 60 m/s, measured by microphone 5 and microphone 72.

baseline jet carries more energy in the acoustic pressure waves, whereas the lobed jet results in more intense acoustic pressure waves at high Strouhal numbers.

On top of that, for both regions, the jet from LB1 shows the same intermediate behaviour between CN1 and LB2 in the SPL spectra, as was also observed in the near-fields of the jets.

The spectra of the far-field noise along the sideline directions are shown in Figure 6.2. The spectra in the region below $100\ Hz$ were filtered to remove the measured reflections that occur with the use of this anechoic windtunnel.
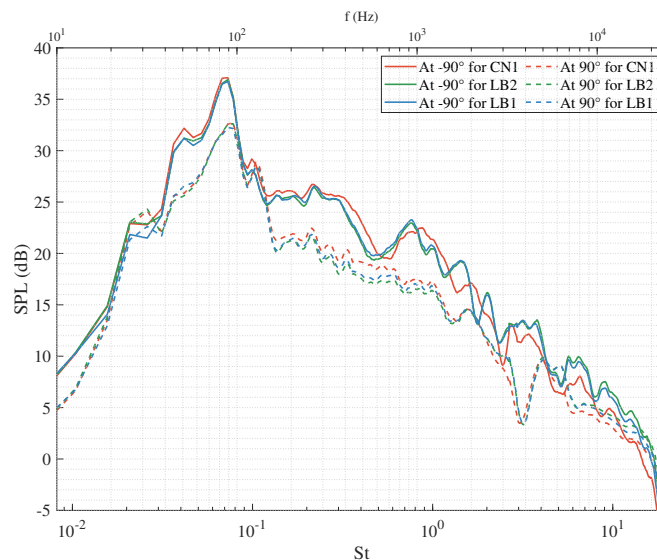
Figure 6.2: Sound-Pressure Level of the isolated nozzles at a jet exit velocity of 60 m/s, measured by microphone 42 and microphone 68.

The spectra in the low-frequency region shows less significant differences between the jets than for the previously observed shallow angles. On the contrary, it appears that the difference in the high-frequency region is slightly larger than for the shallow polar angles. From this observation and the fact that the jet mixing noise is dominant at shallow polar angles, it is expected that the difference between

the jets in the low-frequency region is even larger at very shallow polar angles. Unfortunately, such shallow polar angles were not measured in the conducted experimental campaign.

Moreover, for the polar angle of -90 degrees, it appears that for a Strouhal number higher than 0.4, the spectrum of the jet from the baseline nozzle is shifted slightly towards the high-frequency region with respect to the spectra of the jets from the lobed nozzles. The jet exit velocity is used for the definition of the Strouhal number, whereas also a different reference velocity can be used. Instead of using the jet exit velocity as a reference velocity, the convection velocity can be used. The difference in convection velocity between the jets also differs for the different scale sizes. For the jet from the lobed nozzles, a smaller convection velocity was observed for a similar range of low Strouhal numbers. Using the different convection velocities for the jets to define the Strouhal number gives the spectra as given in Figure 6.3. This clearly shows that the spectra from the three nozzles collapse in the range of Strouhal numbers between 0.4 and 1.0. This is as expected as for a larger convection velocity the noise is perceived at a higher frequency, as more eddies are convected per second. Hence, it is also expected that the same method can be used to collapse the spectra for other ranges of Strouhal numbers.
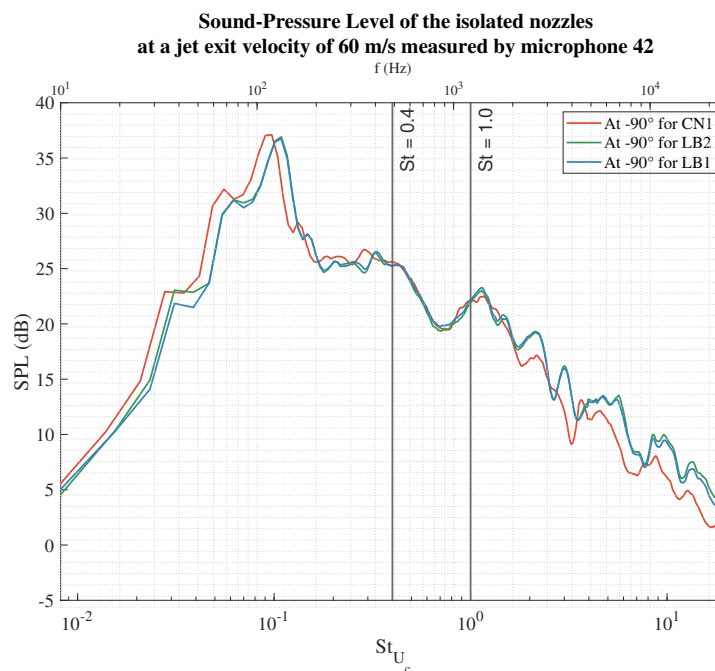
Figure 6.3: Sound-Pressure Level of the isolated nozzles at a jet exit velocity of 60 m/s, measured by microphone 42.

With the observed discrepancy between the microphone in the polar arc and the microphone in the beamforming panel, it has been decided to analyse the difference in SPL between the jets from the different nozzles and compare the results of the microphones. The difference in the SPL spectra along the sideline directions of the jets from the isolated lobed nozzles, with respect to the jet from the isolated baseline nozzle, is shown in Figure 6.4. Similar trends can be observed between the two microphones. At the low frequencies, the lobed nozzles result in a mild noise reduction, whereas at high frequencies the lobed nozzle produces an increase in far-field noise emission. Do note that for the negative sideline direction, large fluctuations can be observed in the difference. This is due to the earlier made observation that the SPL spectra of the lobed nozzles is shifted with respect to the spectrum of the baseline nozzle.

6.2. Installed Jet Nozzles

In this section the perceived far-field noise for the jets with a flat plate in proximity will be analysed. Firstly, the configurations that were tested with the linear array, as presented in the previous chapter, will be analysed. Afterwards, three additional jet-plate configurations will be examined in order to gain more insights into the effect of the jet-plate configuration on the far-field noise.
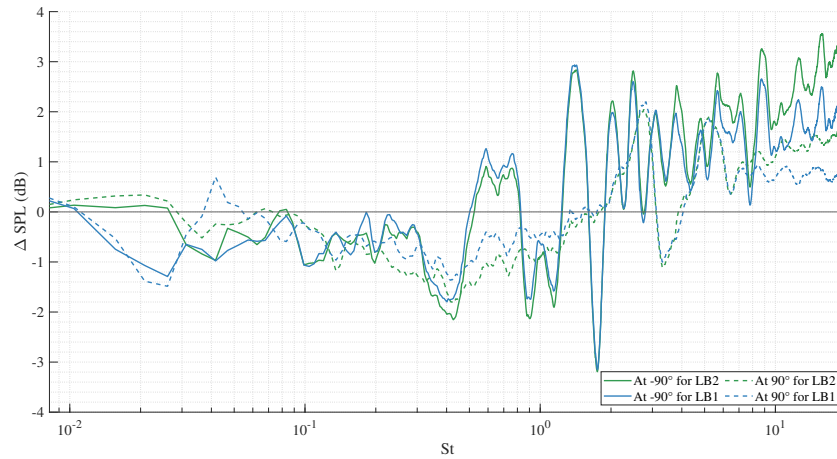
Figure 6.4: Difference in Sound-Pressure Level of the isolated lobed nozzles with respect to the baseline nozzle at a jet exit velocity of 60 m/s, measured by microphone 42 and microphone 68.

6.2.1. Effect of Flat Plate on Far-field Noise

The far-field noise of the jets from CN1 and LB2 when a flat plate is placed in proximity of the jet, can be observed in Figure 6.5a and Figure 6.5b for the shielded and unshielded sides, respectively. For this configuration the distance between the nozzle exit and the trailing-edge in the x-direction, defined as L, is of three diameters and the distance between the jet centre and the flat plate, defined as H, is of one diameter.
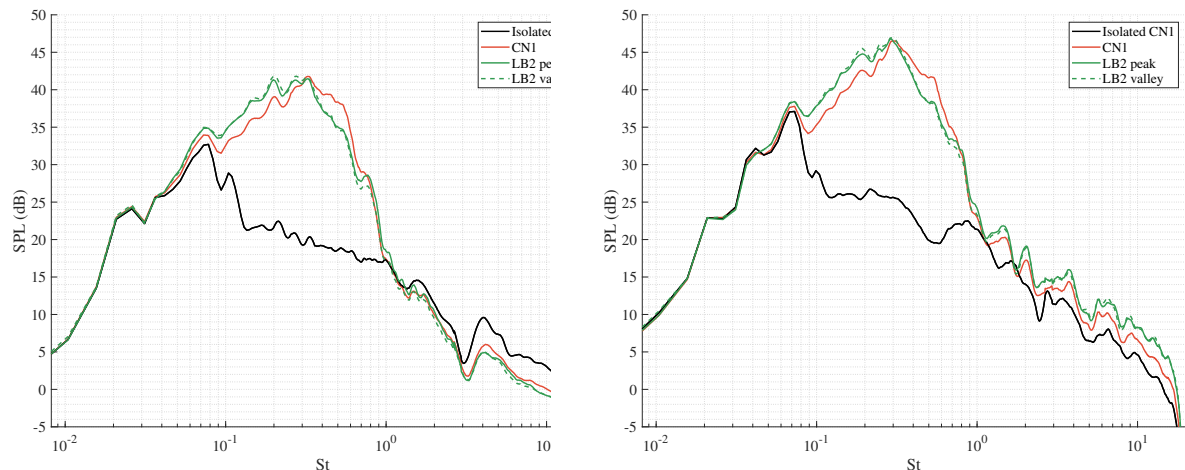
(a) Observed along the sideline direction at the shielded side.

(b) Observed along the sideline direction at the unshielded side.

Figure 6.5: Sound-Pressure Level of the installed baseline nozzle (CN1) and lobed nozzle (LB2) at a jet exit velocity of 60 m/s and for a flat plate length L of three diameters and a separation distance H of one diameter.

For both installed jets it can be observed that the same low-frequency hump occurs as was found in the literature when jet installation noise occurs [33, 52]. This can be observed both at the shielded as the unshielded sides. Comparing between the shielded side and the unshielded side shows that the unshielded side experiences a larger low-frequency hump. This could be attributed to the discrepancy between the microphone at the shielded and the unshielded sides. However, this could also be partly caused by the reflections of the pressure waves from the plate, as well as a potential altering of the jet mixing that occurs due to the convection of reflected and scattered pressure waves through the jet.

In the high-frequency region, it can be observed that the shielded side experiences less noise along the sideline direction than for an isolated jet. This difference occurs as the plate blocks part of the pressure waves that are responsible for the high-frequency noise. On the contrary, at the unshielded side more noise is perceived than the isolated jets. This is a result of the pressure waves of the jet that are reflected from the plate to the far-field. These observations are in agreement with the current

state-of-the-art in the literature [20, 33, 52, 53, 64].

Lastly, for the jet from the lobed nozzle, it can be observed that along both sideline directions, the lobe orientation does not affect that far-field noise significantly. This is consistent with what was observed in the frequency-wavenumber spectra of the near-field measurements of this jet-plate configuration.

Between the jet from the lobed nozzle and the jet from the baseline nozzle, there are significant differences visible between the low-frequency hump. The jet from the lobed nozzle generates more noise in the frequency region left from the low-frequency peak than the jet from the baseline nozzle, whereas this is opposite for the frequency region on the right of the low-frequency peak. With these observations, it appears that the jet installation noise, indicated by the low-frequency hump, is shifted to a lower frequency for the jet from the lobed nozzle, with respect to the jet from the baseline nozzle.

This observation is consistent with what was found previously. From the frequency-wavenumber spectra of this jet-plate configuration, it was concluded that the jet from the lobed nozzles experiences a higher amount of energy in the hydrodynamic pressure waves up to a Strouhal number of 0.2. At higher Strouhal numbers, it was concluded that the jet from the baseline nozzle experiences more energy in the hydrodynamic pressure waves.

Moreover, from the frequency spectra of the HWA signals at a downstream distance of $x/D = 3$, it also became evident that the highest amount of energy in the shear flow of the jet from the lobed nozzle is located in a lower frequency region than for the jet from the baseline nozzle.

Another reason for the larger amount of scattering in noise at the trailing-edge by the lobed nozzle could be attributed to the larger spreading rate of the jet from the lobed nozzle. As already presented previously, the TI development shown in Figure 6.6a evidences a significant difference in the jet spreading when comparing the jets from CN1 and from LB2. Do note that for this analysis the centreline is located at y/D = 0. In reality, the part of the shear flow originated from a lobe peak is located at approximately $0.7 - 0.75 \, y/D$ instead of at $0.5 \, y/D$, as for the jet from the baseline nozzle. This can be observed in Figure 6.6b where the distance between the lobe peaks and the plate is smaller than between the lipline of CN1 and the plate. Hence, it is expected that for such a installed jet configuration part of the shear layer of the lobed nozzles hits the plate surface before reaching the trailing-edge at 3 diameters downstream from the nozzle exit. As a consequence, a boundary layer is formed at the surface of the plate, which is scattered at the trailing-edge, generating even more jet installation noise.

(a) Turbulence intensity development of CN1 and LB2.

(b) Nozzle exit profile of CN1 and LB2 with a flat plate in proximity.
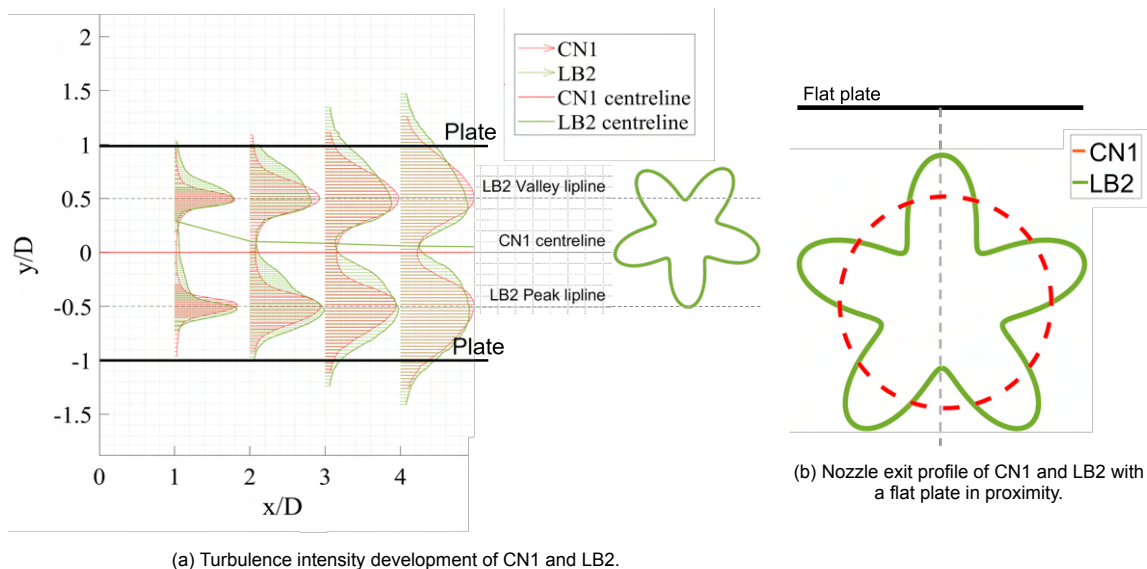
Figure 6.6: Comparison between the baseline nozzle (CN1) and the lobed nozzle 2 (LB2) with respect to the turbulence intensity in their jet and the installed configurations.

In the high-frequency region, it appears that at the shielded side of the configuration, the jet from LB2 is blocked more effectively than the jet from CN1. The spectra of the jet from LB2 either collapses

with the spectra of the jet from CN1 or it is located at a slightly lower amplitude (see Figure 6.5a). Taking into account the previous observation for the isolated jets that showed that the jet from LB2 results in a higher noise level in this high-frequency region, gives additional evidence that the jet from LB2 is blocked more effectively than the jet from CN1. This could be attributed to the fact that a larger part of the jet from LB2 is positioned farther away from the plate than the jet from the baseline nozzle, as can be visualised using Figure 6.6b. As a consequence, the amplitude of a large part of the near-field pressure waves has decayed more when it reaches the plate, than for the jet from the baseline nozzle. The pressure waves with a lower amplitude will be more effectively blocked than the stronger pressure waves.

At the unshielded side, it can be observed that the jet from the lobed nozzle generates more far-field noise in the high-frequency region than the jet from the baseline nozzle. This difference could be attributed to the difference in reflection of the pressure waves by the flat plate surface. However, from the isolated jets it was observed that the jet from the lobed nozzle results in higher noise levels in the high-frequency region, as there are more small-scale structures in the jet than in the jet from the baseline nozzle. Examining the difference in spectra between the isolated jets and the installed jets from CN1 and LB2, as shown in Figure 6.7 shows no significant difference in the high-frequency region. For the jets from both nozzles, a similar average increase in noise can be observed in the high-frequency region. Hence, the difference in high-frequency noise between the installed jets is caused by the difference in jet noise.
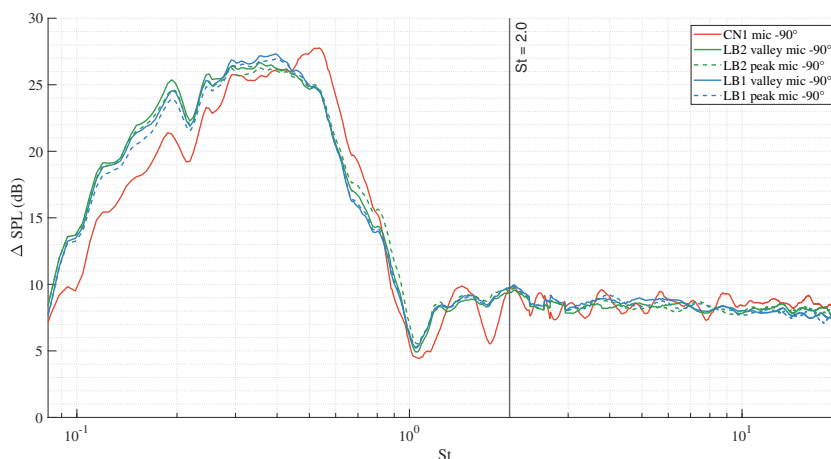
Figure 6.7: Difference in Sound-Pressure Level (SPL) between the installed and isolated nozzle configurations, measured along the sideline direction at the unshielded side.

The perceived far-field noise of the jet from LB1 is similar to what was observed for the jet from LB2. This can be observed for the unshielded side in Figure 6.7. Moreover, comparing the difference between the jet from LB1 and the jet from LB2 with the jet from CN1 shows similar values for both nozzles, as shown in Figure B.19 in Appendix B. The jet from LB1 presents slightly smaller differences with the jet from CN1 than for the jet from LB2. Nevertheless, this difference between the jets from the two lobed nozzles appears insignificant. This is consistent with what was observed in the frequency-wavenumber spectra from the near-field pressure measurement. Hence, it can be concluded that the higher lobe penetration of LB2 does not result in significant differences in the far-field noise with respect to the smaller lobe penetration of LB1.

6.2.2. Effect of Installed Configuration on Jet Installation Noise
The generated jet installation noise is dependent on the distances L and H. This subsection will present the spectra of additional jet-plate configurations, with varying L and H values. This is done as a method of verifying the measurements with the literature, and to gain insights into the acoustic performance of the difference jets when a plate is installed. Only the spectra at the unshielded side will be presented, as the largest low-frequency hump occurs at this side.

The spectra of the different installed configurations, at the unshielded side, is shown in Figure 6.8.

In the left plot, the spectra for the configurations with a separation distance H of $1D$ is shown, and thus also the previous analysed jet-plate configuration. The other configuration shown, consists of a lower streamwise distance L, namely a distance of $2D$ instead of $3D$.

It can be observed that decreasing the distance L results in a smaller low-frequency hump, which also shifts to a higher frequency region. This is consistent with what was found in literature [20, 34, 52, 53]. The shift to a higher frequency can be attributed to the turbulence development of the different jets. From the HWA analysis it could be concluded that the turbulent scales grow when convected downstream, and thus moving the trailing-edge upstream results in noise radiation at higher frequencies as the turbulent scales have grown less. Moreover, moving the trailing-edge upstream increases the distance between the shear layers of the jet and the plate. From the near-field pressure measurements it could be concluded that the amplitude of the hydrodynamic pressure waves decay rapidly over radial distance from the jet. Hence, moving the trailing-edge upstream results in scattering of less strong hydrodynamic pressure waves.
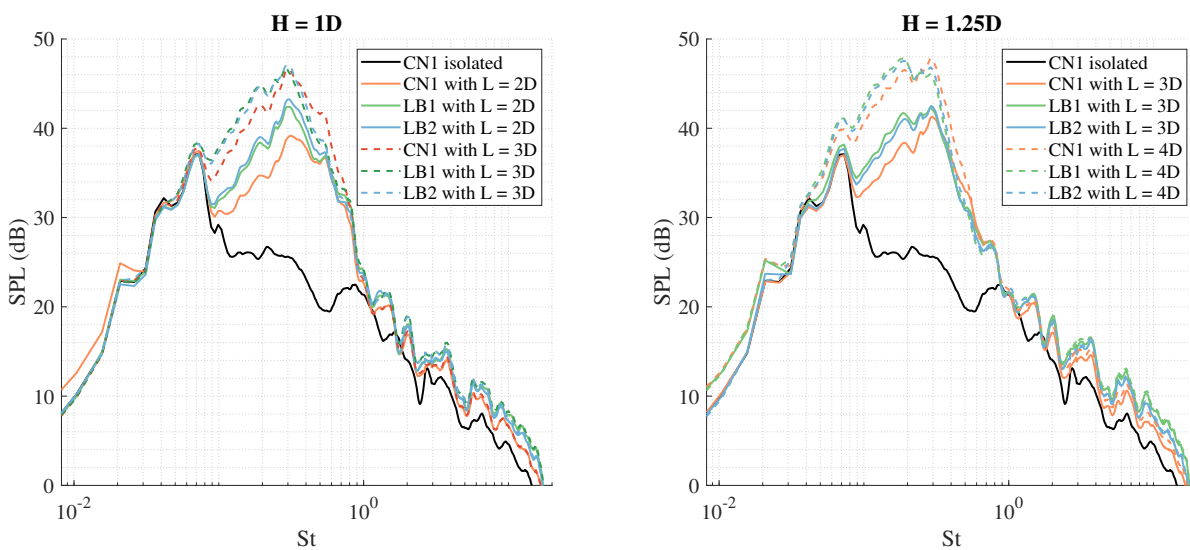
Figure 6.8: Sound-Pressure Level (SPL) of the installed nozzles with varying flat plate lengths L, measured along the sideline direction at the unshielded side. On the left, two installed configurations with a separation distance of $1.25D$ is presented. On the right, the installed configurations with a separation distance of $1D$ is presented.

In the right plot of Figure 6.8, the spectra for the configurations with a larger separation distance H, and a varying distance L, are shown. It can be observed that for this separation distance, the same effects can be observed. Increasing the streamwise distance L results in a significantly larger low-frequency hump.

Moreover, for both plots shown in Figure 6.8, it can be observed that positioning the trailing-edge more downstream with respect to the nozzle exit, will result in a smaller differences in generated jet installation noise between the different jets. This could be attributed to the enhancement of the turbulence development for the jet from the lobed nozzles, which results in a lower amount of large-scale structures in the jet than for the jet from the baseline nozzle. From the frequency spectra of the HWA measurement it became evident that the jet from LB2 start to become significantly more multiscale than the jet from CN1 after five diameters downstream of the nozzle exit. The jet from the baseline nozzle showed a significant amount of large-scale structures up to eight diameters downstream of the nozzle exit. As a consequence, it is expected that if the trailing-edge is positioned at a downstream distance of $5D$ or larger, the jet from LB2 will experience significantly less scattering of pressure waves at the trailing-edge than the jet from CN1. Thus, it is also expected that the jet from CN1 will generate a larger low-frequency hump for such an installed configuration.

From the experimental study of Lyu and Dowling (2019) it was found that for a nozzle similar to LB1, a separation distance of $1.25D$ and a streamwise distance of $4D$, will result in less jet installation noise for the jet from the lobed nozzle than for the jet from the baseline nozzle [37]. This is in contradiction with what can be observed in the right plot in Figure 6.8. This can be attributed to the jet exit velocity used during the experiments. In the study from Lyu and Dowling a jet Mach number of 0.5 and 0.7 was

used, which is significantly larger than the jet exit velocity of $60\ m/s$ (i.e. $M \approx 0.17$) used for the experiment conducted for this work. With the larger jet exit velocity, the jet spreading rate is smaller and thus the distance between the plate and the jet increases for increasing jet exit velocities. Hence, this might prevent grazing of the lobed jets on the plate surface, which significantly reduces the low-frequency jet installation noise generated by the lobed jet and thus also could result in a better acoustic performance than the baseline jet.

Secondly, the spectra of the two configurations with a different separation distance H, but with same streamwise distance L, are shown in Figure 6.9. It can be observed that increasing the separation distance results in a smaller low-frequency hump. This can be attributed to the larger decay of the hydrodynamic pressure waves that occur for a larger radial distance from the shear flow of the jet. Subsequently, the scattered hydrodynamic pressure waves at the trailing-edge are of smaller strength, and thus the generate far-field noise is less.

In addition, it can be observed that for a larger separation distance the low-frequency region of the hump extends to higher frequencies. This can be clearly observed by comparing the change in the frequency region left from the low-frequency peak, and the change at the frequencies higher than the low-frequency peak.

Both observation are consistent with what was found in literature.
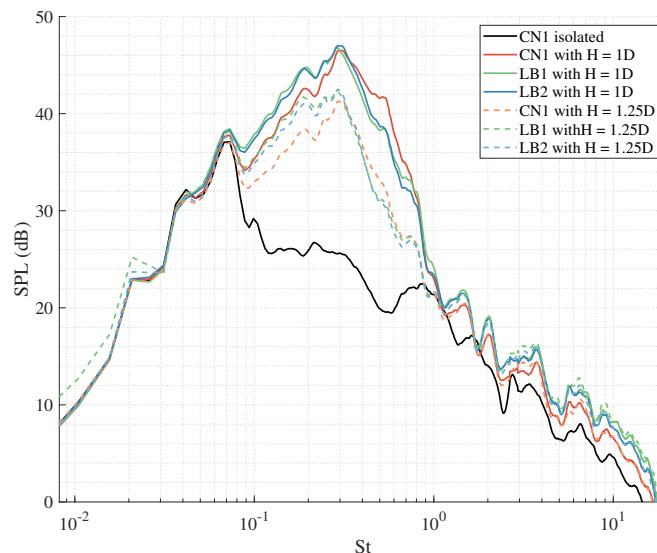
Figure 6.9: Sound-Pressure Level (SPL) of the installed nozzles for a configuration with a flat plate length of three diameters and with varying separation distances H, measured along the sideline direction at the unshielded side.

At the shielded side, the same observations could be made as for the unshielded side. The spectra for the different installed configurations at the shielded side, can be found in Figure B.20 and Figure B.21 in Appendix B.

All in all, it can be concluded that the observed jet installation noise is observed with the same trends as shown in the literature. Moreover, it was found that the jets from the lobed nozzles experience a larger low-frequency hump compared to the baseline nozzle. At the unshielded side it could be observed that the lobed jets radiate more high-frequency noise due to the jet mixing noise. On the contrary, at the shielded side the baseline jet radiates more high-frequency noise to the far-field, meaning that for the lobed jets the plate is more effective in blocking the jet flow noise. This can be attributed to the scale content of the jets from the lobed nozzles.

7

Conclusion

In this chapter the conclusions of this are summarized. These are presented in the form of answering the main research questions that were introduced in chapter 1.

1. How does the lobed nozzle affect the flow development downstream of the nozzle, compared to the jet from the conventional circular nozzle?

From the HWA measurements it could be observed that the jet from the lobed nozzles is initially asymmetric and experiences a larger average width than the symmetric jet from the baseline nozzle. Downstream of the nozzle exit, the annular lobed shear layer of the jet from the lobed nozzles experiences an enhancement in turbulence development with respect to what was observed in the jet from the baseline nozzle. This is induced by the secondary flow associated with the absence of axisymmetry. The enhanced flow development is observed by the fast growing shear layer of the lobed jet, and simultaneously a fast decay in the width of the laminar potential core with respect to the jet from the baseline nozzle. As a consequence, it has been observed that the potential core length is smaller for the jet from the lobed nozzle, whereas the spreading rate is larger for the lobed jet.

After the initial development region, after approximately six diameters downstream of the nozzle exit, the three jets behave similarly. The jet from the lobed nozzle experiences a more axisymmetric structure from this point onwards. It could be observed that the jet from the baseline nozzle develops more rapidly turbulence in this downstream region. This could be attributed to the development of the lobed jet. In literature it was found that a lobed jet deforms into a circular jet with pinched-off structures. The formed circular jet is obtained by the connection of the lobe valleys of the shear flow. If this happens in the lobed jet, the formed circular jet will have a significantly smaller width than for the jet from the baseline nozzle. This could explain the slower flow development for the jet from the lobed nozzles in the transitional region of the jet.

In addition, from the frequency spectra it could be observed that both jets are initially dominated by large-scale structures, which grow when propagated downstream. For the baseline jet, the large-scale structure dominate up to eight diameters downstream from the nozzle exit, whereas for the lobed jet the dominance of the large-scale structures has disappeared already at five diameters downstream from the nozzle exit. As a consequence, it can be concluded that the lobed jet is more mutliscale than the baseline jet.

Moreover, from the near-field pressure measurements a distinction could be made between the different characteristics of the pressure waves in the near-fields of the jets. For the hydrodynamic pressure waves at very low Strouhal numbers it could be observed that the convection velocity is larger for the baseline jet with respect to the lobed jet. However, at higher Strouhal numbers it appears that the convection velocity of the hydrodynamic pressure waves is larger for the lobed jet.

Farther away from the jet, the intensity of the hydrodynamic pressure waves decayed significantly. For the largest radial distance from the jet, it could be observed that the intensity of the hydrodynamic pressure waves was larger for the lobed jet than. On the contrary, it could be observed that the baseline

jet experiences a higher intensity of acoustic pressure waves at lower Strouhal numbers, whereas the lobed jet experiences a higher intensity at higher Strouhal numbers.

2. How does the lobed nozzle affect the overall radiated noise compared to the conventional circular nozzle?

The far-field microphone measurements showed that the jets from the lobed nozzles generate different far-field acoustics than the jet from the baseline nozzle. The jet from the lobed nozzle generates less far-field noise in the low-frequency region, but more far-field noise in the high-frequency region, compared to the jet from the baseline nozzle. The difference in the low-frequency region was more evident at lower polar angles, which could be attributed to the fact that the large-scale structures are dominant at shallow polar angles. On the contrary, the difference in the high-frequency region was more evident along the sideline directions, which could be attributed to the dominance of the noise radiation from small-scale structures to the sideline directions.

On top of that, it could be observed along the sideline directions that the spectra of the different jets are shifted in the frequency domain, with respect to each other. This could be attributed to the difference in convection velocity of the pressure waves. It is expected that an increase in convection velocity increases the convected eddies per second, and subsequently a noise radiation to higher frequencies. Using the convection velocity for the non-dimensional frequency (i.e. the Strouhal number), instead of the jet exit velocity, showed that parts of the spectra collapsed, which strengthens the hypothesis on the effect of the convection velocity on the far-field noise.

3. How does the lobed nozzle affect the jet installation noise generated when a flat plate is placed close to the jet?

The jet from the lobed nozzles generates more far-field noise at frequencies lower than the low-frequency peak. On the contrary, the jet from the baseline nozzle generates more low-frequency noise at frequencies higher than the low-frequency peak. From the near-field pressure measurements it could be observed that a higher intensity of hydrodynamic pressure waves occur at very low frequencies for the lobed jet, whereas this is vice versa at higher frequencies in the low-frequency domain. Hence, the difference in the low-frequency far-field noise can be attributed to the difference in scattering of the hydrodynamic pressure waves at the trailing-edge of the plate.

In the high-frequency region differences could be observed between the shielded and unshielded sides. At the shielded side it could be observed that the jet from the baseline nozzle results in more far-field noise, and thus the flat plate is more effective in blocking the jet noise in case of the jets from the lobed nozzles. On the contrary, at the unshielded side it can be observed that the lobed nozzles result in more far-field noise. This is attributed to the larger amount of energy contained at the small-scales in the jet from lobed nozzles compared to the baseline jet.

Moreover, it has been found that the specific flat-plate configuration has a significant effect on the differences between the generation of jet installation noise, in particular the distance between the nozzle and the trailing-edge of the plate. For increasing the streamwise distance to five-six diameters, it is believed that the jet from the baseline nozzle results in a larger amount of jet installation noise. This is believed with the aforementioned observation that the lobed nozzles exhaust a jet that develops into a multiscale flow at five to six diameters downstream of the nozzle exit, whereas the jet of the baseline nozzle is dominated by large-scale structures up to eight diameters downstream of the nozzle exit.

<div align="right">

8

</div>
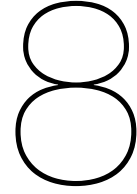
Discussion and Recommendations

In this chapter the recommendations for future work will be given. Firstly, recommendations will be giving regarding additional measurements that can be done to gain insights into the physical phenomena that occur in the jets. Moreover, a recommendation on the experimental conditions will be done. Lastly, a recommendation will be done for the use of a lobed nozzle in future work.

8.1. Additional measurements

From the analyses and the available literature, it is expected that the jet from the lobed nozzle experiences a lobed shear layer [21, 23]. When the jet is convected downstream, it is expected that the peaks of the lobed shear layer are pinched-off, and subsequently that the remaining shear layer forms an annular shear layer. For future work it will be valuable to analyse with Particle Image Velocimetry (PIV) whether the expected behaviour of the jet occurs or not. Moreover, it will give a better insight into the asymmetry of the lobed flow, as well as the behaviour of the large-scale and small-scale structures in the flow.

This work showed an asymmetry of the jet from the lobed nozzles with the HWA and the near-field pressure measurements. It is recommended for future work to map the asymmetry in azimuthal direction around the jet, such that the opportunity exists to analyse the azimuthal modes of the hydrodynamic pressure waves. This will give the opportunity to verify the temporal stability analysis done by Lyu and Dowling [39].

It is also recommended to conduct measurements that are aimed at characterizing the decay of the hydrodynamic pressure waves. This will give insights into the intensity of the hydrodynamic pressure waves that are scattered at the trailing-edge. For this, it is required to conduct pressure measurements at different known distance from the shear layer of the jet.

Regarding the far-field pressure measurements, it is recommended to do a directivity analysis. This will give better insights into the difference in the sound sources.

It is recommended for future work to use a flow visualization technique to analyse whether grazing of the jet on the plate surface occurs for the analysed jet-plate configurations. This will give insights into the additional jet installation noise that might be generated by the scattering of a boundary layer at the trailing-edge.

In addition, it is expected that the lobed nozzle is effective in attenuating the jet installation noise with respect to the jet from the baseline nozzle, if a longer streamwise distance between the plate its trailing-edge and the nozzle exit is used. This is attributed to the fact that after five diameters downstream the jet from the lobed nozzles consists of a significantly lower amount of large-scale structures than for the jet from the baseline nozzle. In order to analyse whether this hypothesis is true, for future work it is recommended to verify this with nozzle-plate configurations with plate lengths of minimal five diameters.

Furthermore, in order to analyse whether the single-stream cold flow is representative to the real-life conditions, it is advised to also conduct a more complex experimental campaign. It is recommend to include a bypass flow into the test-setup in order to assess the effects of the interaction between the cold bypass flow and the hot core flow. Such a configuration will result in a shear layer between the ambient air and the cold bypass flow, as well as between the cold bypass flow and the hot core flow. For these two shear layers it is expected that the turbulent development differs and thus the development of the hydrodynamic pressure waves is expected to be different. It is expected that the convection velocities of the pressure waves in the outer shear layer will be significantly lower than for the single stream jets, as the jet velocity in the cold bypass flow is significantly smaller than the core flow.

Lastly, in the experimental campaign the thrust has not been included and is not considered. However, in order to analyse whether this passive method of attenuating jet installation noise could be a potential method to implement in turbofan engines, it is also required to assess whether a thrust performance difference occurs between the different nozzles. For future work it is recommended to gain insights into the thrust performance of lobed nozzles.

8.2. Effect of Jet Velocity

As the measurements has been done on scale with simulated conditions, it is valuable to assess to what extent the conclusions from the analysis hold for the real-life conditions. In order to do so, the effect of changing the jet exit velocity should be analysed.

Previous analyses has focused on the measurement done for a jet exit velocity of $60\ m/s$. As presented previously, near-field and far-field pressure measurements have also been done with a jet exit velocity of $50\ m/s$ and $70\ m/s$. In Figure 8.1 the difference in far-field noise the three jets for $60\ m/s$ and $70\ m/s$ is shown, of which the difference between the lobed nozzles and CN1 at $50\ m/s$ has been subtracted. The spectra shown are along the sideline directions for the jet-plate configuration with H equal to $1D$ and L equal to $3D$.

It can be observed that for the installed configurations, the difference in far-field noise between the jet from the lobed nozzles and the jet from the baseline nozzle increases for larger jet velocities. Regarding the jet installation noise, it can be observed that the left side of the low-frequency peak increases for an increasing jet velocity, for both the shielded and unshielded sides. This difference is stronger for the jet from LB2 than for the jet from LB1. The benefit in far-field noise for the jets from the lobed nozzles, at the right side of the low-frequency peak, shows an increase and a shift to a higher Strouhal number. This suggests that more or stronger large-scale structures are scattered at the trailing edge, but with a smaller size than for lower jet velocities.

In the high-frequency region, for Strouhal numbers higher than 1.0, it can be observed that the differences for varying jet exit velocity is significantly less than for the low-frequency hump.

All in all, from this preliminary analysis it can be concluded that the jet exit velocity does influence the difference between the jets. This should be taken into account in order to assess whether the lobed nozzle is effective in reducing jet installation noise.

8.3. Nozzle Geometry

In this work the lobe penetration rate differs between the two considered lobed nozzles. However, it has been observed that for the jet installation noise and the near-field pressure waves the difference between the jets from the two lobed nozzles is significantly less than between the jets from CN1 and LB1. Nevertheless, it has been observed that LB2, the nozzle with the largest lobe penetration, affects the flow more than LB1 with respect to the baseline nozzle. Hence, it is expected that the difference between the jets from LB2 and LB1 will be more significant for jet-plate configurations with a streamwise distance L larger than five diameters. Nevertheless, this still remains to be verified.

For future work it is recommended to analyse whether the used number of lobes and lobe penetration is optimal or not. This can be done with a parametric study using flow simulations or far-field noise measurements. Comparing lobed nozzles with different lobe penetrations and different number of lobes will lead to a complete characterisation of the aeroacoustic behaviour of lobed nozzles.
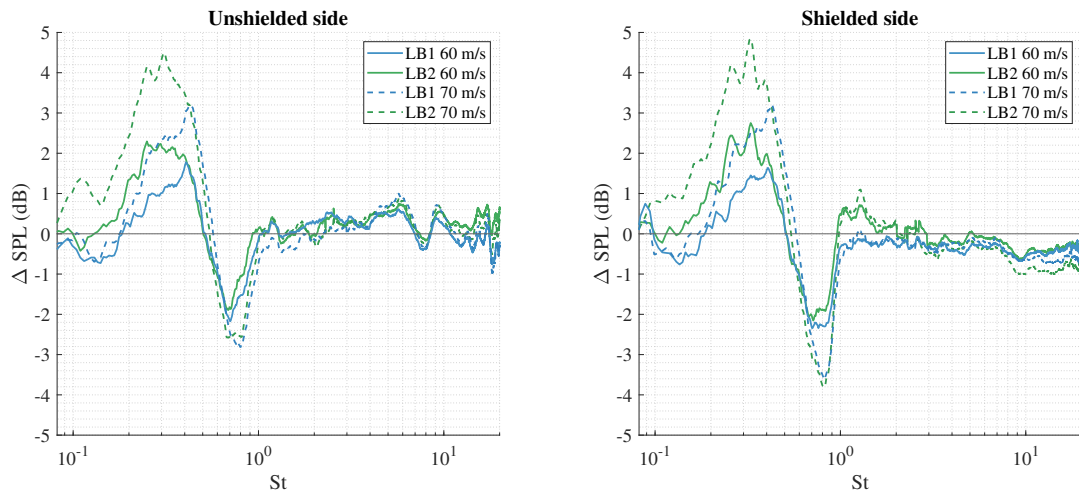
Figure 8.1: Difference in Sound-Pressure Level (SPL) along the sideline directions of the jets from the installed lobed nozzles with respect to the jet from the baseline nozzle for $60\ m/s$ and $70\ m/s$. The differences are subtracted by the difference observed between the installed lobed nozzles and the baseline nozzle at $50\ m/s$.

A
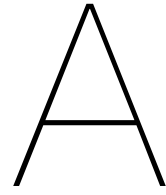
Appendix A

This appendix includes the CAD drawings of the three jet nozzles and the bottom piece of the the nozzles.

B

Appendix B

This Appendix included additional figures obtained from the different measurements. The additional results of the HWA measurements can be found in section B.1. Furthermore, the additional results of the near-field pressure measurements with the jet can be found in section B.2. Lastly, the additional results of the far-field pressure measurements can be found in section B.3.

B.1. HWA Results

B.1.1. Mean Velocity Development
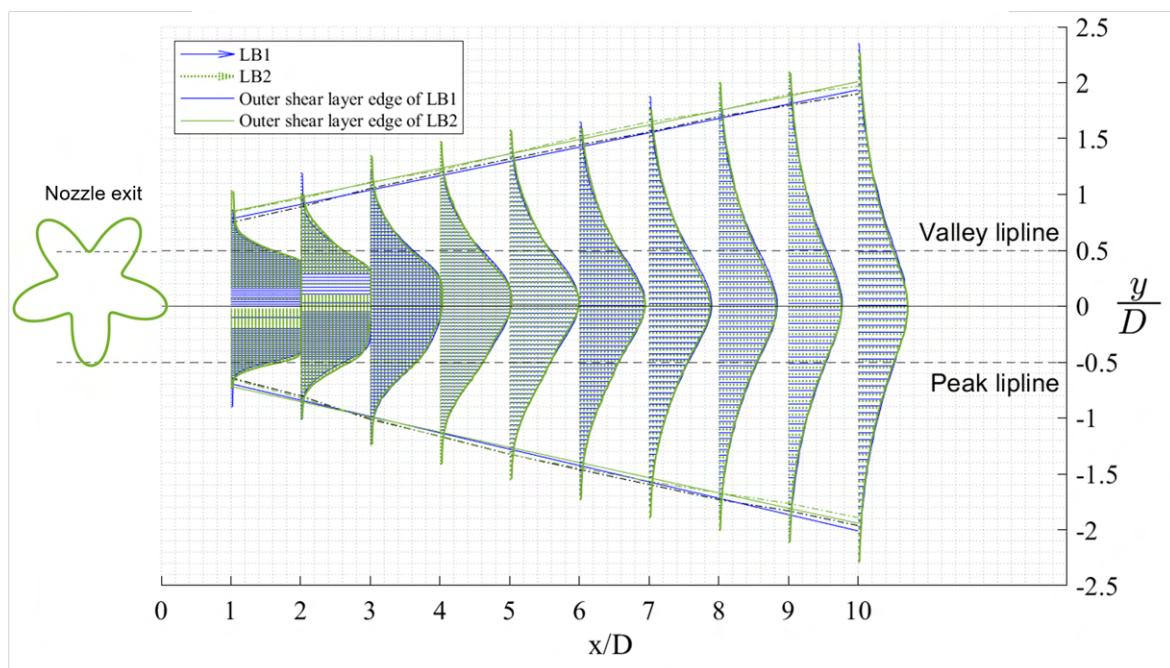
Figure B.1: Development of the mean velocity of the jet from the lobed nozzle 1 (LB1) and the lobed nozzle 2 (LB2).

B.1.2. Frequency Spectra

(a) CN1 at 1D

(b) LB2 at 1D

(c) CN1 at 2D

(d) LB2 at 2D

(e) CN1 at 3D

(f) LB2 at 3D

(g) CN1 at 4D

(h) LB2 at 4D
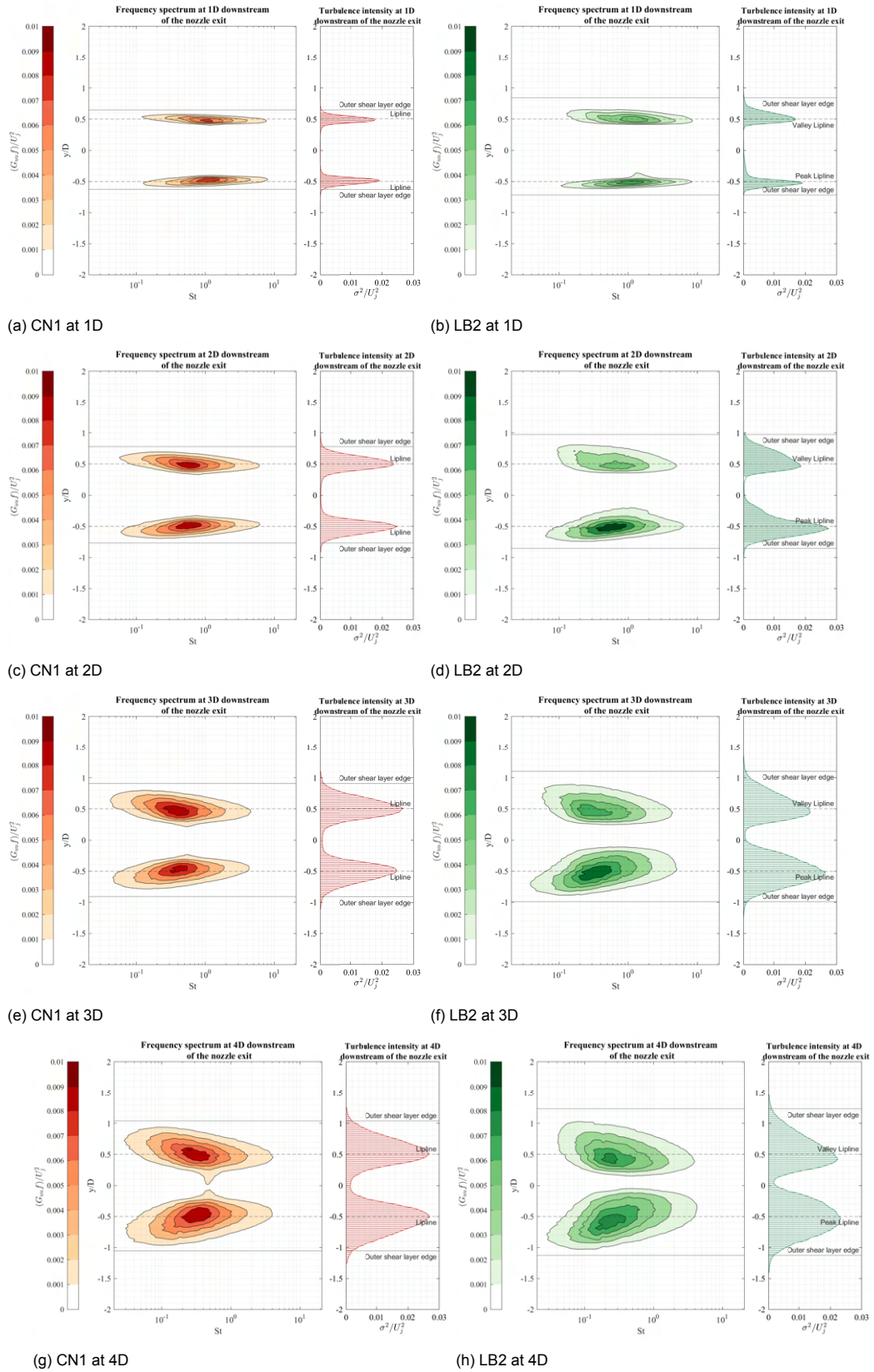
Figure B.2: Normalized energy frequency spectrum of the baseline nozzle (CN1) and lobed nozzle 2 (LB2) at two to four diameters downstream of the nozzle exit.

(a) CN1 at 5D

(b) LB2 at 5D

(c) CN1 at 6D

(d) LB2 at 6D

(e) CN1 at 7D

(f) LB2 at 7D

(g) CN1 at 8D

(h) LB2 at 8D
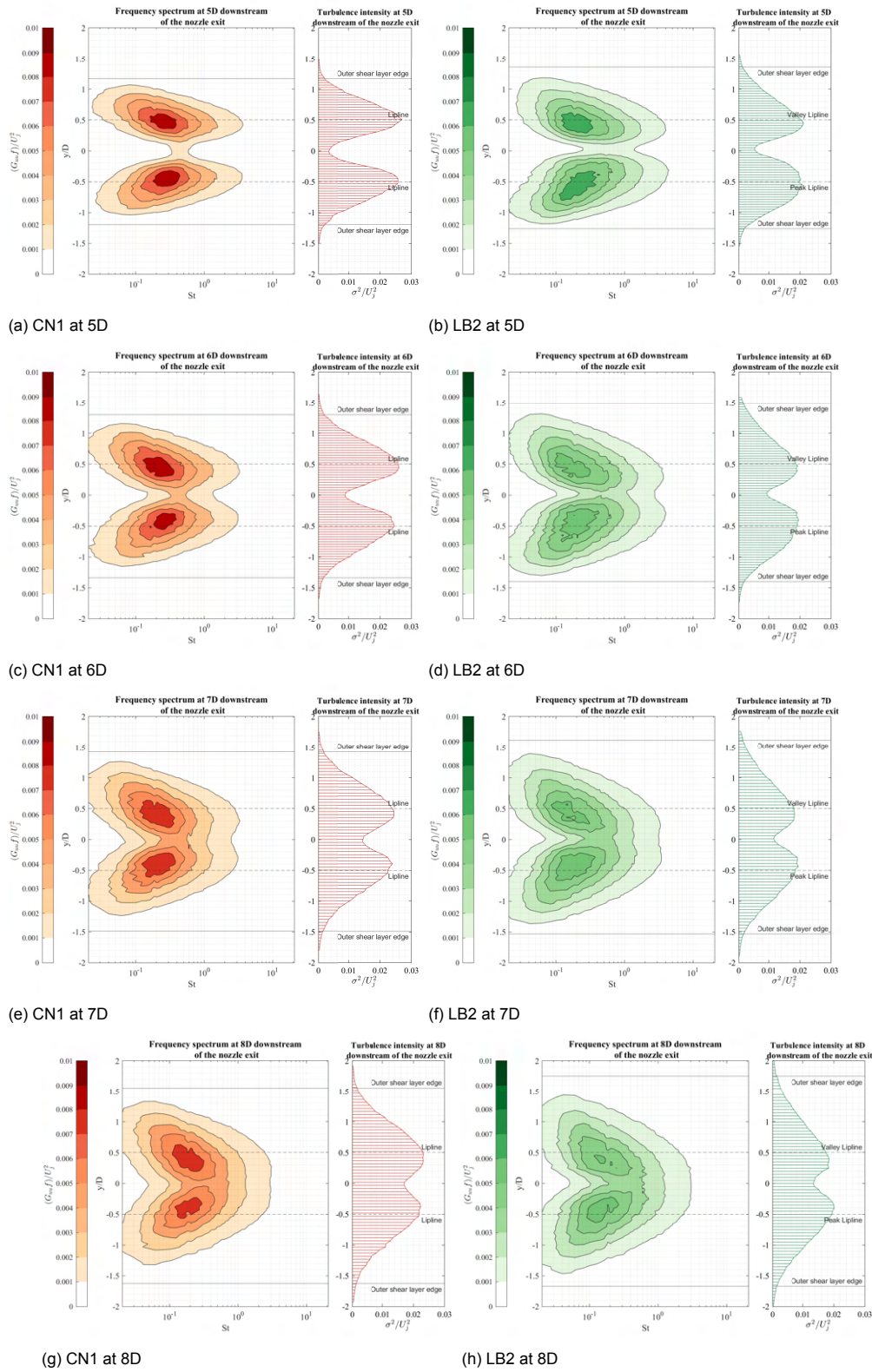
Figure B.3: Normalized energy frequency spectrum of the baseline nozzle (CN1) and lobed nozzle 2 (LB2) at five to eight diameters downstream of the nozzle exit.

(a) CN1 at 9D

(b) LB2 at 9D

(c) CN1 at 10D

(d) LB2 at 10D

(e) LB1 at 1D

(f) LB1 at 2D

(g) LB1 at 3D

(h) LB1 at 4D
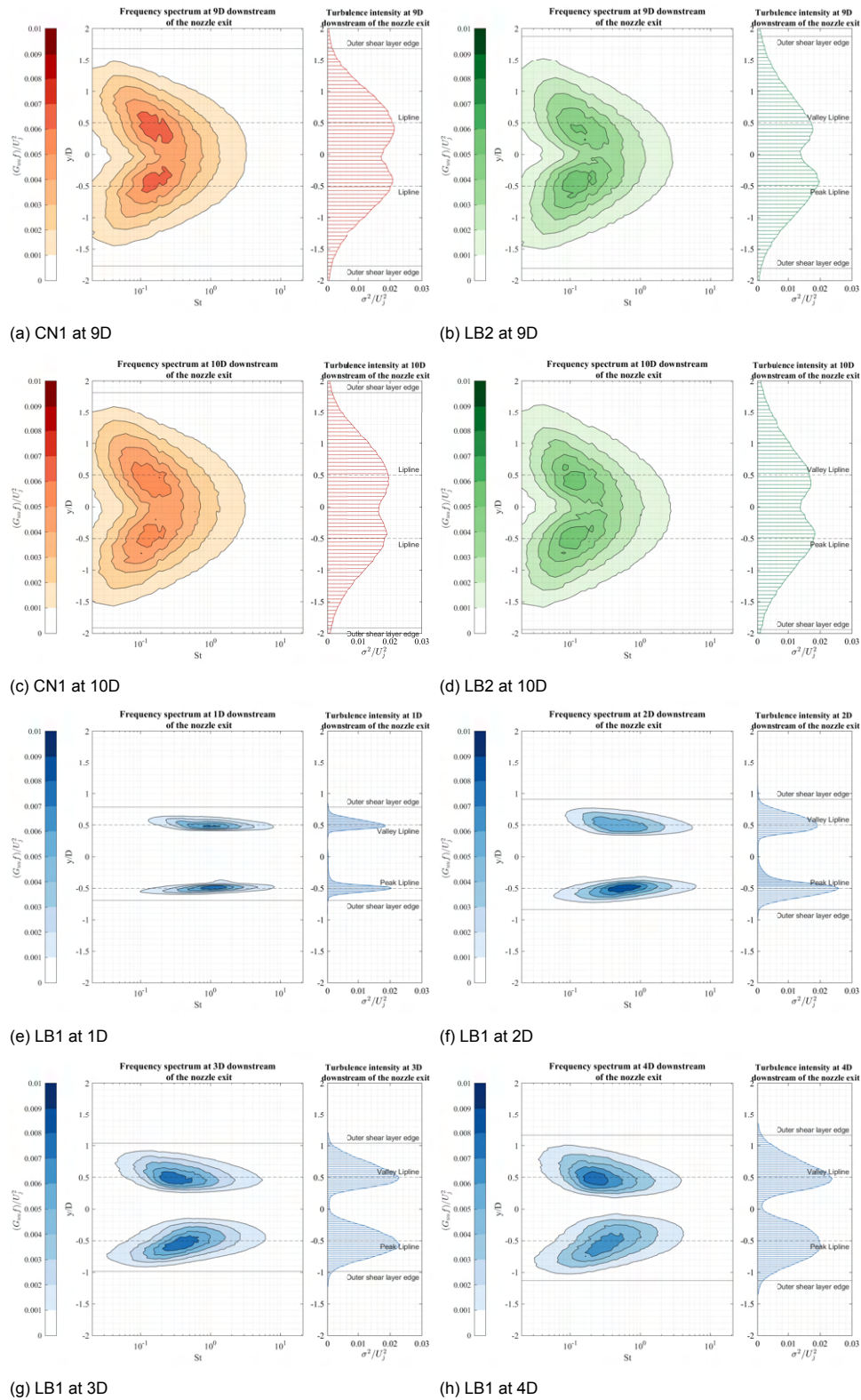
Figure B.4: Normalized energy frequency spectrum of the baseline nozzle (CN1) and lobed nozzle 2 (LB2) at nine and ten diameters downstream of the nozzle exit, as well as for lobed nozzle 1 (LB1) for one to four diameters downstream of the nozzle exit.

B.2. Near-field Pressure Measurements of the Jet

(a) LB1 at 5D

(b) LB1 at 6D

(c) LB1 at 7D

(d) LB1 at 8D

(e) LB1 at 9D

(f) LB1 at 10D
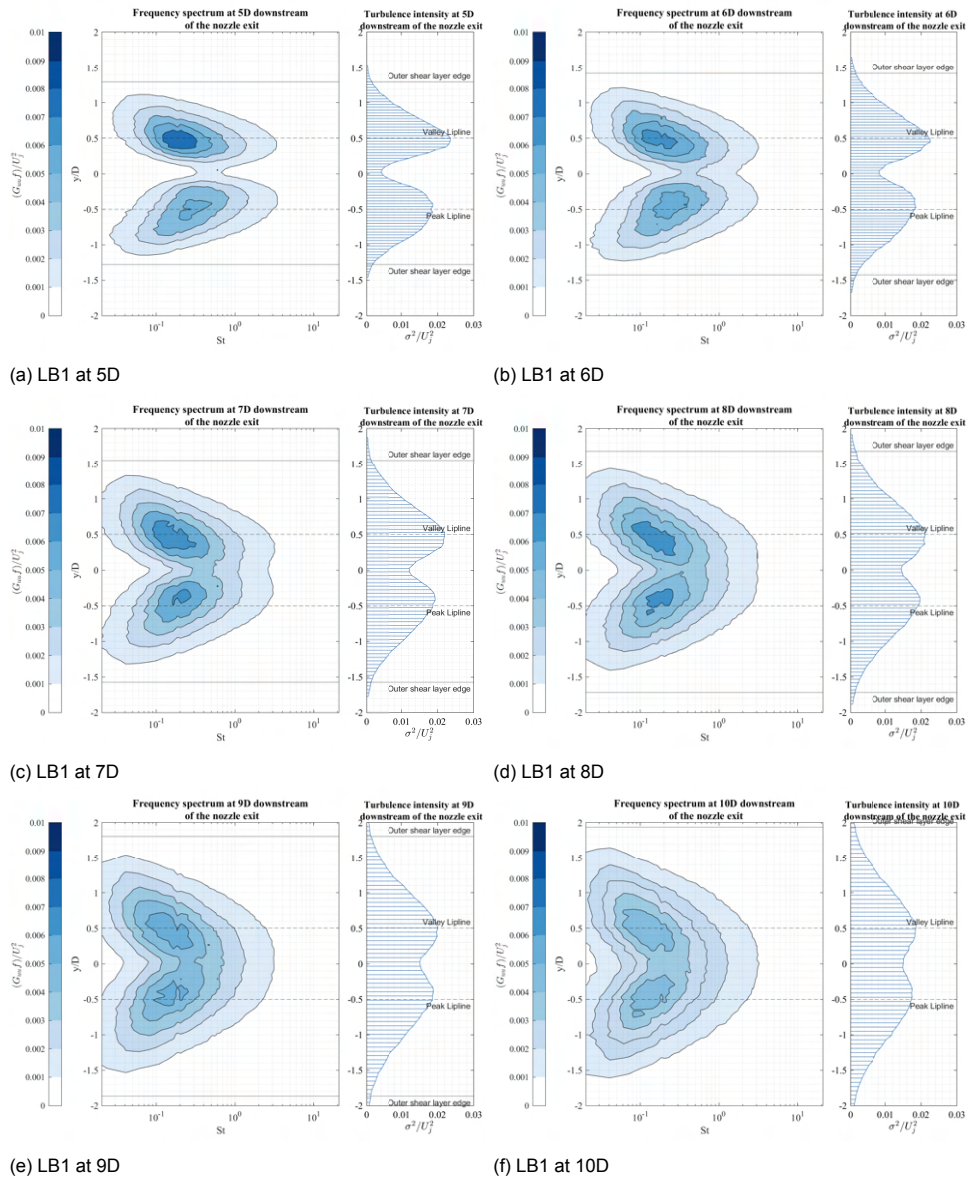
Figure B.5: Normalized energy frequency spectrum of the lobed nozzle 1 (LB1) at five to ten diameters downstream of the nozzle exit.

B.3. Far-field Acoustic Measurents of the Jet
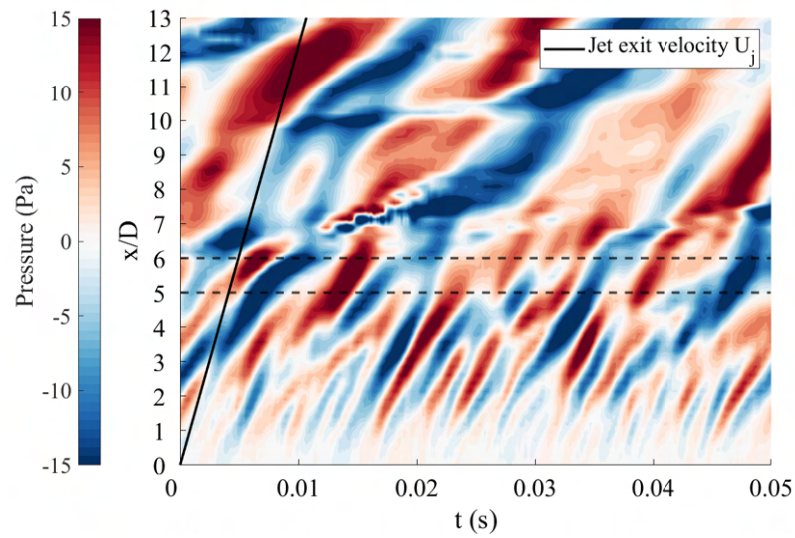
Figure B.6: Space time plot of a sample of the measurements done for the lobed nozzle 2 at $60\ m/s$ and with the linear array positioned at $25\ mm$ from the lipline. For this measurement, a lobe valley was directed towards the linear array.
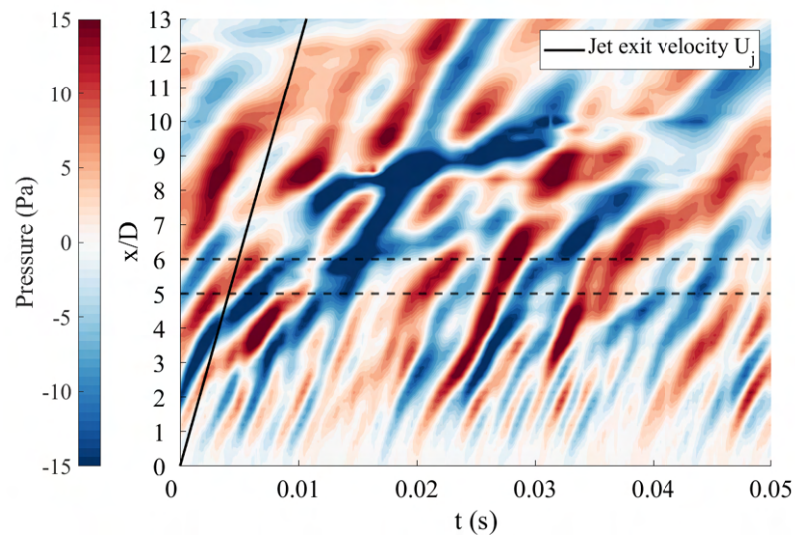
Figure B.7: Space time plot of a sample of the measurements done for the lobed nozzle 1 at $60\ m/s$ and with the linear array positioned at $25\ mm$ from the lipline. For this measurement, a lobe valley was directed towards the linear array.
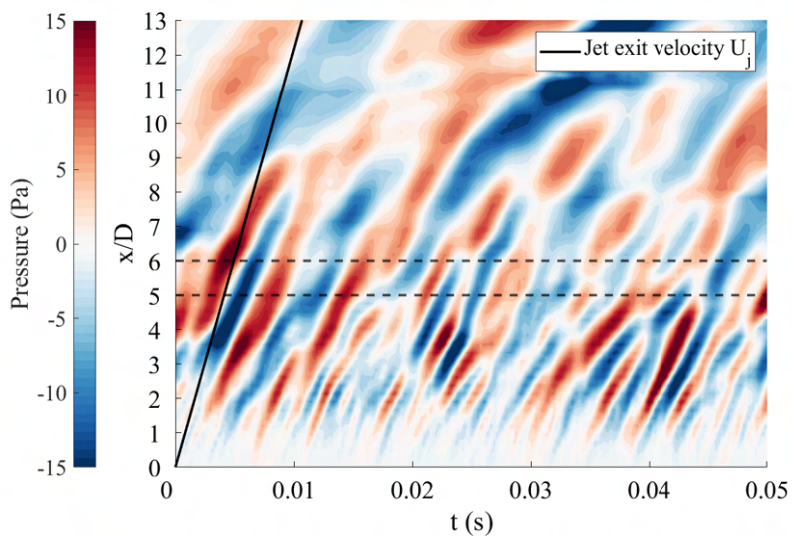
Figure B.8: Space time plot of a sample of the measurements done for the lobed nozzle 1 at $60\ m/s$ and with the linear array positioned at $25\ mm$ from the lipline. For this measurement, a lobe peak was directed towards the linear array.
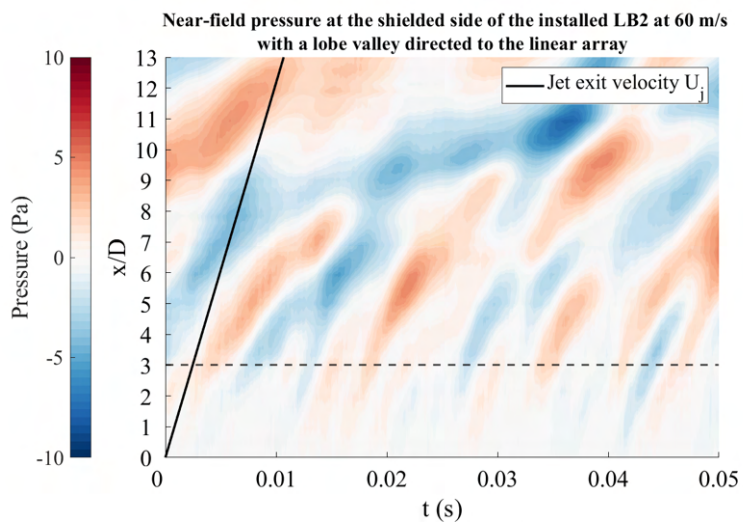
Figure B.9: Space time plot of a sample of the measurements done at the shielded side for the installed LB2 at $60\ m/s$ and with the linear array positioned at $75\ mm$ from the lipline. For this measurement a lobe valley is directed towards the flat plate.
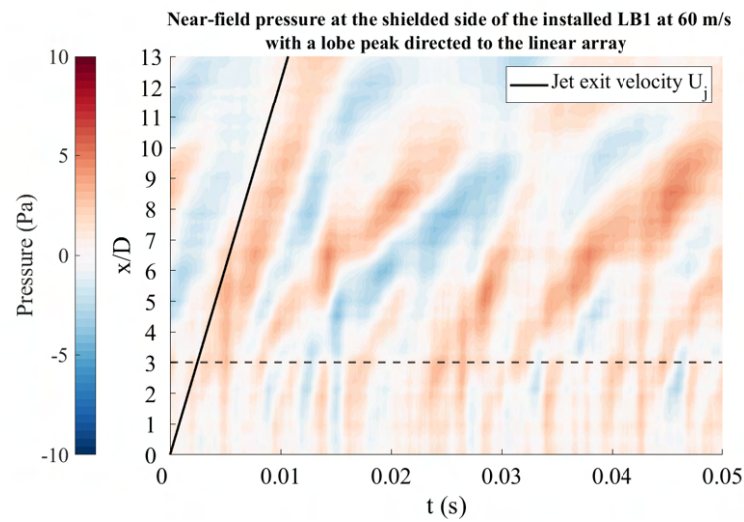
Figure B.10: Space time plot of a sample of the measurements done at the shielded side for the installed LB1 at $60\ m/s$ and with the linear array positioned at $75\ mm$ from the lipline. For this measurement a lobe peak is directed towards the flat plate.
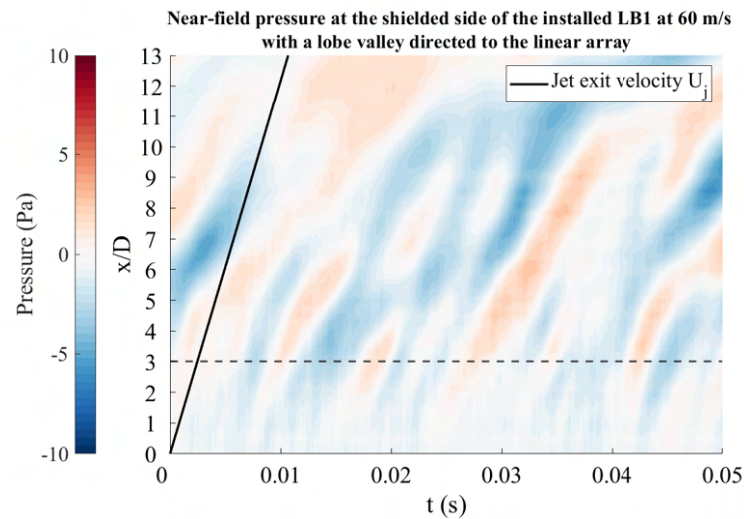
Figure B.11: Space time plot of a sample of the measurements done at the shielded side for the installed LB1 at $60\ m/s$ and with the linear array positioned at $75\ mm$ from the lipline. For this measurement a lobe valley is directed towards the flat plate.
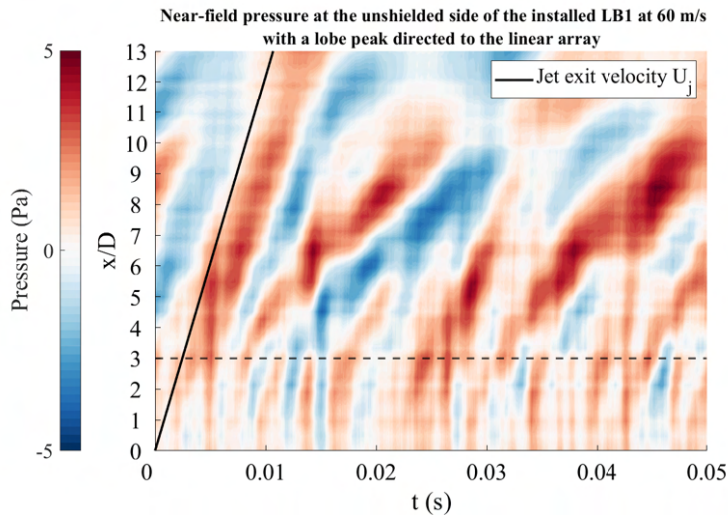
Figure B.12: Space time plot of a sample of the measurements done at the unshielded side for the installed LB1 at $60 \ m/s$ and with the linear array positioned at $75 \ mm$ from the lipline. For this measurement a lobe peak is directed towards the flat plate.
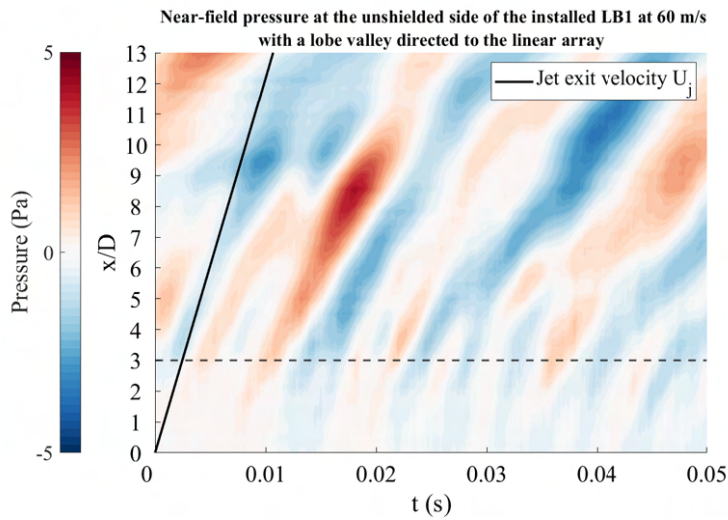
Figure B.13: Space time plot of a sample of the measurements done at the unshielded side for the installed LB1 at $60 \ m/s$ and with the linear array positioned at $75 \ mm$ from the lipline. For this measurement a lobe valley is directed towards the flat plate.

(a) Potential core region.

(b) Transitional region.
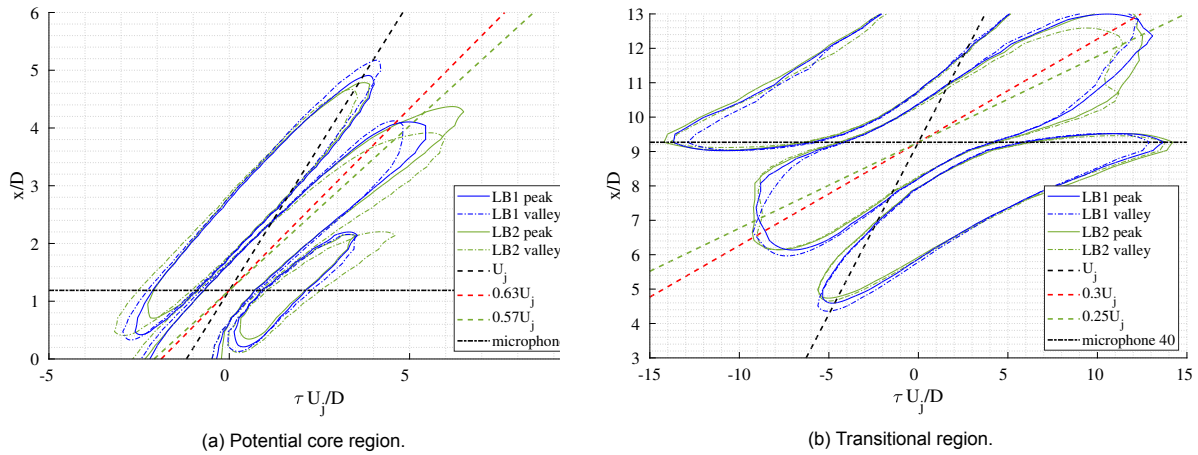
Figure B.14: Two-point cross-correlation with microphone 6 and 40 for the lobed nozzle 1 (LB1) and lobed nozzle 2 (LB2), while operating at a jet exit velocity of $60 \ m/s$.

**Wavenumber-frequency spectrum for LB1 and LB2 at 60 m/s
and with the linear array at a distance of 25 mm from the lipline of CN1**
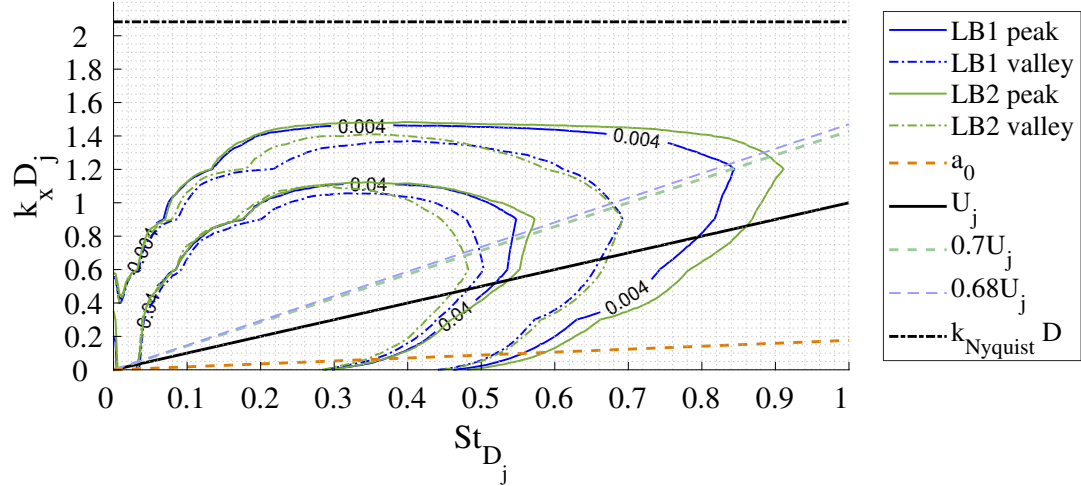
Figure B.15: Ensemble-averaged frequency-wavenumber spectrum for the first 14 microphone measurements of LB1 and LB2 at a jet exit velocity of 60 m/s and the linear array positioned 25 mm from the baseline lipline.

**Wavenumber-frequency spectrum for LB1 and LB2 at 60 m/s
and with the linear array at a distance of 25 mm from the lipline of CN1**
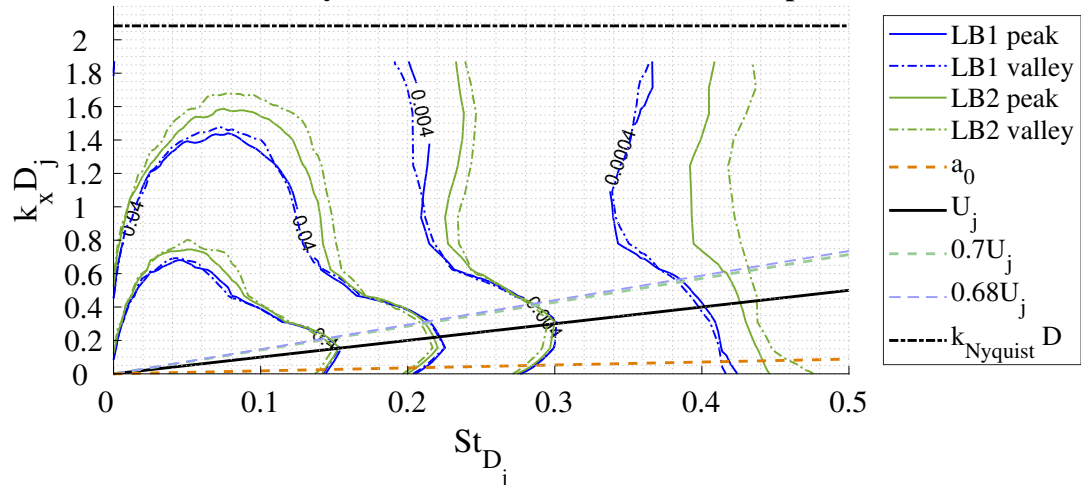
Figure B.16: Ensemble-averaged frequency-wavenumber spectrum for the microphone measurements 30 to 56 of LB1 and LB2 at a jet exit velocity of 60 m/s and the linear array positioned 25 mm from the baseline lipline.

Wavenumber-frequency spectrum at the shielded side for LB1 and LB2 at 60 m/s
and with the linear array at a distance of 75 mm from the lipline of CN1
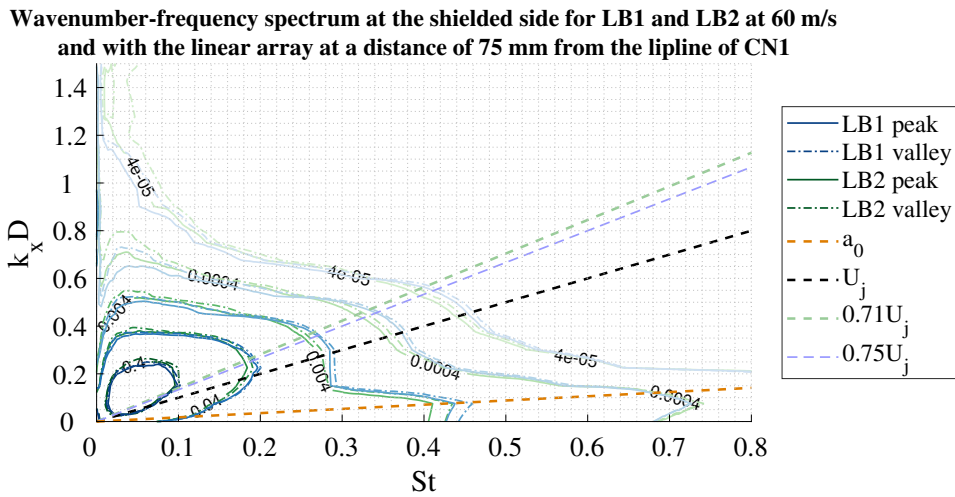
Figure B.17: Ensemble-averaged frequency-wavenumber spectrum for the entire linear array measurement at the shielded side of the installed LB1 and LB2 at a jet exit velocity of 60 m/s.

Wavenumber-frequency spectrum at the unshielded side for LB1 and LB2 at 60 m/s
and with the linear array at a distance of 75 mm from the lipline of CN1
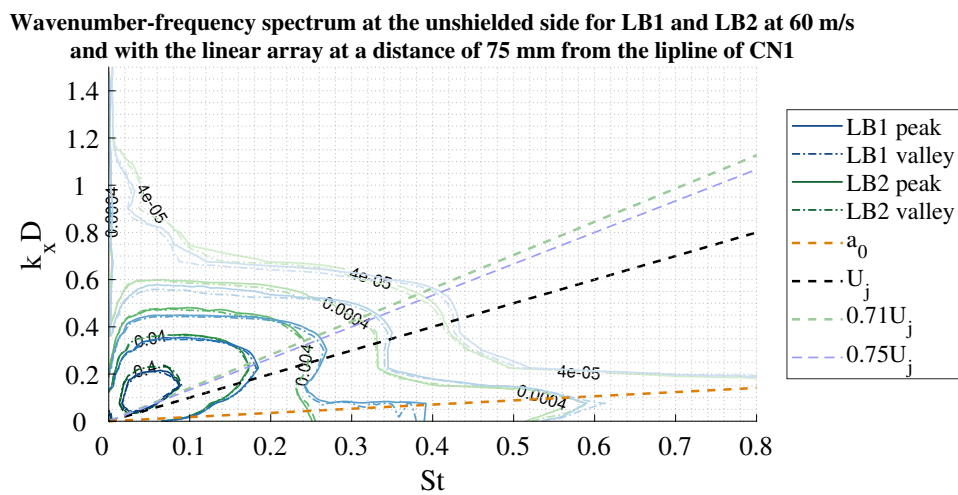
Figure B.18: Ensemble-averaged frequency-wavenumber spectrum for the entire linear array measurement at the unshielded side of the installed LB1 and LB2 at a jet exit velocity of 60 m/s.

Difference in Sound-Pressure Level at the unshielded side of the installed lobed nozzles with CN1
at a jet exit velocity of 60 m/s
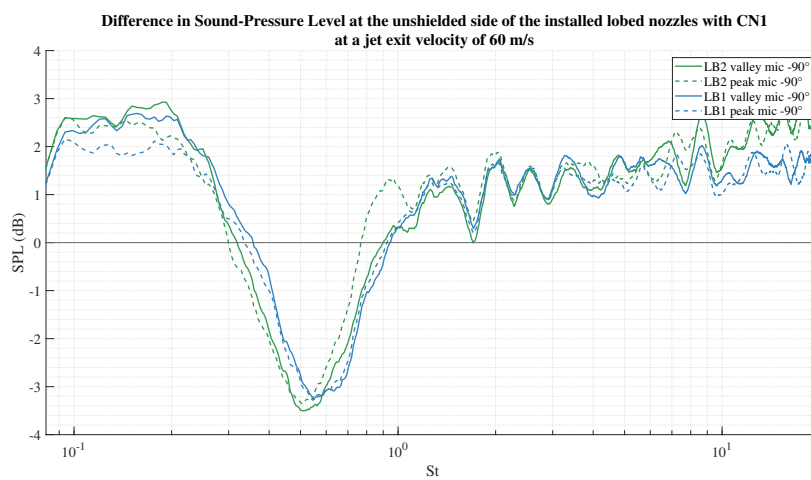
Figure B.19: Difference in Sound-Pressure Level (SPL) between the installed lobed nozzles with the installed CN1, measured along the sideline direction at the unshielded sideline.

Sound-Pressure Level of the installed nozzles
at a jet exit velocity of 60, m/s measured along the sideline direction at the shielded side
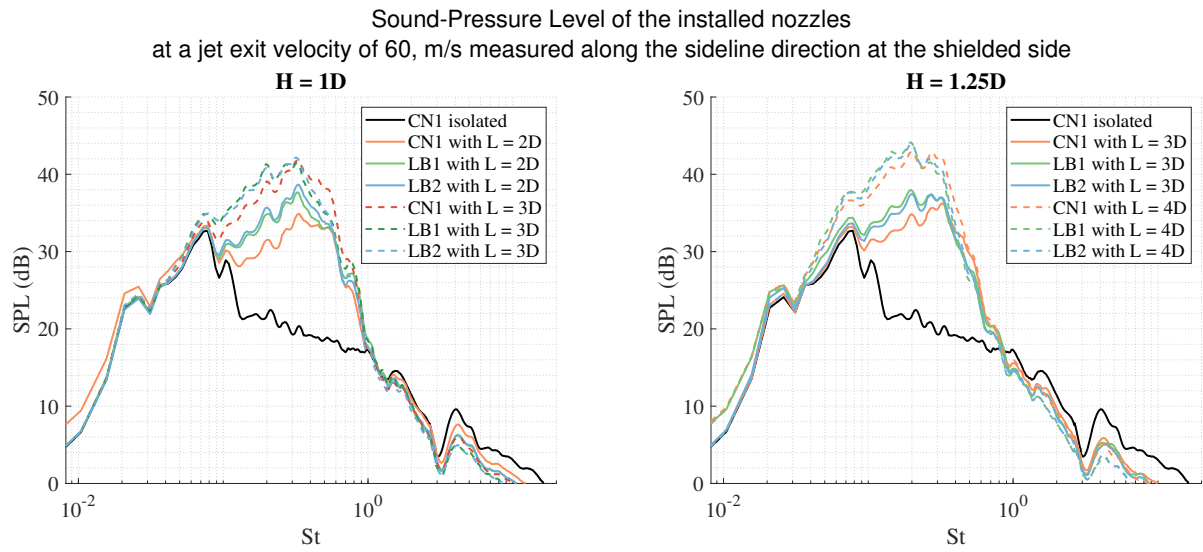
Figure B.20: Sound-Pressure Level (SPL) of the installed nozzles with varying flat plate lengths L, measured along the sideline direction at the shielded sideline. On the left two installed configurations with a separation distance of $1.25D$ is presented. On the right the installed configurations with a separation distance of $1D$ is presented.
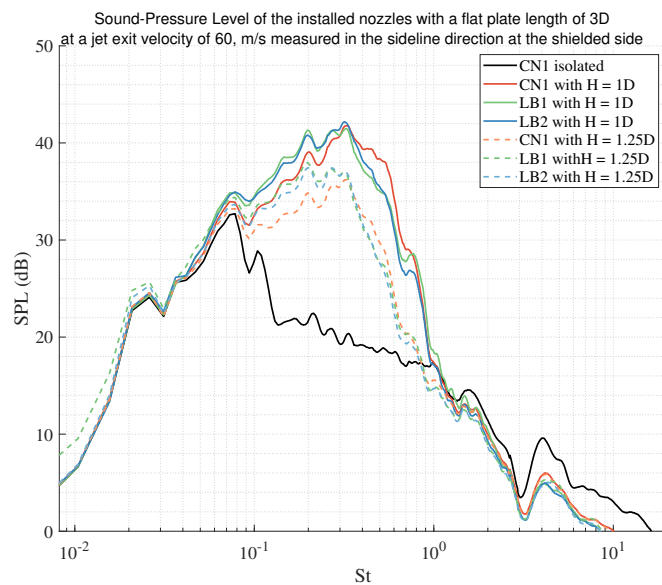
Figure B.21: Sound-Pressure Level (SPL) of the installed nozzles for a configuration with a flat plate length of three diameters and with varying separation distances H, measured along the sideline direction at the shielded sideline.

Bibliography

[1] R. E. A. Arndt, D. F. Long, and M. N. Glauser. "The proper orthogonal decomposition of pressure fluctuations surrounding a turbulent jet". In: *Journal of Fluid Mechanics* 340.(Ithaca, U.S.A.,: Aug. 7-9, 1985) (1997), pp. 1–33. ISSN: 0022-1120. DOI: `/10.1017/S0022112097005089`.

[2] Woutijn J. Baars, Charles E. Tinney, and Edward J. Powers. "POD based spectral higher-order stochastic estimation". In: *48th AIAA Aerospace Sciences Meeting Including the New Horizons Forum and Aerospace Exposition* January (2010). DOI: `10.2514/6.2010-1292`.

[3] L. P. Bastos, C. J. Deschamps, and A. R. da Silva. "Experimental investigation of the far-field noise due to jet-surface interaction combined with a chevron nozzle". In: *Applied Acoustics* 127 (2017), pp. 240–249. ISSN: 1872910X. DOI: `10.1016/j.apacoust.2017.06.008`.

[4] M. Bondarenko, Z. Hu, and X. Zhang. "Large-eddy simulation of the interaction of a jet with a wing". In: *18th AIAA/CEAS Aeroacoustics Conference (33rd AIAA Aeroacoustics Conference)* June (2012), pp. 4–6. DOI: `10.2514/6.2012-2254`.

[5] G. A. Brès et al. "Importance of the nozzle-exit boundary-layer state in subsonic turbulent jets". In: *Journal of Fluid Mechanics* 851 (2018), pp. 83–124. ISSN: 14697645. DOI: `10.1017/jfm.2018.476`.

[6] J. R. Brinkerhoff, H. Oria, and M. I. Yaras. "Experimental and computational study of mixing mechanisms in an axisymmetric lobed mixer". In: *Journal of Propulsion and Power* 29.5 (2013), pp. 1017–1030. ISSN: 15333876. DOI: `10.2514/1.B34601`.

[7] K. Bushell. "Measurement and prediction of jet noise in flight". In: *2nd Aeroacoustics Conference*. Reston, Virigina: American Institute of Aeronautics and Astronautics, Mar. 1975. DOI: `10.2514/6.1975-461`. URL: `http://arc.aiaa.org/doi/10.2514/6.1975-461`.

[8] O. P. Bychkov and G. A. Faranosov. "Analysis of Mode Coupling of Jet Near Field Puslations and Jet–Wing Interaction Noise". In: *Acoustical Physics* 66.1 (2020), pp. 33–43. ISSN: 15626865. DOI: `10.1134/S1063771020010029`.

[9] D. Casalino et al. "Aircraft noise reduction technologies: A bibliographic review". In: *Aerospace Science and Technology* 12.1 (2008), pp. 1–17. ISSN: 12709638. DOI: `10.1016/j.ast.2007.10.004`.

[10] A. V. G. Cavalieri et al. "Scattering of wavepackets by a flat plate in the vicinity of a turbulent jet". In: *Journal of Sound and Vibration* (2014). ISSN: 10958568. DOI: `10.1016/j.jsv.2014.07.029`.

[11] A. V.G. Cavalieri et al. "Axisymmetric superdirectivity in subsonic jets". In: *Journal of Fluid Mechanics* 704 (2012), pp. 388–420. ISSN: 00221120. DOI: `10.1017/jfm.2012.247`.

[12] S. C. Crow and F. H. Champagne. "Orderly structure in jet turbulence". In: *Journal of Fluid Mechanics* 48.3 (1971), pp. 547–591. ISSN: 14697645. DOI: `10.1017/S0022112071001745`.

[13] N. Curle. "The influence of solid boundaries upon aerodynamic sound". In: *Proceedings of the Royal Society of London. Series A. Mathematical and Physical Sciences* 231.1187 (1955), pp. 505–514. ISSN: 0080-4630. DOI: `10.1098/rspa.1955.0191`.

[14] Dantec. "How to measure turbulence with hot-wire anemometers - a practical guide". In: (2002).

[15] D. Dilba. "High-bypass engines of the future". In: *AEROPORT* (Feb. 2018). URL: `https://aeroreport.de/en/innovation/high-bypass-engines-of-the-future`.

[16] W. Dobrzynski. "Almost 40 Years of Airframe Noise Research: What Did We Achieve?" In: *Journal of Aircraft* 47.2 (Mar. 2010), pp. 353–367. ISSN: 0021-8669. DOI: `10.2514/1.44457`. URL: `https://arc.aiaa.org/doi/10.2514/1.44457`.

[17] G. Faranosov et al. "Azimuthal structure of low-frequency noise of installed jet". In: *AIAA Journal* 57.5 (2019), pp. 1885–1898. ISSN: 00011452. DOI: `10.2514/1.J057476`.

[18]   Federal Aviation Administration (FAA). *Code of Federal Regulations Title 14 Part 36 - Noise standards: type and airworthiness certification.* Tech. rep. 2021.

[19]   Romain Fiévet et al. "Acoustic source indicators using LES in a fully expanded and heated supersonic jet". In: *19th AIAA/CEAS Aeroacoustics Conference* May (2013), p. 186. DOI: `10.2514/6.2013-2193`.

[20]   R. Head and M. Fisher. "Jet/surface interaction noise - Analysis of farfield low frequency augmentations of jet noise due to the presence of a solid shield". In: *3rd Aeroacoustics Conference*. 76. Reston, Virigina: American Institute of Aeronautics and Astronautics, July 1976, pp. 0–7. DOI: `10.2514/6.1976-502`. URL: `http://arc.aiaa.org/doi/10.2514/6.1976-502`.

[21]   H. Hu, T. Saga, and T. Kobayashi. "Dual-plane stereoscopic PIV measurements in a lobed jet mixing flow". In: *43rd AIAA Aerospace Sciences Meeting and Exhibit - Meeting Papers* January (2005), pp. 7075–7091. DOI: `10.2514/6.2005-443`.

[22]   H. Hu et al. "Particle image velocimetry and planar laser-induced fluorescence measurements on lobed jet mixing flows". In: *Experiments in Fluids* 29.SUPPL. 1 (2000). ISSN: 07234864. DOI: `10.1007/s003480070016`.

[23]   Hui Hu et al. "Mixing process in a lobed jet flow". In: *AIAA Journal* 40.7 (2002), pp. 1339–1345. ISSN: 00011452. DOI: `10.2514/2.1793`.

[24]   D. L. Huff. "NASA Glenn's Contributions to Aircraft Engine Noise Research". In: *Journal of Aerospace Engineering* 26.2 (2013), pp. 218–250. ISSN: 0893-1321. DOI: `10.1061/(asce)as.1943-5525.0000283`.

[25]   D. L. Huff. "Noise Reduction Technologies for Turbofan Engines". In: *NASA/TM—2007-214495* September (2007), pp. 1–17. URL: `http://www.grc.nasa.gov/WWW/Acoustics/media/200405.Manchester.pdf`.

[26]   International Civil Aviation Organization (ICAO). *Environmental Protection - Volume 1 Annex 16 - Aircraft Noise.* Tech. rep. 2018.

[27]   K. Jones and D. P. Rhodes. "Aircraft Noise, Sleep Disturbance and Health Effects: A Review". In: (2013), p. 84.

[28]   P. Jordan and T. Colonius. "Wave packets and turbulent jet noise". In: *Annual Review of Fluid Mechanics* 45 (2013), pp. 173–195. ISSN: 00664189. DOI: `10.1146/annurev-fluid-011212-140756`.

[29]   M. Kœnig et al. "Jet-noise control by fluidic injection from a rotating plug: Linear and nonlinear sound-sourceÂ mechanisms". In: *Journal of Fluid Mechanics* 788 (2016), pp. 358–380. ISSN: 14697645. DOI: `10.1017/jfm.2015.670`.

[30]   K. G. Kriparaj, R. V. Paul, and P. S. Tide. "Numerical study on the flow characteristics of jets emanating from four lobed corrugated nozzles with varying lobe lengths". In: *International Journal of Applied Engineering Research* 13.3 (2018), pp. 36–39.

[31]   F. C. Lajús et al. "Spatial stability analysis of subsonic corrugated jets". In: *Journal of Fluid Mechanics* 876 (2019), pp. 766–791. ISSN: 14697645. DOI: `10.1017/jfm.2019.573`.

[32]   D. Lasagna, O. R. H. Buxton, and D. Fiscaletti. "On near-field coherent structures in circular and fractal orifice jets". In: (Feb. 2021), pp. 1–22. URL: `http://arxiv.org/abs/2102.05946`.

[33]   J. Lawrence, M. Azarpeyvand, and R. Self. "Interaction between a Flat Plate and a Circular Subsonic Jet". In: *17th AIAA/CEAS Aeroacoustics Conference (32nd AIAA Aeroacoustics Conference)*. June. Reston, Virigina: American Institute of Aeronautics and Astronautics, June 2011, pp. 5–8. ISBN: 978-1-60086-943-3. DOI: `10.2514/6.2011-2745`. URL: `https://arc.aiaa.org/doi/10.2514/6.2011-2745`.

[34]   Jack Lawrence. "Aeroacoustic Interactions of Installed Subsonic Round Jets". PhD thesis. 2014, p. 224.

[35]   H. Li et al. "Wavelet multiresolution analysis of stereoscopic particle-image-velocimetry measurements in lobed jet". In: *AIAA Journal* 40.6 (2002), pp. 1037–1046. ISSN: 00011452. DOI: `10.2514/2.1777`.

[36] M. J. Lighthill. "On sound generated aerodynamically II. Turbulence as a source of sound". In: *Proceedings of the Royal Society of London. Series A. Mathematical and Physical Sciences* 222.1148 (Feb. 1954), pp. 1–32. ISSN: 0080-4630. DOI: `10.1098/rspa.1954.0049`. URL: `https://royalsocietypublishing.org/doi/10.1098/rspa.1954.0049`.

[37] B. Lyu and A. P. Dowling. "An experimental study of the effects of lobed nozzles on installed jet noise". In: *Experiments in Fluids* 60.12 (2019), p. 176. ISSN: 14321114. DOI: `10.1007/s00348-019-2819-x`.

[38] B. Lyu and A. P. Dowling. "Experimental validation of the hybrid scattering model of installed jet noise". In: *Physics of Fluids* 30.8 (2018). ISSN: 10897666. DOI: `10.1063/1.5036951`. URL: `http://dx.doi.org/10.1063/1.5036951`.

[39] B. Lyu and A. P. Dowling. "Modelling installed jet noise due to the scattering of jet instability waves by swept wings". In: *Journal of Fluid Mechanics* 870 (2019), pp. 760–783. ISSN: 14697645. DOI: `10.1017/jfm.2019.268`.

[40] B. Lyu and A. P. Dowling. "On the mechanism and reduction of installed jet noise". In: *23rd AIAA/CEAS Aeroacoustics Conference, 2017* June (2017). DOI: `10.2514/6.2017-3523`.

[41] A. Magrini et al. "A review of installation effects of ultra-high bypass ratio engines". In: *Progress in Aerospace Sciences* 119.November (2020), p. 100680. ISSN: 03760421. DOI: `10.1016/j.paerosci.2020.100680`.

[42] M. Mancinelli, A. Di Marco, and R. Camussi. "Multivariate and conditioned statistics of velocity and wall pressure fluctuations induced by a jet interacting with a flat plate". In: *Journal of Fluid Mechanics* 823 (2017), pp. 134–165. ISSN: 14697645. DOI: `10.1017/jfm.2017.307`.

[43] V. Mengle et al. "Lobed Mixer Design for Noise Suppression Acoustic: and Aerodynamic Test Data Analysis". In: (Aug. 2002).

[44] P. Merati and N. J. Cooper. "Experimental investigation of flow behavior for scalloped and lobed mixers". In: *Advances in Mechanical Engineering* 8.9 (2016), pp. 1–17. ISSN: 16878140. DOI: `10.1177/1687814016668280`.

[45] R. Merino-Martínez et al. "Aeroacoustic design and characterization of the 3D-printed, open-jet, anechoic wind tunnel of Delft University of Technology". In: *Applied Acoustics* 170 (Dec. 2020), p. 107504. ISSN: 1872910X. DOI: `10.1016/j.apacoust.2020.107504`. URL: `https://linkinghub.elsevier.com/retrieve/pii/S0003682X20306083`.

[46] P. A.S. Nogueira, A. V.G. Cavalieri, and P. Jordan. "A model problem for sound radiation by an installed jet". In: *Journal of Sound and Vibration* 391 (2017), pp. 95–115. ISSN: 10958568. DOI: `10.1016/j.jsv.2016.12.015`.

[47] J. Panda and K. B.M.Q. Zaman. "Density fluctuation in asymmetric nozzle plumes and correlation with far field noise". In: *39th Aerospace Sciences Meeting and Exhibit* September 2014 (2001). DOI: `10.2514/6.2001-378`.

[48] V. P. Paul, K. G. Kriparaj, and P. S. Tide. "Numerical predictions of the flow characteristics of subsonic jet emanating from corrugated lobed nozzle". In: *Aircraft Engineering and Aerospace Technology* 92.7 (2020), pp. 955–972. ISSN: 17488842. DOI: `10.1108/AEAT-03-2019-0041`.

[49] S. Piantanida et al. "Scattering of turbulent-jet wavepackets by a swept trailing edge". In: *The Journal of the Acoustical Society of America* 140.6 (2016), pp. 4350–4359. ISSN: 0001-4966. DOI: `10.1121/1.4971425`.

[50] S. B. Pope. *Turbulent Flows*. Vol. 21. 1. Cambridge University Press, Jan. 2002, pp. 139–140. ISBN: 9780521591256. DOI: `10.1016/S0997-7546(01)01166-9`. URL: `https://www.cambridge.org/core/product/identifier/9780511840531/type/book%20https://linkinghub.elsevier.com/retrieve/pii/S0997754601011669`.

[51] A. Proença, J. Lawrence, and R. Self. "Investigation into the turbulence statistics of installed jets using hot-wire anemometry". In: *Experiments in Fluids* 61.10 (2020), pp. 1–19. ISSN: 14321114. DOI: `10.1007/s00348-020-03054-x`.

[52] A. R. Proença. "Aeroacoustics of isolated and installed jets under static and in-flight conditions". PhD thesis. 2018, p. 229.

[53] L. Rego et al. "Jet-installation noise and near-field characteristics of jet-surface interaction". In: *Journal of Fluid Mechanics* 895 (2020). ISSN: 14697645. DOI: `10.1017/jfm.2020.294`.

[54] A. A. Rejniak and A. Gatto. "Application of lobed mixers to reduce drag of boat-tailed ground vehicles". In: *Journal of Applied Fluid Mechanics* 12.6 (2019), pp. 1729–1744. ISSN: 17353645. DOI: `10.29252/JAFM.12.06.29742`.

[55] S. W. Rienstra and A. Hirschberg. *An Introduction to Acoustics*. Eindhoven University of Technology, 2021, pp. 9–13.

[56] R. Rusz. "Design of a Fully Anechoic Chamber". In: (2015). URL: `http://www.diva-portal.org/smash/get/diva2:893785/FULLTEXT01.pdf`.

[57] F. Scarano. *Course Reader: Experimental Aerodynamics*. 2013.

[58] J. G. Shearin. "Investigation of Jet-Installation Noise Sources Under Static Conditions." In: *NASA Technical Paper* (1983). ISSN: 01488341.

[59] A. Sinha et al. "Parabolized stability analysis of jets from serrated nozzles". In: *Journal of Fluid Mechanics* 789 (2016), pp. 36–63. ISSN: 14697645. DOI: `10.1017/jfm.2015.719`.

[60] M. J. T. Smith. *Aircraft Noise*. Cambridge Aerospace Series. Cambridge University Press, 1989. DOI: `10.1017/CBO9780511584527`.

[61] C. K.W. Tam et al. "The sources of jet noise: Experimental evidence". In: *Journal of Fluid Mechanics* 615 (2008), pp. 253–292. ISSN: 00221120. DOI: `10.1017/S0022112008003704`.

[62] C. E. Tinney, M. N. Glauser, and L. S. Ukeiley. *Low-dimensional characteristics of a transonic jet. Part 1. Proper orthogonal decomposition*. Vol. 612. 2008, pp. 107–141. DOI: `10.1017/S0022112008002978`.

[63] C. E. Tinney, L. S. Ukeiley, and M. N. Glauser. "Low-dimensional characteristics of a transonic jet. Part 2. Estimate and far-field prediction". In: *Journal of Fluid Mechanics* 615 (2008), pp. 53–92. ISSN: 00221120. DOI: `10.1017/S0022112008003601`.

[64] J. E.F. Williams and L. H. Hall. "Aerodynamic sound generation by turbulent flow in the vicinity of a scattering half plane". In: *Journal of Fluid Mechanics* 40.4 (1970), pp. 657–670. ISSN: 14697645. DOI: `10.1017/S0022112070000368`.

[65] K. B.M.Q. Zaman, F. Y. Wang, and N. J. Georgiadis. "Noise, turbulence, and thrust of subsonic freejets from lobed nozzles". In: *AIAA Journal* 41.3 (2003), pp. 398–407. ISSN: 00011452. DOI: `10.2514/2.1990`.